

Nuclear Science User Facilities 995 MK Simpson Blvd. Idaho Falls, ID 83401-3553 nsuf.inl.gov

On the front cover:

A surrogate TRISO particle undergoing X-ray computed tomography examination. X-ray computed tomography is a nondestructive technique that can provide 3-D information, allowing researchers to gain insight on nuclear materials' performance after irradiation testing.

Disclaimer

This information was prepared as an account of work sponsored by an agency of the U.S. Government. Neither the U.S. Government nor any agency thereof, nor any of their employees, makes any warranty, expressed or implied, or assumes any legal liability or responsibility for the accuracy, completeness, or usefulness, of any information, apparatus, product, or process disclosed, or represents that its use would not infringe privately owned rights. References herein to any specific commercial product, process, or service by trade name, trade mark, manufacturer, or otherwise, does not necessarily constitute or imply its endorsement, recommendation, or favoring by the U.S. Government or any agency thereof. The views and opinions of authors expressed herein do not necessarily state or reflect those of the U.S. Government or any agency thereof.

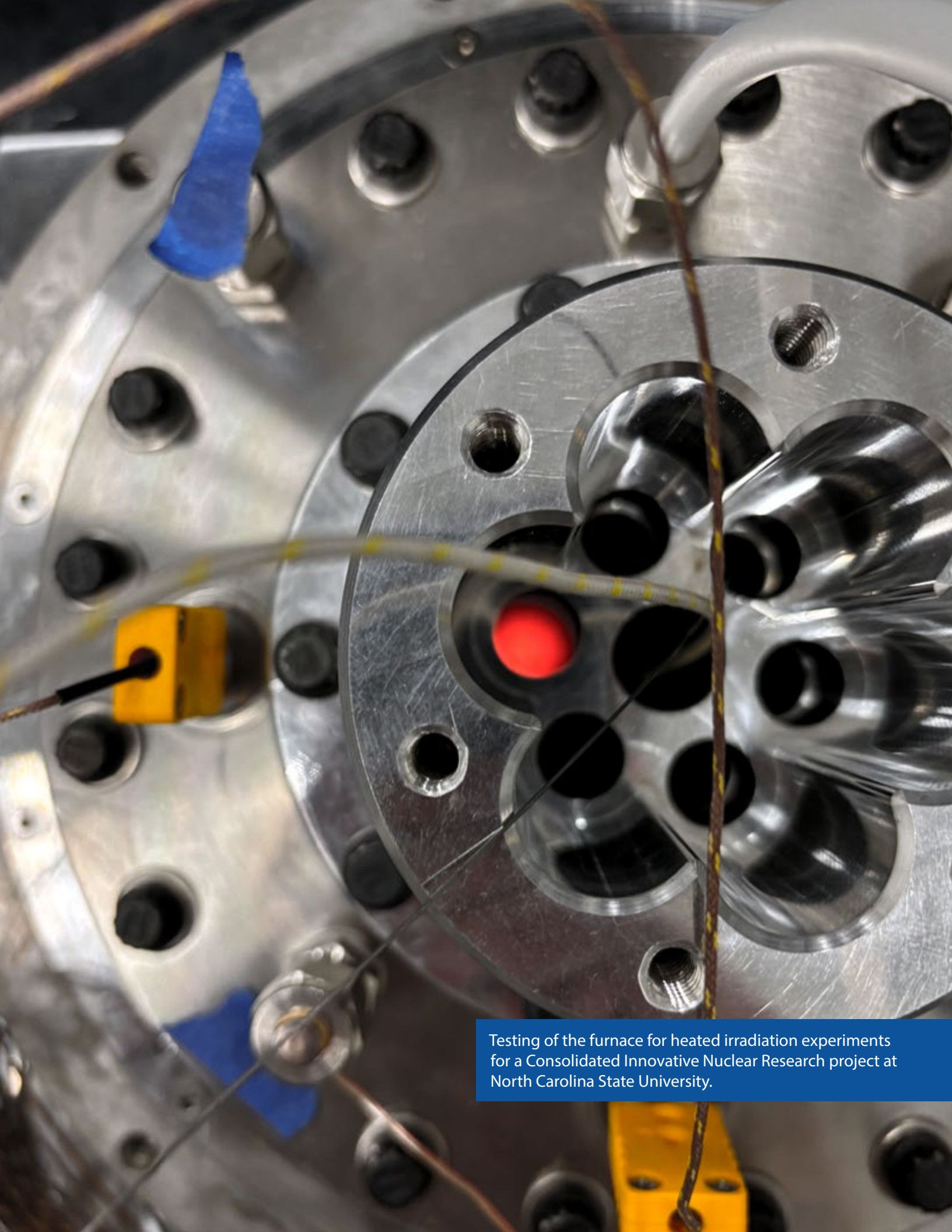
Editors: Alexis Starks, Anna Podgorney, Cory Rodgers Hatch, Devin Bodkin, Jeffrey Pinkham, Barney Hadden

Writers: Alexis Starks, Joel Hiller, Paul Menser, Kelly Cunningham

Graphic Designer: Dallas McCary

TABLE OF CONTENTS

	Nuclear Science User Facilities	
	Our NSUF Program Office Team	
	From the Director	6
	NSUF Overview	
	NSUF by the Numbers	
	NSUF Across the Nation	1(
	NSUF User Institutions	1
	Facilities and Capabilities	12
	Facility and Capability Updates	
	Digital Tools and Resources	
	Highlights from the Year	24
	NSUF Awarded Projects	
	FY24 Awarded Projects	20
	Completed Projects	
	Completed Projects	40
I	Resources	
	List of Acronyms	210
ı		245



OUR NSUF PROGRAM OFFICE TEAM



Collin KnightDeputy Director
collin.knight@inl.gov



ja

Keith Jewell, Ph.D. Chief Scientist james.jewell@inl.gov







Rongjie Song, Ph.D. Chief Scientist rongjie.song@inl.gov

Matt Anderson, Ph.D. High Performance Computing Lead matthew.anderson2@inl.gov





Kelly CunninghamNuclear Fuels and Materials
Library Administrator
kelly.cunningham@inl.gov

Matthew Arrowood Experiment Manager matthew.arrowood@inl.gov





Jason Hales, Ph.D. High Performance Computing Liaison jason.hales@inl.gov







Michael Heighes Mechanical Properties Technical Lead michael.heighes@inl.gov

Travis Howell Experiment Manager travis.howell@inl.gov





Alexis Starks *Communications Lead alexis.starks@inl.gov*

Bradlee Jensen Nuclear Research Data System Lead bradlee.jensen@inl.gov





Renae TrippAdministrative Assistant renae.tripp@inl.gov

Kip Kleimenhagen Experiment Manager kip.kleimenhagen@inl.gov





Derek WhippleConsolidated Innovative
Nuclear Research
Program Administrator
j.whipple@inl.gov

Brett MillerPlanning and Financial
Controls Analyst
brett.miller@inl.gov





Dain WhiteSoftware Engineering
Technical Lead
dain.white@inl.gov

Alina Montrose Experiment Manager alina.montrose@inl.gov





Eric Whiting
Senior Advisor, Scientific
Computing and Artificial
Intelligence
eric.whiting@inl.gov

Anna Podgorney Rapid Turnaround Experiment Program Administrator anna.podgorney@inl.gov

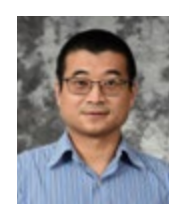




Malwina Wilding Instrumentation Lead malwina.wilding@inl.gov

Aaron Russell Experiment Manager aaron.russell@inl.gov





Peng Xu, Ph.D. Industry User Liaison peng.xu@inl.gov

DIRECTOR



Brenden Heidrich, Ph.D. *Director brenden.heidrich@inl.gov*

2024 was an excellent year for NSUF, with a record number of awards for the post-COVID-19 era. We have steadily built our portfolio of nuclear materials user access research projects over the last seventeen years to 92 Rapid Turnaround Experiments (RTE) and seven Consolidated Innovative Nuclear Research (CINR) awards totaling \$13 million in access funding for researchers last year. This success is thanks to our local program office here at the Idaho National Laboratory (INL) and our federal team at the U.S. Department of Energy Office of Nuclear Energy (DOE-NE). Our devoted community of users has stayed with us the whole time through the challenges of 2020 to 2022, when most research was done remotely, to the current high, which is approaching our peak years from 2017 to 2019. Throughout this time, the NSUF program office has ensured that our goals align with the needs of our research community.

In 2024, we saw a few changes to NSUF. The Office of Reactor Fleet and Advanced Reactor Deployment reorganized and NSUF found itself in the newly formed Office for Strategic Crosscuts, which is still led by NE-7 Deputy Assistant Secretary Alice Caponiti. The Nuclear Energy University
Program was also moved into the
new office, so it would remain easy
to collaborate in the CINR funding
opportunity, where research and
development funding could be tied
to access to NSUF capabilities. U.S.
universities have an unequalled
opportunity through these two
programs to pursue nuclear energy
research topics.

The NSUF program office also had its own changes in 2024. Our longtime financial lead and CINR coordinator, Lindy Bean, retired. J. Derek Whipple joined NSUF from within INL. Derek has been working with users, partners and our DOE sponsor to cover this essential part of the program. Brett Miller also came onboard last year to manage the program's day-today financial activities. Brett is tied into program activities and reports to INL and DOE on these matters. Finally, Jason Hales joined as a senior advisor on computational science. Jason's expertise will be leveraged to integrate the NSUF data with the larger modeling and simulation efforts that are supported by DOE-NE and critical to U.S. nuclear energy.

Several new initiatives started in 2024 that change the way NSUF

supports our community. First, we held a special call in April 2024 for our first set of Super RTE access awards. The idea arose from our Industry Engagement Meeting at EPRI headquarters in Charlotte, North Carolina, in September 2023. We had noted that our commercial users didn't apply to the RTE calls in the same proportion as they did to the larger CINR calls. In summary, the nuclear industry vendors thought that the RTE rules made the awards too small for their needs. With the support of DOE-NE leadership, we formed the Super RTE, allowing roughly twice as large a scope of work as the "regular" RTEs. I underestimated the allure that the larger projects would have for all types of researchers in the NSUF community. We planned an additional \$1 million for five to 10 of the larger awards, expecting two dozen applications. The Super RTE call straddled the second and third normal RTE calls and butted up against the CINR pre-applications. Our user community responded and submitted almost 50 proposals. We worked with our DOE-NE team and found sufficient funding to support 13 Super RTE awards from 13 principal investigators at nine institutions and utilizing 13 NSUF capabilities at 10 partner institutions. Based on the success of 2024, we have integrated the Super RTE into our normal planned CINR and RTE call structure. Now we have rightsized calls for all types of research projects available to our community.

The Super RTEs show how input from the user community can influence how NSUF supports nuclear energy materials research.

We have also initiated efforts to secure and disseminate the data and results from NSUF-supported access projects. All NSUF projects are tracked in our web-based system and progress can be updated by our partner facilities directly in the system. This system helps keep the program office informed about the 100-plus projects underway at any given time. The system also helps ensure that users have their projects closed out properly so they can apply for more funding. A closeout in the system also triggers the request for a completion report for RTEs and for data to be uploaded into our new Nuclear Research Data System (NRDS). For future projects, the system is designed so NSUF partners will use the NRDS for project data storage. NRDS is located on the INL high-performance computing architecture, so data storage serves only as its foundational capability. Visualization, analysis and artificial intelligence/machine learning tools can be applied to the project data all within a web browser. Data management and sharing guidance will be developed in 2025, governing how NSUF data is generated, stored, used, shared and eventually released to the public. We will hold meetings and training sessions with users, partners and stakeholders as we develop an implementation plan.

In 2025 and beyond, NSUF will continue to evolve to support the nuclear energy materials community and to align with DOE-NE goals. NSUF has pivoted to adapt to changes in reactor technologies and add new capabilities, whether developed within the nuclear research community or borrowed from other fields. We must adapt to changes within our program office as familiar colleagues move on to new opportunities, making way for new team members who will soon become familiar faces in their roles supporting our community of users and partners. We greatly appreciate the support of our users in making the new team members feel welcome. There will be more changes to come, some stemming from ideas raised by the users and some coming from outside as technology or direction changes. We intend to update our program strategic plan this year. That update will reflect how we operate in 2025 and highlight key program objectives in support of the DOE-NE mission.

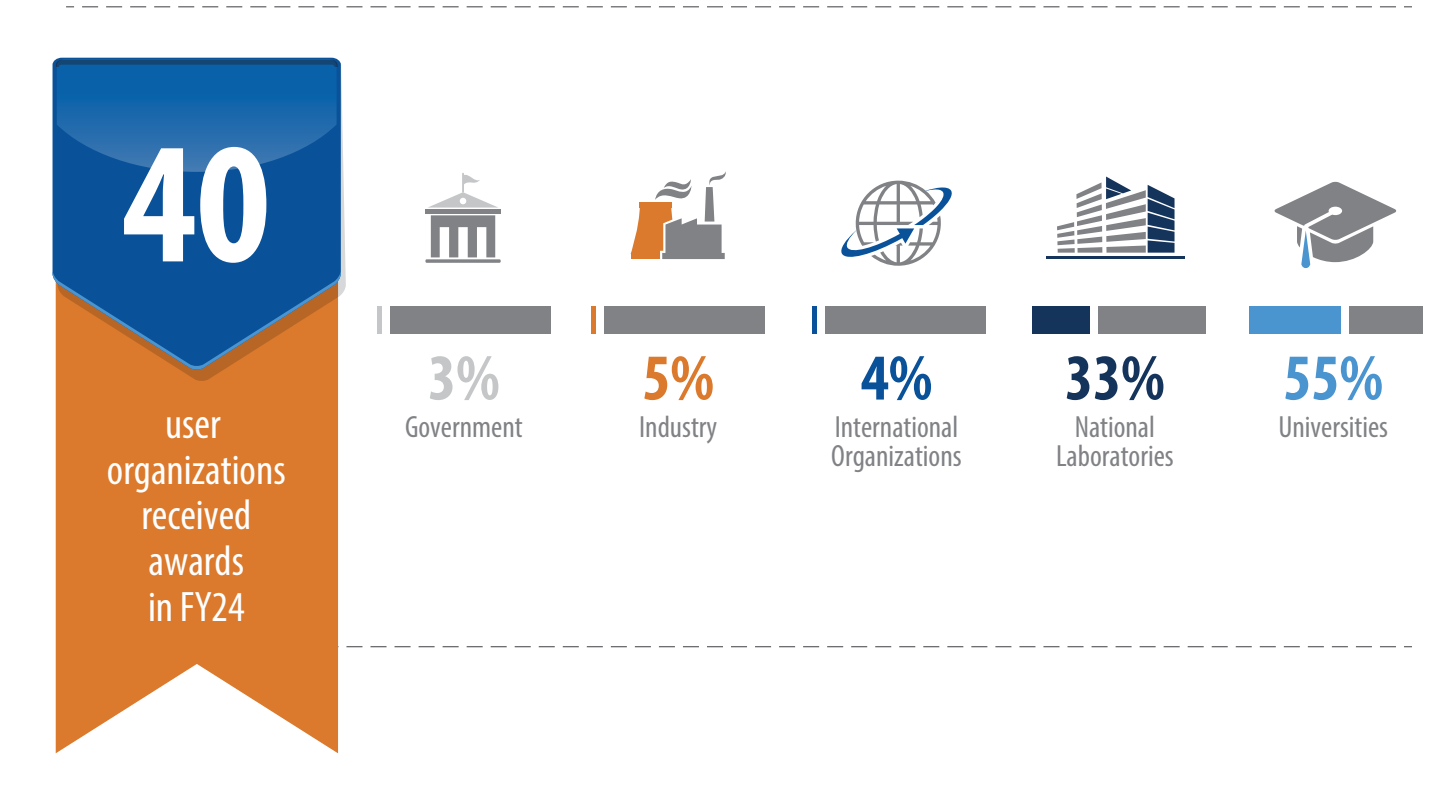
Brenden Heidrich, Ph.D. PE

Jill

NSUF BY THE NUMBERS

Note: Numbers for fiscal year 2024 (FY24) only.

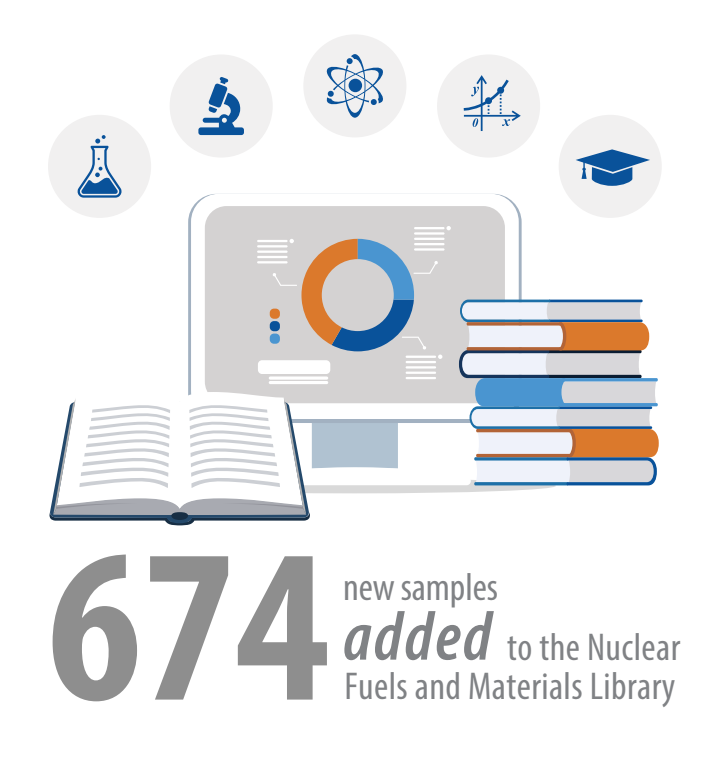


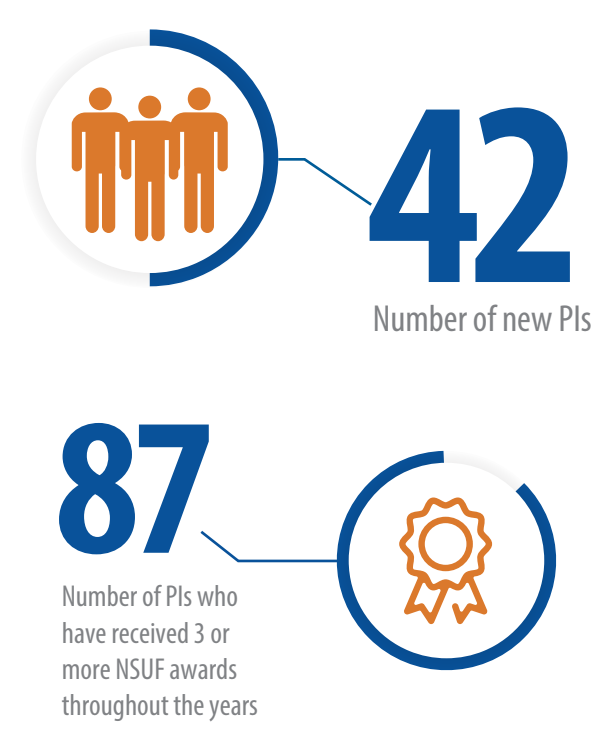




164 NSUF publications

PERCENT of projects involve a graduate student, either as a PI or a collaborator





NSUF ACROSS THE NATION











































NSUF User Institutions (FY24)

Austrailia

Australian Nuclear Science and Technology Organisation

California

General Atomics

Kairos Power LLC

University of California-Berkeley University of California-Irvine

Canada

University of Calgary

Florida

University of Florida

Idaho

Idaho National Laboratory Idaho State University

University of Idaho

llinois

Argonne National Laboratory University of Illinois at Urbana-Champaign

Indiana

Purdue University

Italy

Eni S.p.A.

Istituto Italiano di Tecnologia

Politecnico di Milano

Kansas

Kansas State University

Maryland

U.S. Nuclear Regulatory Commission

Michigan

University of Michigan

New Mexico

Los Alamos National Laboratory

New York

Brookhaven National Laboratory Rensselaer Polytechnic Institute

North Carolina

North Carolina State University

Ohio

NASA Glenn Research Center

Oregon

Oregon State University

Pennsylvania

Carnegie Mellon University
Pennsylvania State University

Westinghouse Electric Company

South Carolina

Clemson University

Tennessee

Oak Ridge National Laboratory

Texas

Texas A&M University
University of North Texas

University of Texas at San Antonio

Utah

Dominion Engineering

Washington

Pacific Northwest National Laboratory

Washington, D.C.

Electric Power Research Institute

Wisconsin

University of Wisconsin-Madison

FACILITIES AND CAPABILITIES

Institution	Facility				
Argonne National Laboratory	Activated Material Laboratory at the Advanced Photon Source	✓		✓	√
	Intermediate Voltage Electron Microscopy - Tandem Facility		i	✓	
	Irradiated Material Laboratory	√		✓	
Brookhaven National Laboratory	NSLS II X-ray Powder Diffraction (XPD) Beamline				√
Center for Advanced Energy Studies	Microscopy and Characterization Suite	√		✓	
Idaho National Laboratory	Analytical Laboratory			✓	
	Electron Microscopy Laboratory	√		✓	
	Irradiated Materials Characterization Laboratory	√		✓	
	Fuels and Applied Science Building (FASB)	√		✓	
	Fuels and Applied Science Building (FASB) Gamma Irradiator		γ		
	Energy Innovation Laboratory Irradiation Suite		γ		
	Hot Fuel Examination Facility			√	
	Advanced Test Reactor Gamma Irradiation Facility		γ		
Lawrence Livermore National Laboratory	Center for Accelerator Mass Spectroscopy		i		
Los Alamos National Laboratory	Lujan Center Beamlines	√		✓	√
	Plutonium Surface Science Laboratory			✓	
Massachusetts Institute of Technology	MIT Nuclear Reactor Laboratory		n	✓	
North Carolina State University	Nuclear Reactor Program		n		√

Neutron Irradiation

V Gamma Irradiation

Ion Beam Irradiation

✓ Irradiated Sample Preparation

✓ Post Irradiation Examination (PIE)

✓ Characterization Beamline (Neutron, Positron, or X-ray)

Institution	Facility				
k Ridge National Laboratory	Low Activation Materials Development and Analysis Facility	√		√	
	Irradiated Fuels Examination Laboratory	√		√	
	Irradiated Materials Examination and Testing Facility			√	
	Gamma Irradiation Facility (HFIR-GIF)		γ		
Pacific Northwest National Laboratory	Radiochemistry Processing Laboratory			√	
	Materials Science and Technology Laboratory			√	
Pennsylvania State University	Radiation Science and Engineering Center		nγ		✓
Purdue University	Interaction of Materials with Particles and Components Testing Facility		i		
Sandia National Laboratories	Ion Beam Laboratory		i	√	
	Gamma Irradiation Facility		γ		
Texas A&M University	Accelerator Laboratory		i		
The Ohio State University	Nuclear Reactor Laboratory		nγ		√
University of California, Berkeley	Nuclear Materials Laboratory	√		√	
University of Florida	Materials Characterization Facility	√		√	
University of Michigan	Michigan Ion Beam Laboratory		i	√	
	Irradiated Materials Testing Laboratory			√	
University of Texas at Austin	Nuclear Engineering Teaching Laboratory		n		✓
University of Wisconsin	Characterization Laboratory for Irradiated Materials			√	
OHIVEISITY OF WISCOUSIII	Wisconsin Tandem Accelerator Ion Beam		i		
Westinghouse	Churchill Laboratory Services	√		√	

UPDATES

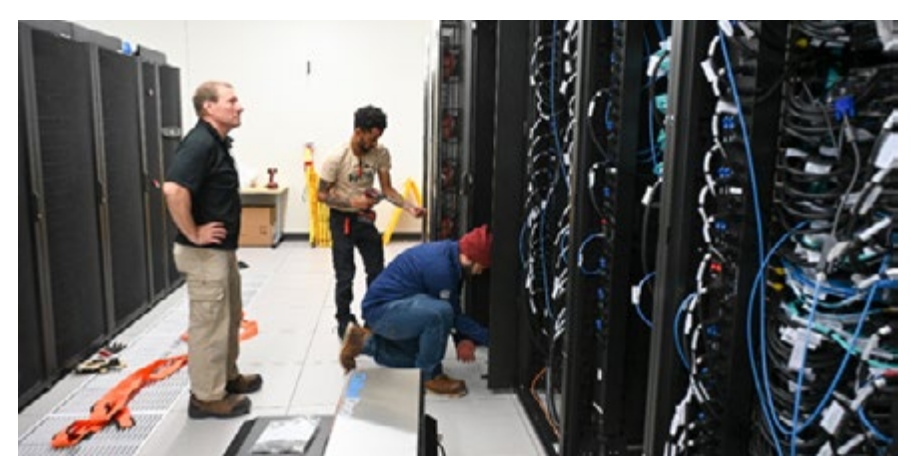
A smooth ride to the future of nuclear

INL's new supercomputer paves the way for advanced nuclear research

By Joel Hiller, INL Communications

If you've ever driven to a remote area, you may have noticed that the drive time is much longer on dirt roads. But once those roads are paved, you can get where you need to go much more quickly. The path to deploying advanced nuclear reactors isn't a straight line, but a new supercomputer named Bitterroot recently installed at the Idaho National Laboratory (INL) is helping to speed the journey through improved access to modeling and simulation tools.

High-performance computing allows engineers and scientists to model a wide variety of complex variables before construction begins, such as how steel or concrete degrade over time or what byproducts build up in nuclear fuel. Through advanced computer codes running on these machines, they can even model how a nuclear power plant will weather seismic events. This allows them to anticipate the reactor's overall performance, safety and longevity.



The installation process for the Bitterroot supercomputer.

NSUF provides a suite of dedicated computing resources at INL for researchers from industry, universities, national laboratories and federal agencies. Now, with the installation of Bitterroot, the NSUF High Performance Computing team at INL have another resource to help speed the journey for nuclear developers around the country. Bitterroot is the name of an Idaho mountain range and continues INL's tradition of naming its high-performance computers after Idaho landmarks.

Bitterroot will supplement the lab's existing supercomputers at its high-performance computing data center — the Collaborative

Computing Center — by adding an additional 43,008 computer processing cores with faster chips and a new capability: highbandwidth memory. This new memory will improve performance for memory-bandwidth-limited applications like the Multiphysics **Object Oriented Simulation** Environment, better known as MOOSE, framework. MOOSE is the foundation for many of the tools that aid advanced nuclear research that support the existing reactor fleet as well as the development and eventual licensing of new designs.

Supercomputing for nuclear innovation

"INL's high performance computing is unique in that 80-90% of our compute cycles are dedicated to nuclear energy research," said Matthew Anderson, manager of the High Performance Computing group. "Bitterroot brings us a new capability and additional capacity as we prepare for additional longterm investments in new computing resources." As the lab makes ongoing investments in hardware such as Bitterroot, it increases INL's ability to support the growing need for modeling and simulation across the nuclear industry.

In addition to access to Bitterroot and the other supercomputers at INL, NSUF provides organizations across the country access to experimental capabilities that would otherwise be unavailable or cost prohibitive, including irradiation and post-irradiation examination facilities for nuclear energy fuels and materials research and development.

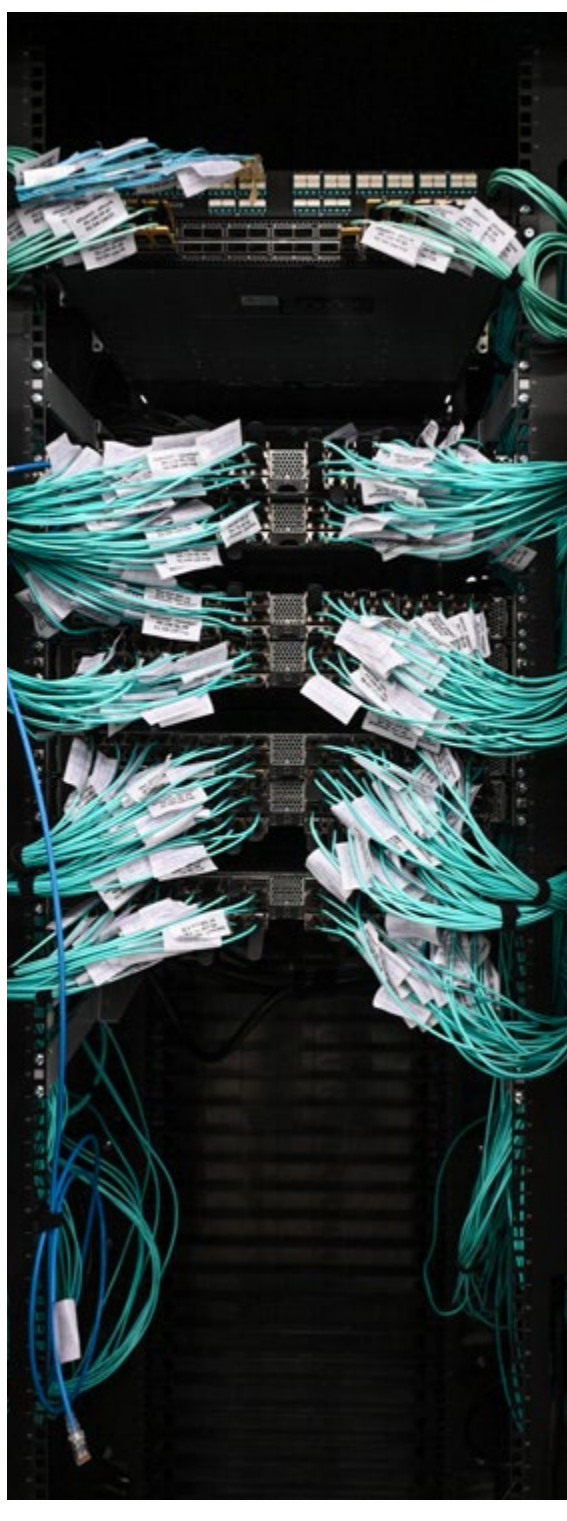
"Not every company in the nuclear industry has its own gamma irradiation facility or supercomputer, but we're all working toward the same goal of deploying more U.S. nuclear energy," said NSUF Director Brenden Heidrich. "You never know who will make the next breakthrough, and partnerships like NSUF are vital to help level the playing field."

The Collaborative Computing Center at INL

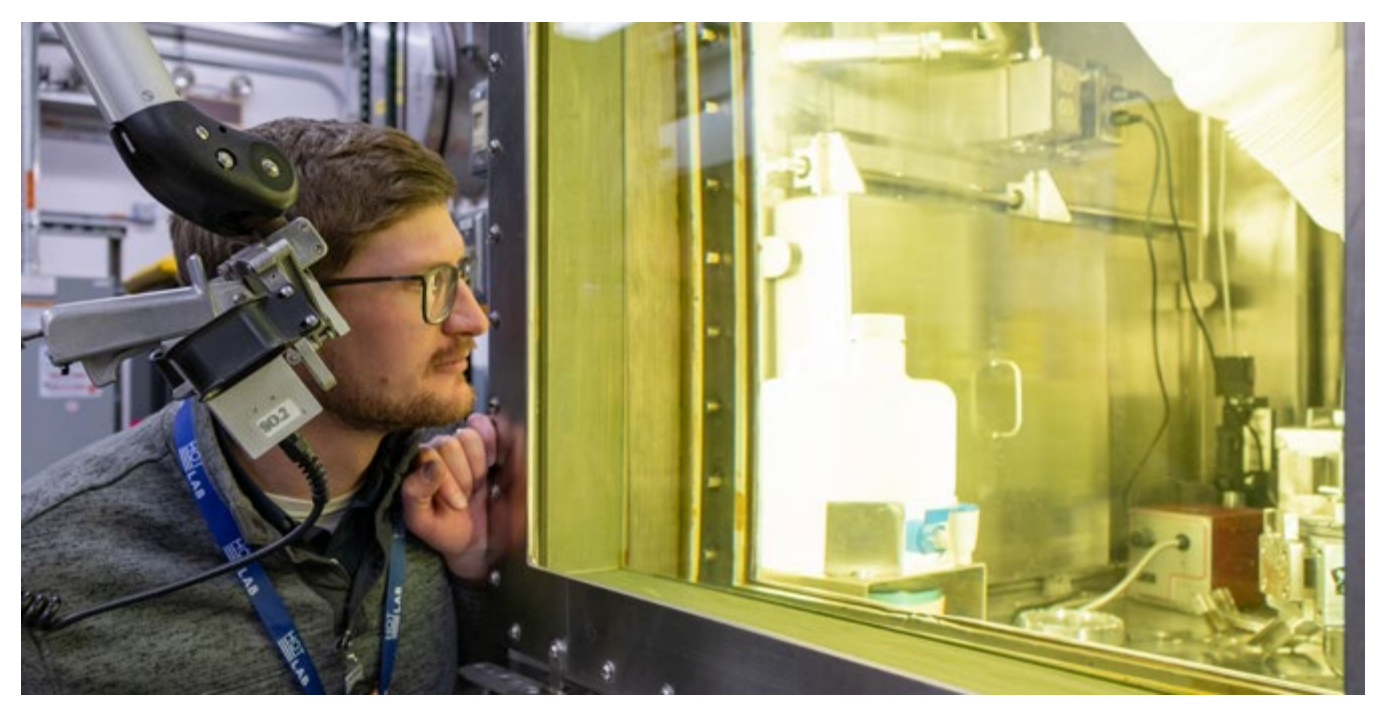
To support high performance computing capabilities and provide a dedicated home for its supercomputers, INL partnered with the state of Idaho to build the Collaborative Computing Center, known as C3, which was completed in 2019. C3 is a 67,000-square-foot facility equipped to host multiple supercomputers. In addition to Bitterroot, C3 is also home to NSUF High Performance Computing's flagship supercomputer Sawtooth, ranked as the 37th fastest performing supercomputer when it was installed in 2020, along with the lab's other systems: Lemhi, Hoodoo and Viz. In fiscal year 2023, INL supercomputers provided users with 939 million core hours on more than 3.7 million jobs.

Bitterroot arrived at INL in March 2024. Following installation and extensive testing activities, it was made available to users a few months later on June 18.

Supercomputers like Bitterroot are improving the nuclear industry's ability to develop and qualify new reactor technologies and avoid delays on the road to commercial deployment. To learn more about how you can access Bitterroot and INL's other supercomputers, visit the INL's HPC website at https://inl.gov/hpc.



Switch rack for Bitterroot facilitating communication among all nodes. The green cables are fiber optic, while the switches include a mix of Ethernet and OmniPath types.



Researcher Phil Petersen observes testing in process on the AMTS.

Stretching the limits

New miniaturized tensile testing comes to the Idaho National Laboratory

By Paul Menser, INL Communications

A new automated testing capability, called the Automated Mechanical Testing System (AMTS), is being used to help accelerate mechanical testing of irradiated materials at the Idaho National Laboratory. The system aims to reduce the time and cost for routine post-irradiation testing in hot cells.

Next-generation materials and manufacturing technologies are currently being explored for use in advanced reactor concepts. This includes several innovative manufacturing technologies for new

and existing materials that offer promise to reduce costs, streamline supply chains, and utilize novel and innovative complex shapes. Before these new materials and manufacturing methods can be qualified for use by the nuclear energy industry, they need to undergo extensive mechanical and environmental testing to evaluate their performance. This typically includes neutron irradiation in a test reactor such as the Advanced Test Reactor to understand how a material responds to radiation damage. However, the high radiation levels accumulated during these tests make characterizing them more complex.

To meet these challenges, INL helped develop the Automated Mechanical Testing System (AMTS),

a mechanical testing device located in a hot cell at the Materials and Fuels Complex's Fuels and Applied Science Building (FASB). The AMTS measures the tensile properties of materials safely and efficiently.

Advantages of automation and miniaturization for irradiated materials

Tensile testing involves pulling apart dog-bone-shaped specimens to measure mechanical properties, including tensile strength and elongation. Until now, tensile tests on radiological materials that have undergone neutron irradiation have been done in a hot cell with a universal test machine that can only perform one test at a time. The process of loading and unloading individual specimens and associated manual hot cell operation can be



Tensile samples are loaded onto the AMTS cartridge for measuring mechanical properties.

a long and challenging process. The AMTS, by comparison, can automatically perform up to 24 individual tests in sequence, using specimens that are eight to 12 times smaller than those used in universal test machines. The system aims to provide a high-throughput solution for tensile testing to increase hot cell testing efficiency while reducing operation costs through automation.

The use of miniature specimens is particularly beneficial to the nuclear industry, said Jason Schulthess, the INL senior staff scientist who has guided AMTS's development and installation in the FASB hot cell. FASB houses small hot cells, gloveboxes, hoods, and other equipment supporting research and development related to nuclear fuel fabrication, used fuel treatment

options, and nuclear waste management. Weighing just over 30 pounds and with a footprint of roughly two feet, AMTS fits right in.

Designing safer and longer-lived nuclear reactor components depends on extensive characterization, which involves exposing test materials to extreme levels of radiation. Not only has AMTS sped up the testing process, it has minimized the risks associated with material handling and characterization. Testing smaller specimens reduces the amount of radioactive waste for disposal and the risk of harmful exposure to researchers.

Talk leads to action

AMTS started with a conversation at a conference in 2018 between

researchers from INL and Missouri University of Science and Technology, which eventually led to an awarded project called "Advanced Mechanical Testing System (AMTS) for highly irradiated materials," under the Department of Energy Small Business Technology Transfer (STTR) program. As part of the award, under STTR Phase II funding, Product Innovation and Engineering LLC, a company based in St. James, Missouri, successfully deployed an AMTS to the INL hot cells.

"We recognized our throughput capacity on tensile materials was pretty limited," Schulthess said. "This is useful to anyone interested in developing new materials or pushing the boundaries of existing materials."

Automated data analysis

To automate data analysis, the design team sought to incorporate software that could use digital image correlation, a non-contact optical technique that uses cameras to measure deformation and strain in materials. Digital image correlation has several advantages over strain gauges and extensometers. It measures the entire optically visible image, providing more data than point-based methods, and can measure a wide range of shapes, sizes and movements. Digital image correlation doesn't require mechanical contact with a test object and can resolve measurements to sub-pixel accuracy.

To protect the camera and other electronics from the intense radiation inside the FASB hot cell, none of these objects have a direct line of sight with the irradiated specimens. "There are always challenges when you're building something from scratch," Schulthess said.

Creating more efficiencies

AMTS offers the advantage of moving tensile testing activities from the Materials and Fuels
Complex's Hot Fuel Examination
Facility (HFEF) to FASB, helping to alleviate scheduling conflicts with other HFEF programs, projects or activities that use HFEF to execute work. At a time when demand for the Materials and Fuels Complex's capabilities is growing, this makes for a better distribution of resources and a more efficient operation.

Wider implications

In the wider world of specimen design and mechanical testing, AMTS could have an impact as well, said Sriram Praneeth Isanaka, assistant research professor at the Missouri University of Science and Technology and principal investigator on the project. Aerospace and high-tech manufacturing immediately come to mind. Whatever the industry is, defects in 3-D printed materials are smaller and harder to detect than those in traditional materials. A tensile testing machine that can fit on a tabletop could be welcome in a lot of places. Meeting Schulthess and his fellow INL researchers and engaging in the AMTS project was a "happy coincidence," he said.



Researcher Phil Petersen observes the live data collection during a tensile test on the AMTS.

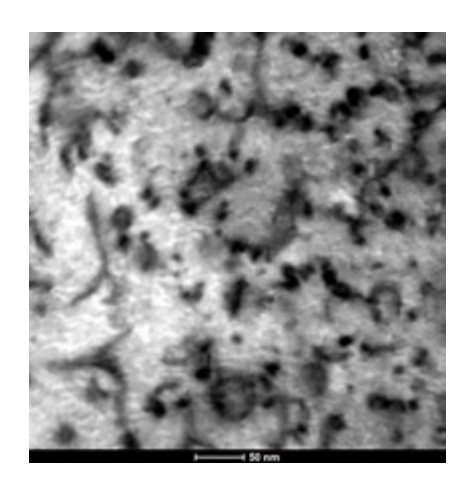


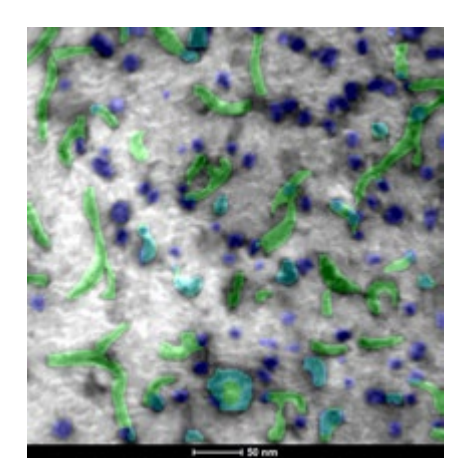
RESOURCES

Nuclear Research Data System

In November 2024, the Nuclear Research Data System (NRDS) companion site, the NRDS Portal (nrds-portal.inl.gov), was released to users. This site provides a collaborative space for principal investigators and instrument scientists to work with data, including the ability to add metadata, upload files and review datasets. The NRDS portal provides an avenue to integrate experimental capabilities with computation and data resources to drive user collaboration, accelerate innovation and improve data reproducibility. In addition to the previous models on the NRDS system, a new artificial intelligence/machine-learning model has been developed called Predictive Automation of Novel Defect Anomalies (PANDA). This model segments dislocation loop and line defects in a transmission electron microscopy (TEM) image, thus enhancing the capabilities of the NRDS ecosystem. For more information on PANDA, please visit our GitHub repository at github.com/idaholab/PANDA. Upcoming publications that use this innovative model will be accessible on the NRDS website.

NRDS is a public-facing data storage solution for nuclear energy researchers, featuring integrated computational resources such as artificial intelligence-enabled hardware and access to graphics processing units.





(Left) Transmission electron microscopy of ion irradiated ODS MA956 collected using an FEI Tecnai G2 F30 S/TEM at the Microscopy and Characterization Suite at the Center for Advanced Energy Studies. (Right) The microscopy image after NRDS enhancement, run through a segment dislocation loop and line defects machine learning model using the You Only Look Once format method.

Nuclear Fuels and Materials Library

The Nuclear Fuels and Materials Library (NFML) is the largest global open archive of irradiated fuel and material samples and related technical data. Owned by the U.S. Department of Energy Office of Nuclear Energy and curated by NSUF, the library includes samples from decommissioned reactors and other sources. Established in 2007, the NFML migrated historical data to an online database in 2016. It holds over 9,600 samples and features a search engine and sample tracking system. Researchers can access the library at nsuf.inl.gov. The NFML continues to evolve to support nuclear energy research.

In FY24, new library samples were added through donations from a cooperative research and development agreement and material harvested from two nuclear power plants and a variety of other sources.

Advanced Test Reactor-Irradiated Alloys XM-19 and X-750

A past cooperative research and development agreement between the Idaho National Laboratory (INL) and the Electric Power Research Institute conducted a series of Advanced Test Reactor (ATR) irradiations to test reactor structural materials, specifically nickel-based superalloy X-750 and nitrogen-

strengthened austenitic stainlesssteel XM-19. This pilot project aimed to set guidelines for future ATR NSUF research. The irradiated samples were then added to the NFML in FY24.

The successful completion of the Electric Power Research Institute Pilot Project demonstrated INL's capability to perform industry collaborative high neutron fluence experiments in environmental conditions typical for boiling water reactors. The project provided quantitative data on crack growth rates and fracture toughness of irradiated alloys X-750 and XM-19, irradiated material for micro-structural examination, and irradiated material for subsequent detailed investigation of crack growth mechanisms.

Nuclear power plant harvested acquisitions

The NFML is gaining national and international recognition as a repository for invaluable nuclear materials essential for research. As nuclear power plants are decommissioned globally, there is a need to harvest, store and curate these materials before they are lost. The NFML uniquely offers access to irradiated and harvested materials from nuclear power plants and industrial experiments, though more harvested material is needed. Aligning research needs

with decommissioning schedules remains challenging. Adding these materials to the library will enhance its value for NSUF users and nuclear energy research.

Zion Unit 1 Nuclear Power Plant: Reactor pressure vessel base metal samples

The Light Water Reactor
Sustainability (LWRS) program and other organizations obtained well-characterized materials from the Zion Unit 1 reactor pressure vessel, including base metal heat B7835-1 and a section of the WF-70 beltline weld. These materials were cut into blocks for mechanical testing and microstructural characterization.
Some A533B test specimens were donated by the LWRS Program to NSUF, listed in the NFML and made available for nuclear energy research.

This project is critically important because access to materials from active or decommissioned nuclear power plants provides an invaluable resource to assess the performance of light-water reactors (LWRs). These specimens can provide critical data to inform relicensing decisions and assessments of degradation models to further develop the scientific basis for understanding and predicting long-term environmental degradation behavior.

304L stainless-steel core shroud boat material donated by BWX Technology to Department of Energy Office of Nuclear Energy

In FY22, BWX Technology and Southern Nuclear Co. transferred 133 irradiated 304L stainless-steel specimens to the U.S. Department of Energy's Office of Nuclear Energy for inclusion in the NFML. Some samples were stored at INL or other NSUF partner facilities, while the rest remained at BWXT in Virginia. NSUF arranged for BWXT to ship the materials to INL in five shipments. The first four shipments occurred in FY23 and FY24. The fifth shipment, initially scheduled for FY24, was delayed due to unscheduled equipment repairs at INL and therefore occurred in March 2025.

Tensile Testing Utilizing the Standard Capsule Irradiation

The tensile testing utilizing the standard capsule irradiation, in support of a Laboratory Directed Research and Development project and using the standard capsules designed by the NSUF SAM-2 team, was completed in FY23. The use of the standard capsule reduces the time and costs of new experiments in ATR using highly available 1.5 cmdiameter "A" positions. Due to the limited timeframe of Laboratory Directed Research and Development projects, no post-irradiation examination was performed on the irradiated multi-principal-element

alloy samples. NSUF agreed to add the samples to the NFML to make them available for further research on these alloys in structural nuclear material, leading to more neutron irradiation data where little exists. In FY24, the capsules containing over 200 SSJ tensile bars were shipped to the Hot Fuel Examination Facility to be disassembled and cataloged. However, unscheduled facility repairs delayed the disassembly into late FY24. The tensile bars will be added to the NFML in FY25.

Yttrium hydride samples

NSUF has accepted a set of yttrium hydride samples irradiated in ATR under the Office of Nuclear Energy Microreactor Program. Yttrium hydride is promising as a reactor moderator due to its ability to maintain high hydrogen density at elevated temperatures, making it ideal for small, high-temperature reactors where conventional moderators like water and graphite are not viable. These samples completed transfer in 2024 and are available through the NFML.

Characterization-scale instrumented neutron dose irradiation samples

A set of U-Zr and U-Mo alloys from a previous cooperative research and development agreement were irradiated in the Transient Reactor Test Facility for characterizationscale instrumented neutron dose irradiation module experiments, which support the irradiation of small fuel samples under controlled temperature conditions. NSUF has agreed to take custody of these irradiated and unirradiated samples will be added to their library in FY25. These valuable samples are intended to aid in understanding the relationship between thermal conductivity and burnup in metallic fuels.

Halden Project Samples

From FY20 to FY23, attempts to acquire Halden Reactor Project samples for the NFML were unsuccessful. In FY24, NSUF received a new offer of alloy 347 and alloy 316L stainless steel samples available for shipment in 2025. The samples have been irradiated in the Halden Reactor and the Würgassen nuclear power plant. Contamination, shipping details and acquisition confirmation have been discussed. Although the NFML has samples of the same alloys, the addition of the Halden samples into the NFML will be reviewed using a new value assessment process.

Project samples made available in FY24

Previously unavailable NSUF project samples are now available for further research. Exclusivity periods have ended for samples from three NSUF projects, making them publicly accessible in the NFML. General Electric-Hitachi samples irradiated in FY20 are available in FY24 after completing a post-irradiation examination. Projects with samples at different radiation damage levels have staggered exclusivity dates reflecting their irradiation end dates. Similar irradiation projects from Boise State University and Idaho State University also have sets of samples removed from the reactor at different times for varying doses, indicating their public availability timelines.

15-8242 Boise State University — Irradiation Influence on Alloys Fabricated by Powder Metallurgy and Hot Isostatic Pressing for Nuclear Applications

This project evaluated the irradiation response of six alloys made via powder metallurgy-hot isostatic pressing (PM-HIP) and conventional methods for light-water reactor (LWR) internals and potential advanced LWR and small modular reactor internals. Original equipment managers are considering PM-HIP techniques to rejuvenate U.S. nuclear

manufacturing. PM-HIP alloys exhibit excellent structural uniformity, superior mechanical properties and enhanced weldability compared to conventional cast or forged alloys. Additionally, the samples provide NSUF users with an opportunity to compare the properties, corrosion behavior, and microstructure of both irradiated and unirradiated 3 dpa PM-HIP samples of additively manufactured 316L, 625, 590, GR91 and SA508.

16-10393 General Electric-Hitachi — Irradiation Testing of Light-Water Reactor Additively Manufactured Materials

This project assessed changes in the properties of irradiated additivity manufactured materials compared to nonirradiated ones. It studied samples of Type 316L stainless steel and alloy 718 produced using direct metal laser melting. These additively manufactured materials have potential applications in the nuclear industry, such as reactor internal repair parts, fuel debris resistant filters and fuel spacers in LWRs. They have shown equivalent mechanical behavior to wrought materials in simulated reactor environments, with added design flexibility, making them attractive for both LWRs and small modular reactors. Access to these samples allows NSUF users to

explore and compare the physical and mechanical properties and microstructure evolution of the irradiated material. The unirradiated samples provide the extra benefit of performing comparison studies.

16-10537 Idaho State University — (2 dpa) Nanostructured Steels for Enhanced Radiation Tolerance

This project assessed the performance of ultrafine-grained and nanocrystalline reactor structural and cladding steels produced via equal-channel angular pressing and high-pressure torsion under neutron irradiation at reactor temperatures. These advanced. low-cost techniques yield stronger alloys than conventional methods. The study targeted austenitic steels for LWRs and ferritic-martensitic steels for advanced fast reactors. By enhancing the microstructure, the project aims to improve radiation tolerance affordably. Experiments performed with these 2 and 6 dpa high-entropy alloys were designed to increase understanding of matrix composition in relation to radiation damage and defect formation.

FROM THE YEAR



Welcoming New NSUF Staff

Brett Miller *Planning and Financial Controls Analyst*

Brett Miller, assigned to support NSUF projects, continues to the provide project leads and managers with the essential information and analysis to make crucial decisions in accomplishing INL's mission to, "discover, demonstrate, and secure innovative nuclear energy solutions." Brett's role as a Planning and Financial Controls Analyst (PFC) is to help work scope managers develop project baselines, schedules, and to ensure that they are costing to the appropriate rates, and charges. He also provides financial reports and analysis to help monitor costs and commitments to stay within the approved funding limits.

Prior to joining INL's team in 2024, he retired from the United States Air Force as an Electrical and Environmental Specialist for aircraft maintenance. While in the Air Force he earned his Business Management degree that helped pave his way throughout his enlisted career. His school training, experience leading teams, and motivation to succeed helped garner important skills ultimately landing him important roles critical to the Air Force's demanding maintenance and flying schedules. These roles included training, quality assurance, and senior positions.

Finally, after utilizing the Air Force Skill Bridge program, Brett was able to intern with INL for a brief period to learn about the Business Management department. This, in turn, led to his hiring and current role at INL as a PFC.

HIGHLIGHTS FROM THE YEAR 2024 ANNUAL REPORT



J. Derek Whipple *NSUF-CINR Program Lead*

J. Derek Whipple, "Derek", has been providing support to the Collaborative Innovative Nuclear Research (CINR) facet of the Nuclear Science User Facilities (NSUF) program since June 2024. He also supports over-all financial and operational aspects of the NSUF program.

Derek graduated from Idaho State University in accounting with an emphasis in operations. Upon graduation, he passed the Certified Public Accountant (CPA) exam in 2011 and has since maintained his Idaho CPA License. Derek joined INL in 2008 as an Internal Audit Intern and participated in the Battelle Intern Program. He then moved into a fulltime role as an Internal Auditor. After a few years as an Internal Auditor, he was deployed to the Information Technology (IT) Department on a rotational assignment. He enjoyed the work scope and stayed in a permanent role much longer than planned for the original rotation. It was there that Derek learned he loved being involved in operations. He was an integral part of the success of the INL IT operational strategy during the years he spent supporting the department (2011-2015).

Subsequently, he moved on to the INL Finance Department where he supported Strategic Partnership Projects as a Planning and Financial Controls Analyst within the rapidly growing National and Homeland Security Directorate (2015–2019). He

made a big impact to this growing INL mission segment that continues to be appreciated today by those he worked with. During this time period, Derek participated in the Battelle Business Leadership Program (BLP) in its inaugural year. A short time later, concurrent to his daytime responsibilities, he served as an INL representative advisor to this same program along with the Early Career Development Program (ECDP) for four consecutive program years (2018–2023).

After working in the INL Finance Department, he moved to the INL General Accounting Department as an Accounting Integration Specialist where he performed complex accounting analyses and research in diverse technical accounting areas (2019–2024).

In each of these different roles, Derek has found joy and fulfillment in finding opportunities for operational efficiencies.

Prior to working in the accounting field, he started his career in the woodworking industry building kitchen cabinets and antique reproduction furniture. After moving off the production floor he became the Inventory Controller (2005–2008). Derek has been married to his lovely wife Brooke for 20 years. When he has spare time, he enjoys keeping his cabinetry skills fresh and learning to restore 1950's Chevy trucks.



Antanae Hanna



Jackie Stone

Celebrating Our 2024 Student Interns

Throughout the summer of 2024, **Antanae Hanna**, a senior from the University of California-Irvine studying chemical engineering, contributed significantly to the NSUF mission through her assistance in organizing the NSUF publications library and materials value assessment plan. Her work not only advanced NSUF initiatives but also provided valuable insights regarding usability and structure of the NSUF Nuclear Fuels and Materials Library.

Hanna has future sights set on a graduate degree in nuclear engineering and joined NSUF to experience new aspects of nuclear research. Excited to be surrounded by professionals working in various fields at the Idaho National Laboratory, Hanna noted that she enjoyed building connections and gaining a wide variety of knowledge.

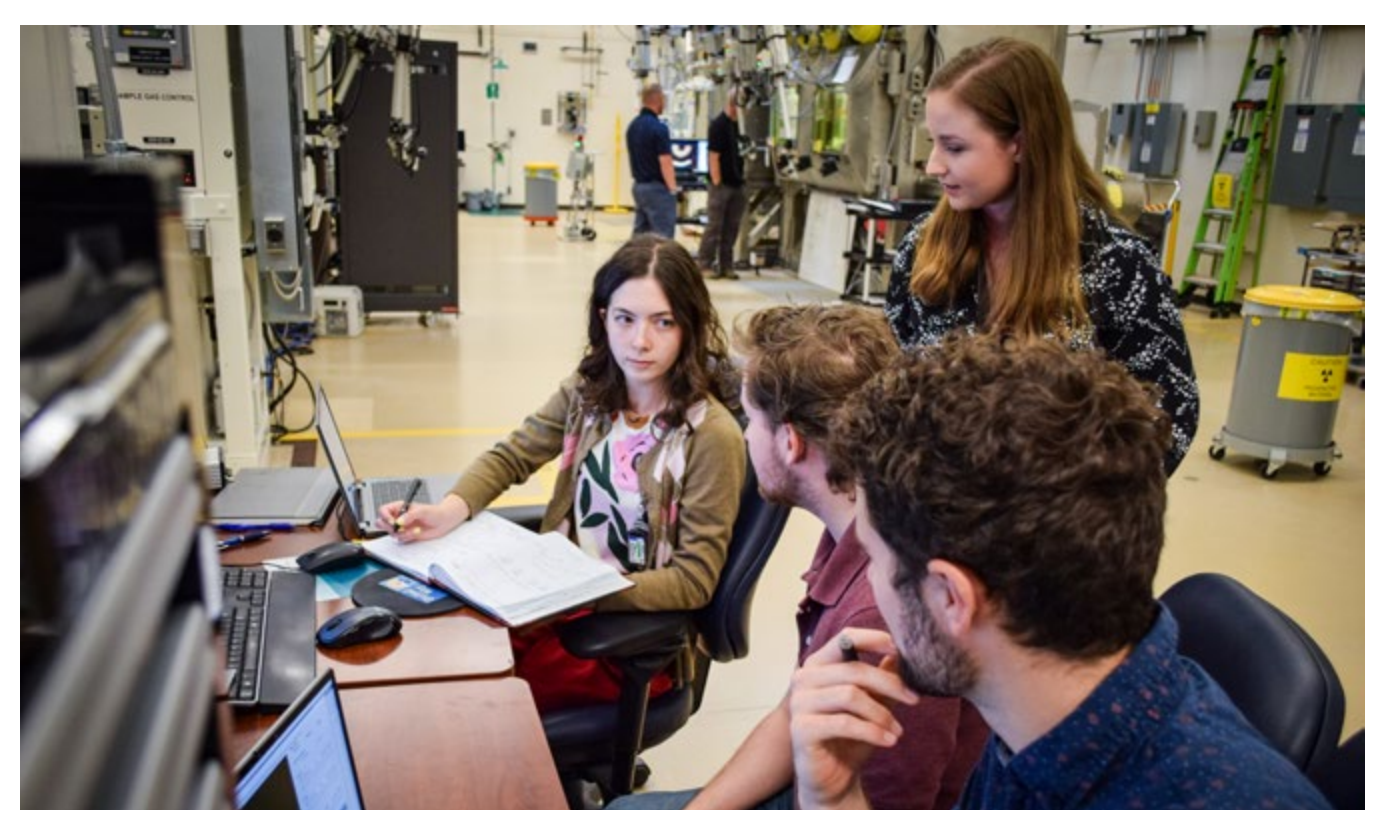
Hanna's ability to navigate complex problems and collaborate effectively with our team has set a high bar for future interns.

Jackie Stone, a senior from Boise State University studying mechanical engineering with a minor in applied mathematics, was inspired to intern with NSUF "to gain more real-world insight into the very niche nuclear field and meet the wonderful professionals that are part of it."

During her internship, Stone enjoyed meeting the professionals who are keeping the nuclear field moving, and getting to see behind the scenes work done at NSUF and the Idaho National Laboratory, particularly the Hot Fuel Examination Facility.

Stone's internship included organizing more than 9,300 materials in the NSUF Nuclear Fuels and Materials Library. She graduated with her bachelor's degree from Boise State University in December 2024, and hopes to build a career in aerospace engineering.

HIGHLIGHTS FROM THE YEAR 2024 ANNUAL REPORT



(From front to back/left to right): Mary Sevart, Ethan Hisle and Isaac Cutler record location information for the thermal conductivity measurements and graph results with NSUF experiment manager Alina Montrose at the Thermal Properties Cell, located in INL's Irradiated Materials Characterization Laboratory at the Materials and Fuels Complex.

Ph.D. student **Mary Sevart** from the University of Florida combined her internship at the Idaho National Laboratory with an NSUF-awarded Rapid Turnaround Experiment (RTE).

Sevart's RTE project focuses on measuring the thermal conductivity of an annular U-10Zr fuel rod. The thermal conductivity of a nuclear fuel is important to measure as it can impact the efficiency of a fuel rod, how much heat it can transfer and ultimately how much energy it can produce.

"I've had a great experience at the Idaho National Laboratory learning from the most knowledgeable experts in my field," said Sevart. "The experience and knowledge that I've gained this summer has already helped me grow as a researcher and will be invaluable to my progress on my dissertation."

New Research, New Materials, New Reactors

Doctoral candidate taps NSUF, lab capabilities to explore microstructural characteristics of alloys

By Paul Menser for INL Communications

There is a new generation of nuclear reactors on the way. These reactors will rely on new designs, new fuels and coolants like molten salt, liquid metal and gas to produce high-temperature heat that may be more efficient and versatile than today's light water reactors.

For researchers and industry, one big question is which materials will withstand the harsher conditions found in the cores of these advanced reactors.

As a graduate student pursuing a doctorate in Materials Science and Engineering at the University of Wisconsin, Nathan Curtis has taken his interest in this matter down to the subatomic level through NSUF and the equipment at INL's Irradiated Materials Characterization Laboratory (IMCL).

Located at the Materials and Fuels Complex west of Idaho Falls, IMCL's shielded instruments allow researchers to characterize highly radioactive fuels and materials at the micro, nano, and atomic levels — the scale at which irradiation damage processes occur. For Curtis, however, the equipment was only



Nathan Curtis points at defects elucidated through high-resolution transmission electron microscopy on steel cladding at the Irradiated Materials Characterization Laboratory at the Idaho National Laboratory.

part of the story. Working with world-leading experts like Grace Burke, Tiankai Yao and Kaustubh Bawane made the experience truly extraordinary. Alina Montrose provided logistic support that was critical to the success of his work.

"It's hard to name only two or three people," he said. "Everyone is so impactful."

Curtis came to INL in the summer of 2024 to pursue an NSUF Consolidated Innovative Nuclear Research project called "Machine Learning on High-Throughput Databases of Irradiation Response and Corrosion Properties of Selected Compositionally Complex Alloys for Structural Nuclear Materials."

He learned how to apply highresolution characterization tools like transmission electron microscopy and atom probe tomography to his project.

The work focused on down-selecting compositionally complex alloys (CCAs) for irradiation tolerance by analyzing void swelling and hardening from heavy ion irradiation, damage that directly relates to mechanical property degradation. Studying and selecting alloys that display the least void swelling and irradiation-induced hardening is a good way to find leading candidates for use in advanced reactors where temperatures

HIGHLIGHTS FROM THE YEAR 2024 ANNUAL REPORT

can reach 600°C and irradiation doses can be three times those experienced by the current fleet.

CCAs, also called "high-entropy alloys," are a class of novel innovative alloys that lack a single principal element. Instead, CCAs are composed of multiple elements in appreciable quantities that derive their properties from the interaction of each element with another. They can retain strength at low temperatures, show superior corrosion resistance, maintain high strength while retaining ductility and have displayed enhanced tolerance to irradiation damage. One caveat, however, is that that these qualities are not all present at the same time and are heavily dependent on alloy composition. Compromises must be made in compositional design for targeted applications like nuclear reactors.

To consider CCAs for structural nuclear applications, Curtis set out to study their irradiation performance at reactor-relevant conditions.

At IMCL, he studied a series of chromium-iron-manganese-nickel (Cr₁₀Fe₃₀Mn₃₀Ni₃₀) samples that had been irradiated in INL's Advanced Test Reactor. The goal was to get a first look into the evolution of neutron-irradiation response of CCAs, focusing on local chemical ordering, which plays a critical role in material performance.

Curtis credited his mentor, Mukesh Bachhav, with guiding him into new regions of study. "He is as good as they get when it comes to atom probe tomography," Curtis said. "He really knows how to push the train of thought along to connect atomic-scale results to industrial-scale implications."

Bachhav said Curtis came with a special skill set and detailed knowledge of fabrication. "He was doing all the heavy lifting for the project," Bachhav said. "The most critical thing for him here was connecting the dots. The work procedures, work controls and safety culture were all slightly different from what he was used to."

Over time, Curtis gained the ability to be an independent user of the equipment, Bachhav said. Curtis was patient and had healthy respect for the safety procedures, to the point where he was able to use the highly sophisticated, highly expensive equipment at IMCL unsupervised.

This is not to say that he worked in isolation. "He was willing to communicate and talk to other folks — and not shy away from learning new techniques and method — and he had ability to explain problems and communicate effectively with other researchers," Bachhav said.

The influence of microstructural control during processing greatly impacts irradiation response, and Curtis' work is some of the first to explore this phenomenon within CCAs. With the need for advanced materials in advanced

reactor designs, such as liquid metal cooled fast reactors, molten salt reactors and small modular reactors, this work supports the U.S. Department of Energy's Office of Nuclear Energy mission.

The work should also support efforts to reduce fabrication and construction costs by exploring CCA development through manufacturing process as an alternative to compositional tuning. And while CCAs are most applicable to advanced reactor implementation, they could provide increased safety and allow for higher efficiency in light water reactors by slowing down the wear and tear on their components.

Curtis first became acquainted with NSUF in 2021 when he received a fellowship through DOE's Nuclear Energy University Program. His 2024 project was one of three NSUF Rapid Turnaround Experiments that he has participated in. "Nuclear energy is a field that requires people from every discipline," he said. "Being able to contribute is something I'm proud of."



NSUF Welcomes New Users Organization Executive Committee

NSUF leadership proudly welcomed a new 2024 Users Organization Executive Committee: Chair Maria Okuniewski from Purdue University, Vice Chair Stephen Taller from Oak Ridge National Laboratory, Secretary Ramprashad Prabhakaran from Pacific Northwest National Laboratory, and Student Representative Malachi Nelson from the Idaho National Laboratory.

"I am excited to work with a group of such talented and experienced NSUF users with representation from national laboratories, academia and industry," said Okuniewski." This year there was overwhelming support and interest from the community for the Users Group Executive Board. This engagement will allow for continued sustainability within the community."

As stated in its charter, the purpose of the Users Organization is to (1) provide a formal and clear channel for the exchange of information, advice and best practices between the investigators who perform reactor-based nuclear technology experiments and NSUF management; (2) educate and inform all stakeholders regarding experimental activities at NSUF; and (3) facilitate communications among NSUF users. The executive committee oversees the organization to facilitate these goals.

"The new Executive Committee for 2024 represents experienced NSUF users and partner facility leads with university and national laboratory experience," said NSUF Director Brenden Heidrich. "I encourage all NSUF users as well as first-time

applicants to the program to join the User's Organization and reach out to them with NSUF questions."

Director Heidrich describes the Users Organization as "the interface between the program office and the user community. They represent a vast library of knowledge on the NSUF, our partners, and the best practices to submit successful proposals and to execute successful projects." The executive committee also spearheads the annual Users Organization meetings.

Membership in the organization is open to all users and potential users of the various NSUF facilities and scientists and engineers engaged in the operation and development of these facilities. Potential members can join by self-nomination.

HIGHLIGHTS FROM THE YEAR 2024 ANNUAL REPORT

2024 Users Organization Executive Committee



Chair | Maria Okuniewski, Purdue University | mokuniew@purdue.edu

Maria Okuniewski is an associate professor in the School of Materials Engineering at Purdue University, where she also holds a courtesy appointment with the School of Nuclear Engineering. Previous to joining Purdue in 2016, she spent approximately 8 years at the Idaho National Laboratory as a research and development scientist and engineer, where she also served as a Technical Lead for NSUF. She has conducted research on transmutation fuels, high-performance research and test reactor fuels, structural materials, and waste storage materials for over 20 years. Okuniewski's research focuses on the nexus of microstructural evolution, processing, mechanical properties, and irradiation performance to improve upon next generation fuels and materials, including minimizing proliferation.



Vice Chair | Stephen Taller, Oak Ridge National Laboratory | tallersa@ornl.gov

Stephen Taller is a research and development associate staff member and Alvin M. Weinberg fellow in the Nuclear Energy and Fuel Cycle Division at Oak Ridge National Laboratory (ORNL). Prior to joining ORNL, he was a postdoctoral fellow at the University of Michigan and completed a Ph.D. in Nuclear Engineering and Radiological Sciences at the University of Michigan. He has extensive experience in designing, conducting and analyzing experiments to study radiation damage effects in neutron irradiated and ion irradiated structural and core materials, primarily using transmission electron microscopy, at multiple NSUF partner facilities. Taller's research focuses on methods to accelerate and optimize the nuclear materials development cycle through microstructural characterization of metals and alloys, analysis of ion irradiation as a supplement or surrogate for neutron irradiation and exploration of advanced manufacturing methods for nuclear technology.



Secretary | Ramprashad Prabhakaran, Pacific Northwest National Laboratory ramprashad.prabhakaran@pnnl.gov

Ramprashad Prabhakaran is a Materials Scientist at Pacific Northwest National Laboratory (PNNL). He has been actively involved in the nuclear fuels, structural, cladding and accelerator materials research and development for over 20 years and has worked at University of Nevada-Las Vegas, and the Idaho National Laboratory before joining PNNL. He has extensive experience in utilizing hotcells, performing corrosion studies, mechanical and microstructural characterizations of nuclear materials and welded/processed alloys, evaluating irradiation effects, and understanding structure-property-processing-dose relationships. He is the PI, Co-PI, and task lead for several USDOE (NE, NNSA and Office of Science) projects supporting NSUF, AMMT, AFC, IMARC, RERTR/M3, RaDIATE, Fusion and Tritium Technology programs. He is the past chair of TMS Nuclear Materials, Corrosion and Environmental Effects, and Young Professionals Committees.



Student Representative | Malachi Nelson, Idaho National Laboratory | Malachi.Nelson@inl.gov Malachi Nelson is an Idaho National Laboratory graduate fellow and final year Ph.D. candidate at the University of California-Berkeley. His research involves nuclear structural materials including mechanical properties and microstructure characterization of zircaloy cladding. Nelson investigates anisotropic viscoplastic properties of cladding in reactor conditions such as pellet-cladding mechanical interactions to improve cladding resilience to reactor power ramping and load following. Outside of work, Nelson is active in energy policy and STEM advocacy and enjoys snowboarding and backpacking.

First Super Rapid Turnaround Experiments Awarded

The U.S. Department of Energy's Office of Nuclear Energy (DOE-NE) awarded the first 13 Nuclear Science User Facilities Super Rapid Turnaround Experiment (Super RTE) projects in August 2024. Each awarded project supports the advancement of nuclear energy.

The 2024 Super RTE awards, totaling approximately \$1.8 million, were granted to seven principal investigators from universities, one principal investigator from industry and five scientists from national laboratories.

The Super RTE, which opened for the first time April 1, 2024, is a user access award process that offers an avenue for researchers to perform a broader scope of irradiation effects studies (i.e., more samples and more access time at Nuclear Science User Facilities partner institutions) than the traditional RTE award process. Super RTE projects must be completed within 12 months of the award.

The 2024 Super RTEs covered a wide range of topics to further post-irradiation knowledge of nuclear materials. Of the 13 Super RTE projects awarded, eight are focused on fuels or structural materials for the next generation of reactors, and five of the projects focus on materials for the current reactor fleet.

All experiments will look at critical properties of materials that have undergone irradiation

at nuclear reactors, under various doses, temperatures, times and made with conventional and advanced manufacturing methods. Researchers will characterize those samples using mechanical testing, microstructural analysis and various microscopy techniques.

Super RTE proposals are expected to be solicited and awarded annually. Like traditional RTE proposals, they will be reviewed and evaluated for technical merit, relevancy and feasibility. The number of awards depends on the availability of funding. The Super RTE Technical Review Process on the NSUF website provides further explanation of the review process. Proposals must support the DOE-NE mission.

FY24 Super Rapid Turnaround Experiment Award Recipients

PI name	Institution	Project title	NSUF Capability Utilized
David Frazer	General Atomics	Advanced microstructure characterization of irradiation impact on corrosion performance of SiC-SiC composite materials	Post-irradiation examination at the Center for Advanced Energy Studies and Pacific Northwest National Laboratory
Yachun Wang	Idaho National Laboratory	<i>In situ</i> TEM heating investigation of M ₂₃ C ₆ stability in neutron irradiated HT9	Post-irradiation examination at the Idaho National Laboratory Irradiated Materials Characterization Laboratory
Robert Okojie	NASA Glenn Research Center	In-operando performance characterization of on-chip integrated SiC pressure/ temperature sensors under irradiation	Neutron Irradiation at the Massachusetts Institute of Technology Nuclear Reactor Laboratory

HIGHLIGHTS FROM THE YEAR 2024 ANNUAL REPORT

PI name	Institution	Project title	NSUF Capability Utilized
Timothy Lach	Oak Ridge National Laboratory	Detailed characterization of in-service IASCC in 316 and 347 stainless steel baffle-former bolts	Post-irradiation examination at the Idaho National Laboratory and Oak Ridge National Laboratory
Caleb Massey	Oak Ridge National Laboratory	The role of helium on microstructure evolution in A709	Ion irradiation at the Michigan Ion Beam Laboratory and post-irradiation examination at the University of Michigan and the Center for Advanced Energy Studies
Brandon Wilson	Oak Ridge National Laboratory	Neutron irradiation and PIE of ZrC coated surrogate particle fuel in IN-Pile Steadystate Extreme Temperature Testbed	Neutron Irradiation at the Ohio State University Research Reactor and post-irradiation examination at the Oak Ridge National Laboratory
Todd Palmer	Pennsylvania State University	Interactions between neutron irradiation and oxide based inclusions in additively manufactured austenitic stainless steels	Post-irradiation examination at the Idaho National Laboratory and the Westinghouse Churchill Laboratory Services hot cells.
Xing Wang	Pennsylvania State University	Deciphering the role of nitrogen on the performance of ferritic-martensitic steels under high-dose irradiation using N-15 isotope doping	lon irradiation at the Michigan Ion Beam Laboratory and post-irradiation examination at the University of Michigan and the Center for Advanced Energy Studies
Jake Fay	Rensselaer Polytechnic Institute	Characterization of U ₈ Pu₁₀Zr fluff sample	Post-irradiation examination at the Idaho National Laboratory Irradiated Materials Characterization Laboratory
Peter Hosemann	University of California, Berkeley	Understanding the effect of helium and neutron irradiation in ODS alloys	Post-irradiation examination at the University of California, Berkeley Nuclear Materials Laboratory
Lin Shao	Texas A&M University	Accelerated evaluation of friction stir welding for on-site repairs using HFIR irradiation, welding, accelerator irradiation, and characterization	Ion irradiation at the Texas A&M Accelerator Laboratory and post-irradiation examination at the Center for Advanced Energy Studies
Patrick Warren	University of Texas at San Antonio	Mechanical assessment of Pd corroded surrogate and irradiated TRISO particles	Post-irradiation examination at the Idaho National Laboratory Irradiated Materials Characterization Laboratory
Matthew Swenson	University of Idaho	Influence of laser welding on deformation mechanisms in irradiated and weld-repaired Ni-Cr alloys	lon irradiation at the Michigan Ion Beam Laboratory and post-irradiation examination at the University of Michigan and the Oak Ridge National Laboratory

NSUF Pilots New User Development Workshop on Irradiation Testing

In May 2024, NSUF convened the pilot User Development Workshop on Irradiation Testing at the Center for Advanced Energy Studies (CAES) and the Idaho National Laboratory (INL). This 4-day pilot workshop specifically recruited STEM students and faculty from institutions not traditionally aligned with nuclear science research, to introduce irradiation testing of nuclear fuel and materials to new researchers, with the goal of expanding the NSUF user community and providing better utilization of NSUF resources to address U.S. energy challenges.

Participants included nine students and four faculty members from North Carolina State University, South Carolina State University, The Ohio State University, the University of California-Berkeley, the University of Idaho, the University of Texas at El Paso, the University of Texas at San Antonio and Virginia Commonwealth University. Three NSUF partner institution research staff also attended from Pennsylvania State University, The Ohio State University and the University of Wisconsin-Madison.

Attendees had an interactive and informative week, involving lectures from INL experts on seminal topics addressing the most pressing challenges facing the nuclear industry, including nuclear fuel development, nuclear structural materials and used fuel disposition and reprocessing. Additionally, the group was informed on the most recent advances in nuclear reactor technology,



The 2024 NSUF User Development Workshop on Irradiation Testing pilot hosted nine students, four faculty and three NSUF partner institution research staff from a total of ten institutions, including North Carolina State University, Pennsylvania State University, South Carolina State University, The Ohio State University, the University of California-Berkeley, the University of Idaho, the University of Texas at El Paso, the University of Texas at San Antonio and Virginia Commonwealth University and the University of Wisconsin-Madison.

HIGHLIGHTS FROM THE YEAR 2024 ANNUAL REPORT

including gas-cooled reactors, irradiation experiment design, post-irradiation examination techniques, high-performance computing capabilities, applications of modeling and simulation, microreactors and current developments in sensors and instrumentation supporting reactor experiments.

Student participants were instructed in radioactive material characterization by Boise State University faculty and received hands-on training in the CAES Microscopy and Characterization Suite by using the scanning electron microscope (SEM) to examine actual NSUF specimens. For many participants, the hands-on work in the microscopy lab was their first time looking at actual nuclear energy materials this way. They were able to learn how the SEM worked, including the range of magnification and resolution, and how ion beam energy affects overall imaging.

The workshop included tours of the Advanced Test Reactor and numerous INL facilities at the Materials and Fuels Complex including the Hot Fuel Examination Facility hot cells, Irradiated Materials Characterization Laboratory, Analytical Research Laboratory, and the Transient Reactor Test Facility. Supplementing the tours, INL and CAES staff discussed the unique capabilities of each site, along with talks from NSUF instrument scientists on research being



Boise State University Research Associate Jana Howard (right) trains Virginia Commonwealth University student Christopher Cogliano (left) on how to use and set up the electron backscatter diffraction on the JEOL 6610LV scanning electron microscope.

supported by NSUF to enhance and provide new capabilities to the NSUF suite of characterization techniques.

Attendees also learned about funding opportunities within the NSUF program area, such as the Rapid Turnaround Experiments (RTEs), Super RTEs, and Consolidated Innovative Nuclear Research awards. Representatives from INL's University Programs office discussed funding opportunities within the Nuclear Energy University Programs.

On the final day of the workshop, participants broke into small groups and engaged with NSUF partner representatives to develop ideas into proposal plans for the NSUF Rapid Turnaround Experiment third call. Two RTE proposals and one

CINR proposal were submitted as a direct result of the workshop.

Overall, this workshop was successful in achieving its goal of introducing a new group of researchers to the theory and practice of nuclear energy relevant irradiation testing and material science. Students who may not have previously considered a pathway in nuclear fuels and materials science were exposed to nuclear scientist expertise, nuclear science facilities and capabilities at the Idaho National Laboratory, and received valuable input on submitting a successful RTE proposal. This workshop strengthened relationships with existing partners, while working to broaden the NSUF user base.

First Innovative NuScale Experiment Cycle Completed

In a major step towards commercial, small modular reactor deployment, progress is being made in testing new materials for NuScale's small modular reactor lower containment vessel.

In 2019, NuScale Power LLC received access to the Idaho National Laboratory's Advanced Test Reactor and Westinghouse Churchill Laboratory Services through the Nuclear Science User Facilities (NSUF) as part of the Consolidated Innovative Nuclear Research funding opportunity. The access award allowed NuScale to obtain irradiation data on F6NM, a martensitic stainless steel, with the intent of using F6NM for its lower containment vessel as part of the NuScale Power Module™ design for small modular reactors.

The NuScale lower containment vessel, which is capable of withstanding pressures during reactor operations, is a safety feature that prevents fission products from being transported to the outside atmosphere. In its current design, NuScale uses FXM-19, an austenitic stainless steel that is resistant to irradiation embrittlement and corrosion and has higher American Society of Mechanical Engineers design specifications than other common austenitic stainless steels.



Advanced Test Reactor canal operators load NuScale specimens inside a basket in preparation for irradiation.

The downfall? FXM-19 is expensive to cast and fabricate in large sizes needed for the containment vessel.

F6NM, to compare, is also corrosion resistant, more cost effective and more readily available than FXM-19 – and it has higher design specifications, so long as it performs as expected after irradiation.

September 2023 marked the completion of the first of four cycles, which began in July 2023 at the Advanced Test Reactor.

After irradiating the high-fluence target specimens, NSUF shipped them to Westinghouse, an industry partner facility, for post-irradiation examination to include Charpy and tensile testing.

This experiment is uniquely complex, requiring novel approaches, such as direct specimen contact with water, the reactor's primary coolant, to achieve the experiment's low-temperature requirement, and the use of three

high-power, short-duration Power Axial Locator Mechanism (PALM) cycles to meet the experiment's low-fluence requirements.

Currently, the low-fluence target specimens have completed one of three PALM cycles and irradiation. These specimens were sent to Westinghouse in July.

According to NuScale's 2019 CINR research proposal, the qualification of F6NM would "reduce manufacturing cost and schedule for NuScale module production." The data and material specimens generated by this experiment will be publicly available through the **NSUF Nuclear Fuels and Materials** Library following the completion of NuScale's research project and would "[benefit] the industry by promoting the adoption of higher strength steels with improved thermal efficiency for other nuclear vessel applications."



PROJECTS

Awarded Consolidated Innovative Nuclear Research projects FY24

PI Name	Institution	Project Title	
Julie Tucker	Oregon State University	Neutron/Proton Round Robin: What role does irradiation type play in enhancing ordering in Ni-Cr-based alloys?	
Lingfeng He	North Carolina State University	Radiation Effects of High Entropy Alloys	
James Stubbins	University of Illinois at Urbana- Champaign	Characterization of Irradiation-Assisted Stress Corrosion Cracking in 316 Stainless Steel Baffle-Former Bolts Harvested from Commercial Pressurized Water Reactor	
lgor Jovanovic	University of Michigan	Measurement of Time-Dependent Transmissivity of Materials for Optical Sensors and Instrumentation	
James Wall	Electric Power Institute, Inc.	Nondestructive Evaluation of Fracture Properties in Irradiated Light Water Reactor Pressure Vessel Steels	
Aditya Shivprasad	Los Alamos National Laboratory	Advanced hydride moderator irradiations for microreactor and space nuclear reactor deployment	
Mychailo Toloczko	Pacific Northwest National Laboratory	Elemental effects on radiation damage in tempered martensitic steels neutron irradiated to high doses at fast reactor relevant temperatures	



Rapid Turnaround Experiment (RTE) Projects Awarded FY24 First Call

PI Name	Institution	Project Title		
Fei Teng	ldaho National Laboratory	Development of an Experimental-Simulation Benchmarking Database for Irradiation-Enhanced Long Range Ordering in Ni-Cr-Mo alloys		
Nance Ericson	Oak Ridge National Laboratory	Irradiation of GaN HEMTs and SiC JFETs for Near Core Rad-hard Electronics		
Sobhan Patnaik	Idaho National Laboratory	Advanced characterization of irradiated FAST rodlets using Transmission Electron Microscopy and Atom Probe Tomography		
Robert Okojie	NASA Glenn Research Center	Reliability Assessment of Irradiated Integrated Silicon Carbide Pressure/ Temperature Sensors for Lunar Fission Surface Power Reactor		
Kourtney Wright	Idaho National Laboratory	Fuel - Cladding Chemical Interaction of U10Zr Fuel and HT-9 Cladding Using <i>in situ</i> Heated TEM		
Sneha Prabha Narra	Carnegie Mellon University	Investigating the evolution of M23C6 and MX-type precipitates in additively manufactured Grade 91 steel under high temperature simultaneous and sequential stress and irradiation		
Mohammad Umar Farooq Khan	University of Michigan	Investigating the effect of Te embrittlement and depleted Uranium on IN617 in molten salt conditions		
Md Ali Muntaha	Purdue University	Phase Field Modeling of Irradiation-Induced Crystallization in Amorphous Nuclear Oxides		
Weicheng Zhong	Oak Ridge National Laboratory	Radiation Tolerance of MX-Type Precipitates Revealed Through <i>In situ</i> Ion Irradiations		
Sukanya Majumder	Purdue University	<i>In situ</i> TEM Characterization of Ion-Irradiated U-10Mo Alloys at Sub-Eutectoid Temperatures		
Di Chen	ldaho National Laboratory	Post-Irradiation Analysis of U-Pu-Zr Fuel Incorporating Am and Np Actinides: Fuel-Cladding Interactions in EBR-II and Advanced Microscopic Examination		
Timothy Lach	Oak Ridge National Laboratory	Co-Location of Solute Clusters and Dislocations in Additively Manufactured 316L Stainless Steels		
Hi Vo	Los Alamos National Laboratory	Dislocation-precipitate interaction under irradiation - <i>in situ</i> TEM nanomechanical testing during heavy ion irradiation		
Carlo Mapelli	Politecnico di Milano	Innovations in Austenitic Manganese Steels for Nuclear Applications: Insights from <i>In situ</i> TEM Irradiation Experiments at the IVEM Facility		
Rashed Almasri	North Carolina State University	In situ irradiation of ZrC and ZrN above 800°C		

AWARDED PROJECTS 2024 ANNUAL REPORT

Jasmyne Emerson	Purdue University	Phase Characterization of Neutron Irradiated Surveillance Reactor Pressure Vessel Weld	
Maxim Gussev	Oak Ridge National Laboratory	The effect of radiation temperature on H/He core-shell structures in nuclear structural materials	
Cheng Sun	Clemson University	Phase stability of partially-stabilized-zirconia under irradiation	
Chinthaka Silva	Pacific Northwest National Laboratory	An evaluation of effects of ion irradiation on crystal, mechanical, and microstructural properties of Alloy 709	
Fabio Di Fonzo	Istituto Italiano di Tecnologia	Study of the behavior under ion irradiation of amorphous oxide protective coatings developed for lead fast reactors	
Stephen Taller	Oak Ridge National Laboratory	The Role of Dislocation Cell Walls on Cavity Nucleation in Additively Manufactured 316H Steel	
Maria Kosmidou	Los Alamos National Laboratory	Irradiation performance of defective Uranium Mononitride: The role of impurities in the defect accumulation using <i>In situ</i> TEM ion irradiation	
Geeta Kumari	Oak Ridge National Laboratory	Evolution of Heterogeneous 316LSS Microstructures Under Neutron Irradiation	
Ahmed Alade Tiamiyu	University of Calgary	Radiation behavior of grain boundary-decorated nanocrystalline high-entropy alloy	
Sarah Hamilton	Idaho National Laboratory	High Resolution Studies of Uranium Mononitride/Zirconium Carbide Composites for Advanced Fuels Applications	
Fei Xu	Idaho National Laboratory	Advanced characterization to identify phases formed of irradiated annular U-4Pd-13Zr fuel	
Riley Moeykens	Massachusetts Institute of Technology	Understanding the effects of proton irradiation and air oxidation in Cr alloyed UB2 at high temperatures by synchrotron X-ray scattering	

Rapid Turnaround Experiment (RTE) Projects Awarded FY24 Second Call

PI Name	Institution	Project Title	
Ramprashad Prabhakaran	Pacific Northwest National Laboratory	APT study of HT-9 to evaluate the effect of neutron irradiation temperature, alloying elements and heat treatment	
James Edgar	Kansas State University	Electron spin properties of boron vacancies in hexagonal boron nitride single crystals created by neutron irradiation	
Jia-Hong Ke	Idaho National Laboratory	Thermal stability of solute-defect clusters in structural alloys under irradiated environments	
Priyanka Agrawal	University of North Texas	Examination of ion irradiated Additive Friction Stir Manufactured metastable high entropy alloy	
Matthew Lynch	University of Michigan-Ann Arbor	A novel high-throughput method for quantification of materials swelling via microscale dilation techniques	
Janelle Wharry	Purdue University	Synergetic Effects of Irradiation, Temperature, and Strain on Ordering in Ni-Based Alloys	
Morgan Smith	Purdue University	Porosity Evolution in High Burnup and Low Irradiation Temperature U-10wt.%Zr Fuel Subregions	
Andrea Mattera	Brookhaven National Laboratory	Measurement of Fission Product production yields	
Maria Okuniewski	Purdue University	Low fluence effects of neutron irradiation on the phase evolution of U-10wt.%Zr specimens	
Indrajit Charit	University of Idaho	TEM characterization of neutron irradiated HT-9 as a function of irradiation temperature and dose	
Mahmud Hasan Ovi	University of Illinois	Post-test tensile fractography and microstructure of HT-9 alloys following ATR irradiation to doses between 0.01 and 10 dpa at 300, 450 and 550°C	
Sobhan Patnaik	ldaho National Laboratory	Advanced characterization of irradiated FAST aLEU U-Mo rodlets using Transmission Electron Microscopy and Atom Probe Tomography	
Mary Sevart	University of Florida	Thermal Conductivity Measurements of Irradiated Annular Low Burn-Up U-10Zr Fuel	
Chuck Marks	Dominion Engineering	Concentration Measurements of Helium and Boron in Degraded Stainless Steel Nuclear Plant Components	
Jason Harp	Oak Ridge National Laboratory	High Temperature Testing of Fully Ceramic Microencapsulated Fuel	
Wei-Ying Chen	Argonne National Laboratory	Irradiation Damage Rate Effect on the Dislocation Cell Structure of Additively Manufactured 316L	

AWARDED PROJECTS 2024 ANNUAL REPORT

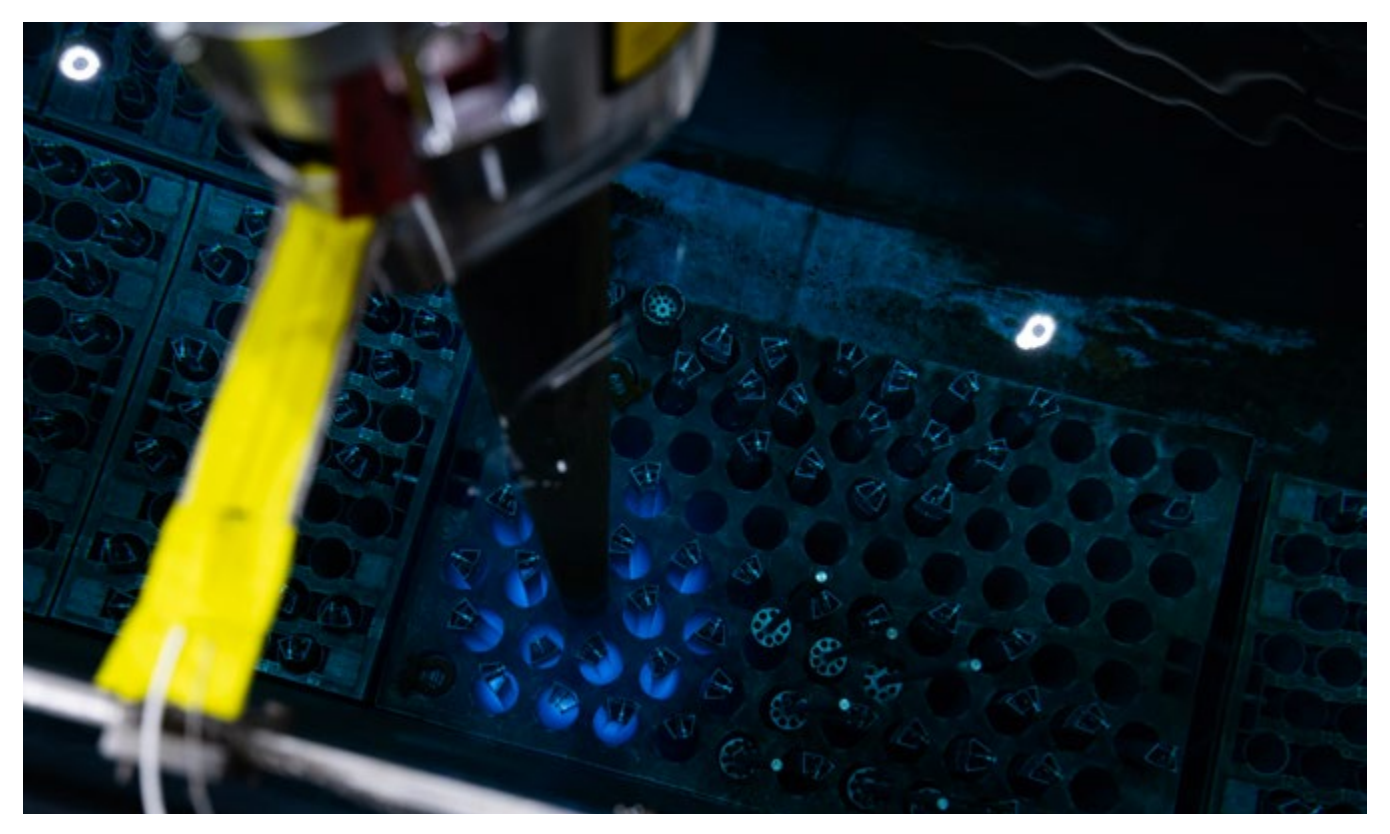
Soyoung Kang	Oak Ridge National Laboratory	Impact of re-irradiation on strain-induced structure in heavy irradiated austenitic steel	
Arya Chatterjee	Purdue University	Understanding the Remarkable Strain-Hardening Capacity of Irradiated PM-HIP 316L SS	
Amey Khanolkar	Idaho National Laboratory	Examination of irradiation effects on printed strain gauges	
Artem Matyskin	Pennsylvania State University	Testing purity of molten salts — neutron activation analysis study	
Xinghang Zhang	Purdue University	In situ dual beam radiation on additively manufactured oxide dispersion strengthened alloy 718	
Oran Lori	University of California-Irvine	In situ TEM Characterization of surrogate oxides microstructure under fission gas retention and reactor-relevant temperatures using ion beam implantation	
Joshua Rittenhouse	Idaho National Laboratory	Nanoindentation Creep Testing and Characterization of High Temperature Irradiated HT-9 Cladding	
Calvin Lear	Los Alamos National Laboratory	Direct Confirmation of Grain Boundary Roughening Using In Situ Irradiation	
Kieran Dolan	Kairos Power LLC	Quantifying gamma irradiation tolerance of high-emissivity coatings on stainless steel	
Nicole Rodriguez Perez	Purdue University	Analysis of FCCI and phase decomposition on Zr-lined U-10Mo specimens using Transmission Electron Microscopy and Atom Probe Tomography	
Yogesh Kumar	University of Florida	Quantification of Zr Redistribution in Irradiated U-Zr Annular Fuel using EPMA	
Ericmoore Jossou	Massachusetts Institute of Technology	Three-dimensional imaging and quantification of neutron radiation induced porosity in U-10Zr fuels	
Todd Sherman	Idaho State University	Post Irradiation Examination of High Entropy Carbides	
Kevin Tsai	Idaho National Laboratory	Temperature effects of rhodium self-powered neutron detectors in a gamma field	
Benjamin Mejia Diaz	Texas A&M University	Hybrid proton and heavy ion irradiation for void swelling testing	
Daniele Salvato	Idaho National Laboratory	Stability limits of the gas bubble superlattice in neutron irradiated U-Mo fuel: A 3-D multi-modal and multi-scale study	
Sadman Sakib	North Carolina State University	Self-Alpha Irradiation of UO ₂ -UB ₂ fuel	

Rapid Turnaround Experiment (RTE) Projects Awarded FY24 Third Call

PI Name	Institution	Project Title	
Robert Aughterson	Australian Nuclear Science and Technology Organisation	Natural zirconolites and pyrochlores as test cases for wasteform matrices	
Rijul Chauhan	Texas A&M University	High-throughput ion irradiation approach for temperature-dependent swelling measurement in additively manufactured 316L alloy	
Caleb Clement	Westinghouse Electric Company	Unveiling long-term irradiation and thermal aging effects on solute segregation in commercial reactor pressure boundary material	
Kenneth Cooper	Texas A&M University	Comparative analysis of Hastelloy X and 316L stainless steel under simultaneous irradiation and corrosion for advanced reactor applications	
Jake Fay	Rensselaer Polytechnic Institute	Nano indentation hardness of U ₁₀ Zr	
Lucia Rebeca Gomez Hurtado	North Carolina State University	In situ TEM study of microstructural evolution and deformation in FFTF irradiated HT-9 cladding	
Zhihan Hu	Texas A&M University	Formation and dissolution of carbides and precipitates in self-ion irradiated HT9 alloy, and the impact on its mechanical properties	
Djamel Kaoumi	North Carolina State University	Probing the effect of specific chemical elements on the irradiation-induced defects formation and evolution in multi-principal element alloys (MPEAs) at high temperature	
Elizabeth Kautz	North Carolina State University	Visualizing the impact of irradiation damage on alloy element redistribution accompanying Zr alloy corrosion via atom probe tomography	
Xingyu Liu	Pennsylvania State University	Investigating effect of dose rate on microstructure evolution in 800H alloy at high doses	
Junliang Liu	University of Wisconsin-Madison	In situ TEM study of irradiation effects in zirconium oxides	
Korukonda Murty	North Carolina State University	Mechanical and microstructural characterization of neutron irradiated ultra-fine-grained and conventional ferritic steel	
Bao-Phong Nguyen	University of Florida	In situ TEM nanomechanical testing of neutron irradiated U-10Zr	

AWARDED PROJECTS 2024 ANNUAL REPORT

Jeffrey Poehler	Nuclear Regulatory Commission	Microstructural characterization of pressurized water reactor harvested core barrel weld materials
Allison Probert	University of Florida	Irradiation effects on thermal conductivity and phase evolution in low burnup U-10Pu-10Zr
Caleb Schenck	North Carolina State University	Investigating ion irradiation at high temperatures on high entropy carbide ceramics using correlative positron annihilation spectroscopy and transmission electron microscopy
Mary Sevart	University of Florida	Quantification of radial constituent redistribution in annular U-10Zr irradiated fuel using EPMA
James Stubbins	University of Illinois at Urbana-Champaign	TEM determination of dislocation structure formation at 4% tensile deformation in a neutron irradiated Fe-9Cr model alloy
Peng Wang	University of Michigan-Ann Arbor	Nanostructural analysis of cold-sprayed Cr-coated Zircaloy-4 under proton irradiation and corrosion



An overhead view of the Advanced Test Reactor gamma tube, surrounded by recently irradiated fuel elements at the Idaho National Laboratory.

Super Rapid Turnaround Experiment (SuperRTE) Projects Awarded FY24

PI name	Institution	Project title	
David Frazer	General Atomics	Advanced microstructure characterization of irradiation impact on corrosion performance of SiC-SiC composite materials	
Yachun Wang	Idaho National Laboratory	In situ TEM heating investigation of $M_{23}C_6$ stability in neutron irradiated HT9	
Robert Okojie	NASA Glenn Research Center	In-operando performance characterization of on-chip integrated SiC pressure/temperature sensors under irradiation	
Timothy Lach	Oak Ridge National Laboratory	Detailed characterization of in-service IASCC in 316 and 347 stainless steel baffle-former bolts	
Caleb Massey	Oak Ridge National Laboratory	The role of helium on microstructure evolution in A709	
Brandon Wilson	Oak Ridge National Laboratory	Neutron irradiation and PIE of ZrC coated surrogate particle fuel in IN-Pile Steadystate Extreme Temperature (INSET) Testbed	
Todd Palmer	Pennsylvania State University	Interactions between neutron irradiation and oxide based inclusions in additively manufactured austenitic stainless steels	
Xing Wang	Pennsylvania State University	Deciphering the role of nitrogen on the performance of ferritic-martensitic steels under high-dose irradiation using N-15 isotope doping	
Jake Fay	Rensselaer Polytechnic Institute	Characterization of U ₈ Pu ₁₀ Zr fluff sample	
Peter Hosemann	University of California, Berkeley	Understanding the effect of helium and neutron irradiation in ODS alloys	
Lin Shao	Texas A&M University	Accelerated evaluation of friction stir welding for on-site repairs using HFIR irradiation, welding, accelerator irradiation, and characterization	
Patrick Warren	University of Texas at San Antonio	Mechanical assessment of Pd corroded surrogate and irradiated TRISO particles	
Matthew Swenson	University of Idaho	Influence of laser welding on deformation mechanisms in irradiated and weld-repaired Ni-Cr alloys	



PROJECTS

RTE 18-1213: Investigation of Gas-Bubble Behavior in Metals Using *In Situ* Ne-, Ar-, and Kr-Ion Irradiation

Principal Investigator: Jian Gan (INL)

Collaborator: Cheng Sun

Facility: Argonne National Laboratory

Gas-bubble superlattices (GBSs) have been observed for decades; they can form either by gas-ion implantation or nuclear transmutation. Understanding the fundamental mechanism of nanopatterned GBS formation in irradiated materials is crucial for the development of advanced nuclear fuel concepts. Although many possible GBS-formation mechanisms have been proposed previously, forming nanopatterned GBSs is still challenging, and a clear formation mechanism remains missing. In this project, we studied the ordering of inert-gas bubbles in molybdenum (Mo) under ion irradiation using an in situ irradiation capability at Argonne National Laboratory.

The order-disorder transition was clearly observed in Mo during ion irradiation. Mo sheets with a purity of 99.95 wt.% were purchased from Goodfellow. The He ions at 40 keV of energy were implanted in the Mo TEM specimens at 300°C to a dose of 1 x 10^{17} He/cm² at a constant flux of 7.6 x 10^{12} He/cm²/s. The ion source used to implant He ions is a plasma-discharge ion source in Model 921-A, provided by the DANFYSIK Company. The Mo specimens were perforated using jet polishing at ~5°C in 12.5 vol.% sulfuric acid-methanol solution to create the thin regions needed for TEM characterization. The perforated

Mo TEM specimens with He GBSs were irradiated with Kr ions at 1 MeV of energy at 300°C to a dose up to 1.25×10^{15} Kr/cm² with a flux of $\sim 1.0 \times 10^{12}$ Kr/cm²/s. Hitachi-9000 TEM with 300 keV of electron beam energy was used to study the evolution of He GBSs under Kr-ion irradiation. The He GBSs gradually become disordered under Kr-ion irradiation at 300°C, and the order-disorder transformation process completes at 2.5 dpa. Both TEM and synchrotron-based small-angle X-ray scattering reveal that the order-disorder transformation of He GBSs is associated with a slight increase in average bubble size.

Impact

This work provides scientific insights into the formation mechanisms and the stability of GBSs under irradiation. This fundamental understanding can be applied to the design and assessment of new nuclear fuel concepts.

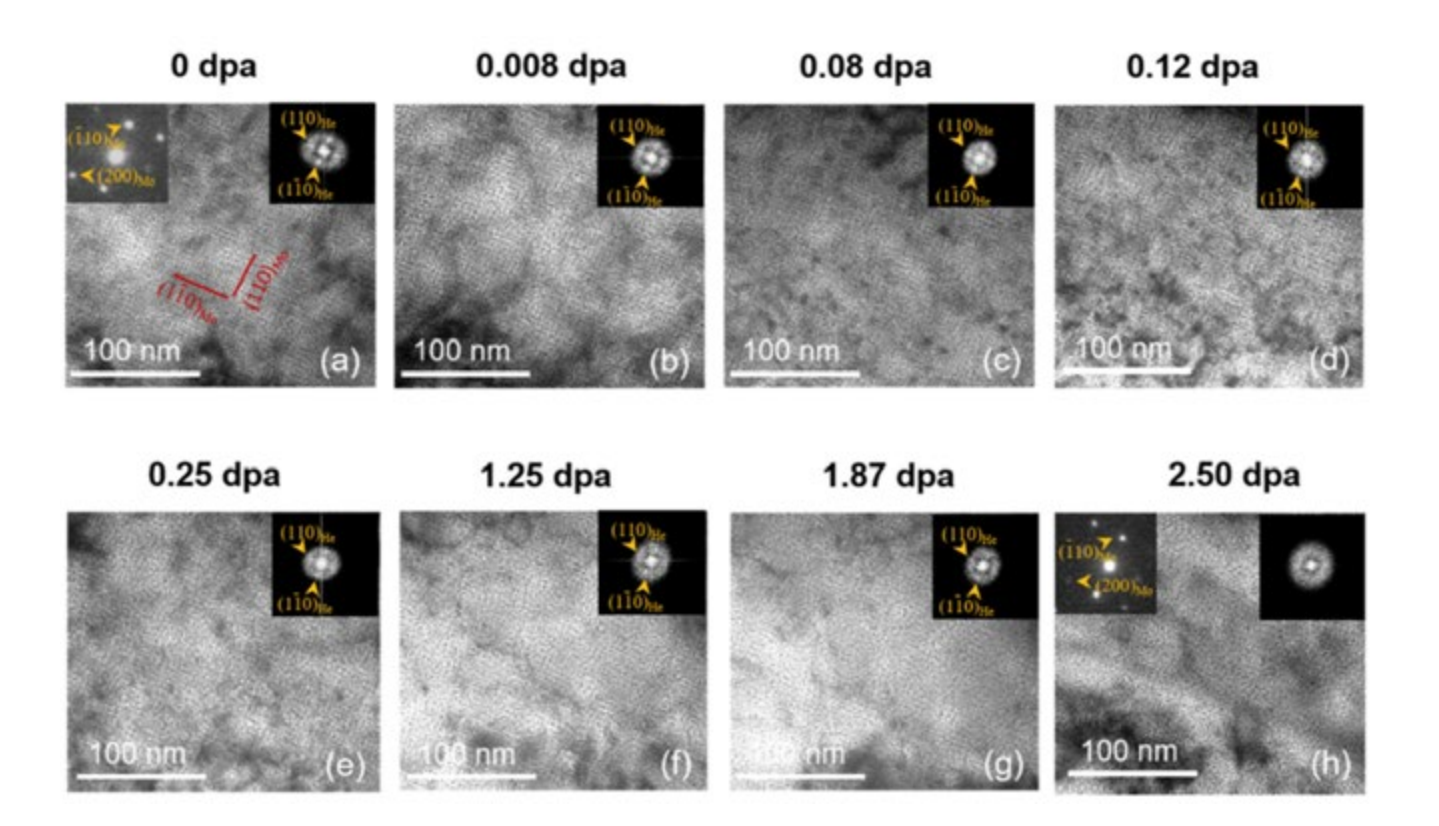


Figure 1. In situ Kr-ion irradiation of Mo with a He gas-bubble superlattice at 300°C observed through TEM. (a–h): Snapshots of Mo microstructure under Kr-ion irradiation up to a dose of 2.5 dpa. Disordering of the gas-bubble superlattice gradually occurs, completing at 2.5 dpa. [C. Sun, et al., J. Nucl. Mater. 539 (2020): 152315.].

RTE 1245: In situ Dual-Beam Irradiation on Strong and Ductile Steels

PI: Xinghang Zhang

Co-PI: Zhongxia Shang, Tianyi Sun (Purdue University)

Technical Leads: Meimei Li, Mark Kirk

Facility: Intermediate Voltage Electron Microscopy-Tandem Facility, Argonne National Laboratory

Objective, Relevance, Novelty, and Expertise

The main objective of this RTE is to use in situ dual-beam radiation technique (at the Intermediate Voltage Electron Microscope [IVEM] Facility at Argonne) to investigate irradiation-induced microstructural evolution in strong and ductile steels processed by different heat-treatment methods. We hypothesize that nanostructured steels may have outstanding resistance to He-induced damage at doses. The systems to be studied are nanotwinned (NT) steels and gradient nanolaminated FeCrAl steels. We summarize our major findings in the following sections. Six journal articles have been published to date.

In situ studies on radiation response of a nanotwinned steel [Zhongxia Shang, Tongjun Niu, Tianyi Sun, Sichuang Xue, Cuncai Fan, Wei-Ying Chen, Meimei Li, Haiyan Wang, Xinghang Zhang. In situ study on radiation response of a nanotwinned steel, Scripta Materialia 220 (2022) 114920.]

Recent radiation studies on NT pure metals, such as Cu and Ag, show that twin boundaries are appealing defect sinks because twin boundaries can transport and eliminate radiation-produced defects. However, the response of twin boundaries in NT structural steels under irradiation is rarely explored. Here, we investigated the microstructural evolution of a NT steel via in situ Kr++ irradiation at room temperature to 4 dpa. The in situ study shows that nanotwins in steels can effectively suppress the formation of dislocation-loop rafts. Also, the formation of loop rafts and Frank loops was found to depend prominently on twin spacing. The underlying mechanisms of the enhanced radiation tolerance in NT steel are discussed. The present study provides a positive step towards the application of NT structural materials to nuclear reactors.

In situ heavy-ion irradiation was performed on a NT austenitic steel at room temperature to 4 dpa. Major findings are summarized as follows:

- Heavy-ion irradiation generates mainly Frank loops and loop rafts in the NT steel. The formation of loop rafts consists of two steps: formation of raft embryos and interconnection between the embryo segments.
- 2. Coherent twin boundaries (CTBs) are able to truncate continuous loop rafts into discrete perfect loops, thus suppressing the formation of long loop rafts. The raft density depends prominently on twin spacing. At a critical twin spacing of 50–60 nm, loop rafts significantly diminish.
- The dissociations of Frank loops into CTBs were frequently observed, and results in defective CTBs, including thick CTBs with high-density slip faults (SFs) and sharp CTBs loaded with interstitial loops. The dissociation is rationalized by dislocation reaction and recombination of interstitial- and vacancy-type defect clusters.

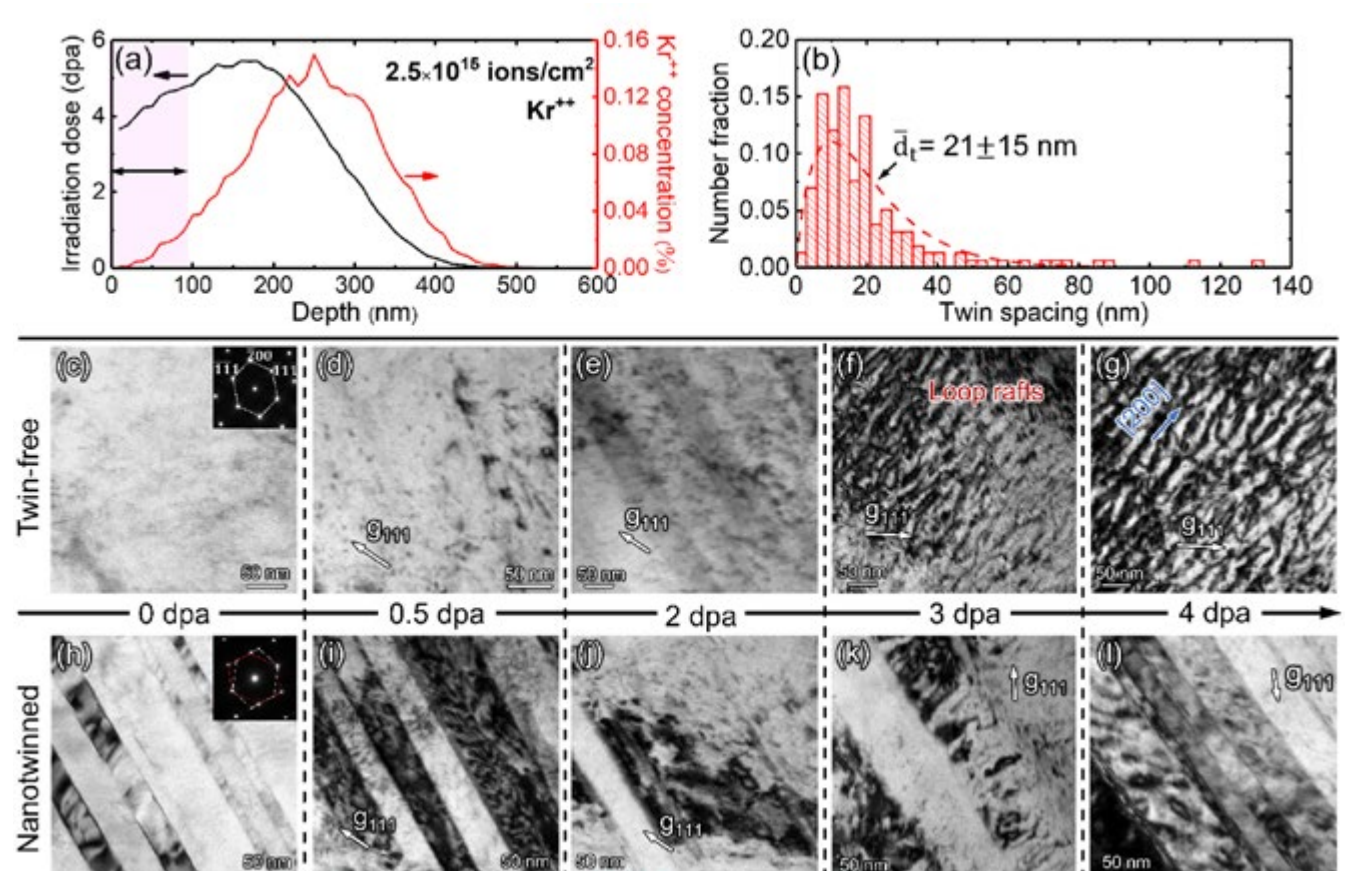


Figure 1. (a) Stopping and Range of lons in Matter (SRIM) calculations illustrate the variation of irradiation dose and Kr^{++} concentration profiles as a function of damage depth. The average radiation dose is 4 dpa in the first 100 nm corresponding to the TEM foil thickness. While most Kr ions penetrate through the sample, (b) the statistical distribution of twin spacing in the irradiated area shows an average twin spacing of 21 nm. In situ TEM snapshots show the microstructure evolution in (c-g) the twin-free region and (h-l) the NT region at various doses (0-4 dpa). The microstructures of both regions at 0 dpa are relatively clean after the annealing at 500°C. High-density well-aligned loop rafts along $\{200\}$ direction formed in the irradiated twin-free region by 3 dpa while dislocation loops still dominate in the NT region. All the TEM bright-field (BF) images were captured close to <110> zone axis with g111 strongly excited.

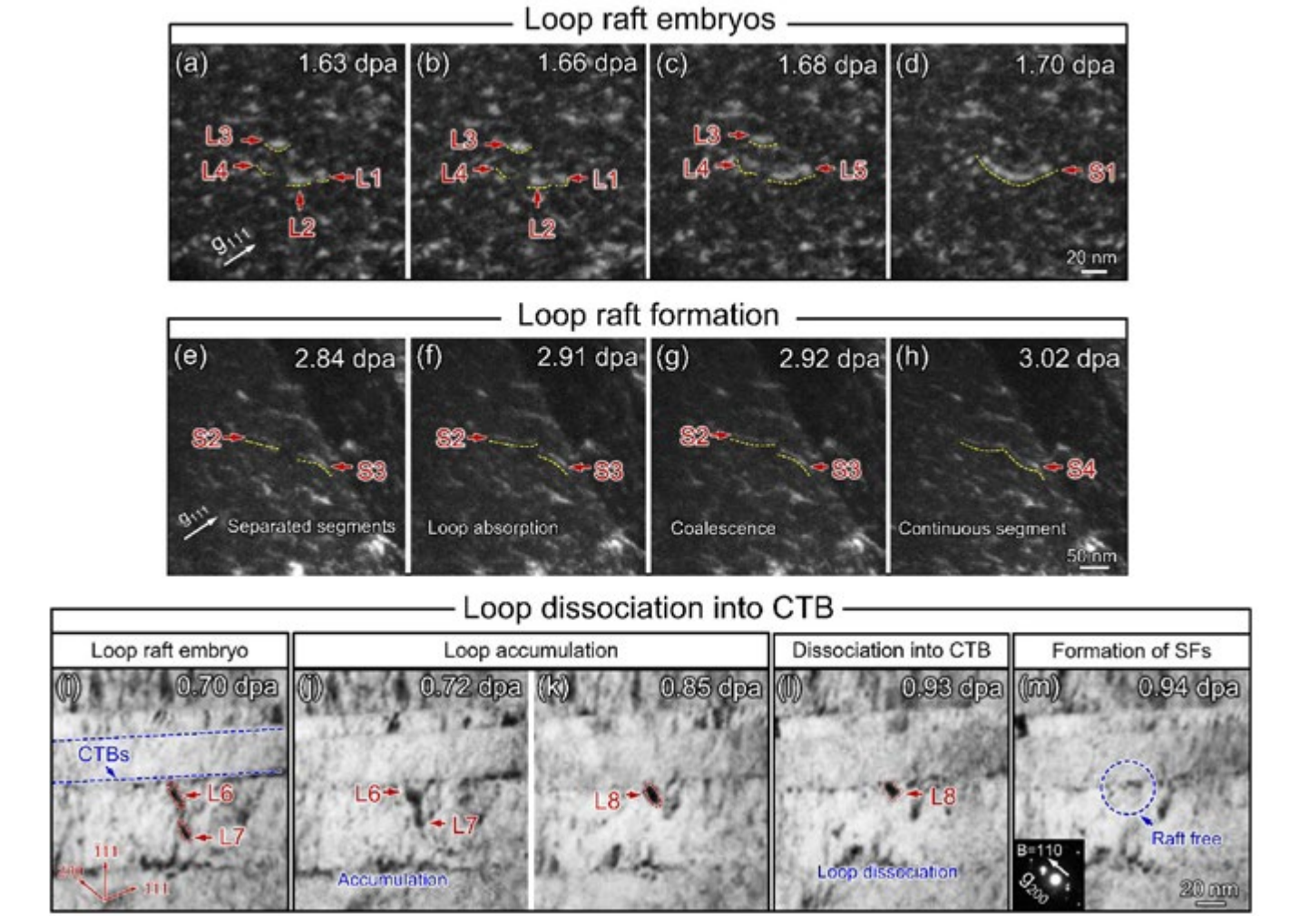


Figure 2. (a-d) Representative in situ video snapshots illustrating the formation of a loop-raft segment (S1) via loop accumulation (L1–L5) at 1.63–1.70 dpa. (e-h) Representative in situ video snapshots showing the loop-raft formation (S4) by coalescence of two preexisting segments (S2 and S3) during 2.84–3.02 dpa. (i-m) Representative in situ video snapshots capturing the absorption of irradiation-produced dislocation loops (L6, L7 and L8) by a CTB at 0.7–0.94 dpa.

An in Situ Study on the Effect of Grain Boundaries on Helium Bubble Formation in Dual Beam Irradiated FeCrAl Alloy [Published. Tianyi Sun, Tongjun Niu, Zhongxia Shang, Wei-Ying Chen, Meimei Li, Haiyan Wang, Xinghang Zhang, An in situ study on the effect of grain boundaries on helium bubble formation in dual beam irradiated FeCrAl alloy, Acta Materialia 245 (2023) 118613.]

FeCrAl alloy is one of the promising cladding materials in advanced nuclear reactors. Here we compare the irradiation response of the nanolaminate (NL) and coarsegrained (CG) FeCrAl alloys by performing He-ion irradiation, followed by in situ Kr-ion irradiation in a transmission electron microscope at 450°C. NL alloy has reduced He-bubble-induced swelling and decreased the density of dislocation loops in comparison to

the CG alloy. The distribution of He bubbles appears to be dependent on misorientation angles of highangle grain boundaries. A new type of nanoprecipitate was identified in the irradiated CG FeCrAl without noticeable chemical segregation. Chemical segregation occurred along the laminate boundaries in the irradiated NL FeCrAl alloy.

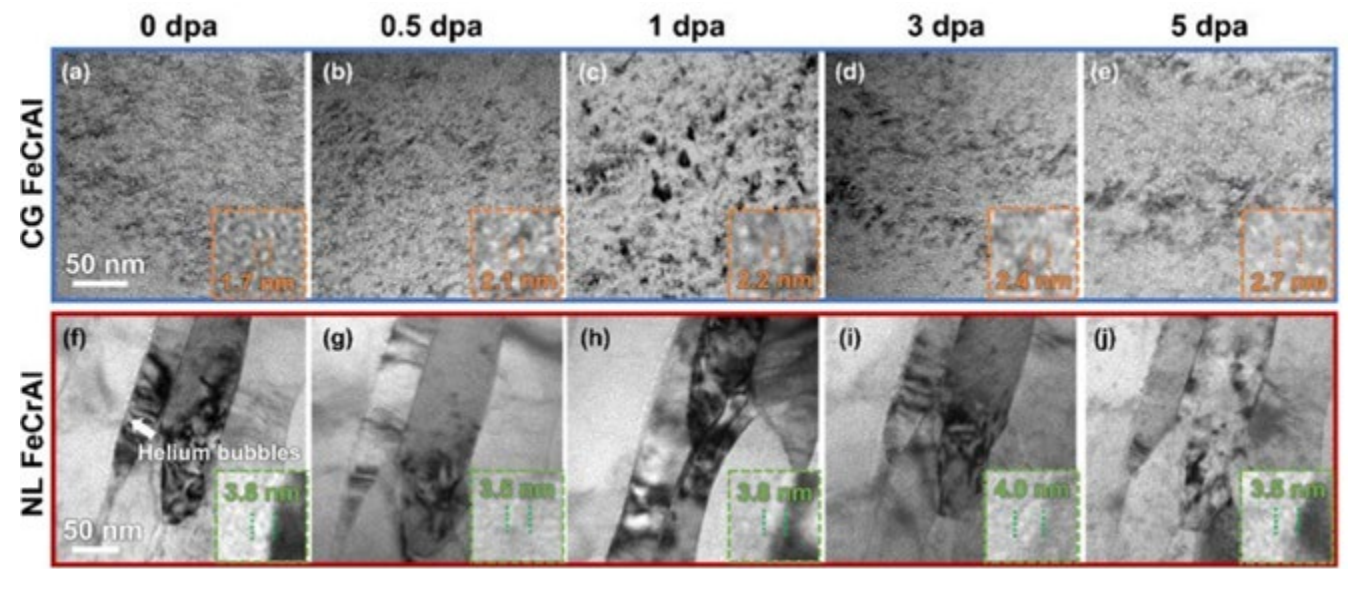


Figure 3. In situ TEM snapshots showing the microstructure evolution of helium (1 at.%) pre-irradiated CG and NL FeCrAl alloys after various Kr-ion irradiation doses at 450° C. (a–e) Helium bubble evolution in the matrix of CG FeCrAl. (f–f) He bubbles along the laminate grain boundaries in NL FeCrAl. Inserts show magnified view of He bubbles.

In situ radiation has been performed on CG and NL FeCrAl with 12-keV He ion and 1-MeV Kr ion at 450°C. He bubbles nucleated homogeneously in the grain interior of CG and NL FeCrAl. These bubbles grew during the Kr-ion radiation through bubble migration and coalescence. Overall, the He-bubble-induced swelling is much less evident in the matrix of NL FeCrAl relative to CG FeCrAl. He bubbles preferentially nucleated along the GBs of the NL FeCrAl. The size and density of GB bubbles varied with misorientation angles. Both <100> and 1/2<111>

dislocation loops were found in the irradiated CG and NL FeCrAl. The NL FeCrAl has a lower dislocation-loop number density than that of the CG FeCrAl because of the sink effect of the high-density laminate GBs. A new type of nanoprecipitates with face-centered cubic (fcc) structure was discovered in the irradiated CG FeCrAl for the first time. These precipitates have a Bain orientation relationship with the body-centered cubic (bcc) matrix. EDS analyses revealed that the GBs in the NL FeCrAl were depleted with Fe and Cr, enriched with Al.

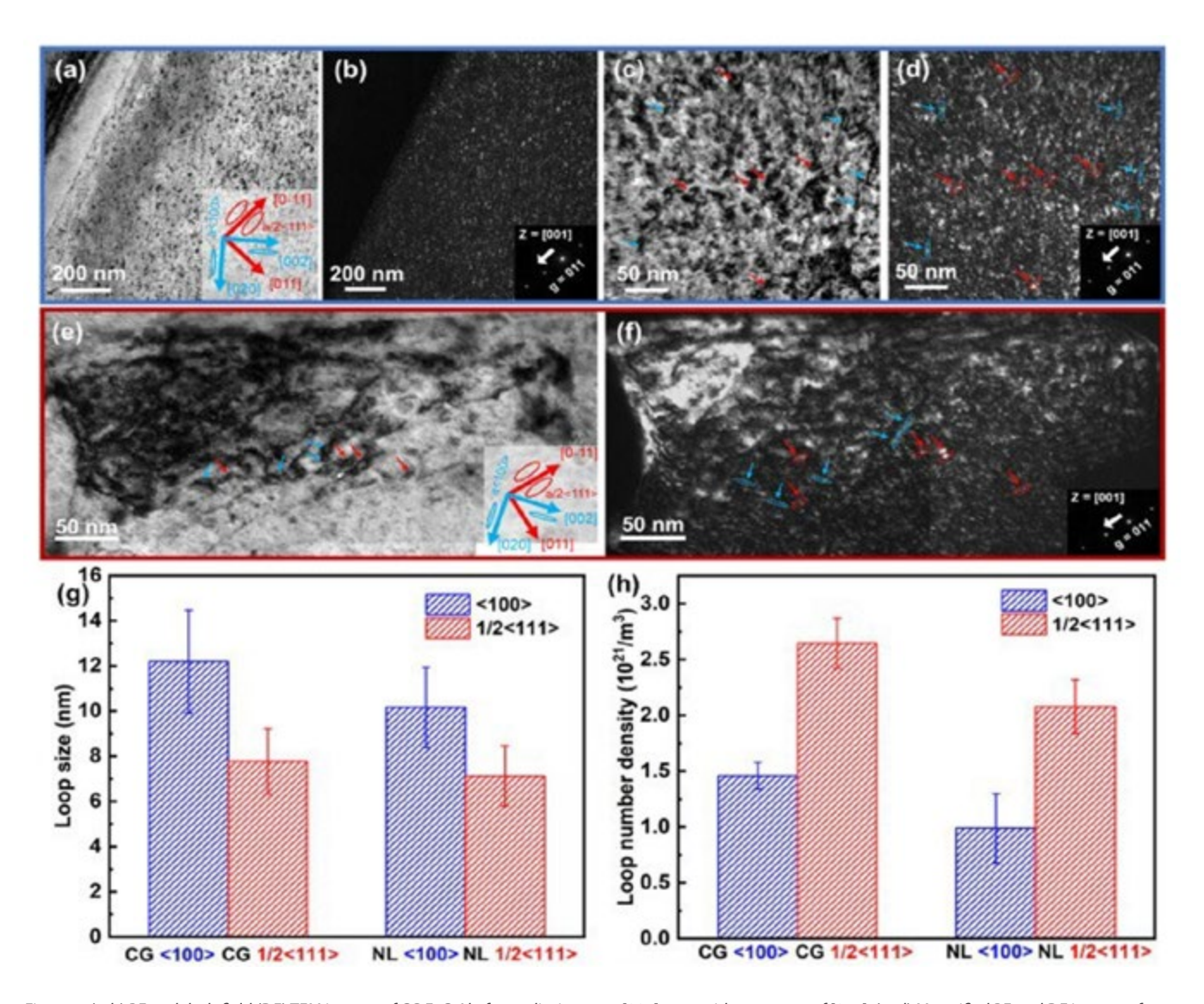


Figure 4. (a-b) BF and dark-field (DF) TEM images of CG FeCrAl after radiation near [001] zone with a g vector of [011]. (c-d) Magnified BF and DF images of irradiated CG FeCrAl showing <100> (blue) and 1/2 < 111> (red) dislocation loops. (e-f) BF and DF TEM images of irradiated NL FeCrAl near [001] zone axis (g = [011]). (g, h) Size and density of <100> and 1/2 < 111> dislocation loops in CG and NL FeCrAl.

RTE 1665: Defect Clustering in 316H Stainless Steel and High-Entropy Alloy Under *In Situ* Irradiation at 600–700°C

PI: Wei-Ying Chen, Argonne National Laboratory (ANL)

Facility: Intermediate Voltage Electron Microscopy-Tandem Facility, Argonne National Laboratory

Type 316H stainless steel has been dominantly adopted by molten-salt reactor vendors because of its code-qualification status and acceptable corrosion rate under proper redox conditions. However, its insufficient high-temperature strength is of great concern. Therefore, Department of Energy, Office of Nuclear Engineering (DOE-NE) called for new materials exhibiting high-temperature (around 700°C) strength, and resistance to molten-salt corrosion. Among many candidates, high-entropy alloys (HEAs) have been actively considered. This work proposes to perform in situ observation on HEAs, 316H stainless steel (reference commercial material) and nickel (reference modal material) under irradiation at 600–700°C in the IVEM Facility with a focus to reveal the dynamic processes of primary damage and the following microstructural evolution.

The following in situ experiments were performed during the RTE project:

- Al_{0.3}CoCrFeNi irradiated at 600°C to 1 dpa
- CoCrFeMnNi irradiated at 600°C to 1 dpa
- 316H irradiated at 600°C to 1 dpa
- Ni irradiated at 600°C to 3 dpa
- Al_{0.3}CoCrFeNi irradiated at 700°C to 3 dpa
- 316H irradiated at 700°C to 1 dpa
- Ni irradiated at 700°C to 1 dpa.

All materials are fully annealed; therefore, they started as defect-free crystals. Figure 1. shows the microstructure evolution of Al0.3CoCrFeNi irradiated at 600°C to 1 dpa. Faulted and perfect dislocation loops are observed as a function of dose. No voids are observed up to 1 dpa. Compared to a previous study at 500°C, the loop size is larger and the density smaller [1]. In contrast, Figure 2 shows the microstructure evolution of the same Al_{0.3}CoCrFeMnNi under irradiation at 700°C. At this temperature, no loop formation is observed. The result for Ni irradiated at 700°C is similar.

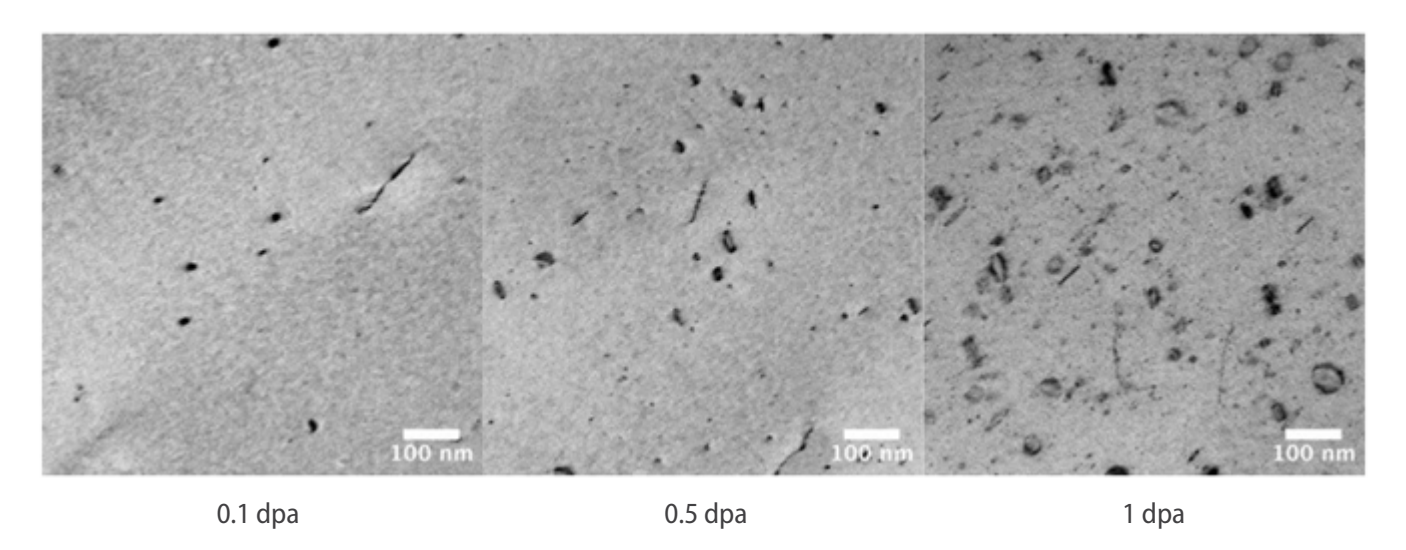


Figure 1. Al0.3CoCrFeMnNi under in situ 1 MeV Kr-ion irradiation at 600° C to a final dose of 1 dpa. The images were taken from nearby areas of same grain. Imaging condition is g = 200 near 011 zone axis.

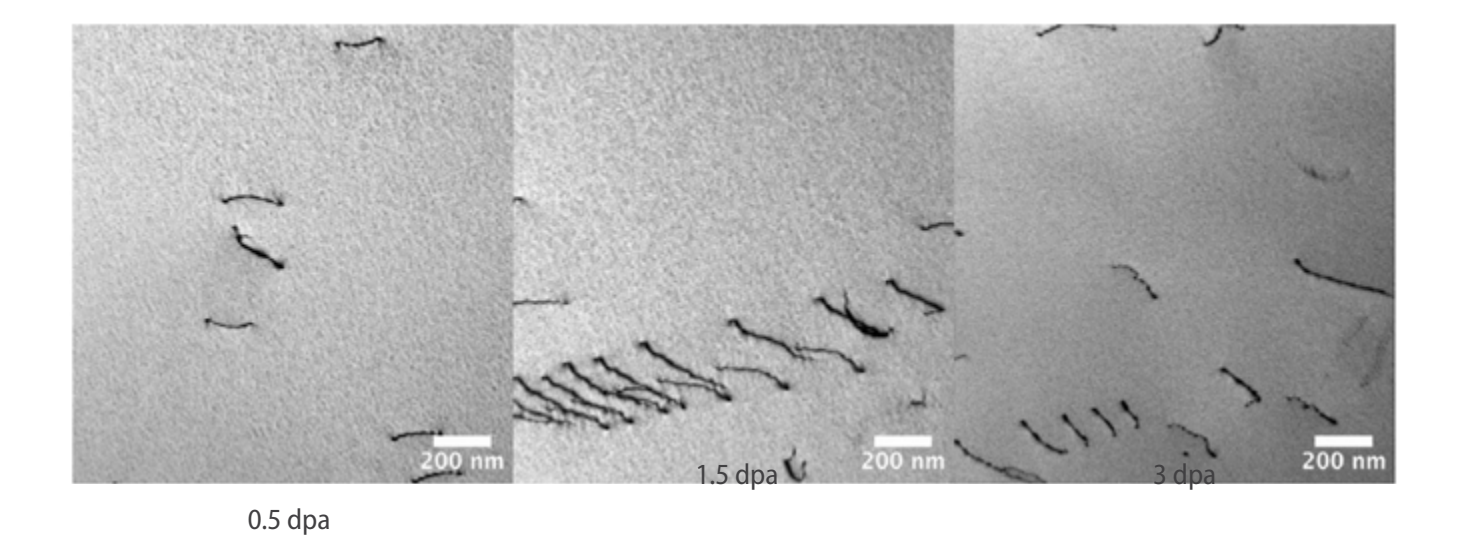


Figure 2. Al0.3CoCrFeMnNi under in situ 1 MeV Kr-ion irradiation at 700° C to a final dose of 3 dpa. The images were taken from nearby areas of the same grain. Imaging condition is g = 200 near 011 zone axis.

Figure 3 shows the microstructure evolution of CoCrFeMnNi irradiated at 600°C to 1 dpa. In addition to the large dislocation loops, line segments are formed under irradiation. The nature of these contrasts must still be investigated. This type of contrast was not observed in Al0.3CoCrFeNi and 316H, or CoCrFeMnNi irradiated at 500°C [1]. Besides, a grain boundary in CoCrFeMnNi after irradiation at 600°C to 1 dpa is shown in Figure 4. It appears to have a denuded zone of dislocation loops near the grain boundary. However, a high concentration of dislocation loops is also observed in the very vicinity of the grain boundary. This phenomenon needs to be further investigated. One of the questions will be whether the dislocation loops observed near grain boundaries and away from grain boundaries are of the same nature (i.e., interstitial or vacancy).

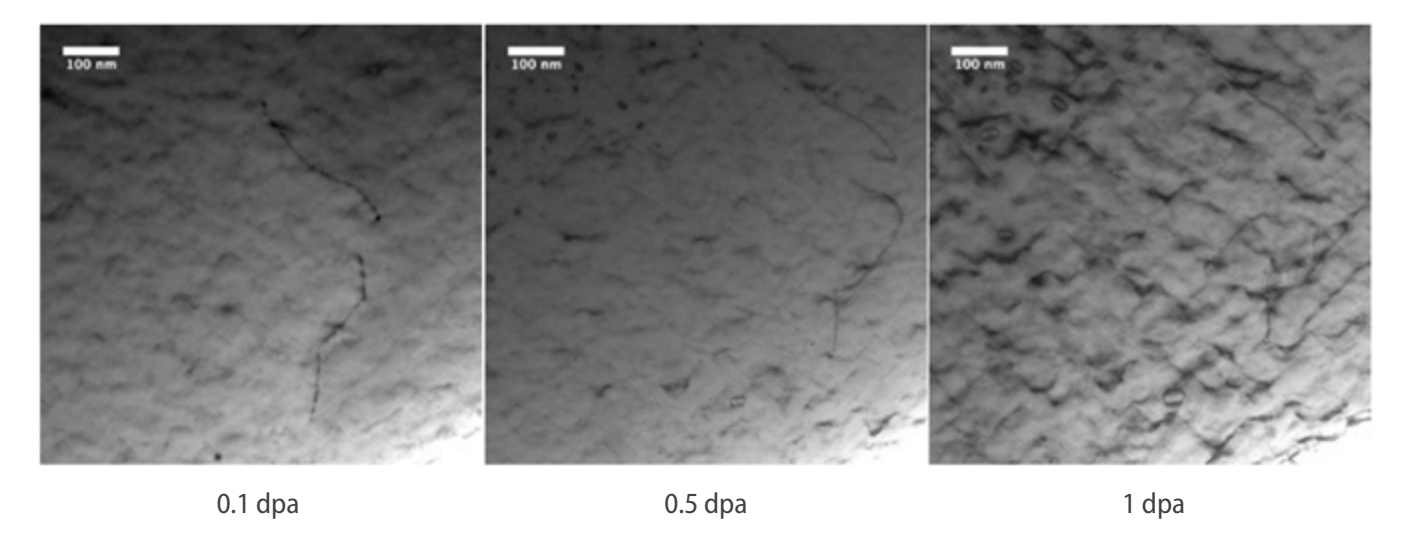


Figure 3. CoCrFeMnNi under in situ 1 MeV Kr-ion irradiation at 600° C to a final dose of 1 dpa. The images were taken from nearby areas of the same grain. Imaging condition is g = 200 near 001 zone axis.

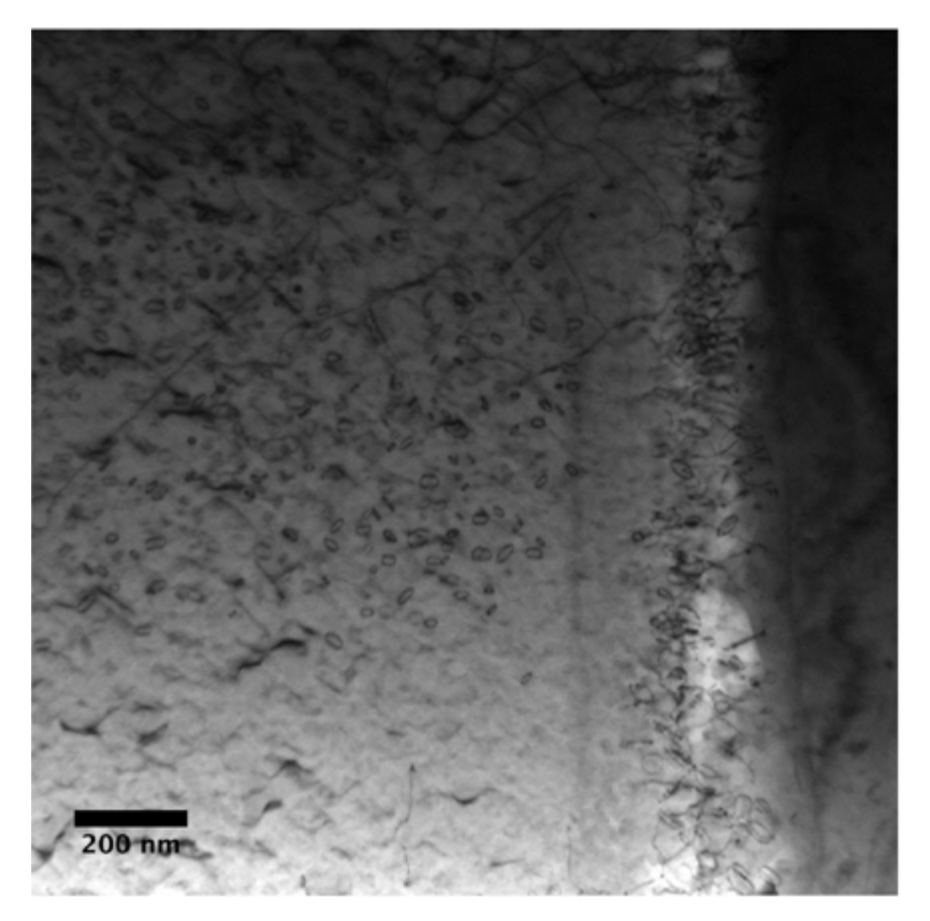


Figure 4. BF TEM image near a grain boundary of CoCrFeMnNi irradiated in situ with 1 MeV Kr ions at 600° C to 1 dpa. Imaging condition is g=200 near 001 zone axis.

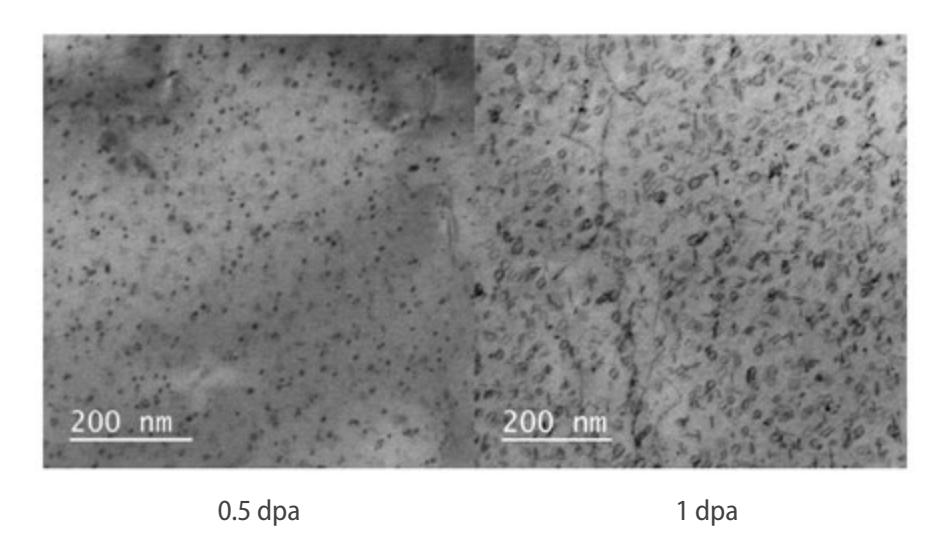


Figure 5. BF TEM image near a grain boundary of 316H irradiated in situ with 1 MeV Kr ions at 600° C to 1 dpa. Imaging condition is g = 200 near 001 zone axis.

Figure 5 shows the defect evolution of 316H stainless steel, irradiated at 600°C to 1 dpa. The loop density is higher than that in the two HEAs. Figure 6 shows an image of 316H stainless steel irradiated at 700°C to 0.1 dpa. Stripes with a size of about 20–100 nm are uniformly observed. These features might be precipitates, but must be further investigated. Figure 7 shows Ni under in situ 1 MeV Kr-ion irradiation at 600°C to 1 dpa. Voids and both perfect and faulted dislocation loops are observed.

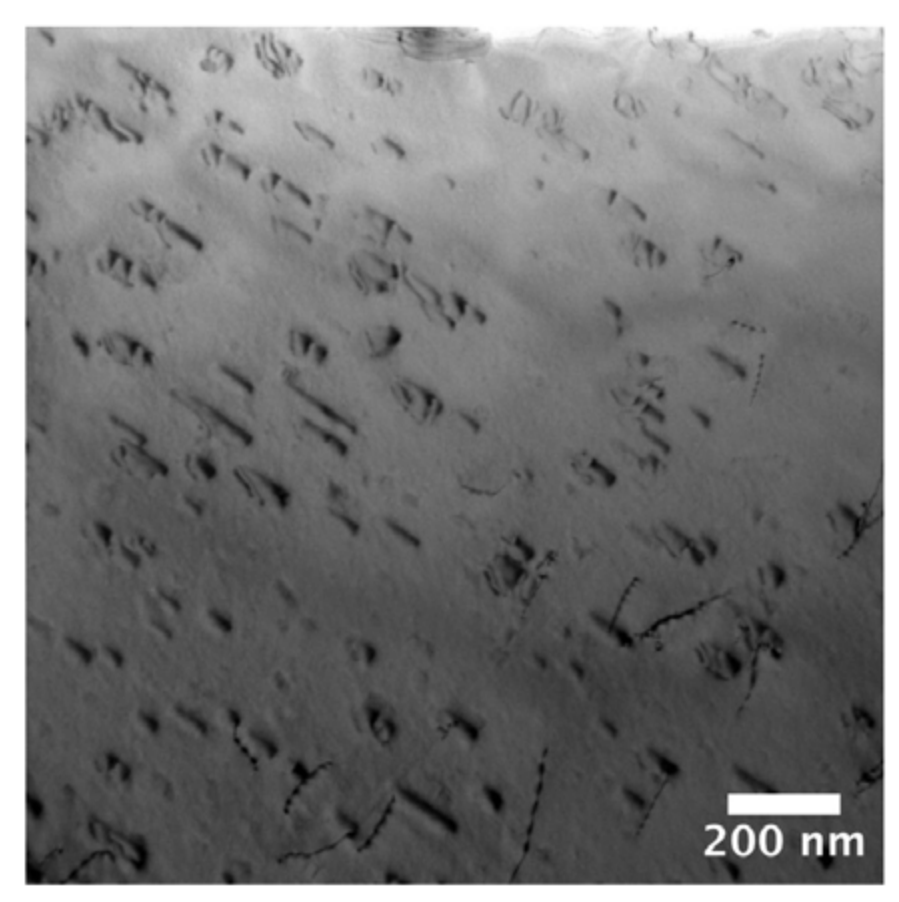


Figure 6. BF TEM image of 316H stainless steel after in situ 1 MeV Kr-ion irradiation at 700° C to 0.1 dpa.

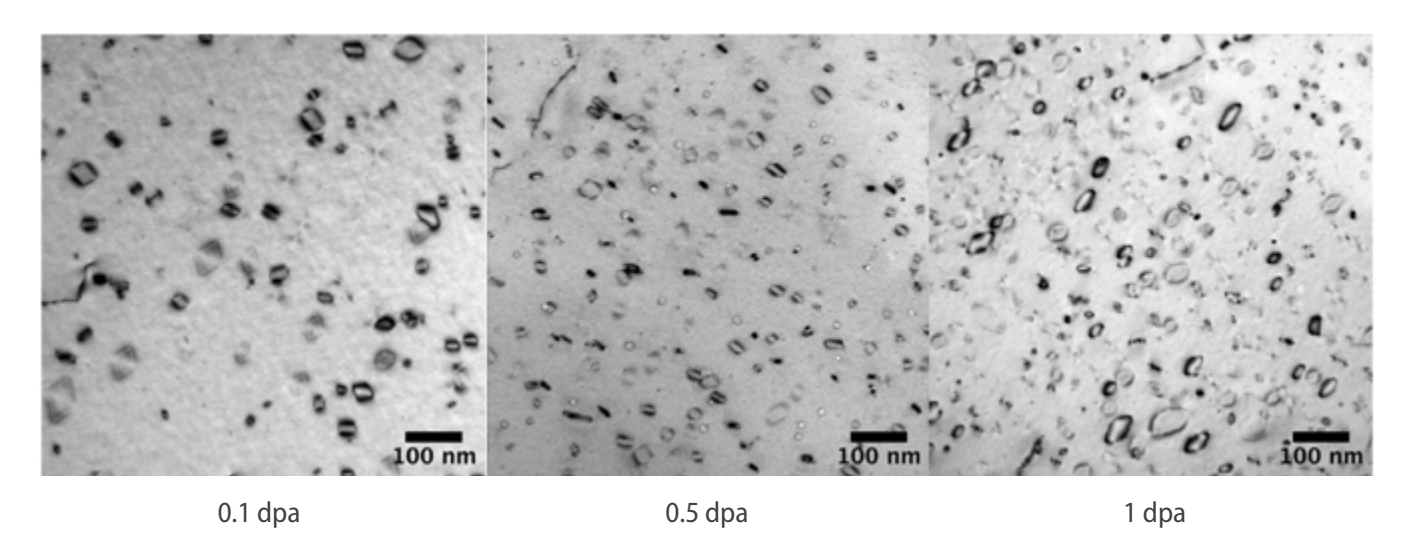


Figure 7. Ni under in situ 1 MeV Kr-ion irradiation at 600° C to a final dose of 1 dpa. The images were taken from nearby areas of same grain. Imaging condition is q = 200.

Potential Impact to the State-of-Art Knowledge

The findings of this study offer several insights to advance the understanding of radiation resistance of HEAs at high temperatures.

Al_{0.3}CoCrFeNi, CoCrFeMnNi, 316H, and Ni all shows irradiation-induced dislocation loops after irradiation at 600°C. The higher loop density in 316H suggests greater hardening of 316H relative to Al_{0.3}CoCrFeNi and CoCrFeMnNi HEAs at 600°C. This supports the notion that HEAs offer advantages for high-temperature applications in nuclear reactors.

At 700°C, no dislocation loops were observed in Al_{0.3}CoCrFeNi, 316H, and Ni, indicating that 700°C is beyond the stable temperature range for interstitial loops in these materials. Nevertheless, the precipitate-like features observed in 316H, if they can be confirmed as precipitates, indicate that 316H is more susceptible to phase instability under irradiation-enhanced diffusion than are HEAs. This further supports the superiority of HEAs over 316H for operation at even higher temperatures, such as 700°C.

The 600°C observation of voids in Ni, but not in Al_{0.3}CoCrFeNi, shows the void-swelling resistance of HEAs relative to Ni metal. However, we did not see void swelling in 316H, either, so we do not know whether HEAs are better than 316H in regard to their resistance to void swelling. Nevertheless, based on the knowledge obtained in this project, it is established that a dose higher than 1 dpa is required to generate voids at 600°C in both HEAs and 316H for meaningful comparison.

Reference

[1] W.-Y. Chen, M.A. Kirk, N. Hashimoto, J.-W. Yeh, X. Liu, Y. Chen, Irradiation eOects on Alo. 3CoCrFeNi and CoCrMnFeNi high-entropy alloys, and 316H stainless steel at 500° C, Journal of Nuclear Materials 539 (2020) 152324

RTE 1770: *In Situ* Nanomechanical Characterization of Neutron-irradiated HT-9 Steel

PI: Tanvi Ajantiwalay, Pacific Northwest National Laboratory (PNNL, previously University of Florida)

Collaborators: Megha Dubey, Yaqiao Wu (Center of Advanced Energy Sciences), Patrick Warren (University of Texas and San Antonio, formerly Purdue University), Janelle Wharry (Purdue University), Brandon Bohanon, Assel Aitkaliyeva (University of Florida)

Facility: Electron Microscopy Laboratory, Idaho National Laboratory; Ion Beam Laboratory, Sandia National Laboratories

Summary

Nanocompression tests were used to investigate the behavior of HT-9 steel neutron-irradiated to 4.29 dpa at 469°C. The deformation of both as-received and neutron-irradiated HT-9 was monitored in situ with a transmission electron microscope, which allowed linking microstructure of the material with the evolution of mechanical properties and identifying the mechanisms governing irradiation-induced hardening of these

steels. In nanocompression tests, inhibition of dislocation glide was identified as the primary hardening agent. Sample preparation was performed using the FIB at the Materials and Fuels Complex (MFC), INL, and nanocompression tests were performed at CAES to correlate the microstructure and mechanical properties.

The as-received nanopillars show a size effect, where the yield strength increases with a decrease in the

minimum dimension of the pillar (thickness, in this case). Irradiation to 4.29 dpa leads to hardening of the material associated with an increase in an average yield strength value from 1.00 ± 0.81 to 1.42 ± 0.40 GPa. Generally, irradiated nanopillars also follow the "smaller is stronger" linear trend that we observed in as-received HT-9, with the pillar thickness having the largest impact on yield strength. See Figure 1(c) for graphical illustration.

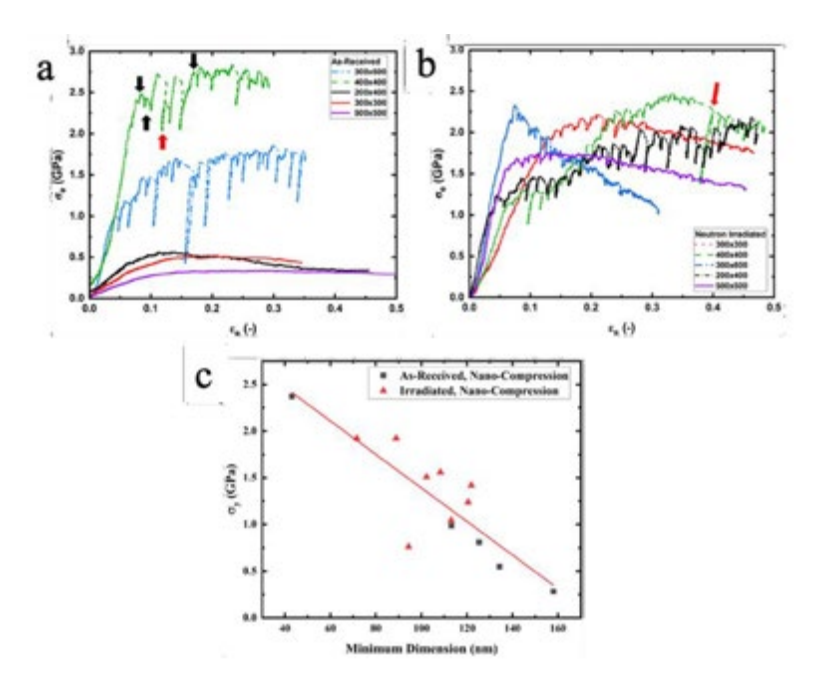


Figure 1. Stress-strain curves for the nanopillar compression tests in (a) the as-received and (b) neutron-irradiated HT-9. Black arrows indicate load drops attributed with dislocation movement while the red arrows correspond to slip events. (c) Evolution of the yield strength with the minimum pillar dimension for both as-received and neutron-irradiated HT-9. The red line represents the power law commonly used to represent the relation between sample size and yield strenath.

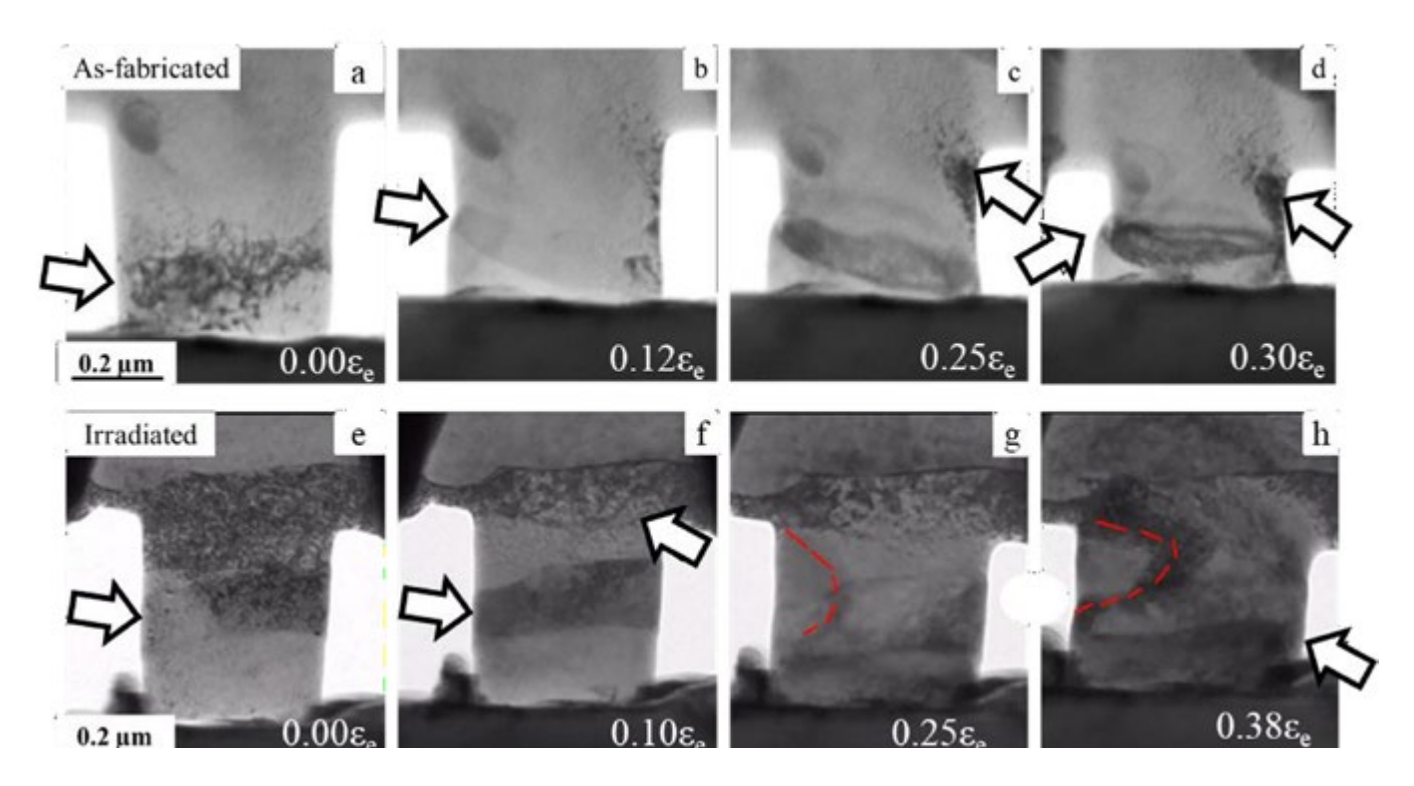


Figure 2. Snapshots taken during nanocompression testing of the as-received (a-d) and neutron-irradiated (e-h) 400 \times 400 pillars.

TEM examination of each nanopillar prior to compression showed few secondary-phase precipitates (one such precipitate is highlighted by the white arrow in Figure 2[e]). It is likely that neutron-irradiated samples also contained nanoclusters and/or micron-sized dislocation loops, which are known to cause hardening of the materials. However, TEM data was collected at relatively low magnifications, and these micron-sized features were not at an ideal condition to be discernible. The main goal of this work was to visualize irradiation hardening mechanisms after neutron irradiation in HT-9 steels. From the above data, the primary hardening agent in irradiated nanopillars was identified as dislocation networks, which inhibit the dislocation glide under compression.

RTE 1802: Microstructure Characterization of Neutron-Irradiated Fe-Cr-C Model Alloys

PI: James Stubbins, University of Illinois at Urbana-Champaign (UIUC)

Co-Pls: Xiang Liu (INL), Hoon Lee (UIUC)

Facility: Hot Fuel Examination Facility / Irradiated Materials Characterization Laboratory, Idaho National Laboratory

Summary of Work Completed and Data Obtained

This RTE was awarded to perform microstructural examination on four Fe-₁₂Cr- 0.2C model alloys that were irradiated in ATR under award "Irradiation Performance of Fe-Cr Base Alloys," 08-92 as part of a large irradiation program on model and

commercial steels for advanced-reactor applications. The choice of this model-alloy condition was made for its similarity to commercial alloy HT-9, which has the same base composition, including the same C level, but with alloying additions of 1% Mo and 0.5% W.

The alloy conditions were Fe-₁₂Cr-0.2C irradiated to 300°C to 0.01, 0.1, 0.5, and 1.0 dpa. This temperature and these doses for each specific sample were calculated from the ATR operational parameters, and the calculated temperatures and doses are provided in Table 1.

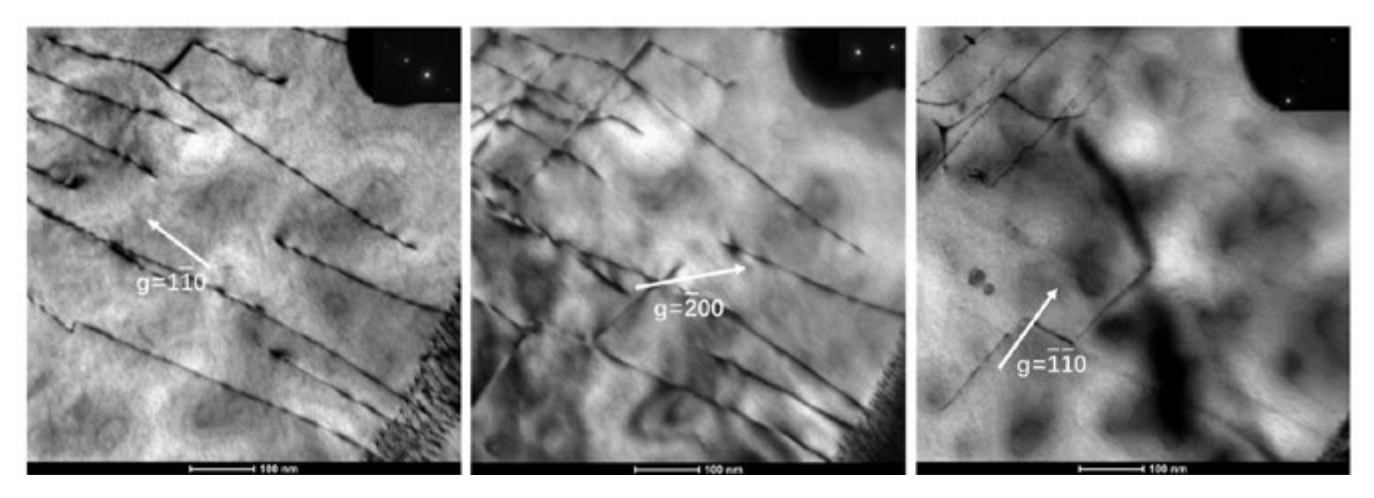
Table 1. Sample irradiation conditions.

Sample	Sample ID	As-Run Temp	As-Run Dose	Fluence
Fe- ₁₂ Cr-0.2C	KGT 1184	291.40°C	0.012 dpa	6.03 x 10 ¹⁹
Fe- ₁₂ Cr-0.2C	KGT 1153	287.45°C	0.11 dpa	5.98 x 10 ²⁰
Fe- ₁₂ Cr-0.2C	KGT 720	375°C	0.6 dpa	2.23 x 10 ²¹
Fe- ₁₂ Cr-0.2C	KGT 898	340°C	1.01 dpa	3.86 x 10 ²¹

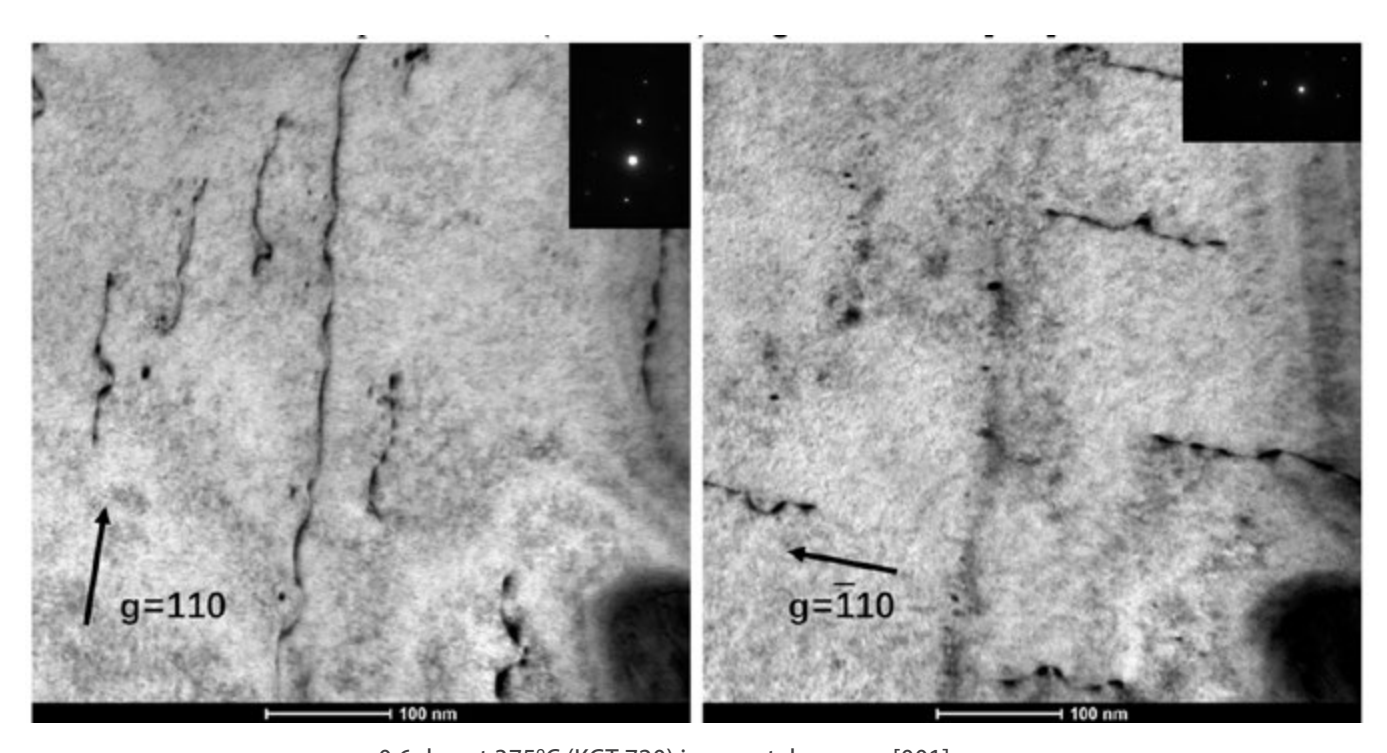
The experimental work included sample preparation and STEM characterization of neutron-irradiated Fe $_{-12}$ Cr-0.2C model alloys (i.e., NSUF Specimen Library identification numbers KGT 720, KGT 898, KGT 1153, and KGT 1184). The experimental analyses were conducted at the Electron Microscopy Laboratory and the IMCL, INL. The radioactive samples were twin jet-polished to perforation using a Struers Tenupol-5 polisher.

The dislocation structures of four different irradiated Fe-₁₂Cr-0.2C model alloys were characterized using kinematic BF STEM imaging near the [001] zone axis. At least two different diffraction vectors were used for grain-boundary analysis.

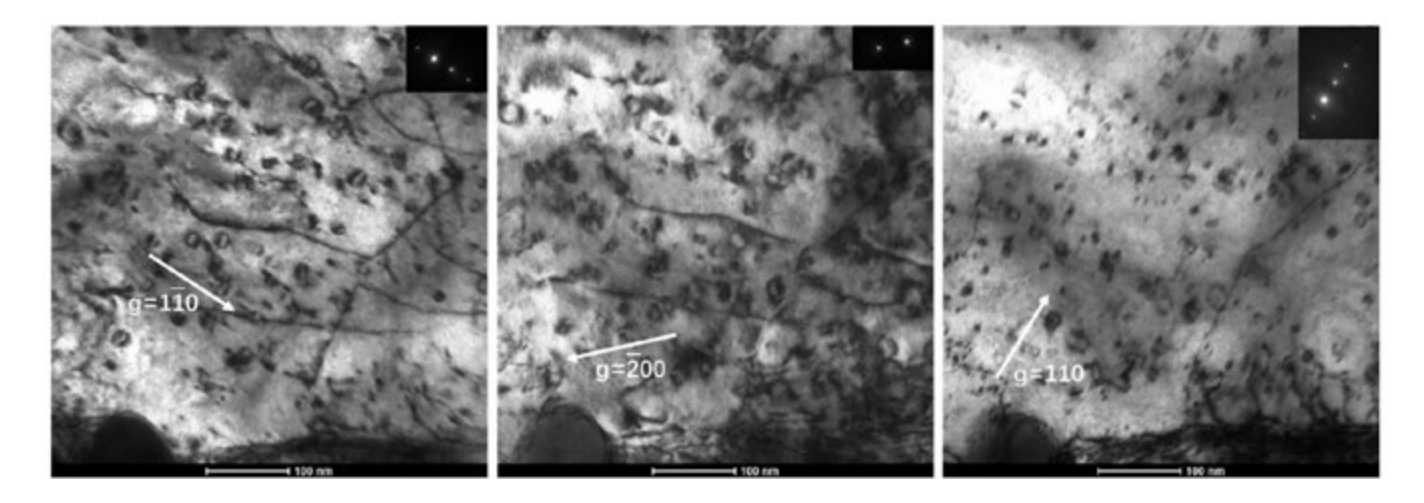
Figure 1 shows results of different dislocation and dislocation-loop structures found in these irradiated $Fe_{-12}Cr$ -0.2C model alloys.



0.012 dpa at 291°C (KGT 1184) images taken near [001] zone.



0.6 dpa at 375°C (KGT 720) images taken near [001] zone.



1.1 dpa at 340°C (KGT 898) images taken near [001] zone.

Figure 1. Irradiated Fe-12Cr-0.2C model alloys, showing dislocation and dislocation-loop structures. Insertions at the top right are corresponding diffraction patterns.

These alloys were part of a set of in situ Synchrotron tensile experiments conducted at the Argonne National Laboratory (ANL) Advanced Photon Source through Award 15-CINR-8305, "In situ Synchrotron Wide-Angle X-ray Scattering (WAXS) Tensile Investigation of Neutron Irradiated Ferritic Alloys." This TEM work was used to support the microstructural analysis of HT-9 under Nuclear Energy University Program (NEUP) DOE INL Project 12-3882, Irradiation Performance of Fe-Cr Base Alloys, and NSUF access-only Project 15-8312. As demonstrated by the TEM images, significant increase in hardening and yield strength in this model alloy are achieved by ~1 dpa through the evolution of a substantial loop microstructure. The initiation of the development of small black-dot-sized loops can be seen between doses of 0.01 and 0.1 dpa. These loops have been shown to be mobile in many cases, and their association with the existing dislocation structures at 0.1 dpa is clear. By ~1 dpa, a much more-uniform distribution of loops has evolved.

Description of the Potential Impact to the State of Knowledge

This work is part of a large program to characterize a selected number of Fe-Cr base alloys following neutron irradiation in the ATR from 0.01 to 10 dpa at target temperatures of 300, 450 and 550°C. The Fe-Cr alloys include model alloys of Fe- $_9$ Cr and Fe- $_{12}$ Cr to understand the effect of carbon on irradiation material performance from 0 to 5% C, depending on the alloy composition. The program also includes similar irradiation conditions for T91 and HT-9 which represent commercial alloys with the same Cr alloying additions.

This study is part of an ongoing effort to time the irradiation-induced microstructural evolution to mechanical properties, primarily hardness and tensile properties, to correlate the microstructure to changes in mechanical-deformation behavior. The value of this particular RTE was to study the early microstructural evolution under irradiation in a model alloy, Fe-₁₂Cr-0.2C, which represents HT-9. The results have potential applications to elucidate the early, low-temperature hardening behavior of HT-9 that has been found in other parts of the larger program.

Because this experiment uses activated, ATR neutron-irradiated material, the use of NSUF facilities was critical to examine these alloys under irradiated conditions.

RTE 2904: Investigation of the Irradiation-Induced Porosity in Concrete Aggregates With X-ray Computed Tomography and Helium Pycnometry

Ippei Maruyama (Nagoya University), Christa E. Torrence (Texas A&M University), Ercan Cakmak, J. David Arregui-Mena, Thomas M. Rosseel, Elena Tajuelo Rodriguez, and Philip D Edmondson (ORNL)

Facility: Oak Ridge National Laboratory

Introduction

Concrete plays a critical role as a structural component and radiation shield in U.S. nuclear power plants (NPPs). However, the harsh environmental conditions within NPPs can lead to the deterioration of concrete components, potentially impacting their mechanical strength and longevity. Neutron irradiation,

in particular, induces a phenomenon known as radiation-induced volumetric expansion, which can cause significant damage to concrete aggregates and cement paste.

Methodology

To investigate the effects of neutron irradiation on concrete aggregates, X-ray computed tomography (XCT)

scans were performed on neutronirradiated specimens obtained from the Japanese Concrete-Aging Management Program at the JEEP II reactor in Norway's Institute for Energy Technology. The mineral composition and irradiation conditions of each specimen characterized with this grant are detailed in Table 1.

Table 1. Summary of the irradiation conditions, and mineral composition of the specimens.

Mineral type	Mineral composition	ID specimens	Neutron fluence(n/cm²)
E (Sandstone)	Quartz 47%, Albite 23%, Sericite 10%, Anorthite 7%, Microcline	E260 E31	_
	4%	E050, E06	8.25 x 10 ¹⁹
F (Altered tuff)	Quartz 91%, Microcline 3%, Anorthite 2%, Others 4%	F260, F33	_
		F23	7 x 10 ¹⁸
		F11	1.28 x 10 ¹⁹
		F17	4.12 x 10 ¹⁹
		F06	8.25 x 10 ¹⁹
G (Sandstone)	G (Sandstone) Quartz 40%, Albite 30%, Microcline 9%, Sericite 7%, Chlorite 4%,		_
	Calcite 3%, Others 7%	G11	1.28 x 10 ¹⁹
		G17	4.12 x 10 ¹⁹
		G05, G06	8.25 x 10 ¹⁹
J (Sandstone)	Albite 34%, Quartz 24%, Calcite 18%, Sericite 13%, Chlorite 11%	J260, J05, J06	8.25 x 10 ¹⁹
K (Limestone)	Calcite 91%, Amorphous 9%	J05, K06	8.25 x 10 ¹⁹

The XCT scans were analyzed using Zeiss Xradia Vera scanner and Avizo Fire software.

Results

The XCT scans revealed extensive cracking in the neutron-irradiated aggregates, as indicated by blue arrows in Figure 1. The volumetric expansion of aggregates due to neutron-induced amorphization of minerals led to significant damage and a potential decrease in mechanical properties.

Discussion

The research findings provide valuable insights into the detrimental effects of neutron irradiation on concrete aggregates, highlighting the importance of identifying minerals susceptible to such damage. This information can contribute to reducing uncertainties in predicting the state of concrete components within NPPs. Further research will focus on identifying minerals with more-extensive damage to better mitigate the adverse effects of neutron irradiation.

Conclusion

The investigation into neutron-irradiation effects on concrete aggregates in NPPs underscores the significance of understanding and addressing potential structural vulnerabilities. By identifying the specific minerals prone to damage, this research offers valuable information to enhance the resilience of concrete components in NPPs.

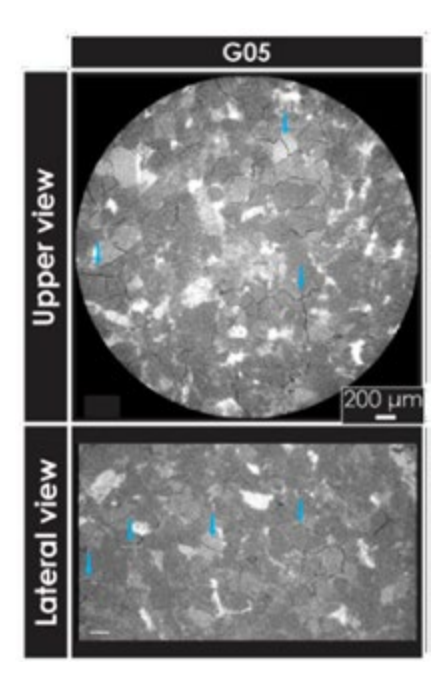


Figure 1. XCT scans of G05 neutron-irradiated sample.

RTE 2986: Correlating Microstructure to the Thermal Conductivity of Irradiated U-20Pu-10Zr Fuels

PI: Allison Probert (University of Florida)

Collaborators: Assel Aitkaliyeva (University of Florida), Luca Capriotti, Cynthia Adkins, Tsvetosalov Pavlov, Ethan Hisle (INL)

Facility: Microscopy and Characterization Suite, Center for Advanced Energy Studies; Irradiated Materials Characterization Laboratory, Idaho National Laboratory

This work measured the local thermal diffusivity of irradiated U-19Pu-10Zr fuel (irradiated to ~11 at.% burnup) and correlated thermal-conductivity changes to the phases present in four constituent redistribution regions of the fuel (Figure 1). Several diffusivity measurements within each constituent redistribution region were taken using thermo-reflectance methods in the thermal conductivity microscope (TCM) at INL's IMCL because it was determined that the microscope was more sensitive to diffusivity than to conductivity. Because the fuel sample had been examined in the past, the TCM measurement locations were planned along TEM lift-out locations. The diffusivity data are correlated to microstructural information leveraging optical microscopy and scanning electron microscopy (SEM), electron-probe microanalysis (EPMA) to obtain chemical compositions of the phases, and TEM-based selective-area electron diffraction (SAED) analysis to obtain crystallographic information for each phase. The local thermal conductivity at each position will be calculated using the measured diffusivity and the specific heat capacity and density determined via the chemical composition and crystallographic information. Finally, porosity analysis will be conducted across the diameter of the fuel section to inform density and conductivity changes.

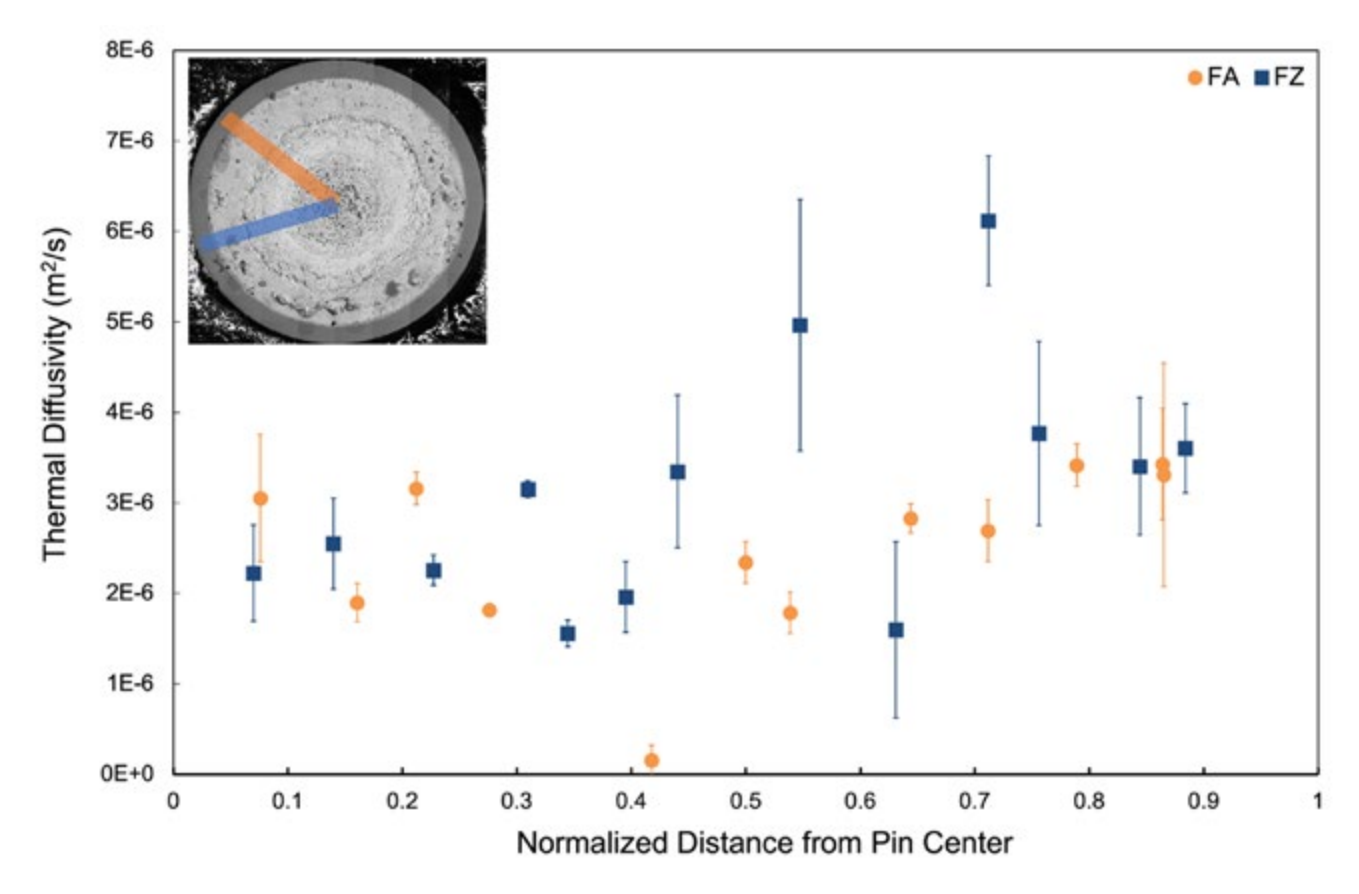


Figure 1. Radial evolution of thermal diffusivity.

RTE 2997: Post-irradiation Microstructure Characterization of Radiation-Tolerant Piezoelectric Materials

Shawn Riechers, Edgar Buck, Lucas Sweet, Shalini Tripathi, Andy Casella (PNNL), Eva Zarkadoula, Pradeep Ramuhalli (ORNL)

Facility: Materials Science and Technology Laboratory, Pacific Northwest National Laboratory

Previous research by PIs Ramuhalli and Daw led to an ~18-month irradiation campaign in the Massachusetts Institute of Technology Reactor (Figure 1) that demonstrated the survivability of bismuth titanate-based ultrasonic sensors to a total dose of up to ~10²¹ neutrons/cm² and at a temperature of approximately 400°C. Measurements collected from these sensors demonstrate a decrease in the response of BiT. In this work, BiT samples were potted in a 2-in.-diameter and 2-in.-thick epoxy to protect the sample, facilitate polishing, and provide safer handling of irradiated material. Pristine and irradiated BiT samples were embedded into epoxy-resin blocks and polished by standard methods to a colloidal silica finish. SEM was conducted with an FEI Quanta 250FEG (Thermo Fisher, Inc., Hilsboro, Oregon) equipped with EDAX Hikari (EDAX, Inc., Mahwah, New Jersey) electron backscattered diffraction (EBSD) system and an EDAX Apollo X EDS system. Piezo response was measured with the NSUF MF3PD Infinity Atomic Force Microscope (Oxford/Asylum Research, Santa Barbara, California) located in the Radiation Microscopy Suite at Pacific Northwest National Laboratory using dual alternating current (AC) resonance tracking piezoresponse force microscopy (PFM) mode with conductive atomic force microscopy (AFM) probes (Oxford Instruments, Asyalec-01-R2). The potted and polished samples were embedded in epoxy, which insulates the piezo material from contacting the second electrode on the sample stage. A hole was slowly drilled through the epoxy using a hand-operated drill bit until contact was made with the BiT. Silver paint (Leitsilber 200, Ted Pella Inc.) was then applied to secure a wire and make electrical contact with the sample. This technique enables a comparison between applying a bias only at the tip, providing a more-localized electric field, or through the entire thickness of the BiT sample.

BiT samples were polished after neutron irradiation and exhibited a somewhat smoother surface, with an average roughness of ~23 nm, punctuated by pits 0.9 ± 0.4 µm in diameter and 130 ± 16 nm in depth (Figure [1a]). It was observed that, unlike the pristine case, in irradiated BiT there were no indications of individual grains, and variation in piezo response was only observed at higher applied voltages, (Figure 1[b, e]). In addition, no measurable difference was seen in the d_{33} of the insulated vs electrically contacted samples, and little change in contrast (Figure 1).

The irradiated BiT appears amorphous under SEM analysis. While the same pitted surface is observed there is no longer any evidence of grain structure in the image. In addition, SEM-EBSD was not able to identify the crystallattice surface (Figure 2). This is evidence that the radiation damage in the BiT accumulated to the point that the material is at least partially amorphous.

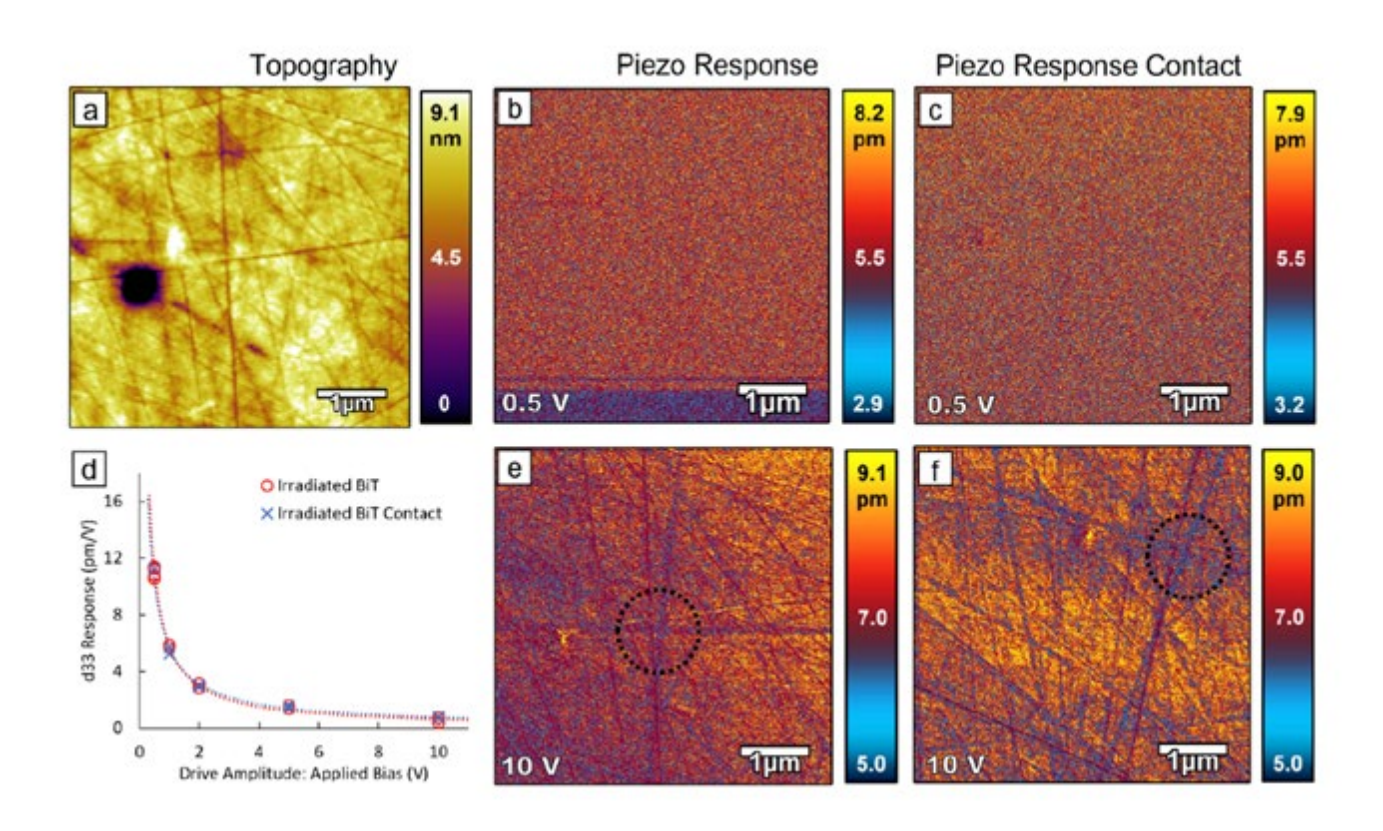


Figure 1. Piezo-response mapping of irradiated BiT. Topography (a) and piezo response of irradiated BiT at 0.5 V (b, c) and 10 V (e, f) without (b, e) and with (c, f) electrical contact with the bottom of the BiT sample.

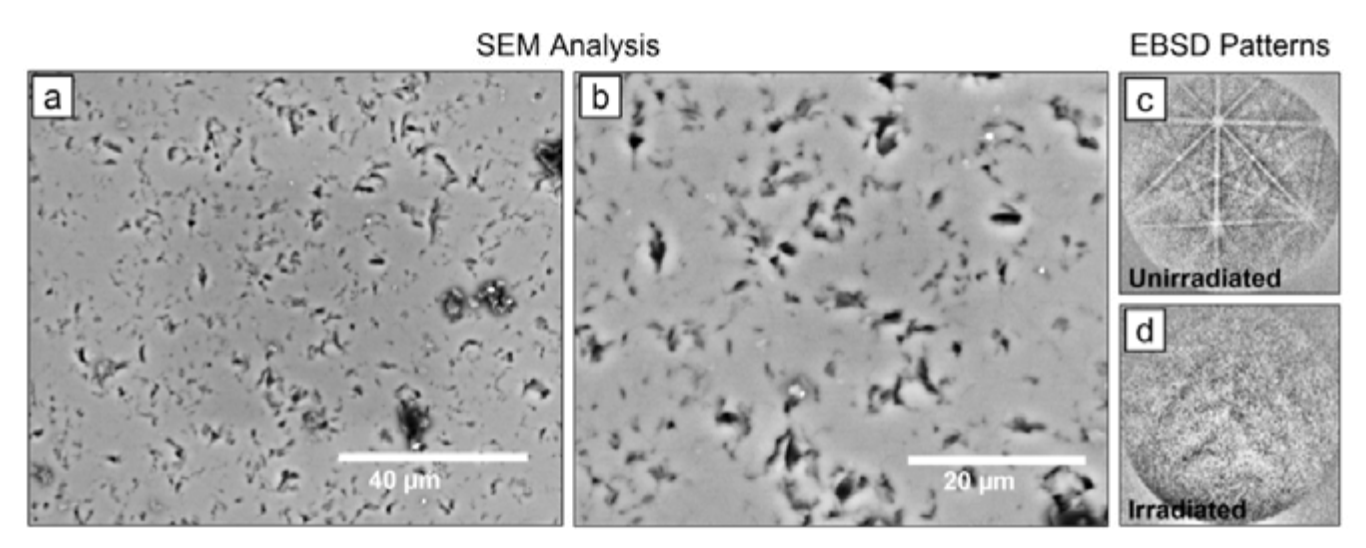


Figure 2. SEM analysis of irradiated BiT. SEM imaging (a, b) and comparison of EBSD patterns of the unirradiated (b) and irradiated BiT (d) showing the complete loss of crystallinity in the reactor-irradiated material.

Program Relevance

It is critical for nuclear-energy advancement that the nuclear industry understand the evolution of sensors' efficiency in nuclear-reactor conditions. The degradation due to irradiation-induced damage affects the piezoelectric response of sensor materials. To this end, it is crucial to understand the correlation of microstructure to the piezoelectric response. PFM and microstructure characterization are capabilities key to understanding the microstructure-piezoresponse relations and accelerate the design of advanced sensors for nuclear environments.

Potential Impact to the State of Knowledge

The correlation between microstructure—including defect types, nature and size—and piezoelectric response is not understood, and it is non-trivial to address. The methodologies developed for this project addressed challenges in measurements and characterization for obtaining insights into this correlation. The information obtained in this project pertain to both the characterization methods and to the correlation of structural response to piezoresponse.

RTE 4112: Ion Irradiation and Examination of Metastability-Engineered Stainless High-Entropy Alloy

PI: Rajiv Mishra, University of North Texas (UNT)

Co-Pls: Ramprashad Prabhakaran (PNNL), Lin Shao, Texas A&M University (TAMU)

Facility: Microscopy and Characterization Suite, Center for Advanced Energy Studies; Accelerator Laboratory, Texas A&M University

The advanced metastable stainless-steel alloy $Fe_{40}Mn_{20}Cr_{15}Co_{20}Si_5$ alloy (CS-HEA) [1], has been extensively explored and found to exhibit superior properties: yield strength of ~700 MPa, ultimate tensile strength of ~1175 MPa, ductility of >35%, and corrosion resistance comparable to 304 and 316 stainless steels [2–4]. This work investigated CS-HEA, which exhibits transformation-induced plasticity (TRIP) from γ -fcc \rightarrow e-hexagonal close-packed (hcp), as a probable candidate for nuclear applications. The objective of this study was to investigate the influence of heavy-ion irradiation on metastability in CS-HEA to address key questions:

- 1. (1) y/ε interfaces—does the irradiation impact these boundaries?
- 2. C/a ratio change—these metastable alloys have demonstrated unique evolution of the c/a ratio in ε -hcp phase during deformation [3,5]. Does irradiation induce a c/a ratio change in the ε -phase?
- 3. Do y/y and ε/ε boundaries behave differently?
- 4. Does the metastability of the alloy change due to irradiation?

For this purpose, material was provided by UNT in sheet form and homogenized. The resulting microstructure consisted of equiaxed γ -fcc grains with an average grain size of ~30 μ m with annealing twins and ϵ -hcp at the triple junctions. The irradiation experiments were performed at TAMU using a 3.0 MV NEC tandem accelerator with a static beam [6] using 5 MeV Fe selfions over a temperature range of 350–500°C to 25–100 dpa. The doses were determined using the SRIM code under KP mode. The irradiated samples were characterized at MaCS at CAES, Boise State University, Idaho, and the Microscopy Research Facility (MRF), UNT. Table 1 gives a summary of the progress of the project.

Table 1. Summary of accomplishment of this proposal.

Material (at%)	$Fe_{40Mn_{20}Cr_{15}Co_{20}Si_{5}}(at\%)$			
Techniques (NSUF)	Irradiation	✓		
	Nanoindentation	✓		
	FIB for TEM sample	✓		
	TEM	✓		
Techniques (non-NSUF @ UNT)	X-ray diffraction (XRD)	✓		
	Nanoindentation	✓		
	Detailed TEM	✓		

Figure 1 gives a summary of the effect of irradiation and temperature that led to the recently-proposed concept of "self- healing" by Agrawal et al. [7] in TRIP alloys. The irradiated alloy undergoes a ϵ -hcp martensitic transformation at a lower temperature, whereas a reverse transformation to α -fcc austenite is observed with an increase in temperature by a recovery mechanism. This leads to self- healing of the alloy possible due to the TRIP effect, therefore minimizing irradiation damage. Thus, the results suggest the metastability of the alloy is affected by irradiation.

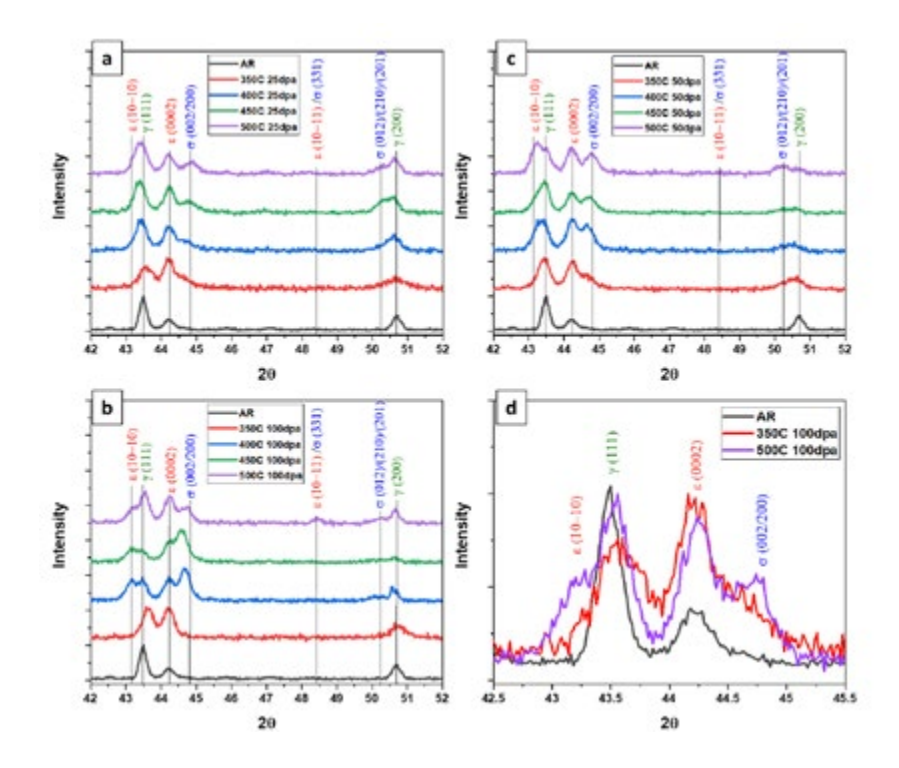


Figure 1. XRD results for irradiated CS-HEA as compared to as-received at different temperatures and doses: (a) 25, (b) 50, (c) and 100 dpa, and (d) comparison of samples irradiated to 100 dpa for the extreme temperature conditions of 350 and 500°C, demonstrating self-healing mechanism in TRIP HEA.

This alloy demonstrated unique evolution of the c/a ratio during deformation for unirradiated samples, as earlier explored by Sinha et al. [2] and Frank et al. [3]. The c/a ratio of pristine sample is lower than the ideal results in the activation of the non-basal deformation mode [8]. With irradiation, a minimum in c/a is observed for 25 dpa for all temperatures except 350°C. The a-fcc shows inverse trends as compared to c/a evolution [8]. As for transformation volume, ΔV , the negative change suggests volumetric contraction. The lower values of $|\Delta V|$, (Figure 2) show the shape-memory effect except for higher dpa conditions for 400 and 450°C. These data points were reasoned to show anomalous behavior due to the presence of ordered fcc in that temperature range along with σ -bct for all conditions. Thus, the effect of irradiation on the evolution of c/a ratio and lower values reported for $|\Delta V|$ make this alloy a candidate for exhibiting shape-memory effect and, thus, a self-healing effect.

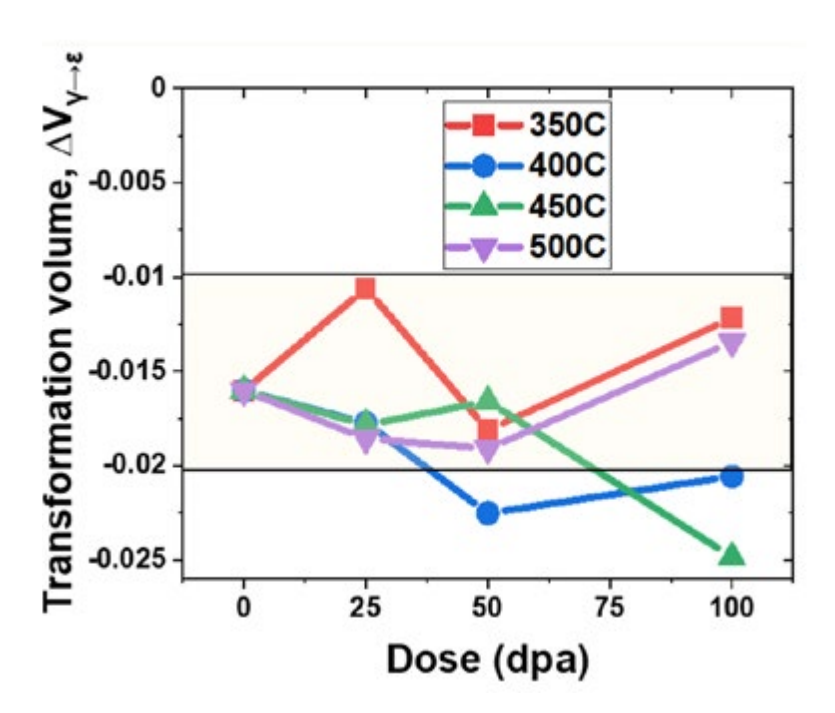


Figure 2. Evolution ΔV with irradiation.

The nanoindentation studies at room temperature were performed to understand the mechanical response of CS-HEA metastable alloy with irradiation. Figure 3 gives average hardness plots for γ-fcc and ε-hcp phases at different irradiation conditions. The green trends are for y-fcc at two extreme temperatures whereas red trends are for ε -hcp. For y-fcc, in general, hardness increases with an increase in dose. With an increase in temperature to 500°C, hardness values decrease due to the annihilation of defects. For ε-hcp, hardness values are higher than y-fcc. An interesting trend for ε -hcp is that, at 500°C, hardness values are higher than

for 350°C. The basic trends for both are similar, with a spike at 25 dpa. We will go ahead and reason the general trend for 500°Cs being higher than 350°C for ε-hcp. Now the evolution of lattice parameters and transformation volume can be used when nanoindentation is carried out at the temperatures to which they were irradiated. But the current results are for nanoindentation measurements done at room temperature. So, we must return to the basic microstructure observed after irradiation. When we compare the XRD plots of both temperatures in Figure 1, 500°C result in distinct σ-body-centered tetragonal (bct) peaks. From the literature

[9,10] and our past study [11], the stacking-fault energy (SFE) of the system decides the martensitic sequence during deformation. For low-SFE material (<20 mJ/m²) the martensitic sequence was reported to be $\gamma(fcc) \rightarrow \epsilon(hcp) \rightarrow \sigma(bcc/bct)$ [9,12,13] whereas the transition from $\gamma(fcc) \rightarrow \sigma(bcc/bct)$ reported for high-SFE systems (>20 mJ/m²) [9,10,12] is direct. In the present case, σ-bct observed as a result of high irradiation dose and temperature is due to Cr diffusion [7]. In the current case, we suspect the σ -bct to be present in the ε-hcp phase, thus increasing its hardness at a higher temperature of 500°C.

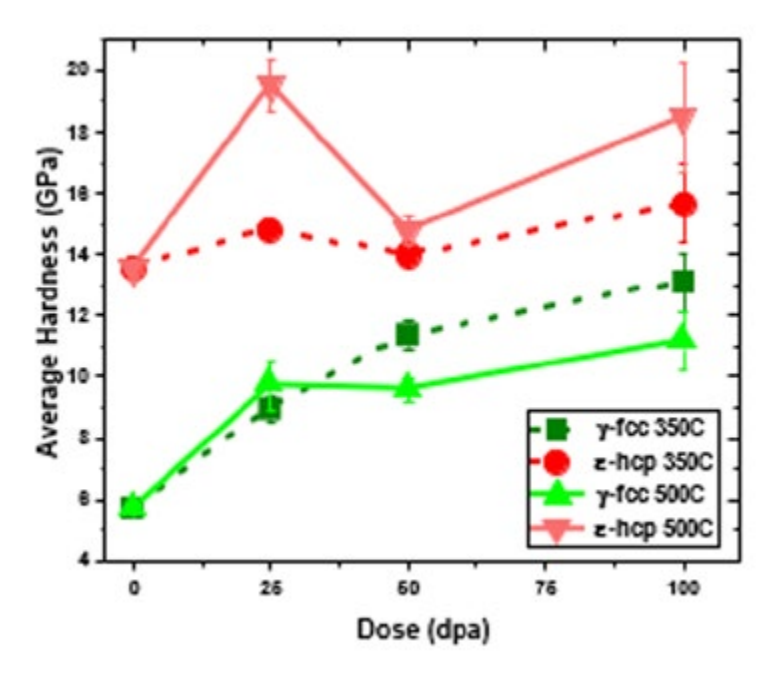


Figure 3. Average hardness values at room temperature as a function of dose for extreme temperature conditions.

The TEM study addressed key questions: does the irradiation impact γ/ϵ interfaces and do γ/γ and ϵ/ϵ boundaries behave differently. Figure 4 shows the TEM image of the most severe condition of 100 dpa/500°C. The image shows γ -fcc and ϵ -hcp phases being affected differently due to irradiation, as seen in Figures 4 (a

and b). Figures 4 (c–e) are results from TEM-based orientation image mapping—precession electron diffraction (PED)—where ϵ -hcp is observed at the interface due to irradiation. The STEM-EDS in Figures 4 (f and g) are for γ/ϵ and γ/γ interfaces, respectively. There is elemental partitioning due to homogenization as seen from the

matrix elemental map, where Cr has partitioned to ϵ -hcp phase whereas Fe is partitioned to γ -fcc. Due to irradiation, there is radiation-induced precipitation (RIP) of σ -bct, radiation-induced segregation (RIS) at the γ/ϵ interface whereas no RIS is observed at the γ/γ interface.

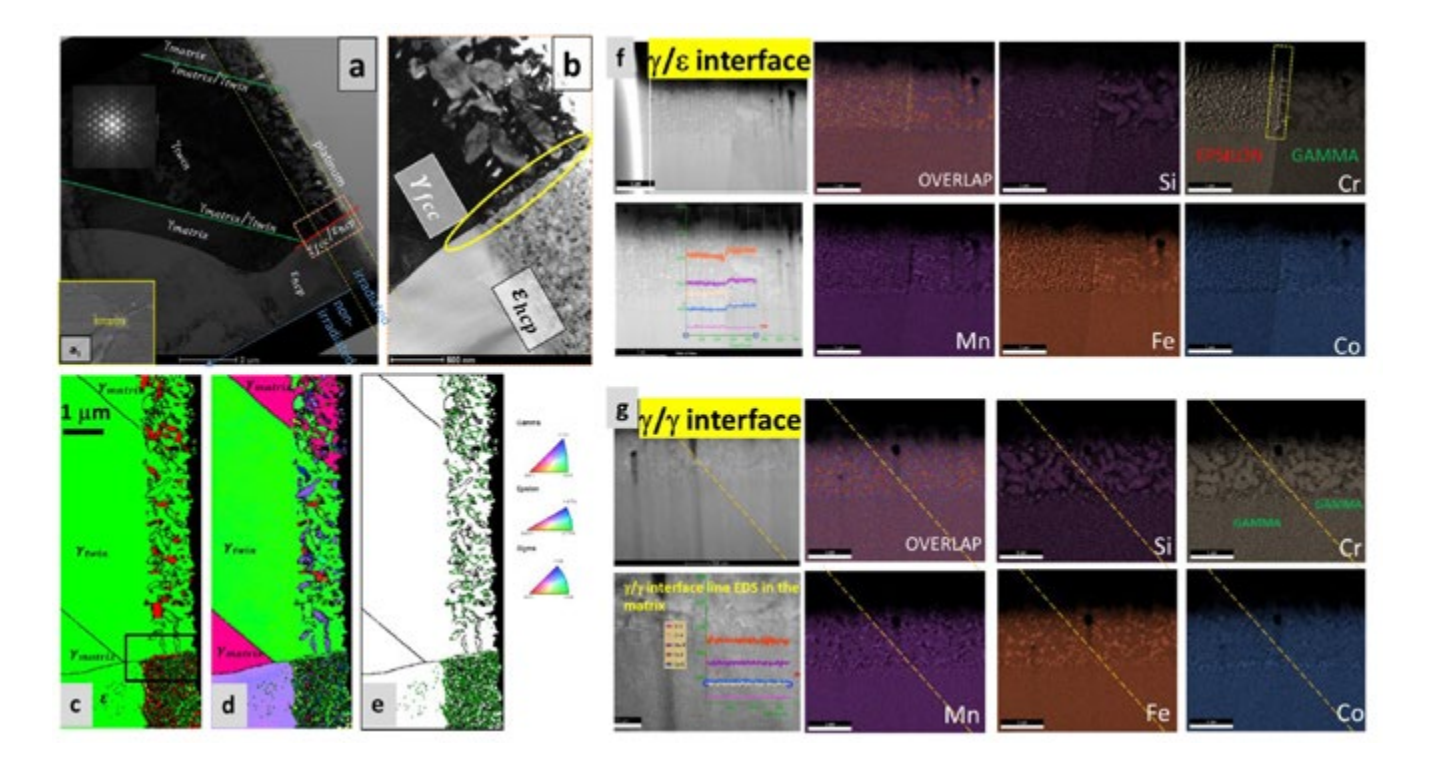


Figure 4. TEM image for the extreme condition of 500° C and 100 dpa sample. (a) Low-magnification image showing the different phases and interfaces affected differently by irradiation with inset labeled (a_1) of the SEM image, (b) high-magnification image of γ/ϵ interface. TEM-PED (c) phase map, (d) orientation image map, and (e) high-angle grain boundary map. STEM-EDS mapping (f) γ/ϵ interface, and (g) γ/γ interface.

References

[1] S. S. Nene, M. Frank, K. Liu, S. Sinha, R. S. Mishra, B. McWilliams, and K. C. Cho. 2018. "Reversed strength-ductility relationship in microstructurally flexible high entropy alloy." *Scripta Materialia* 154: 163–167. https://doi.org/10.1016/j. scriptamat.2018.05.043.

- [2] S. Sinha, S. S. Nene, M. Frank, K. Liu, P. Agrawal, and R. S. Mishra. 2019. "On the evolving nature of c/a ratio in a hexagonal close-packed epsilon martensite phase in transformative high entropy alloys." *Scientific Reports* 9: 13185. https://doi.org/10.1038/s41598-019-49904-5.
- [3] M. Frank, Y. Chen, S. S. Nene, S. Sinha, K. Liu, K. An, R. S. Mishra. 2020. "Investigating the deformation mechanisms of a highly metastable high entropy alloy using in-situ neutron diffraction." *Materials Today Communications* 23: 100858. https://doi.org/10.1016/j.mtcomm.2019.100858.
- [4] S. Sinha, S. S. Nene, M. Frank, K. Liu, R. A. Lebensohn, and R. S. Mishra. 2020. "Deformation mechanisms and ductile fracture characteristics of a friction stir processed transformative high entropy alloy." *Acta Materialia* 184: 164–178. https://doi.org/10.1016/j.actamat.2019.11.056.
- [5] S. Sinha, S. S. Nene, M. Frank, K. Liu, P. Agrawal, R. S. Mishra. 2019. Scientific Reports 9: 1–14.
- [6] J.G. Gigax, E. Aydogan, T. Chen, D. Chen, L. Shao, Y. Wu, W.Y. Lo, Y. Yang, and F.A. Garner. 2015. "The influence of ion beam rastering on the swelling of self-ion irradiated pure iron at 450°C." *Journal of Nuclear Materials* 465: 343–348. https://doi.org/10.1016/j.jnucmat.2015.05.025.
- [7] P. Agrawal, S. Gupta, A. Dhal, R. Prabhakaran, L. Shao, and R. S. Mishra. 2023. "Irradiation response of innovatively engineered metastable TRIP high entropy alloy." *Journal of Nuclear Materials* 574: 154217. https://doi.org/10.1016/j.jnucmat.2022.154217.
- [8] P. Agrawal, A. Dhal, Z. Hu, L. Shao, R. Prabhakaran, and R. S. Mishra. 2023. Journal of Nuclear Materials. Under Review.
- [9] G. B. Olson and M. Cohen. 1972. "A mechanism for the strain-induced nucleation of martensitic transformations." *Journal of the Less Common Metals* 28: 107–118. https://doi.org/10.1016/0022-5088(72)90173-7.
- [10] A. J. Bogers and W. G. Burgers. 1964. "Partial dislocations on the {110} planes in the B.C.C. lattice and the transition of the F.C.C. into the B.C.C. latticeDislocations partielles dans les plans {110} du reseau C.C. et transition du reseau C.F.C. en reseau C.C. Halbversetzungen auf {110}-ebenen im KRZ. gitter und der übergang vom KFZ. ins KRZ. gitter." *Acta Metallurgica* 12: 255–261. https://doi.org/10.1016/0001-6160(64)90194-4.
- [11] P. Agrawal, S. Shukla, S. Gupta, P. Agrawal, and R. S. Mishra. 2020. "Friction stir gradient alloying: a high-throughput method to explore the influence of V in enabling HCP to BCC transformation in a γ-FCC dominated high entropy alloy." *Applied Materials Today* 21: 100853. https://doi.org/10.1016/j.apmt.2020.100853.
- [12] J. A. Venables. 1961. "The martensite transformation in stainless steel." *Philosophical Magazine* 7: 35–44. https://doi.org/10.1080/14786436208201856.
- [13] R. Lagneborgj. 1964. "The martensite transformation in 18% Cr-8% Ni steelsLa transformation martensitique dans les aciers a 18% Cr ET 8% NiMartensit-umwandlung von 18% Cr-8% Ni-stählen." *Acta Metallurgica* 12: 823–843. https://doi.org/10.1016/0001-6160(64)90176-2.

RTE 4114: Study of the Effect of Water Chemistry on the Performance of SiC-Based ATF Cladding Materials

K. Lambrinou, B. T. Clay (University of Huddersfield), R. D. Hanbury, K. Sun (University of Michigan), J. A. Silverstein, K. H. Yano, L. Riechers (PNNL), D. M. Frazer, P. Xu (INL), E. J. Lahoda (Westinghouse Electric Company), C. P. Deck (General Atomics) R.L. Oelrich (PNNL), G.S. Was (University of Michigan)

Facility: Michigan Ion Beam Laboratory, University of Michigan

Introduction

Chemical vapor Deposition (CVD) of β-SiC is considered a candidate coating material for SiC/SiC composite accident-tolerant fuel (ATF)-cladding materials intended for use in Gen-II/III light-water reactors (LWRs). These CVD SiC coatings, mainly used as outer protection of CVI-infiltrated SiC/SiC composite fuel claddings—typically characterized by a fraction of porosity in their asfabricated state)—aim at reducing material losses in nominal operation conditions (i.e., in contact with flowing water of strictly controlled chemistry). SiC losses in water are mainly attributed to the formation and subsequent dissolution of silica (SiO₂); however, little is known on the degradation of CVD SiC in contact with flowing water of controlled chemistry.

Experimental Procedure

In this project, three synergistic proton-irradiation, aqueous-corrosion tests were performed to study the degradation behavior of CVD SiC supplied by GA. The CVD SiC batch supplied by GA was intentionally fabricated with a high density of defects, such as stacking faults and intricate dislocation networks (loops, lines), to study the effect of processing-induced defects on material performance (Figure 2). The tests were conducted in the irradiationaccelerated corrosion (IAC) cell (Figure 1a) that is available at the Michigan Ion Beam Laboratory (MIBL) at the University of Michigan. The test specimens were CVD SiC discs (\emptyset 3 \pm 0.5 mm, ~50 μ m in thickness). All irradiations were performed using a 5.4 MeV proton (p+) beam at the following test conditions: (a) 320°C, standard pressurized water reactor (PWR) water with 3 ppm H₂, (b) 320°C, PWR water with 0.1 ppm H₂, and (c) 288°C, boiling-water reactor (BWR) water with 2 ppm O₂ and added H₂SO₄ to control the conductivity in the beginning of the test at 0.15 µS/cm. In all cases, the test duration was 48 h, which resulted in a displacement dose of 0.1 dpa (based on full-cascade SRIM calculations). Testing produced three distinct areas on the water-exposed facets of the CVD SiC discs, each one of which degraded differently. The SiC degradation mechanisms in these three areas were: (I) proton irradiation and water radiolysis, (II) water radiolysis, and (III) aqueous corrosion (Figure 1b). The CVD SiC samples were studied before and after testing by SEM, EDS, AFM, FIB, STEM, electron energy loss spectroscopy (EELS), time-of-flight secondaryion mass spectroscopy (ToF-SIMS), and micropillar compression.

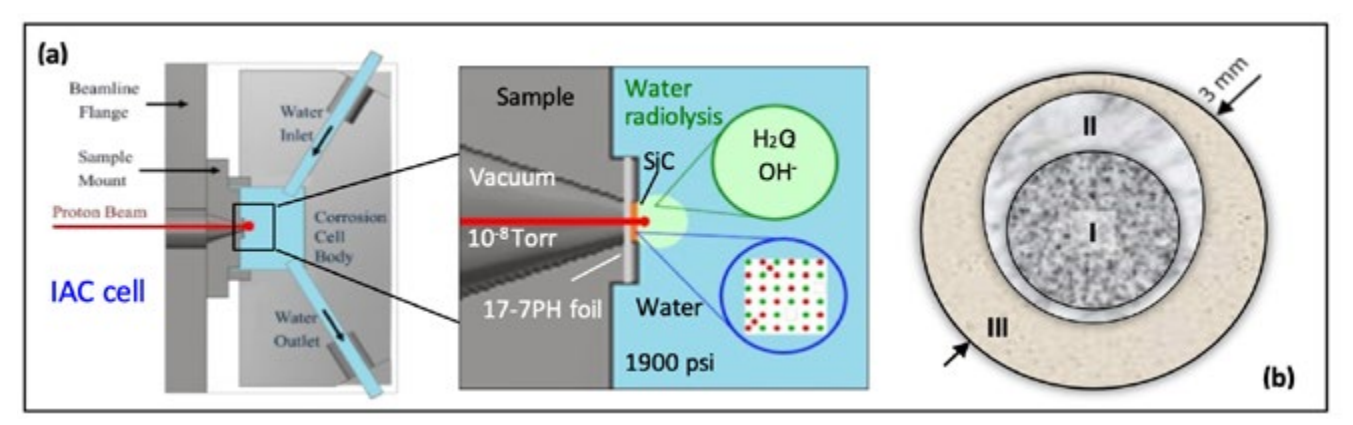


Figure 1. (a) The IAC cell used for the synergistic proton irradiation and corrosion testing of CVD SiC. (b) Area-specific degradation mechanisms: (l) proton irradiation and water radiolysis, (ll) water radiolysis, and (lll) aqueous corrosion.

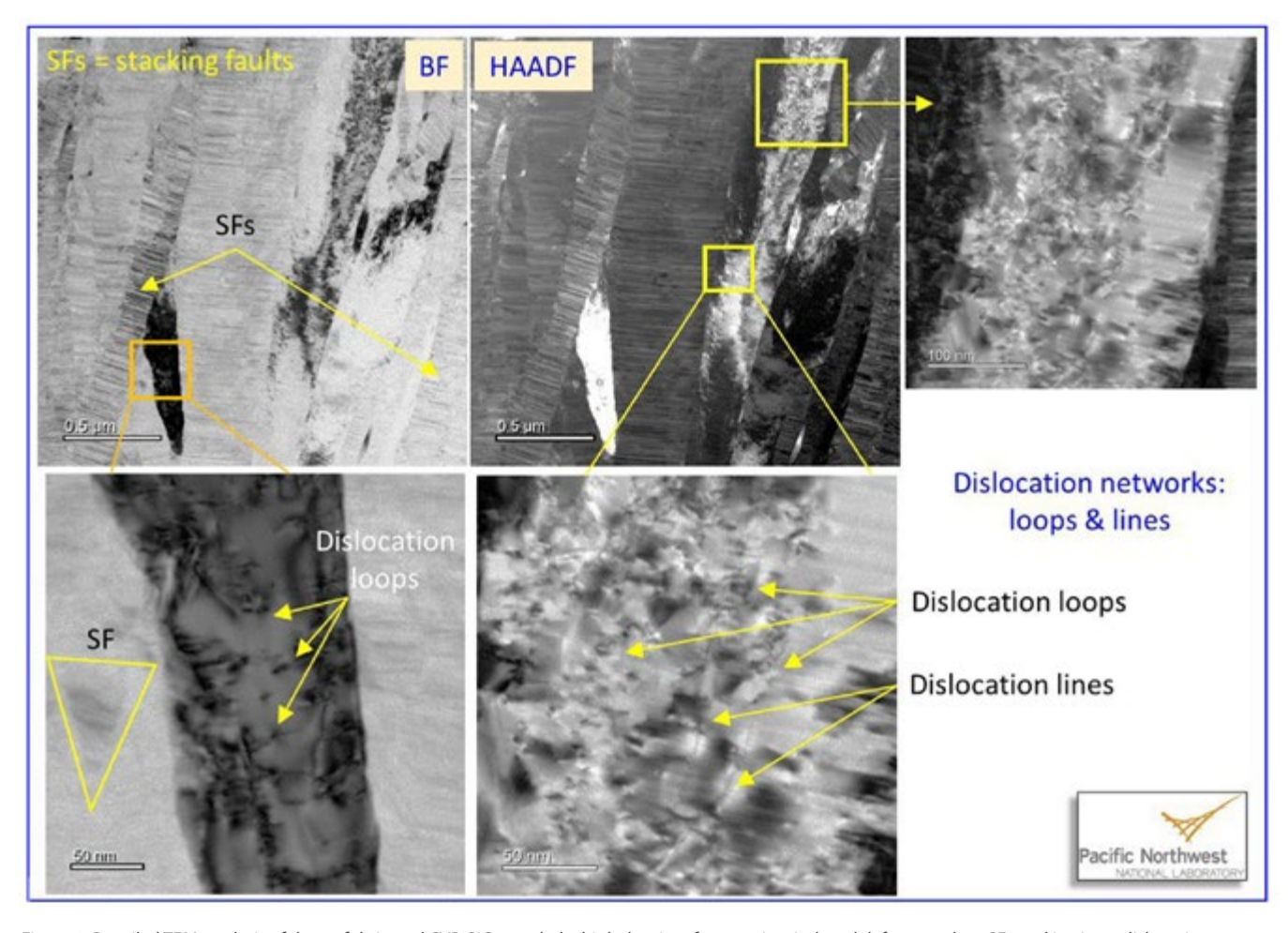
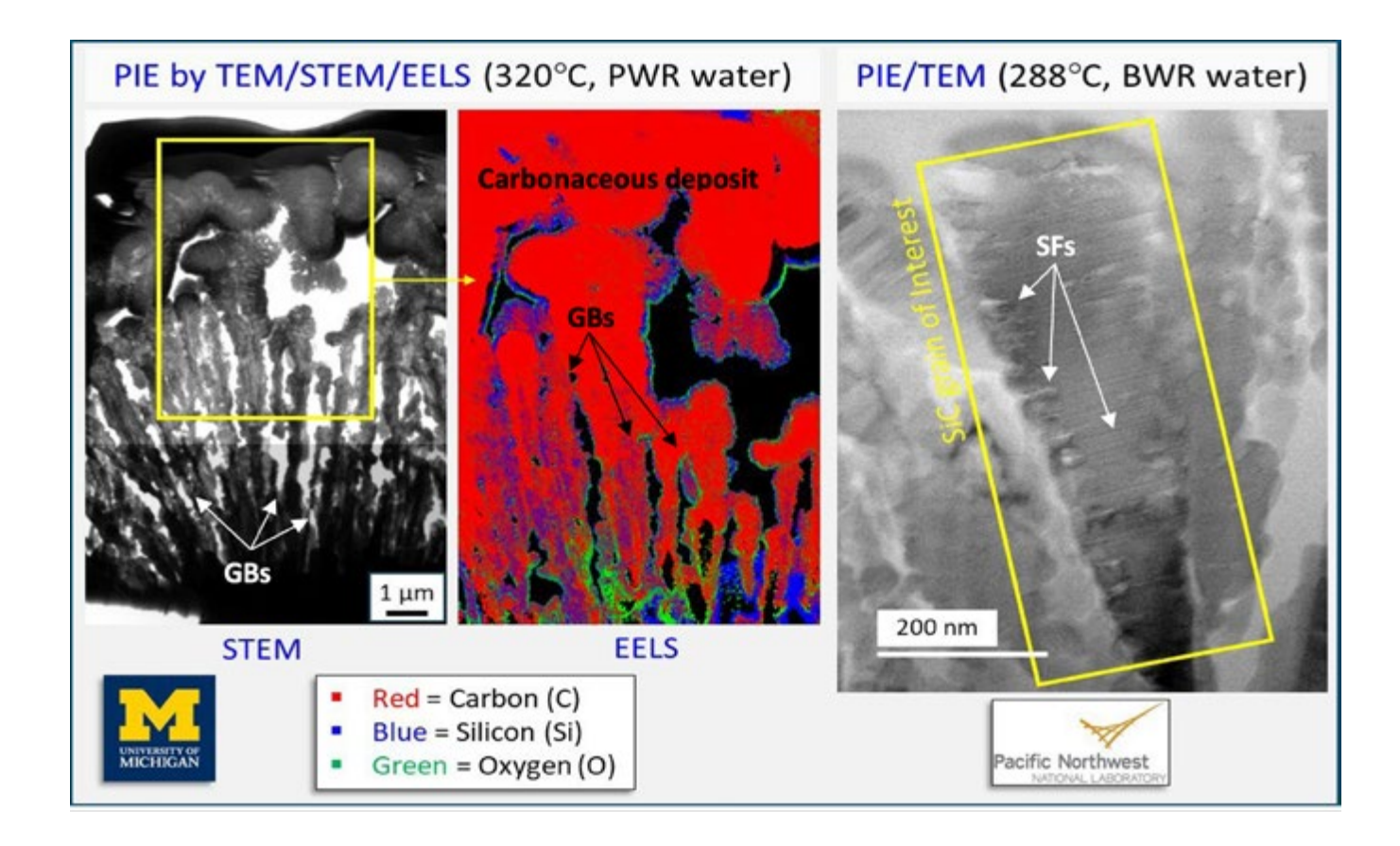


Figure 2. Detailed TEM analysis of the as-fabricated CVD SiC revealed a high density of processing-induced defects, such as SFs and intricate dislocation networks (e.g., loops, lines).



Results and Discussion

The post-irradiation examination (PIE) of all three CVD SiC samples by means of STEM/EELS revealed that processing-induced material defects, such as grain boundaries and stacking faults, were preferentially attacked by water radiolysis species, especially hydrogen (H+). In this study, H+ is a water-radiolysis product that is also supplied by the p+ beam (99% of the protons end in the water bath). It appears that during testing, H+ cuts the Si-C bonds at such inherent material weaknesses as grain boundaries and SFs, via the so-called "hydrogen scission reaction" [1]. Interestingly, hydrogenated water (i.e., a PWR with 3 ppm H₂) attacked CVD SiC more than water with less hydrogen (i.e., a PWR with 0.1 ppm H₂). This is in contradiction with the results of many autoclave tests (i.e., tests without irradiation), which showed consistently that hydrogenated water reduced material losses (possibly because excess hydrogen restricts the formation of water-soluble silica, SiO₂).

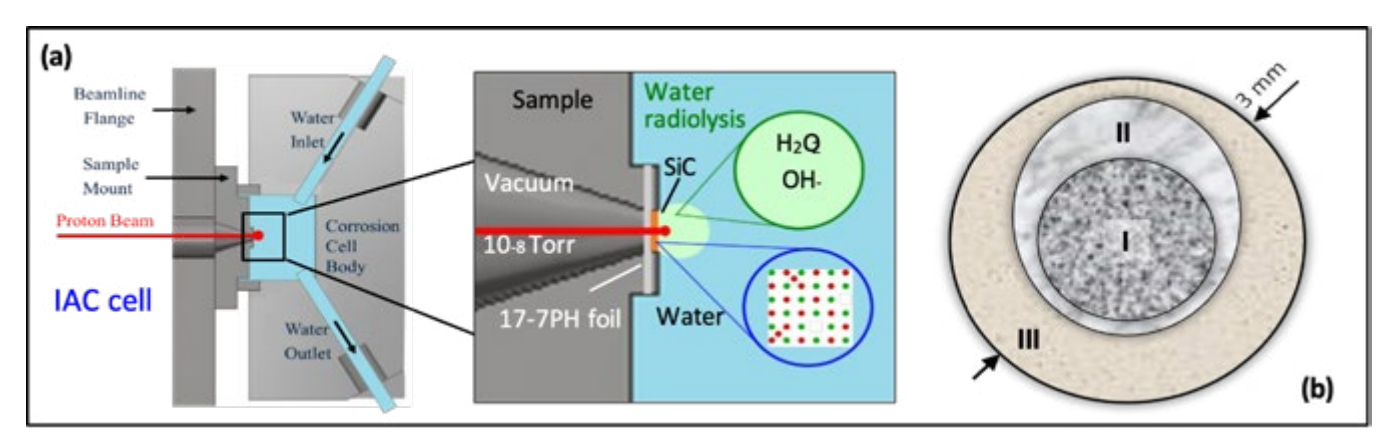


Figure 3. TEM, STEM, and EELS analysis of the CVD SiC samples tested for 48 h (a) at 320°C in contact with PWR water with 3 ppm H_2 (left) and (b) at 288°C in contact with BWR water with 2 ppm O_2 (right) reveal extensive material attack at grain boundaries and SFs.

References

[1] J. Xi, C. Liu, D. Morgan, and I. Szlufarska, Deciphering water-solid reactions during hydrothermal corrosion of SiC, *Acta Materialia* 209 (2021) 116803

Acknowledgements

This work was financially supported by (a) the U.S. Department of Energy, Office of Nuclear Energy under DOE Idaho Operations Office Contract DE-AC07-051D14517 as part of a NSUF experiment, and (b) the EURATOM research and training programme 2014–2018 under Grant Agreement No. 740415 (H2020 IL TROVATORE).

RTE 4138: *In Situ* Nanotensile Testing of Neutron-Irradiated HT-9 Steel

PI: Tanvi Ajantiwalay (PNNL, previously University of Florida)

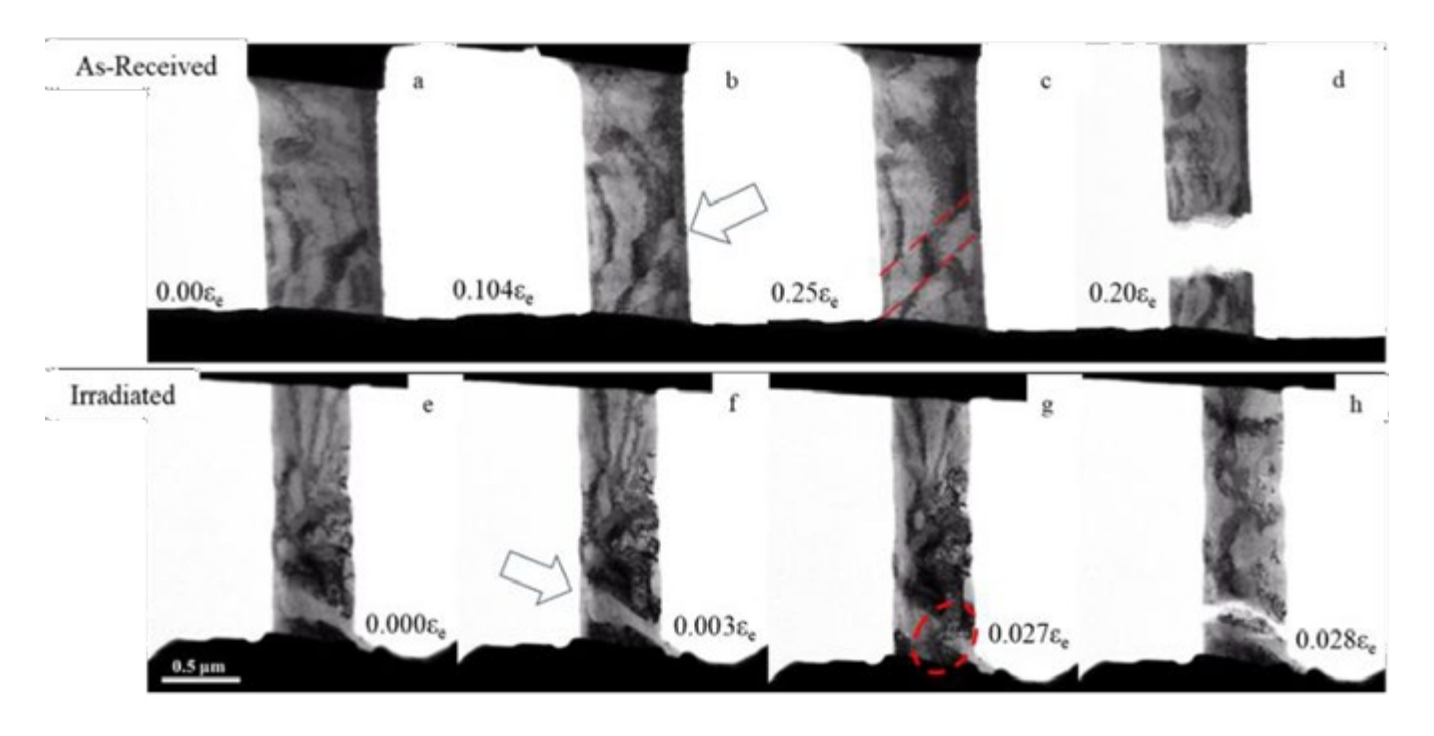
Collaborators: Megha Dubey, Yaqiao Wu (CAES), Brandon Bohanon, Assel Aitkaliyeva (University of Florida)

Facility: Microscopy and Characterization Suite, Center for Advanced Energy Studies

Summary

Nanotensile tests were used to investigate the behavior of HT-9 steel neutron irradiated to 4.29 dpa at 469°C. The deformation of both as-received and neutron-irradiated HT-9 was monitored in situ with a transmission electron microscope, which allowed linking microstructure of the material with the evolution of mechanical properties and identifying the mechanisms governing irradiation-induced hardening of these steels. Nanotensile tests demonstrate that while dislocations contribute to hardening, grain boundaries govern the deformation and eventual fracture of HT-9. Sample preparation was performed using the FIB, and nanocompression tests were performed in situ by TEM, both at CAES to correlate the microstructure and mechanical properties.

The stress-strain curve shows a lack of strain hardening and one intermittent load drop (back arrow) associated with the formation of a slip band, as opposed to dislocation burst-type load drops. As shown in Figures 1 (a-d), plastic deformation in the as-received nanotensile sample eventually takes place above the grain boundary in the form of migration or multiplication of dislocations. The as-received nanotensile sample fractured through the grain boundary at a strain of 20.4% (see Figure 1 [d]). Two tests were performed on an irradiated HT-9 sample, which showed moderate hardening of the material, as demonstrated by the slight increase in yield strength from 1.05 GPa to 1.13 GPa for NI-1 and 1.43 GPa for NI-2. TEM examination of the irradiated HT-9 revealed a large density of dislocation networks prior to straining the of the nanotensile samples, as shown in Figure 1 (e). With applied tension, dislocations migrate and multiply in the center of the sample, next to a grain boundary (see Figures 1 [f-g]). As shown by the dashed red oval in Figure 1 (g), dislocation activity initiates at the grain boundary, right before fracture occurs along the top of the boundary (Figure 1 [h]). This dislocation activity could correspond to dislocation emission, absorption, or transmission through the grain boundary, and interaction with other smaller irradiation-induced defects.



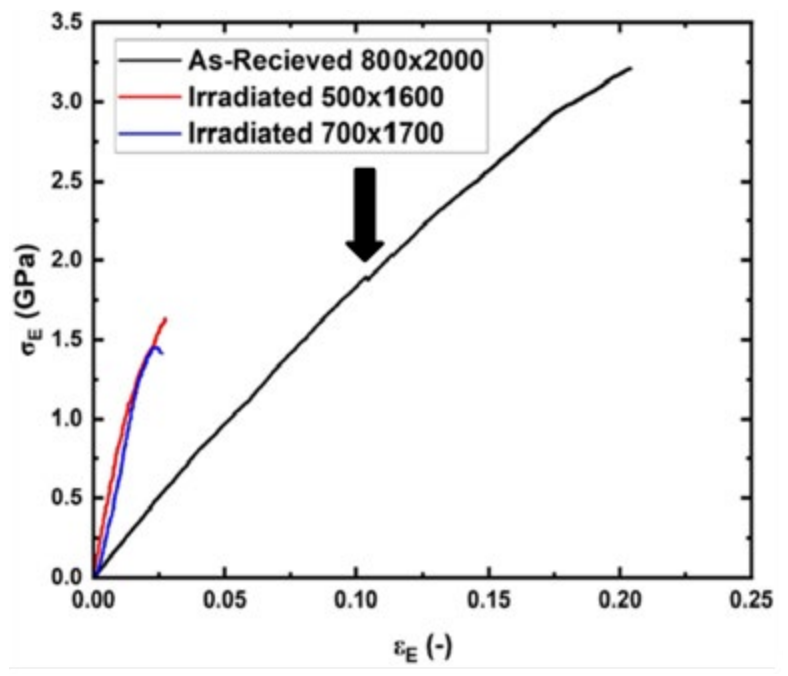


Figure 1. Snapshots taken during nanotensile testing of the as-fabricated (a–d) and NI₂ (e–h) sample. The white arrows indicate the areas with grain boundaries. The dashed red lines highlight the grain boundary in the as-received samples while the dashed red oval shows the areas of dislocation activity prior to fracturing, (i) stress-strain curves for the nanotensile tests on the as-received and neutron irradiated HT-9. The black arrow points to the load drop caused by the formation of a slip boundary.

RTE 4180: *In situ* Radiation on Advanced Alloys with Precipitates, Nanotwins and Phase Boundaries

PI: Xinghang Zhang

Co-Pls: Zhongxia Shang, Tongjun Niu, Tianyi Sun (Purdue University)

Technical Leads: Meimei Li, Mark Kirk

Facility: Intermediate Voltage Electron Microscopy-Tandem Facility, Argonne National Laboratory

The main objective of this proposal is to use an in situ dual-beam radiation technique (at IVEM, ANL) to investigate irradiation-induced microstructural evolution in additively manufactured Haynes 230 Ni alloys, nanotwinned steels, and metallic nanocomposites with triple junctions and gradientnanostructured steels. The ultimate goal is to develop advanced alloys with enhanced resistance to heliumbubble-induced swelling under high-temperature radiation. We will summarize our major findings in the following sections. Six journal articles have been published to date.

In situ dual beam radiation on additively manufactured Haynes 230 Ni alloys with precipitates

In situ sequential dual-beam irradiation was performed on additive manufactured (AM) and CG Haynes 230 alloy. The specimens were first implanted using 12 KeV He ions to about 1 at.% at 50°C, followed by 1 MeV Kr-ion irradiation at 525°C up to 3 dpa. Uniform nucleation of He bubbles, with an average size less than 1 nm, was observed in both AM and CG Haynes 230 alloys. Meanwhile, He injection produced high-density dislocation loops, as evidenced in Figure 1 (a1) and (b1). Upon irradiation to 1 dpa, both AM and CG Haynes 230 alloys experienced an increase in He-bubble density, possibly due to continuous transformation of the initially invisible He-vacancy clusters into detectable bubbles. The dislocation loops interacted with each other and resulted in the formation of comparatively larger loops, which later transformed into short-dislocation segments. The density of He bubbles remained relatively unchanged when dose level increased to above 1 dpa in both AM and CG Haynes 230 alloys, as shown in Figure 1(c). It is worthwhile to note that the He-bubble density and size of AM Haynes 230 alloy are lower than that of CG Haynes 230 alloy, suggesting a suppressed bubble swelling in AM Haynes 230 alloy.

Post-irradiation TEM analyses were performed to characterize the defect structure in Haynes 230 alloy. The BF and corresponding DF in Figure 2 (a–b) reveals high-density dislocation segments generated by irradiation damage. It is interesting to note that the M23C6 carbides became amorphous after irradiation, as shown in Figure 2(c).

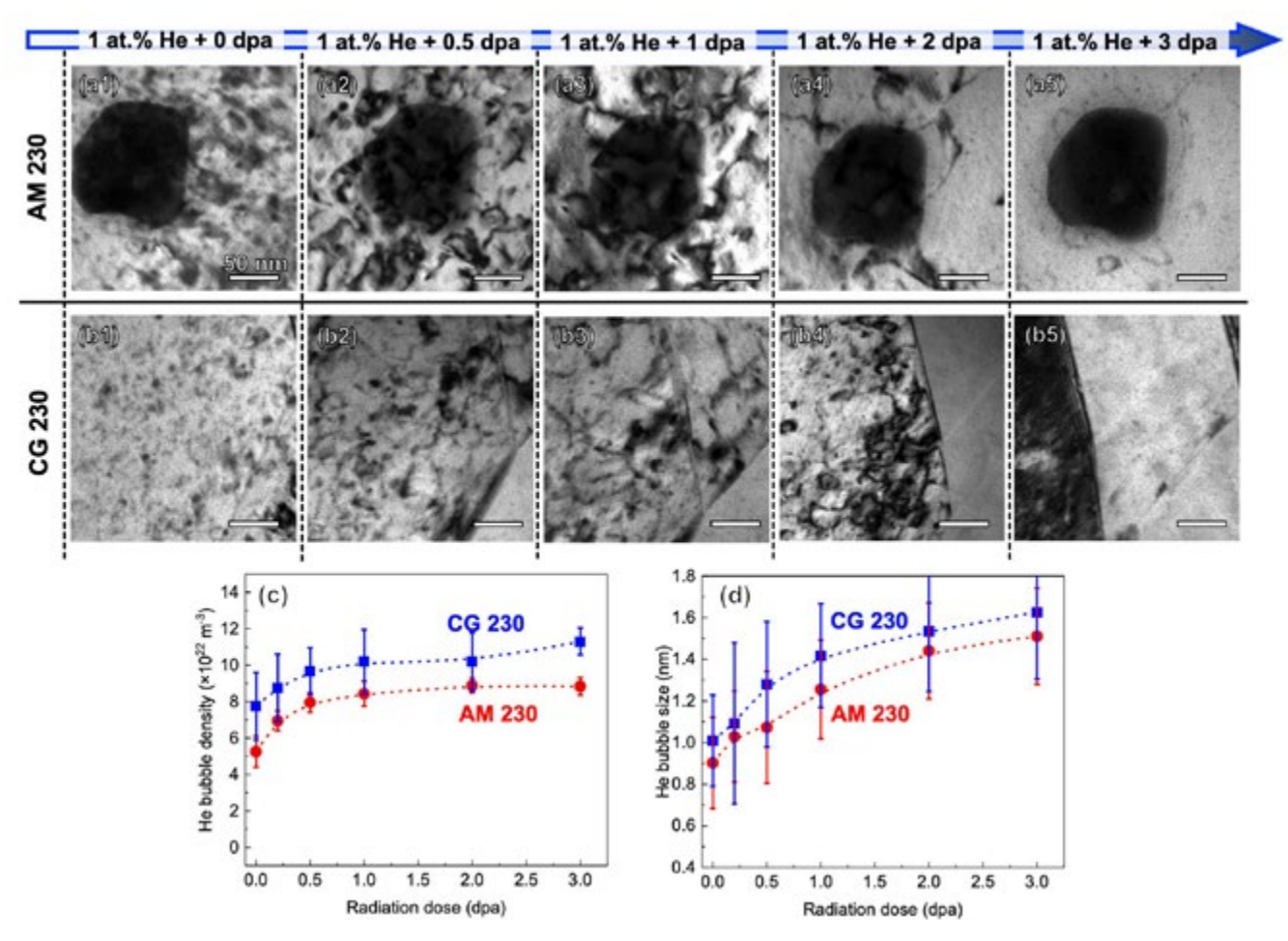


Figure 1. In situ radiation snapshots showing the microstructural evolution of (a1-a5) AM Haynes 230 alloy and (b1-b5) CG Haynes 230 alloy at different dpa levels during Kr-ion irradiation at 525°C. Comparison of dose-dependent He-bubble (c) density and (d) size evolution in AM and CG Haynes 230 alloy during Kr-ion irradiation at 525°C.

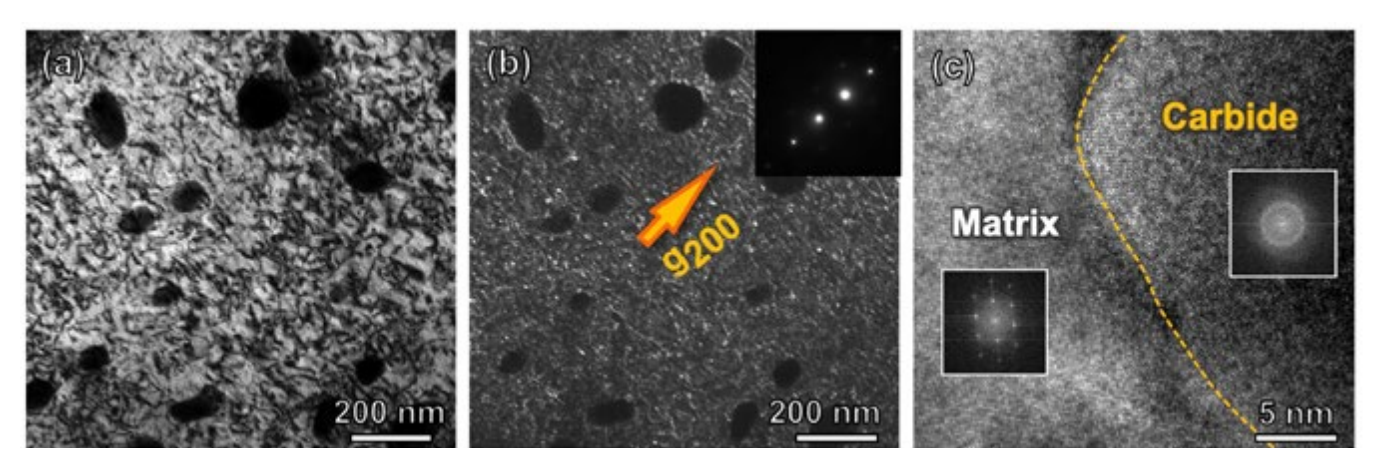


Figure 2. Post-irradiation TEM analyses on AM Haynes 230 alloy. (a) BF and (b) corresponding DF TEM micrographs showing the high-density dislocation segments surrounding the precipitates. The BF image was obtained close to [011] zone axes with g200 strongly excited. (c) HR-TEM micrograph showing the amorphization of M23C6 carbides after irradiation.

In situ studies on radiation response of a nanotwinned steel

[Zhongxia Shang, Tongjun Niu, Tianyi Sun, Sichuang Xue, Cuncai Fan, Wei-Ying Chen, Meimei Li, Haiyan Wang, Xinghang Zhang, In situ study on radiation response of a nanotwinned steel, Scripta Materialia 220 (2022) 114920.]

Recent radiation studies on nanotwinned pure metals, such as Cu and Ag, show that twin boundaries are appealing defect sinks because twin boundaries can transport and eliminate radiation-induced defects (RIDs). However, the response of twin boundaries in nanotwinned structural steels under irradiation is rarely explored. Here, we investigate the microstructural evolution of a nanotwinned steel via in situ Kr⁺⁺ irradiation at room temperature to 4 dpa. The in situ study shows that nanotwins in steels can effectively suppress the formation of dislocation-loop rafts. Also, the formation of loop rafts and Frank loops was found to depend prominently on twin spacing. The underlying mechanisms of the enhanced radiation tolerance in nanotwinned steel are discussed. The present study provides a positive step towards the application of nanotwinned structural materials to nuclear reactors.

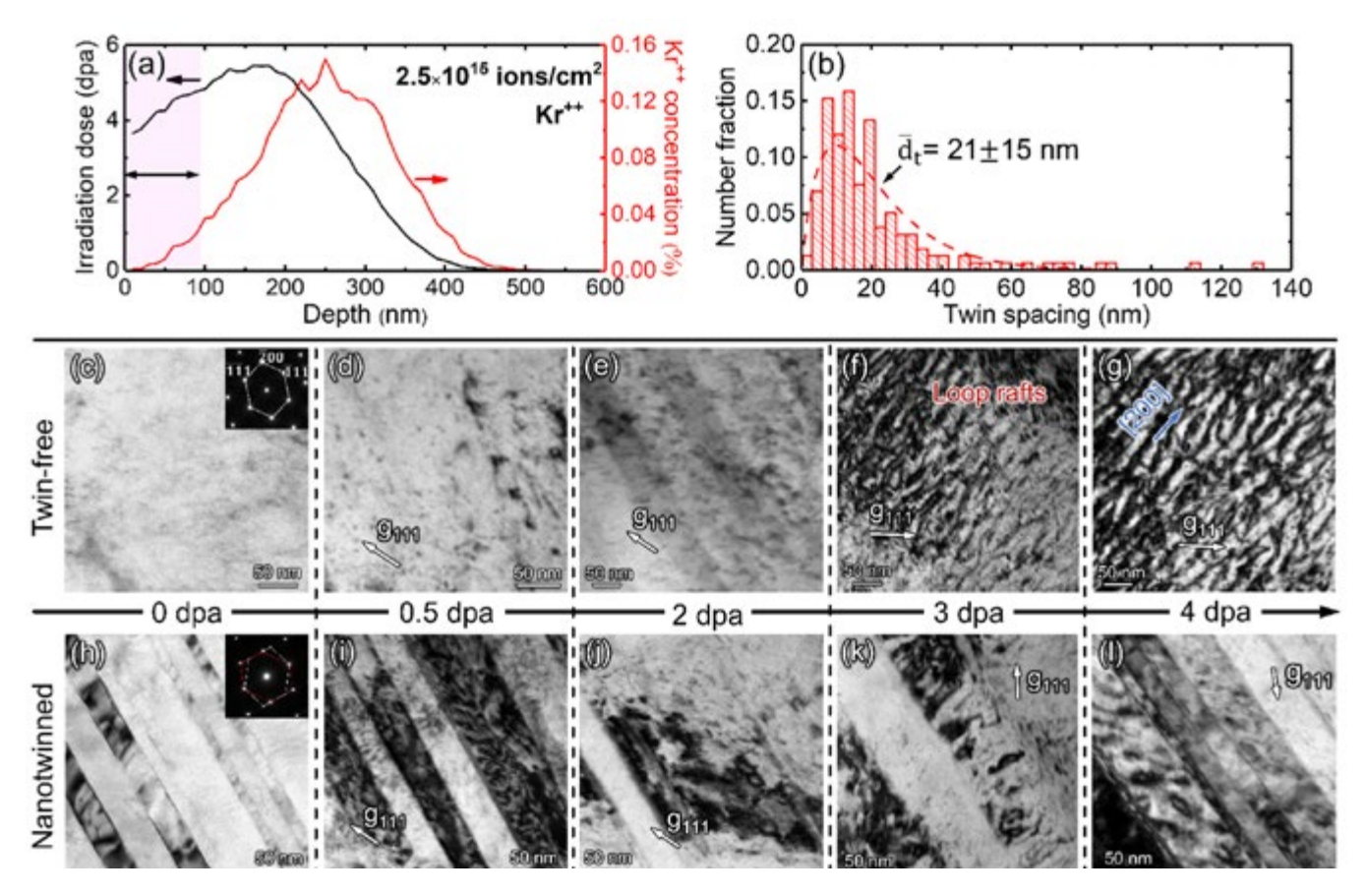


Figure 1. (a) SRIM calculations illustrate the variation of irradiation dose and Kr^{++} concentration profiles as a function of damage depth. The average radiation dose is 4 dpa in the first 100 nm, corresponding to the TEM foil thickness. While most of the Kr ions penetrate through the sample, (b) the statistical distribution of twin spacing in the irradiated area shows an average twin spacing of 21 nm. In situ TEM snapshots show the microstructural evolution in (c-g) of the twin-free region and in (h-l) of the NT region at various doses (0-4 dpa). The microstructures of both regions at 0 dpa are relatively clean after the annealing at 500°C. Well-aligned high-density loop rafts along the [200] direction formed in the irradiated twin-free region by 3 dpa while dislocation loops still dominate in the NT region. All the TEM-BF images were captured close to <110> zone axis with g111 strongly excited.

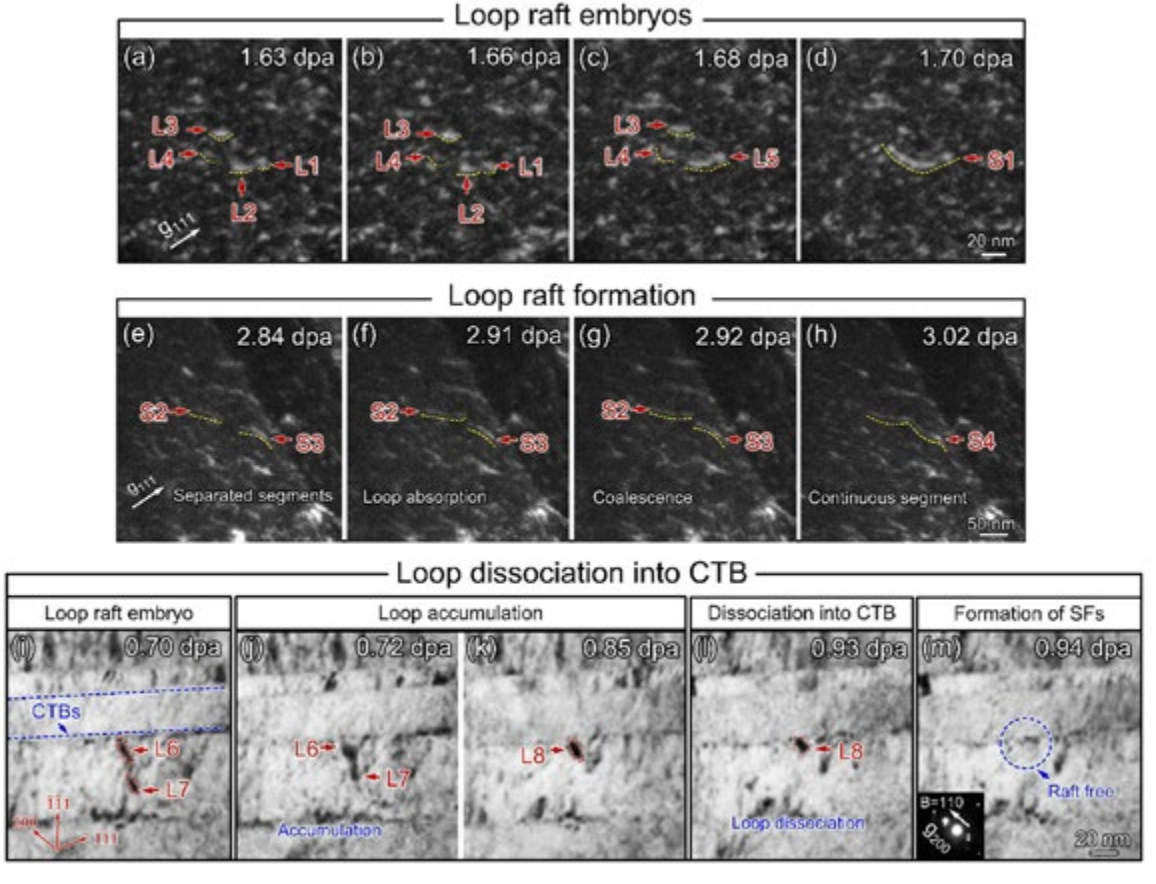


Figure 2. (a–d) Representative in situ video snapshots illustrating the formation of a loop-raft segment (S1) via loop accumulation (L1–L5) during 1.63–1.70 dpa. (e–h) Representative in situ video snapshots showing loop-raft formation (S4) by coalescence of two preexisting segments (S2 and S3) during 2.84–3.02 dpa. (i–m) Representative in situ video snapshots capturing the absorption of irradiation-induced dislocation loops (L6, L7, and L8) by a CTB during 0.7 to 0.94 dpa.

In situ heavy-ion irradiation was performed on an NT austenitic steel at room temperature to 4 dpa. Major findings are summarized as follows:

- 1. Heavy-ion irradiation generates mainly Frank loops and loop rafts in the NT steel. The formation of loop rafts consists of two steps: formation of raft embryos and interconnection between the embryo segments.
- 2. CTBs are able to truncate continuous loop rafts into discrete perfect loops, thereby suppressing the formation of long loop rafts. And the raft density depends prominently on twin spacing. At a critical twin spacing of 50–60 nm, loop rafts significantly diminish.
- 3. The dissociations of Frank loops into CTBs were frequently observed, and this results in defective CTBs, including thick CTBs with high-density SFs and sharp CTBs loaded with interstitial loops. The dissociation is rationalized by dislocation reaction and recombination of interstitial- and vacancy-type defect clusters.

An in situ study on the effect of grain boundaries on helium bubble formation in dual beam irradiated FeCrAl alloy

[Tianyi Sun, Tongjun Niu, Zhongxia Shang, Wei-Ying Chen, Meimei Li, Haiyan Wang, Xinghang Zhang, An in situ study on the effect of grain boundaries on helium bubble formation in dual beam irradiated FeCrAl alloy, Acta Materialia 245 (2023) 118613.], Acta Materialia 245 (2023) 118613.]

FeCrAl alloy is one of the promising cladding materials for advanced nuclear reactors. Here we compare the irradiation response of the nanolaminate (NL) and CG FeCrAl alloys, by performing He-ion irradiation, followed by in situ Kr-ion irradiation in a transmission electron microscope at 450°C. NL alloy has reduced He-bubble-induced swelling and decreased density of dislocation loops relative to the CG alloy. The distribution of He bubbles appears to be dependent on misorientation angles of high-angle grain boundaries. A new type of nanoprecipitate was identified in the irradiated CG FeCrAl without noticeable chemical segregation. Chemical segregation occurred along the laminate boundaries in the irradiated NL FeCrAl alloy.

In situ radiation was performed on CG and NL FeCrAl with 12-keV He ions and 1-MeV Kr ions at 450°C. He bubbles nucleated homogeneously in the grain interior of CG and NL FeCrAl. These bubbles grew during the Kr-ion radiation through bubble migration and coalescence (Figure 1). Overall, the He-bubble-induced swelling is much less in the matrix of NL FeCrAl than in the CG FeCrAl matrix. He bubbles preferentially nucleated along the GBs of the NL FeCrAl. The size and density of GB bubbles varied with misorientation angles. Both <100> and 1/2 <111> dislocation loops were found in the irradiated CG and NL FeCrAl (Figure 2). The NL FeCrAl has a lower dislocation-loop-number density than does CG FeCrAl because of the sink effect of the high-density laminate GBs. A new type of nanoprecipitates with fcc structure was discovered in the irradiated CG FeCrAl for the first time. These precipitates have the Bain-orientation relationship with the bcc matrix. EDS analyses revealed that the GBs in the NL FeCrAl were depleted with Fe and Cr, enriched with Al.

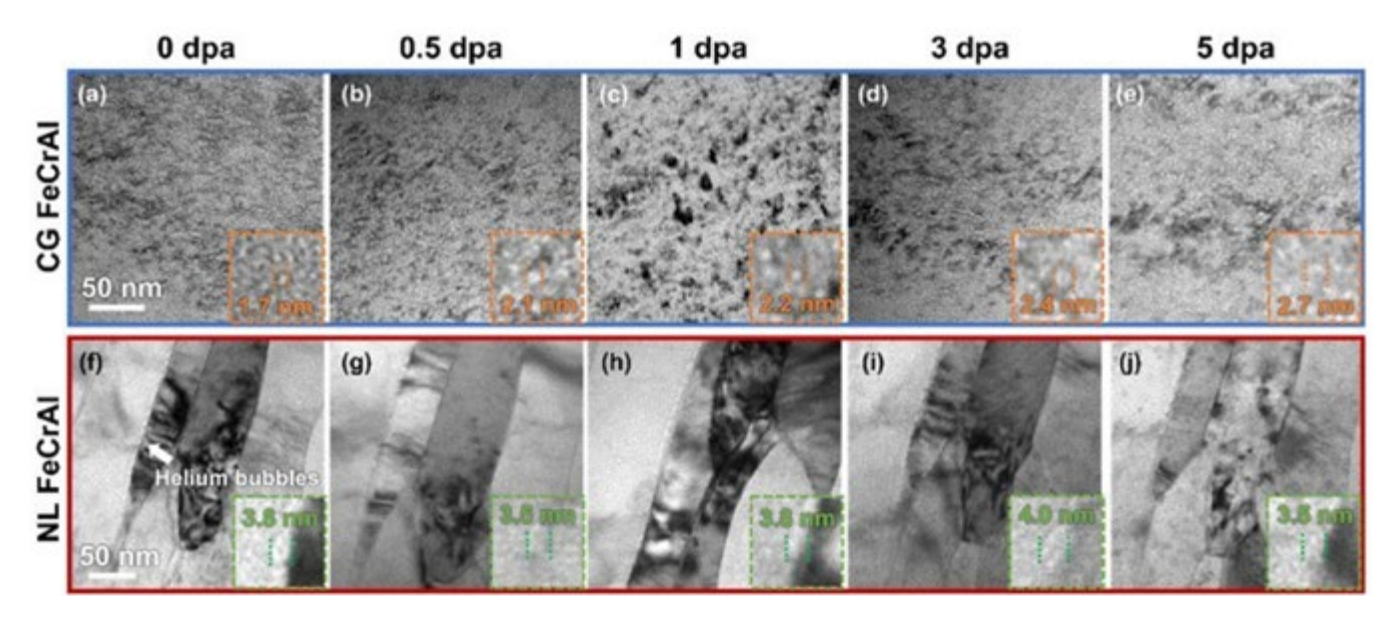


Figure 1. In situ TEM snapshots showing the microstructure evolution of helium (1 at.%) pre-irradiated CG and NL FeCrAl alloys after various Kr-ion irradiation doses at 450° C. (a–e) Helium bubble evolution in the matrix of CG FeCrAl. (f–j) He bubbles along the laminate grain boundaries in NL FeCrAl. Inserts show magnified view of He bubbles.

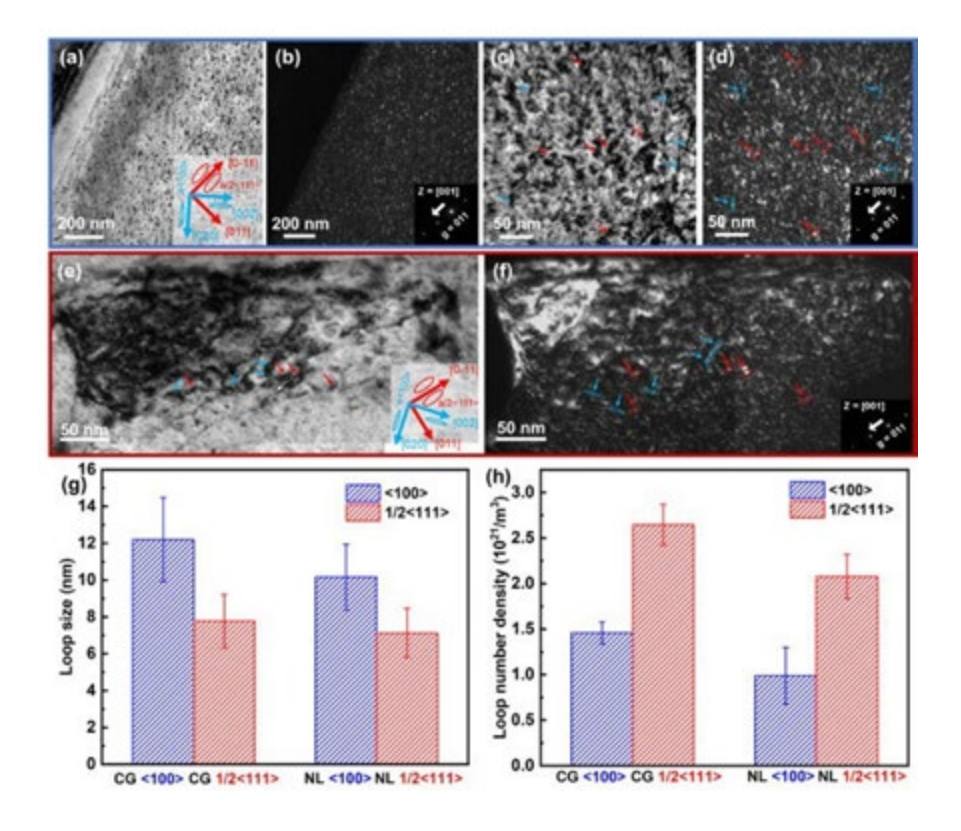


Figure 2. (a–b) BF and DF TEM images of CG FeCrAl after radiation near [001] zone with a g vector of [011]. (c–d) Magnified BF and DF images of irradiated CG FeCrAl showing <100> (blue) and 1/2 <111> (red) dislocation loops. (e–f) BF and DF TEM images of irradiated NL FeCrAl near [001] zone axis (g = [011]). (g, h) Size and density of <100> and 1/2 <111> dislocation loops in CG and NL FeCrAl.

Helium in Cu-Ag-Fe triphase immiscible nanocomposites: An in situ sequential dual beam TEM study

[T Niu, T Sun, Z Shang, Y Zhang, Z He, WY Chen, M Li, H Wang, X Zhang, Helium in Cu-Ag-Fe triphase immiscible nanocomposites: An in situ sequential dual beam TEM study, Journal of Nuclear Materials 574 (2023) 154153.]

Helium generated during irradiation is notorious for inducing volumetric swelling and GB embrittlement. It is imperative to design advanced materials with effective capability to manage He. Here, we report a largely different bubble-swelling behavior in $Cu_{50}Ag_{50}$, $Cu_{45}Ag_{45}Fe_{10}$ and $Cu_{33}Ag_{33}Fe_{34}$ nanocomposites with similar grain sizes. In situ He pre-injection leads to similar He-bubble size and density in all three alloy systems. After subsequent Kr irradiation, the average bubble size and swelling in $Cu_{33}Ag_{33}Fe_{34}$ is much less than $Cu_{50}Ag_{50}$. Additionally, while bubble size is much greater along triple junctions (TJs) and GBs than in matrix in $Cu_{50}Ag_{50}$, the bubble size at the triple junctions in $Cu_{33}Ag_{33}Fe_{34}$ is much less, suggesting the vital role of Cu-Ag-Fe triphase triple junctions and phase boundaries in managing He. The present study provides a new perspective for improving the radiation tolerance of nanocrystalline alloys by microstructure design.

In this study, we present a fresh perspective of alleviating He-bubble-induced swelling by the design of Cu-Ag-Fe triphase immiscible nanocrystalline alloys. In situ sequential dual-beam (i.e., He and Kr) irradiations were performed on $Cu_{50}Ag_{50}$, CAF_{10} and CAF_{34} alloys with similar grain sizes. He pre-injection at 50°C to 1at% led to bubbles with similar bubble size and density in all three alloys. After subsequent Kr irradiation at 300°C to 1.5 dpa, the average bubble size was merely 1.6 nm in CAF_{34} alloy, with a swelling less than 0.2%, less than that in $Cu_{50}Ag_{50}$ alloy. Additionally, in contrast to the large bubbles along TJs and GBs in $Cu_{50}Ag_{50}$, bubbles in CAF_{34} were similar and consistently smaller (Figure 2). The enhanced bubble swelling resistance in CAF_{34} alloy can be attributed to the removal of vacancy-typed stacking fault tetrahedra (SFTs) by phase boundaries and TJs, and strong He-trapping and storage capability of phase boundaries and TJs.

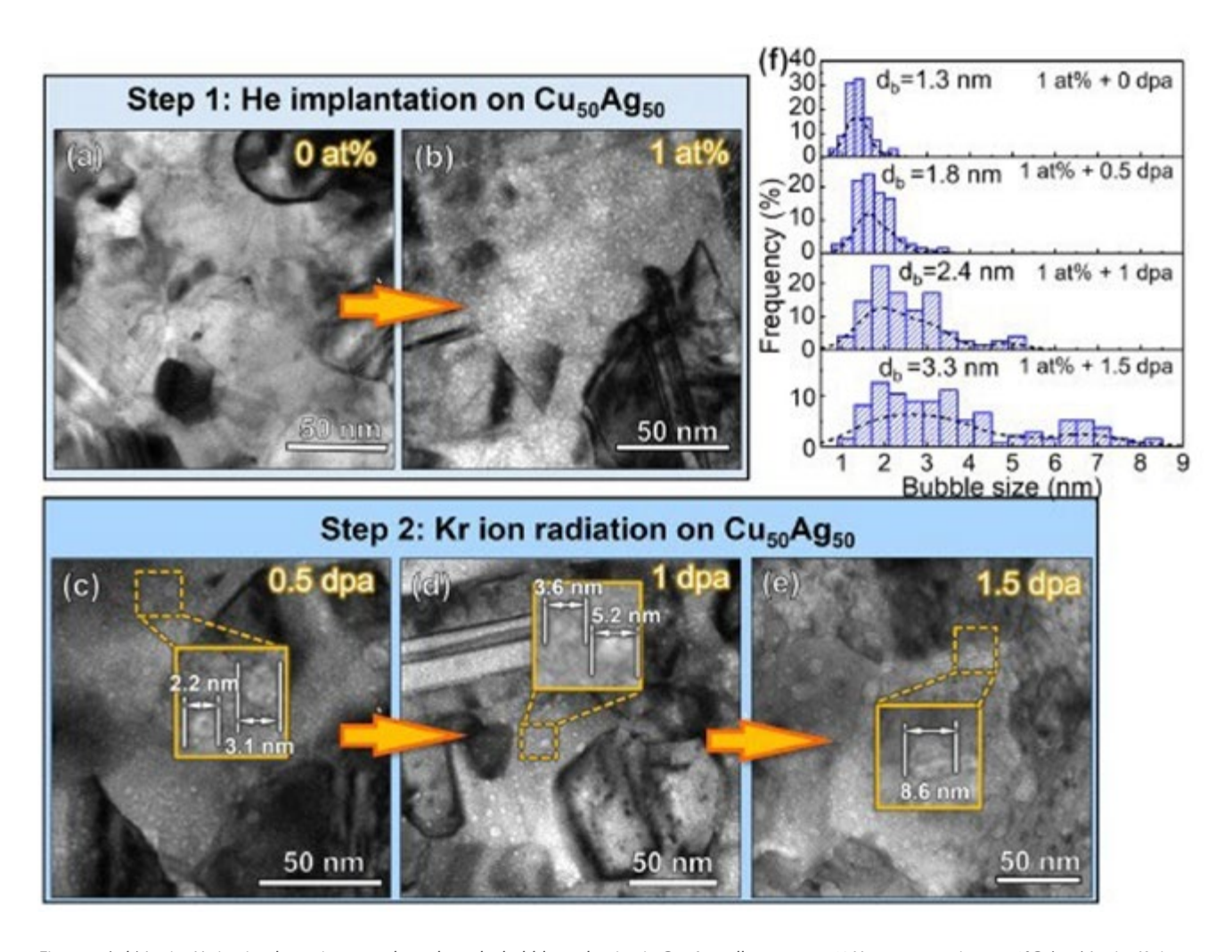


Figure 1. (a,b) In situ He ion implantation snapshots show the bubble nucleation in $Cu_{50}Ag_{50}$ alloy up to 1at% He concentration at 50°C. (c-e) In situ Kr-ion irradiation snapshots reveal the microstructure evolution up to 1.5 dpa at 300°C. The insets magnify bubbles at TJs and GBs at different dose levels. (f) Statistical bubble-size distribution at different doses. A pronounced bimodal bubble-size distribution in $Cu_{50}Ag_{50}$ alloy was observed after 1.5 dpa Kr irradiation with 1 at% implanted He.

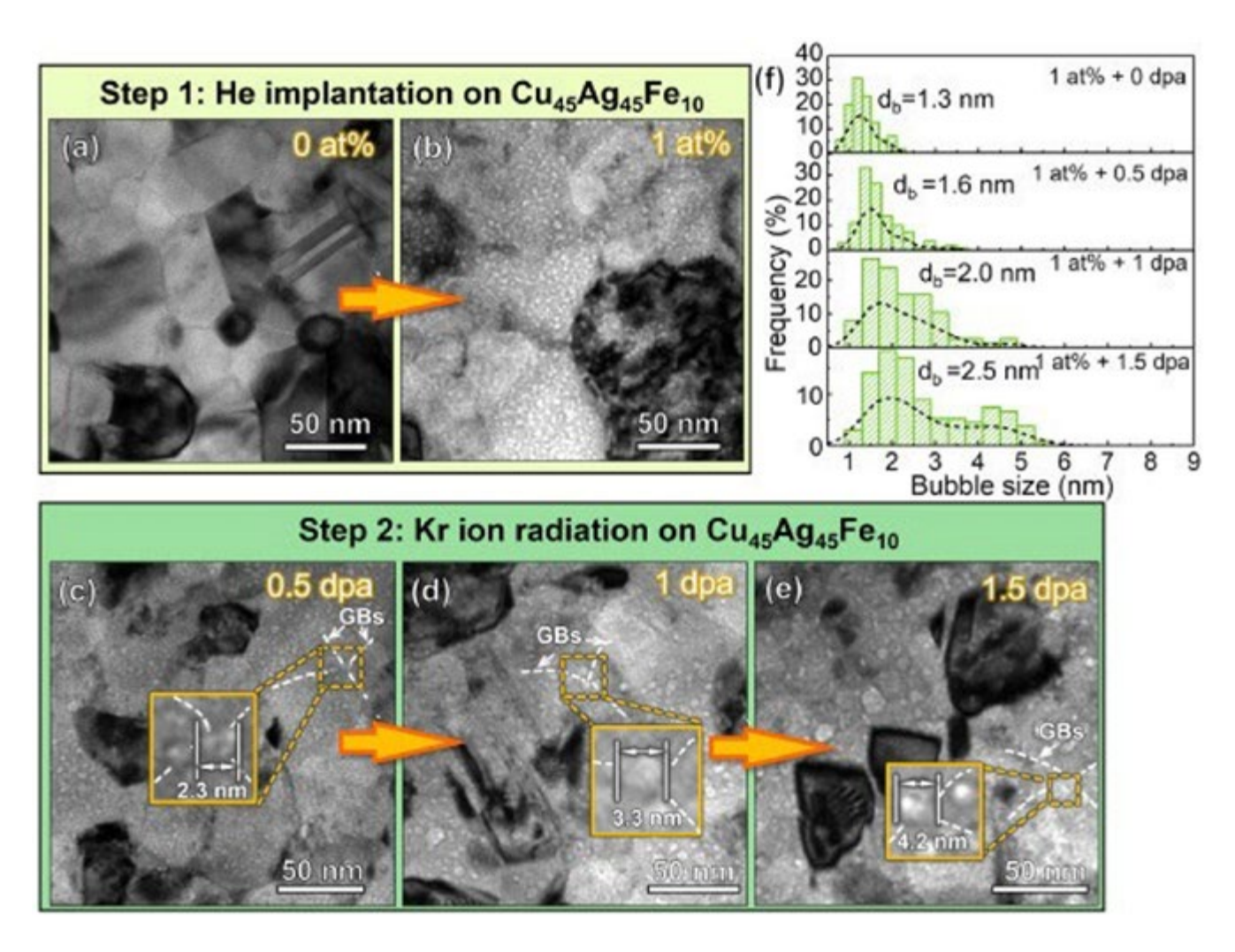


Figure 2. (a,b) In situ He ion implantation snapshots show the bubble nucleation in CAF₁₀ alloy up to 1 at% He concentration at 50°C. (c-e) In situ Kr-ion irradiation snapshots showing the bubble-size evolution up to 1.5 dpa at 300°C. The insets display bubbles at TJs and GBs at different dose levels. (f) Statistical bubble-size distributions at different dose levels reveal a prominent bubble growth with dose and moderate bimodal bubble-size distribution in CAF₁₀ alloy.

List of Publications

[1] Tianyi Sun, Tongjun Niu, Zhongxia Shang, Wei-Ying Chen, Meimei Li, Haiyan Wang, Xinghang Zhang, "An *in situ* study on the effect of grain boundaries on helium bubble formation in dual beam irradiated FeCrAl alloy," *Acta Materialia* 245 (2023) 118613.

- [2] Zhongxia Shang, Tongjun Niu, Tianyi Sun, Sichuang Xue, Cuncai Fan, Wei-Ying Chen, Meimei Li, Haiyan Wang, Xinghang Zhang, "In situ study on radiation response of a nanotwinned steel," Scripta Materialia 220 (2022) 114920.
- [3] T Niu, T Sun, Z Shang, Y Zhang, Z He, WY Chen, M Li, H Wang, X Zhang, "Helium in Cu- Ag-Fe triphase immiscible nanocomposites: An *in situ* sequential dual beam TEM study," *Journal of Nuclear Materials* 574 (2023) 154153.
- [4] Tongjun Niu, Sreekar Rayaprolu, Zhongxia Shang, Tianyi Sun, Cuncai Fan, Yifan Zhang, Chao Shen, Md Nasim, Wei-ying Chen, Meimei Li, Yexiang Xue, Haiyan Wang, Anter El- Azab, Xinghang Zhang, "In situ study on heavy ion irradiation induced microstructure evolution in single crystal Cu with nanovoids at elevated temperature," Materials Today Communications 33 (2022) 104418.
- [5] Cuncai Fan, Zhongxia Shang, Meimei Li, Haiyan Wang, Anter El-Azab, Xinghang Zhang, "The influence of helium and heavy ion irradiations on radiation responses of single crystal Cu with nanovoids: An *in situ* TEM study," *Acta Materialia* 240 (2022) 118293.
- [6] M Nasim, ARG Sreekar, T Niu, C Fan, Z Shang, Jin Li, H Wang, A El-Azab, Y Xue, X Zhang, "Unraveling the size fluctuation and shrinkage of nanovoids during *in situ* radiation of Cu by automatic pattern recognition and phase field simulation," *Journal of Nuclear Materials* 574 (2023) 154189.
- [7] Tongjun Niu, Bo Yang, Zhongxia Shang, X. Zhang, "In situ radiation studies on radiation damage in additively manufactured Haynes 230 alloys with nanoprecipitates, in preparation."

RTE 4259: Microstructural Characterization of Neutron Irradiated NF616 (Grade 92) As a Function of Doses and Temperatures

PI: Ramprashad Prabhakaran (PNNL)

Collaborators: Dan Edwards, Mychailo Toloczko (PNNL), Kumar Sridharan (University of Wisconsin-Madison)

Facility: Materials Science and Technology Laboratory, Pacific Northwest National Laboratory

Introduction

Ferritic-martensitic (F-M) steels (9–12 wt%) are being considered as candidate in-core structural materials for fast and advanced light-water reactors due to their excellent resistance to radiation-induced void swelling, good irradiation-creep properties, microstructural stability, and thermal conductivity. HT-9, a first-generation F-M steel, has a relatively large irradiation mechanical and microstructural database [1–5]. The third-generation steel that shows the most promise is NF616 (T92). Creep-rupture properties of NF616 (9Cr-0.5Mo-1.8W-V-Nb) are much higher relative to HT-9, T91, and the reduced-activation steels [2]. Based on elevated-temperature creep-rupture strength and impact toughness, HT-9 has significant weaknesses relative to NF616 [2]. NF616 is under consideration for nuclear applications due to greater strength that tends to provide increased safety margins and design flexibility and lower cost for reactor components [6]. Although elevated-temperature mechanical properties favor NF616, neutron-irradiation data are limited.

As a part of the UW-Madison NSUF Pilot Irradiation Experiment, NF616 (Grade 92) was neutron irradiated in the ATR at various temperatures (388–469°C) and doses (3–8 dpa). PNNL recently won an NSUF RTE (2879) award to perform mechanical characterization of neutron irradiated NF616 as a function of irradiation dose and temperature to evaluate the degree of low-temperature (~425°C) neutron-irradiation hardening. Samples were shipped from the NSUF library to PNNL, and tensile and microhardness testing were performed there. Our team has NF616 control samples. Maximum impact of this work will be obtained by performing microstructural characterization on the neutron-irradiated samples present at PNNL to correlate the measured hardening with microstructural features.

Project Objectives

The objective of the RTE Project 4259 was to perform microstructural characterization of NF616 as a function of irradiation dose and temperature. TEM was used to evaluate control and irradiated samples and observe the general grain structure, prior austenite grains, martensite packet, lath structure, and primary carbide structure because these parameters can significantly affect the mechanical behavior and radiation resistance of NF616. TEM was also be employed to study (the size and number density of) dislocation loops, radiation-induced cavities, segregation, and phase transformation. For irradiated F-M steels, the increase in yield strength is quite steep up to around 10 dpa [5]. Hence, a comprehensive understanding of the mechanical behavior and microstructural features of NF616 after irradiation to lower doses (1–10 dpa) would be beneficial for more-accurate extrapolation to high doses.

Tables 1 and 2 show the chemical composition and heat treatment performed on NF616. Table 3 shows the summary of ATR neutron-irradiated NF616 samples that were studied at PNNL under this RTE award.

Table 1. Chemical composition of NF616 heats (weight %).

Alloy/heat	Cr	C	Si	Mn	W	V	Мо	Ni	Others; Fe: balance
NF616 JAEA	8.82	0.11	0.10	0.45	1.87	0.19	0.47	0.17	N 0.047; AI 0.005; P 0.012; S 0.003 O 0.004; Nb 0.064; B 0.0017

Table 2. Heat treatment performed on NF616.

Alloy (heat/supplier)	Heat Treatment (Normalizing and Tempering); AC: air cooling
NF616 (JAEA)	1070°C/120 minutes/AC; 770°C/120 minutes/AC

NOTE: AC: Air cooling

Table 3. Summary of ATR neutron-irradiated samples studied under this RTE award.

Alloy/Heat	ID	Irradiation Temp. (°C)	Dose (dpa)	Tensile-Tested [†] Temp. (°C)	Vickers Microhardness Testing†	ТЕМ
NF616	NF-SP1	_	_	RT, 388 and 452	RT	✓
JAEA	KGT 407	388	4.1	RT and 388	RT	✓
	KGT 3507	452	3.9	RT and 452	RT	✓
	KGT 3509*	448	4.8	N/A	RT	✓
	KGT 3511*	450	3.0	N/A	RT	✓

NOTES:

Research Work

Materials: NF616 was neutron-irradiated in the ATR at various temperatures and doses (see Table 3). PNNL received these samples from the INL NSUF library, and mechanical characterization (tensile testing at room and irradiation temperature; and microhardness testing at room temperature) of NF616 was performed as a function of irradiation dose and temperature under RTE Project 2879. Failed tensile-specimen shoulders and TEM discs (control and irradiated) were employed for RTE Project 4259.

PIE: Under RTE Project 4259, microstructural characterization (by TEM) of control and neutron-irradiated NF616 samples (see Table 3) was performed at PNNL, a partner NSUF facility with well-established capabilities for performing microstructural studies.

Task 1: Preparation of TEM lamellae from tested tensile specimen shoulders and discs at PNNL: As a part of prior funded RTE work (Project 2879) to perform microhardness testing, samples were already mounted and polished to a 1-micron condition. TEM lamellae were prepared using FIB from NF616 samples (one control and four irradiated).

Task 2: Perform TEM studies on NF616 (control and neutron irradiated):

The microstructures of five NF616 samples (one control and four irradiated) were studied using TEM, and researchers obtained the following information: STEM characterization, overview imaging, dislocation imaging, collected EDS maps of each sample around precipitates (Figures 1–3), and some atomic-column imaging, where possible.

^{*} TEM disc

[†] Tensile and microhardness testing was performed under a different RTE award (#2879; PI: Ramprashad Prabhakaran)

Ongoing Work

Image- and EDS-analysis techniques are being employed to quantify the TEM data. Currently, efforts are ongoing to understand the effects of radiation damage on NF616 at LWR- and fast-reactor-relevant temperatures and to develop appropriate correlations between structural properties and temperature-dose conditions. The microstructural information obtained from RTE Project 4259, along with mechanical characterization performed under RTE Project 2879 (PI: Ramprashad Prabhakaran) will aid in understanding the effect of neutron irradiation as a function of irradiation temperature and dose. The information obtained from these RTE studies could be extended beyond NF616; it would be relevant to many F-M steels.

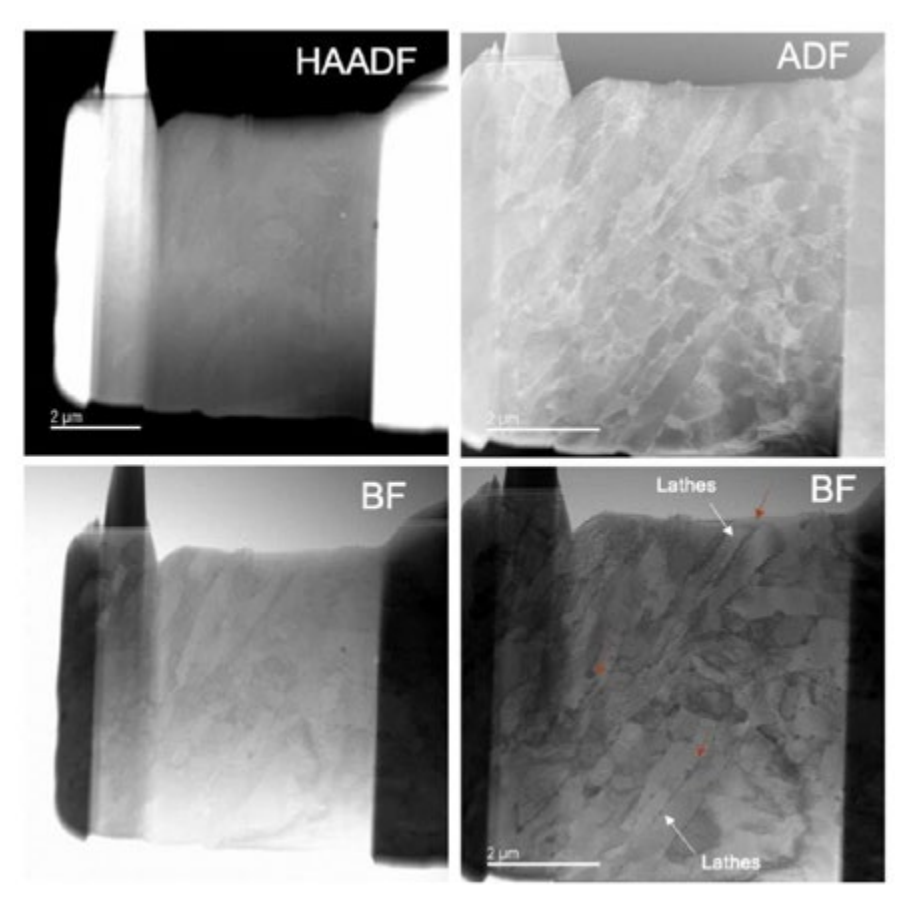


Figure 1. Neutron-irradiated NF616; KGT 407 (388°C, 4.1 dpa): overview (red arrows: carbides).

Conference Presentations

[1] Ramprashad Prabhakaran, Indrajit Charit, Dan Edwards, Mychailo Toloczko, Stuart Maloy, Kumar Sridharan, "Mechanical and microstructural characterization of neutron irradiated HT-9 and NF616 (Grade 92) at LWR and fast reactor relevant temperatures," 2023 TMS Annual Meeting and Exhibition, Mar 19-23, 2023, oral presentation.

[2] Ramprashad Prabhakaran, Indrajit Charit, Dan Edwards, Mychailo Toloczko, Stuart Maloy, Kumar Sridharan, "Mechanical and microstructural characterization of neutron irradiated HT-9 and NF616 (Grade 92) at LWR and fast reactor relevant temperatures," Materials in Nuclear Energy Systems (MiNES) 2023, New Orleans, LA, Dec 10-14, 2023, oral presentation.

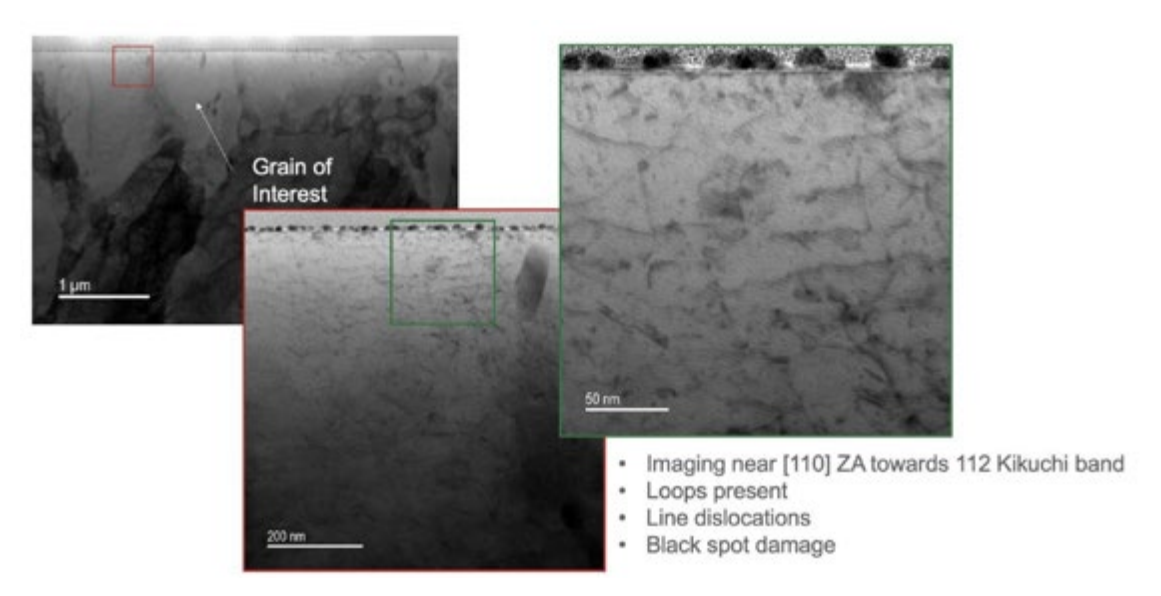


Figure 2. Neutron-irradiated NF616; KGT 3511 (450°C, 3 dpa): dislocation imaging.

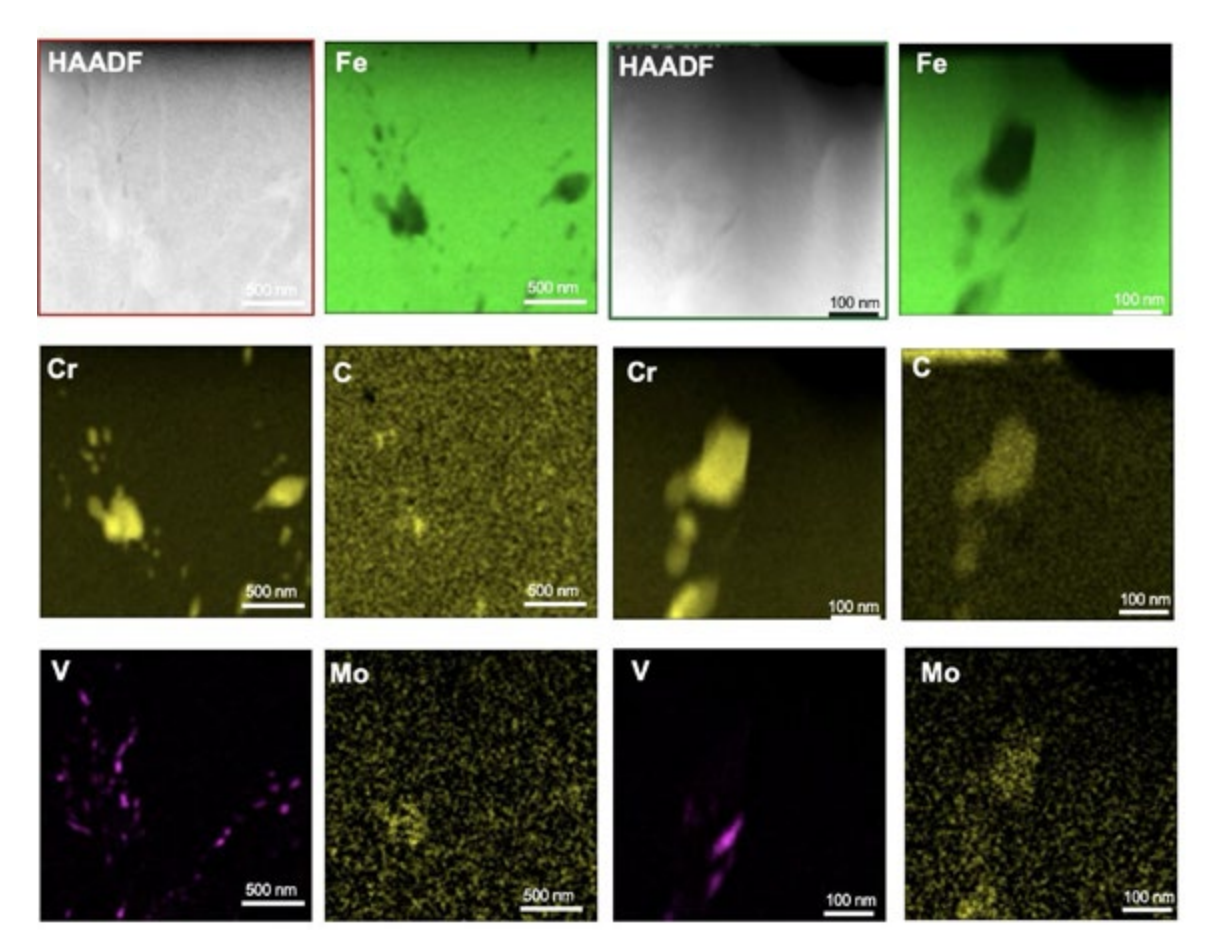


Figure 3. Neutron-irradiated NF616; KGT 3511 (450°C, 3 dpa): STEM-EDS maps of two regions.

Acknowledgements

The PIE at PNNL was supported primarily by the U.S.-DOE, Office of Nuclear Energy under DOE Idaho Operations Office Contract DE-AC07-051D14517 as part of NSUF experiments, RTE 4259. The PI would like to acknowledge the assistance of Collin Knight and other NSUF staff at INL for their help in identifying samples and shipping to PNNL. The PI would also like to recognize the technical support of Kayla Yano for preparing TEM lamellae using FIB instrument and performing TEM studies. The PI would like to acknowledge Stuart Maloy (PNNL NSUF technical lead) for NSUF RTE project coordination.

References

- [1] S. A. Maloy et al. 2011. "Core materials development for the fuel cycle R&D program." *Journal of Nuclear Materials* 415: 302–305. https://doi.org/10.1016/j.jnucmat.2011.04.027.
- [2] R. L. Klueh and A. T. Nelson. 2007. "Ferritic/martensitic steels for next-generation reactors." *Journal of Nuclear Materials* 371: 37–52. https://doi.org/10.1016/j.jnucmat.2007.05.005.
- [3] T. S. Byun et al. 2012. "Impact properties of irradiated HT9 from the fuel duct of FFTF." *Journal of Nuclear Materials* 421: 104–111. https://doi.org/10.1016/j.jnucmat.2011.11.059.
- [4] M. B. Toloczko and F. A. Garner. 1996. "Irradiation creep and void swelling of two LMR heats of HT9 at \sim 400°C and 165 dpa." *Journal of Nuclear Materials* 289: 233–237. https://doi.org/10.1016/S0022-3115(96)00413-8.
- [5] O. Anderoglu et al. 2013. "Mechanical Performance of Ferritic Martensitic Steels for High Dose Applications in Advanced Nuclear Reactors." *Metallurgical and Materials Transactions* A 44A: 70–83. https://doi.org/10.1007/s11661-012-1565-y.
- [6] L. Tan et al. 2017. "Microstructural evolution of neutron-irradiated T91 and NF616 to ~4.3 dpa at 469 °C." *Journal of Nuclear Materials* 493: 12–20. https://doi.org/10.1016/j.jnucmat.2017.05.041.

RTE 4269: Preoxidation Effect on ATF Cladding Performance by Characterization of Irradiated FeCrAl-UO₂ Capsules

Vipul Gupta (GE Research), Kevin Field (University of Michigan), Keyou Mao (Florida State University), Andrew Hoffman, Raul Rebak (GE Research), Fabiola Cappia (INL), Jason Harp (ORNL)

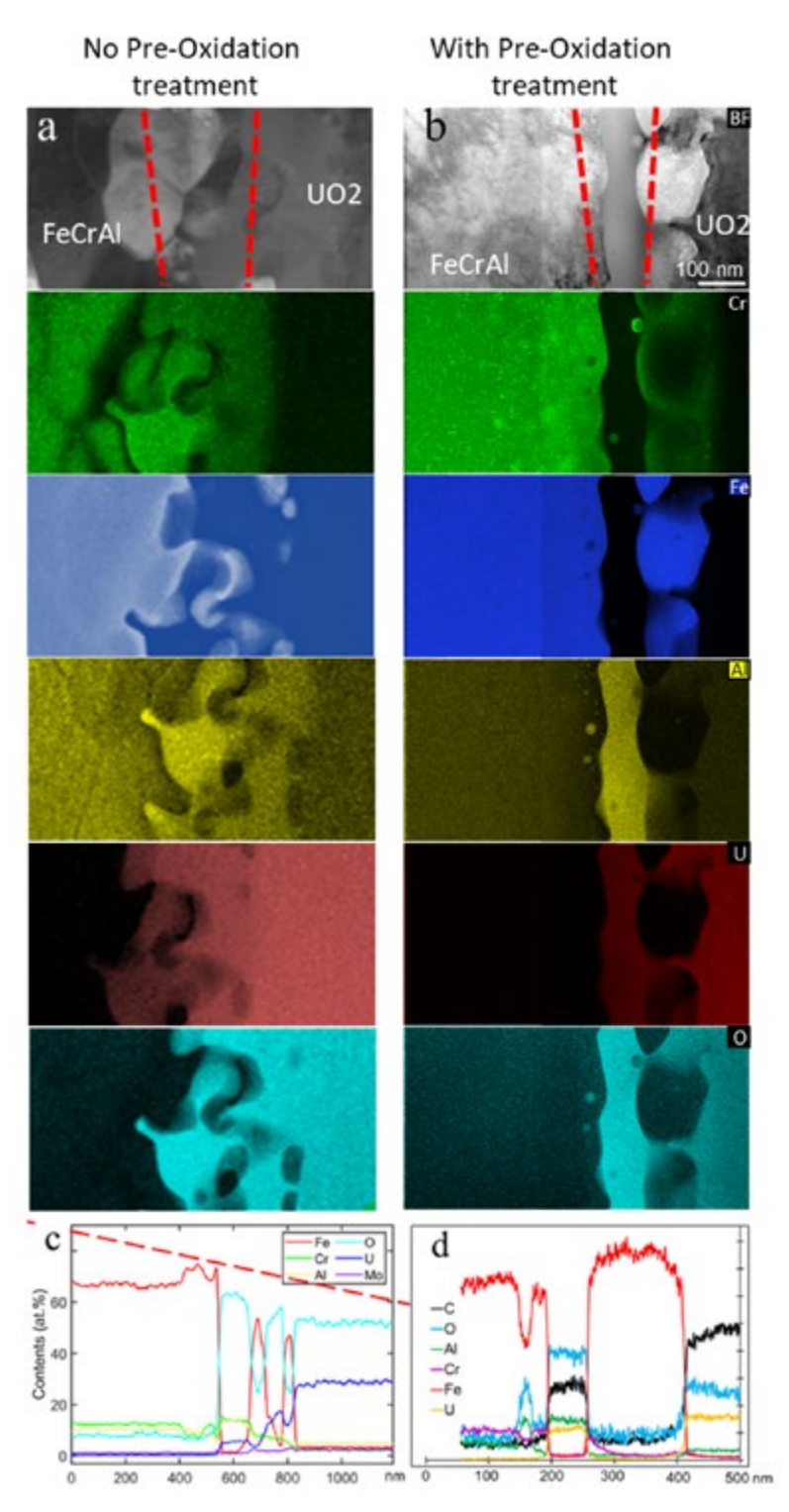
Facility: Low Activation Materials Development and Analysis Laboratory, Oak Ridge National Laboratory

This RTE project investigates the fuel/cladding chemical interaction (FCCI) behavior of two FeCrAl C₃₅M (Fe₋₁₃Cr₋₅Al₋₂Mo_{-0.2}Si_{-0.03}Y wt.%) alloys, with and without preoxidation treatment, after neutron irradiation. H-cup diffusion multiples of FeCrAl alloys and ceramic UO₂ fuel were irradiated at a temperature of ~360°C to a total estimated burnup of 26 GWd/tHM. Irradiations were performed as part of the GE's Accident Tolerant Fuel Program with the U.S. Department of Energy, GE Research, Global Nuclear Fuel, GE-Hitachi, and several U.S. national labs. The Idaho National Laboratory (INL) and Oak Ridge National Laboratory (ORNL) sponsored the shipment sets of neutron-irradiated samples of diffusion couples from INL to ORNL. Detailed sample information is shown in Table 1. Sample preparation was performed using the shielded FIB at the Low Activation Materials

Development and Analysis (LAMDA) Facility and was followed by TEM and STEM analysis at LAMDA Facility to elucidate microstructural and chemistry changes. PIE results demonstrate the excellent degradation resistance of FeCrAl alloys as ATF cladding materials in LWR conditions. The study concludes that there were no irradiation-induced defects observed in either of the FeCrAl claddings. The formation of amorphous AI/U mixed oxide was observed at the fuel-clad interface, which can serve as a tritium-permeation barrier and protect against potential chemical attack from the fuel. The study attributed the formation of amorphous AI/U mixed oxide to the low-temperature and limited time of neutron irradiation. The preoxidation prevents the further formation of the Cr-Fe rich intermetallic phase at the interface.

Table 1. Summary of accomplishment for Proposal 21-4269.

Sample and capsule ID	Specimen condition	FIB lift-out for TEM sample preparation	TEM data acquisition
C35M 1a	As machined, 360°C	✓	✓
C35M 1a	As machined, 360°C	✓	✓
C35M 2a	Pre-oxidized 800°C/2h, 360°C	✓	✓
C35M 2a	Pre-oxidized 800°C/2h, 360°C	✓	✓
C35M 3a	Pre-oxidized 1000°C/2h, 362°C	✓	_



TEM data were collected to study effects of preoxidation on the distribution of Cr and other solute elements—e.g., Fe and Cr. Selected datasets (from C35M 1a and C35M 2a) are shown in Figure 1 to highlight the type of information obtained and the data analysis carried out to elevate understanding of microstructural changes. The size, shape, and number density of a Cr-enriched cluster and the formation of AI/U mixed oxides are crucial to understanding the effects of preoxidation treatment and irradiation resistance of advanced FeCrAl alloys. This RTE study was designed to test the hypothesis that the reduced interfacial attack of fission product at the diffusion-couple interface is due to preexisting Al_xO_v near the FeCrAl side. The STEM-EDS data suggest that the Al oxide region is typically concentrated with U (>20 at%) while the Fe- or Cr-Ferich intermetallic regions are observed to have minor U (<5 at%).

From all the data sets we have acquired, no irradiation-induced defects are observed in either of the FeCrAl claddings. Amorphous Al/U mixed oxide develops at the fuel-clad interface after neutron irradiation for both specimens. The amorphous Al/U mixed oxide formation is attributed to the low-temperature and limited time of neutron irradiation in the current study. The microstructural and compositional results observed from the current study demonstrate the promising degradation resistance of FeCrAl alloys used as ATF cladding materials in the LWR conditions.

RTE 4307: Ion Irradiation and Examination of Additive Friction Stir Manufactured 316 Stainless Steel Component

PI: Rajiv Mishra, University of North Texas (UNT)

Co-Pls: Ramprashad Prabhakaran (PNNL), Lin Shao (TAMU)

Facility: Microscopy and Characterization Suite, Center for Advanced Energy Studies; Accelerator Laboratory, Texas A&M University

This proposal explored solid-state additive friction stir deposition (AFSD) as a modular manufacturing technology enabling a more-rapid and streamlined onsite fabrication process for large, meter-scale structural nuclear components with fully dense parts. Austenitic 316 stainless steel is an excellent candidate to demonstrate AFSD, as it is a commonly used structural material for nuclear applications. There are a very few studies reported on the irradiation performance of 316SS produced via fusion-AM but no data are available for AFSD 316SS. The objective of this work is to fill the gap in the literature by performing studies to document the irradiation performance of AFSD 316SS, which is extremely relevant for nuclear applications.

The goal was achieved by carrying out (a) AFSD at the Center for Agile and Adaptive Additive Manufacturing, UNT, using the MELD-B8 machine, (b) self-ion irradiations at TAMU using a 3.0 MV NEC tandem accelerator at temperatures relevant to multiple reactor concepts and closer to the maximum swelling temperature, and (c) nanoindentation and TEM at the MaCS, CAES, Boise State University, Idaho, and Materials Research Facility (MRF), UNT, to examine irradiation-induced microstructural changes and mechanical properties.

Table 1. Summary of accomplishment of this proposal.

Material	316 SS	
Techniques (NSUF)	Irradiation	✓
	Nanoindentation	✓
	FIB for TEM sample	✓
	TEM	✓
Techniques (non- NSUF @ UNT)	AFSD	✓
	TEM for faulted loops	✓

Current manufacturing technologies—forging, rolling, etc.—for core structural materials like low alloy steels, stainless steels, Ni alloys, etc., used in LWRs and advanced-reactor concepts can be costly for large components and be restrictive in geometrical designs for parts as complex as heat exchangers. Enabling technologies, such as laser- and electron-beam-based fusion AM and friction stir welding have caught the imagination of manufacturing and materials engineers. It is important to note that powder-bed fusion AM techniques are inherently limited by the size of the machines and have limitations in the production of fully dense parts. For safety-compliant parts, HIP is typically required, but this adds cost to an already expensive manufacturing method. Parallel work initiated on solid-state manufacturing technologies in the last decade resulted in the development of a friction stir-based technique called AFSD as a highly efficient solid-state AM substitute for fusion-based AM techniques [1,2], patented by U.S.-based MELD Manufacturing Corporation [3].

Irradiation leads to degradation in mechanical properties—attributed to RIDs like voids, dislocation loops, and dislocation networks—evaluated via radiation-induced hardening. RIDs are imaged with the help of TEM for the AFSD 316SS samples and compared with non-AFSD samples for critical conditions. Figure 1 (a) shows that, at extreme conditions of 100 dpa/600°C, AFSD 316SS did not exhibit voids whereas non-AFSD samples resulted in voids with an average size of 12 ± 13.3 nm, as seen in Figure 1(b). For comparison, 85% cold-worked (CW) 316SS microstructure from the literature [4] is presented in Figure 1 (c) with nanovoids. Comparing the void swelling percentage of AFSD with direct energy deposition (DED) and laser powderbed fusion (LPBF) fusion-based AM routes and CW samples in Figure 1 (d) shows that the sample processed via AFSD is resistant to void swelling, even at these extreme irradiation-dose and temperature conditions. This shows that among the AM processes, the solid-state process of AFSD not only provides improved strength and ductility [5,6] (Figure 1 [a]), but also leads to a swelling-resistant product.

Conventional TEM (CTEM) relrod DF imaging was carried out to image faulted loops using a diffraction vector of ½31T near [011] zone axis. For 2600°C, as shown in Figure 2 (a–c), 25 and 50 dpa do not show a notable change in the number of faulted loops with an increase in dose, but 100 dpa leads to an evident, but not sweeping increase.

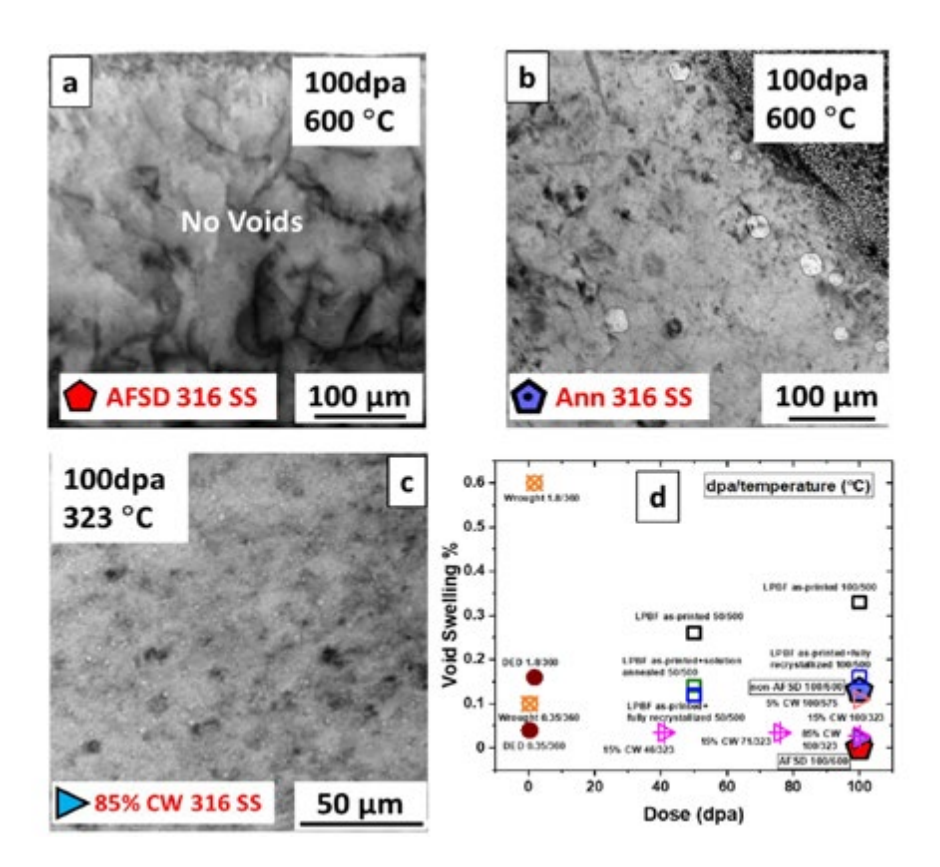


Figure 1. Imaging of voids for extreme irradiation condition of 100 dpa. 600°C for (a) AFSD sample, (b) annealed non-AFSD feed rod, (c) 85% CW sample from the literature [4], and (d) void-swelling percentage comparison plot for different AM routes and void-swelling-resistant CW samples in the number. At a lower temperature of 300°C, (see Figure 2.[d and e]), the number of loops drastically increased relative to 600°C, suggesting an increased hardness of samples irradiated at 300°C. Conditions of 25 dpa/300°C resulted in finer loops relative to 100 dpa/300°C, signifying an increase in loop size with dose. Figure 2.(f) gives the image for non-AFSD 100 dpa/600°C that, when compared with AFSD 100 dpa/600°C in Figure 2.(c), shows an increased number of faulted loops, displaying the potential of the AFSD route to improve radiation tolerance.

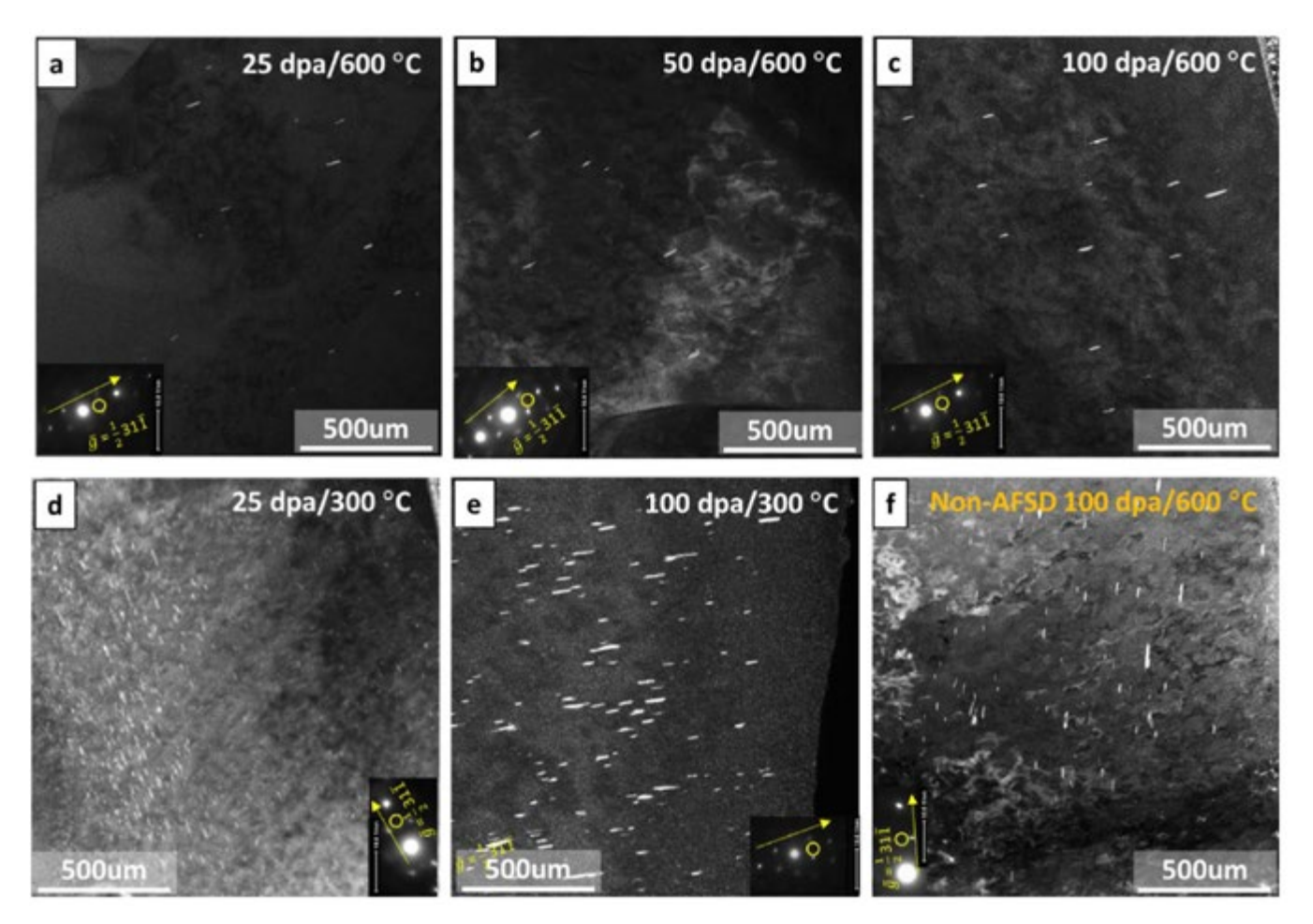


Figure 2. Relrod CTEM DF imaging with B = [110], $g\vec{g} = \frac{1}{2}31T(a)$ AFSD 25 dpa/600°C, (b) AFSD 50 dpa/600°C, 2(c) AFSD 100 dpa/600°C, (d) AFSD 25 dpa/300°C, (e) AFSD 100 dpa/300°C, and (f) non-AFSD 100 dpa/600°C.

Mechanical Response at Room Temperature of Irradiated AFSD and Non-AFSD Samples

The nanoindentation results aided in obtaining information on radiation-induced hardening, as shown in Figure 3. The hardness of 600°C increased relative to the pristine sample. At 300°C, there is a drastic increase in hardness for all the dose levels relative to 600°C. This result was expected both because it is reported in the literature and because the number of faulted loops, which are the major contributor to radiation-induced hardening, was higher at 300°C. For both temperatures, the number of faulted loops increased with an increase in dose levels. No voids were observed in AFSD samples even for the extreme condition of 100 dpa/600°C, as shown in Figure 1.

Additive Friction-Stir Deposition: A Solid-State AM Route to Radiation-Tolerant Components

AFSD leads to a drastic improvement in ductility while still retaining the strength attributed to refined recrystallized grain size, as compared to different AM-processing routes and conventional routes. AFSD, due to its refined grain size, results in increased sink sites for the RIDs and, thus, no voids, decreased density of dislocation loops and networks, coarser solute clustering, and weaker RIS relative to non-AFSD feed rods and 316SS processed via different conventional and fusion-based AM routes [6]. The AFSD samples exhibited improved radiation tolerance where the most significant observation was the absence of voids, even for the extreme condition of 100 dpa/600°C.

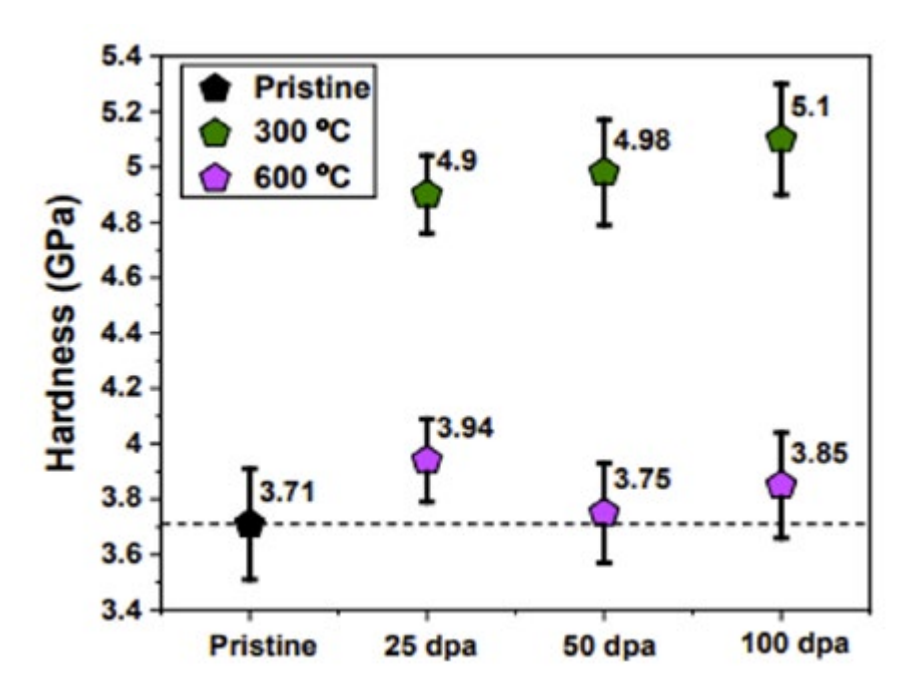


Figure 3. Nanoindentation hardness data for AFSD samples.

References

- [1] H. Z. Yu and R. S. Mishra. 2020. "Additive friction stir deposition: a deformation processing route to metal additive manufacturing." *Materials Research Letters* 9(2): 71–83. http://dx.doi.org/10.1080/21663831.2020.1847211.
- [2] R. S. Mishra, R. S. Haridas, and P. Agrawal. 2022. "Friction stir-based additive manufacturing." *Science and Technology of Welding and Joining* 27(3): 141–165. https://doi.org/10.1080/13621718.2022.2027663.
- [3] MELD. 2025. "Technology Overview." *MELD Manufacturing*. 2025. https://www.meldmanufacturing.com/technology-overview/.
- [4] X. Zhang, K. Hattar, Y. Chen, L. Shao, J. Li, C. Sun, K. Yu, N. Li, M. L. Taheri, H. Wang, J. Wang, and M. Nastasi. 2018. "Radiation damage in nanostructured materials." *Progress in Materials Science* 96:217–321. https://doi.org/10.1016/j.pmatsci.2018.03.002.
- [5] P. Agrawal, R. S. Haridas, S. Yadav, S. Thapliyal, A. Dhal, R. S. Mishra. 2023. "Additive friction stir deposition of SS316: Effect of process parameters on microstructure evolution." *Materials Characterization* 195: 112470. https://doi.org/10.1016/j.matchar.2022.112470.
- [6] P. Agrawal, C-H. Shiau, A. Sharma, Z. Hu, M. Dubey, Y. Lu, L. Shao, R. Prabhakaran, Y. Wu, R. S. Mishra. 2024. "Ion irradiation and examination of Additive friction stir deposited 316 stainless steel." *Materials & Design* 238: 112730. https://doi.org/10.1016/j.matdes.2024.112730.

RTE 4389: Irradiation Effects on Microstructure and Mechanical Properties in a Laser-Welded Oxide Dispersion-Strengthened Alloy

M. J. Swenson (University of Idaho), E. Getto, B. Baker (United States Naval Academy)

Facility: Microscopy and Characterization Suite, Center for Advanced Energy Studies

Objectives and Significance

The objective of this project is to evaluate the combined effects of laser-weld joining and irradiation on the microstructure and mechanical properties of a commercial oxide dispersion-strengthened (ODS) alloy candidate for advanced nuclear-reactor applications. For this study, these effects are evaluated on the commercial ODS alloy MA956. The complete study encompasses various complementary techniques including:

- 1. Industry-representative laser-weld joining of sheet components
- 2. Fe²⁺ ion irradiation
- 3. PIE of microstructures
- 4. Mechanical property characterization
- 5. Nanocluster evolution modeling
- 6. Dispersed-barrier hardening analysis.

The focus of this RTE project is on the PIE and microscopy activities, which enable all subsequent tasks for characterizing and describing the combined effects of both laser welding and ion irradiation on the alloy's performance.

Experiment Methods

Laser welding of MA 956 specimens was completed at MacKay Manufacturing, Inc., (Spokane, Washington) via welding two physical pieces together. Laser-welded samples were subsequently irradiated at Sandia National Laboratories with Fe²⁺ ions at 400°C to 1 dpa and, separately, to 25 dpa. Following irradiation, PIE was executed via access to the MaCS at CAES. FIB was used to fabricate local-electrode atom-probe (LEAP) and TEM samples, and characterization was completed via STEM imaging with the SuperX EDS (ChemiSTEM) facilities and with the LEAP at MaCS. This experiment is also designed to enable direct comparison with prior characterization results from friction-stir welding of the same MA 956 alloy (accomplished via RTE 17-906) to the same 1 dpa and 25 dpa irradiation conditions.

Results

Atom Probe Tomography

Needles for LEAP analysis were lifted from within the laser-welded region of the joint in the unirradiated condition and following irradiation to 1 dpa and 25 dpa. Figure 1 illustrates atom-probe tomography (APT) reconstructions from each sample, indicating that Y-Ti-O-based oxides are clearly present following the laser-welding process and following irradiation with Fe²+ ions to 1 dpa at 400°C. The average size and number density of the oxide nanoclusters are found to be 5.44 ± 0.11 nm and 179×10^{21} m⁻³, respectively. This is a finer morphology than that found in the bulk unwelded material from a prior RTE project, which exhibited a size and number density of 7.42 ± 0.10 nm and 40×10^{21} m⁻³, respectively. Interestingly, after irradiation with Fe²+ ions to 1 dpa at 400° C, the oxide nanoclusters have coarsened some, with a resulting size and number density of 6.09 ± 0.18 nm and 115×10^{21} m⁻³, respectively. This initial result confirms that oxide nanoclusters are able to survive the laser-welding process and may indicate that the oxide nanoclusters may be stable upon irradiation to a low dose.

More investigations are planned to:

- 1. Evaluate solute migration to and from the nanoclusters.
- 2. Determine the oxide-nanocluster morphology following irradiation to 25 dpa.
- 3. Measure mechanical properties (via nanoindentation) of the bulk material, laser-weld region, and irradiated specimens to determine the effects on hardness and yield strength.
- 4. Systematic correlation between the resultant microstructures and the mechanical properties to separate the effects of each microstructure feature and its influence on changes in yield strength.

Microscopy

Figure 2a shows a cross section of the laser-weld, imaged via EBSD. In addition to the growth of columnar grains, there are large voids throughout the weld (in black). Figure 2 (b and c) shows STEM imaging of the weld before and after ion irradiation of 400°C, 25 dpa. The dispersoids were quantified, and the diameter and number density are presented in Figure 3.

Figure 1. Representative solute reconstructions of laser-welded MA 956 as a) unirradiated, and b) irradiated with Fe^{2+} ion at 400° C to 1 dpa.

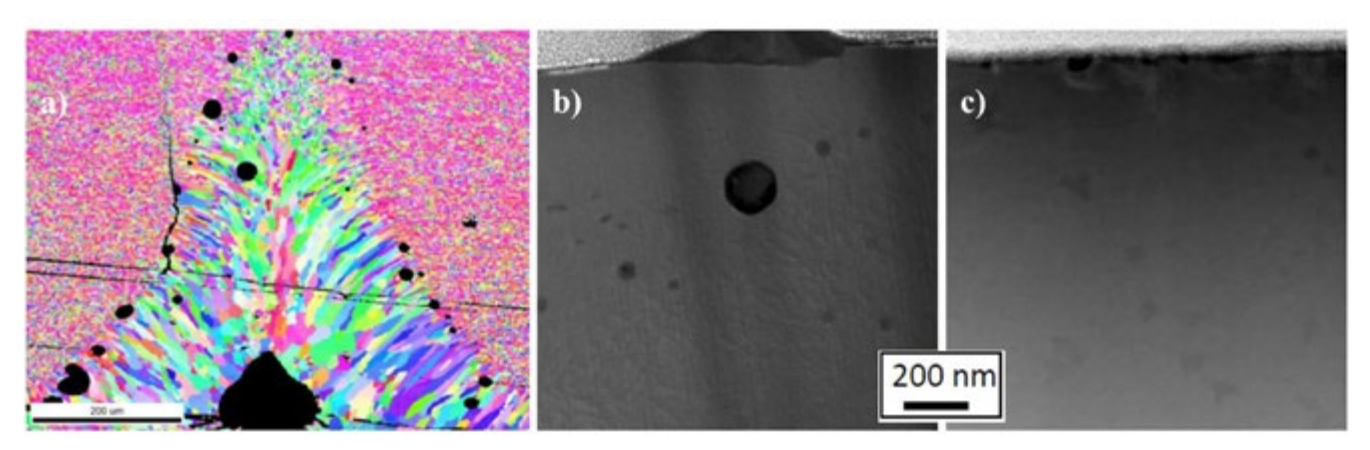
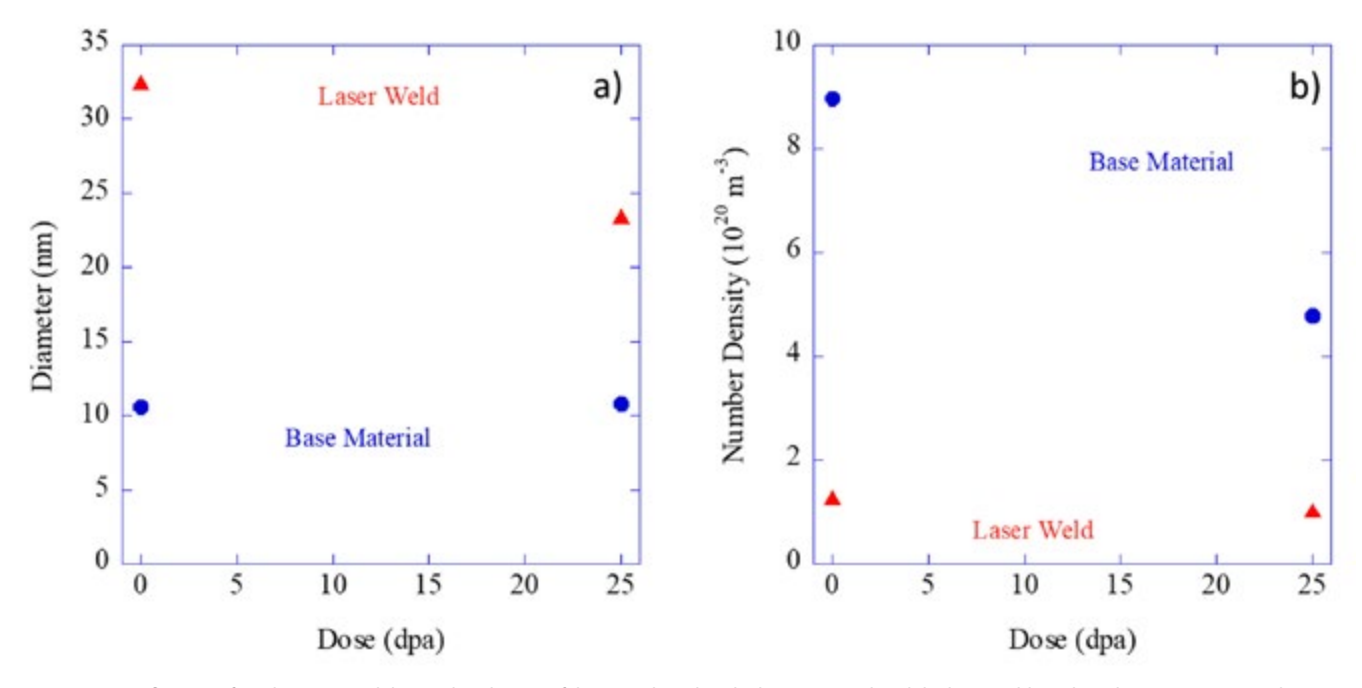


Figure 2. Imaging of laser-welded MA 956 using a) EBSD of unirradiated weld joint, and STEM imaging of dispersoids as b) unirradiated, and c) irradiated with Fe^{2+} ion at 400° C to 25 dpa.



 $Figure~3.~Quantification~of~(a)~diameter~and~(b)~number~density~of~dispersoids~within~the~base~material~and~the~laser~weld~irradiated~at~400^{\circ}C~up~to~25~dpa.$

RTE 4397: Synchrotron Characterization of Corrosion Growth on Gamma-Irradiated Aluminum Nuclear Spent-Fuel Alloys

PI: Trishelle Copeland-Johnson (INL)

Collaborators: Simerjeet Gill (BNL), Gregory Holmbeck (INL)

Facility: National Synchrotron Light Source-II, Brookhaven National Laboratory

Project Summary

The The U.S. Department of Energy (DOE) is currently evaluating options for the safe extended storage of nearly 18 MT of aluminum-clad spent nuclear fuel (ASNF). However, the extent of molecular hydrogen gas (H₂) produced by ASNF cask materials, stored in inert helium (He) environments, is a particular safety concern. Unfortunately, the presence of He alongside the corrosion products appears to facilitate H₂ production via a radiolysis effect, increasing the risk of embrittlement pressurization, which ultimately may result in cask rupture due to overpressurization of trapped flammable gases. Furthermore, correlating this yield to structural changes and corrosion products under different environmental conditions enhances the accuracy of complementary modeling efforts. Most notable is the potential relationship between the H₂ yield and the aluminum (oxy)hydroxide polymorphs compromising the corroded surface. Synchrotron XRD is a high-resolution technique capable of quantifying the polymorphic composition of surface aluminum (oxy)hydroxides, especially at low concentrations. In addition, synchrotron x-rays have been demonstrated to generate an effective dose that can be compared to that obtained from gamma irradiation.

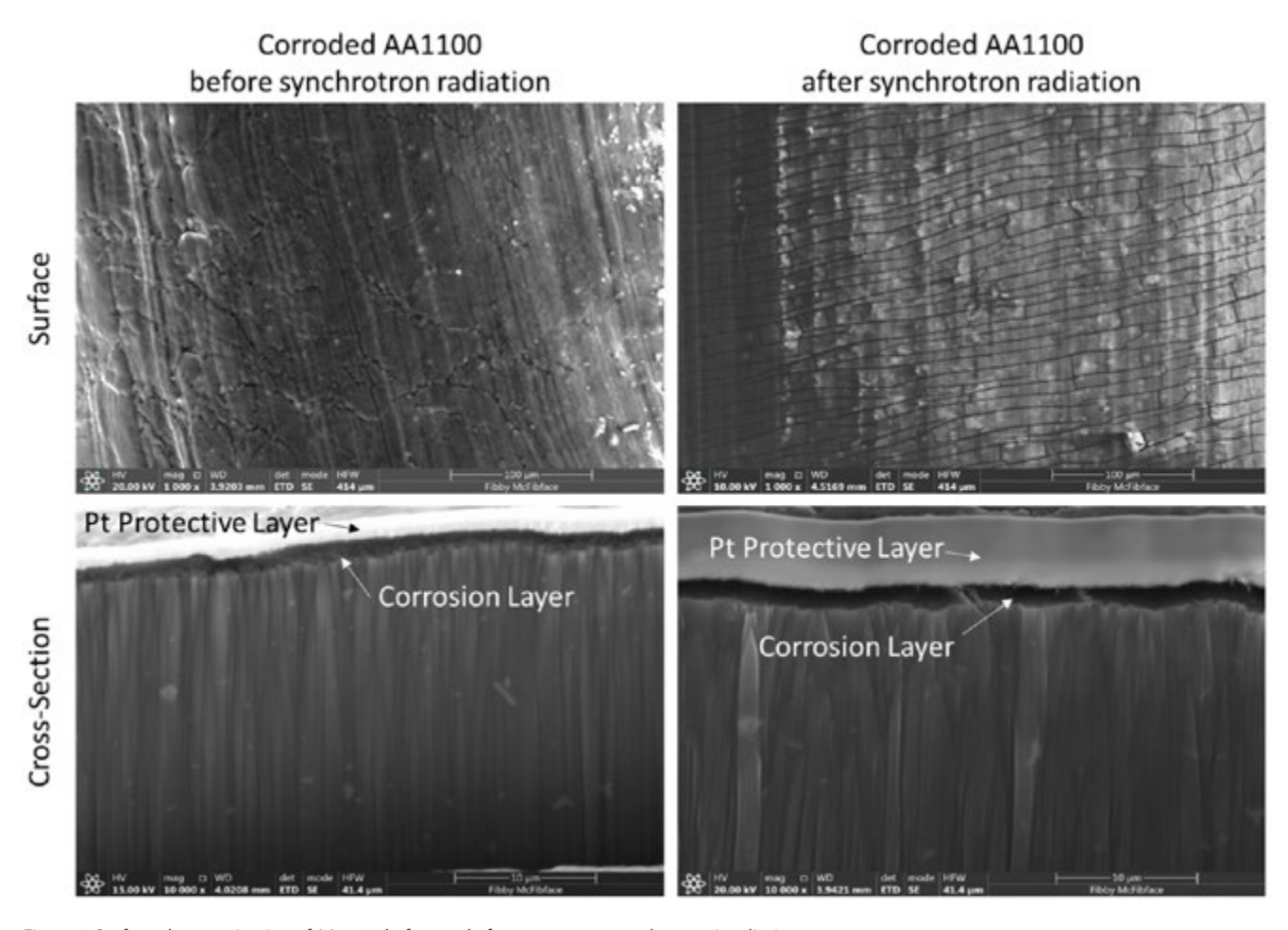
For this RTE project, the effects of synchrotron x-rays on accelerating radiolysis in corroded AA 1100 alloys and detection of surface aluminum (oxy) hydroxide species were investigated. Specimens were subject to different temperatures, gamma-irradiation doses, and

humidity levels before differences in aluminum (oxy) hydroxide corrosion products and crystal structure were quantified with in situ and ex situ synchrotron XRD techniques. Specimens were prepared using facilities at INL's Energy Innovation Laboratory and Center for Radiation Chemistry Research (CRC). The efficacy of the synchrotron x-rays to characterize polymorphs and induce a radiolysis effect was determined by comparing two different experimental specimen groups. The first experimental group was 650 µm diameter AA 1100 wires corroded in an aqueous environment before being flame sealed in a quartz tube backfilled with 0, 50, or 100% relative humidity He gas before being exposed to 5 MGyd of gamma irradiation. This level of gamma irradiation had been documented to induce a radiolysis effect in past investigations (see report titled "Milestone 1.2.15: Feasibility of In Situ Accelerated Aluminum Coupon Radiolysis by Synchrotron X-Rays" [https://www.osti. gov/biblio/2298951]). Gamma-irradiated specimens were exposed using the Foss Therapy Services (North Hollywood, California) Model 812 Co-60 gamma irradiator available through the CRC. These specimens served as the baseline for the experiment and were referred to as the ex situ specimens. A complimentary experimental group of wire specimens, referred to as the in situ, were also corroded and sealed with humid He gas, but in 1.5-mm-diameter by 2-mm-long capillary quartz tubes for synchrotron study. A detailed list of the specimens is shown in Table 1.

Table 1. Aluminum sample conditions investigated by this study.

Specimen	Experiment Type	Headspace Conditions	Gamma Irradiation Dose (MGy)
(A) As-received AA1100	ex situ	Vacuum	0
(B) Non-corroded AA1100	ex situ	He and ∼0% added RH	5
(C) Non-corroded AA1100	ex situ	He and 100% added RH	5
(D) Corroded AA1100	ex situ	He and ∼0% added RH	5
(E) Corroded AA1100	ex situ	He and 100% added RH	5
(F) Corroded AA1100	in situ	He and ∼0% added RH	0
(G) Corroded AA1100	in situ	He and 100% added RH	0

Synchrotron XRD analysis was performed using the x-ray powder diffraction (XPD) beamline at the National Synchrotron Light Source II. The equivalent dose of gamma irradiation experienced by the specimens exposed to synchrotron radiation was originally calculated to be between 26 and 101 MGy. A detailed explanation of how these values were calculated is available in "Milestone 1.2.15: Feasibility of In Situ Accelerated Aluminum Coupon Radiolysis by Synchrotron X-Rays." Based on these calculations, the scientific hypothesis of this investigation was that synchrotron irradiation should be more than feasible to induce the radiolysis effect on an accelerated time scale relative to that of gamma irradiation. Results from this investigation indicate that for both in situ and ex situ analysis the thickness of the aluminum (oxy)hydroxide surface layer with respect to the AA 1100 substrate was critical for capturing diffraction information from that region. SEM analysis estimated the extent of corrosion at $1.3 \pm 0.3 \, \mu m$ (Figure 1). Prior investigations were able to identify surface polymorphs using X-ray diffraction with a grazingincidence configuration at an operating energy of 40 keV, corresponding to a very shallow penetration depth. However, the XPD beamline operates at a higher energy level (40-70 keV) and is configured to analyze specimens in a transmission configuration, capturing most information from the bulk of the material instead of the surface. For the surface species to be detected, the extent of corrosion needs to be on the same order of magnitude as the bulk material, which is most feasible by employing a smaller-diameter wire.

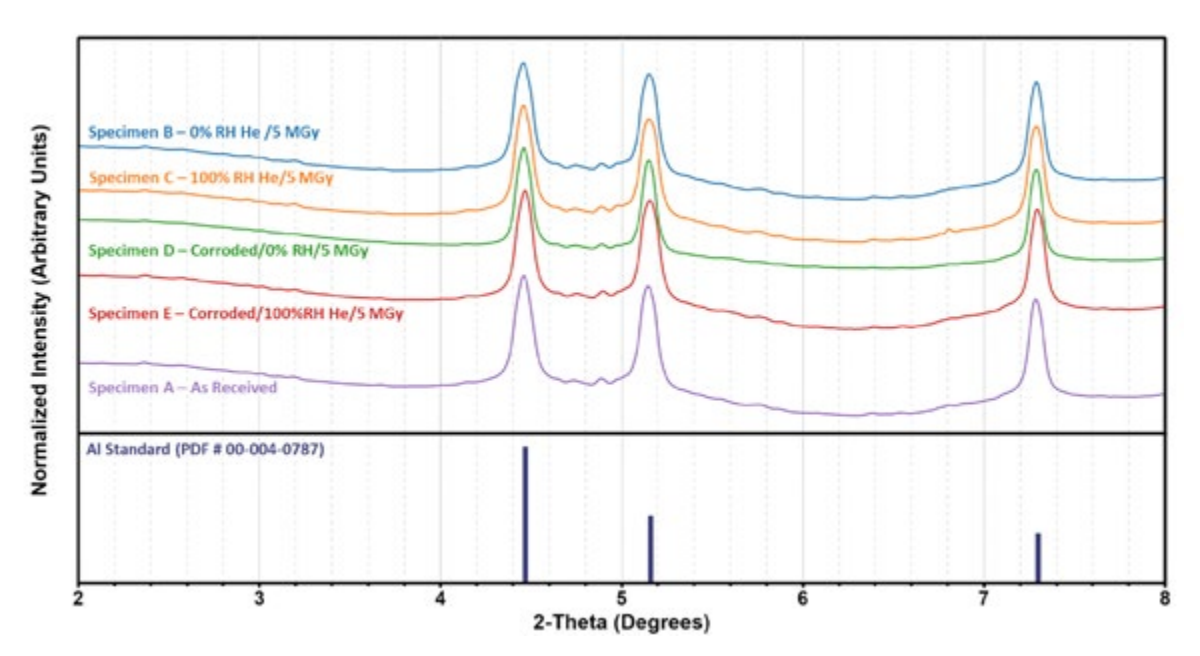


 $Figure\ 2.\ Surface\ characterization\ of\ AA\ 1100\ before\ and\ after\ exposure\ to\ synchrotron\ irradiation.$

In addition, for the purposes of in situ analysis, the minimum beamspot dimensions for real-time data acquisition at the XPD beamline have a significant impact on the ability of the incident beam to induce a radiolysis effect. While the maximum reported spot size of the XPD beamline was 0.04 cm², the corresponding flux was too weak for simultaneous data acquisition for in situ studies and to capture information from a significant portion of the sample for ex situ studies. Theoretical calculations on

the equivalent gamma-irradiation dose were based on the maximum reported spot size. The actual spot size for this study was reduced to 400×450 and 705×286 µm for the ex situ and in situ studies, respectively. Recalculating the equivalent dose from gamma irradiation yields 817 Gy, which is well below what has been reported to induce a radiolysis effect. As a result of these two factors, the ability to detect surface polymorphs (Figure 2) and induce a radiolysis effect using X-ray synchrotron data

remains inconclusive (Figure 3).
Our preliminary studies found no evidence for radiation-induced changes in corrosion layer structure although this may have been due to sample thickness and beam profile. Based on this investigation, a recommendation for follow-up investigations is to employ a quasi in situ and ex situ experimental design utilizing thinner specimens.



 $Figure \ 3. \ XRD \ patterns \ acquired \ from \ ex \ situ \ analysis \ of \ AA \ 1100 \ wires, specimen \ condition \ given \ in \ Table \ 1.$

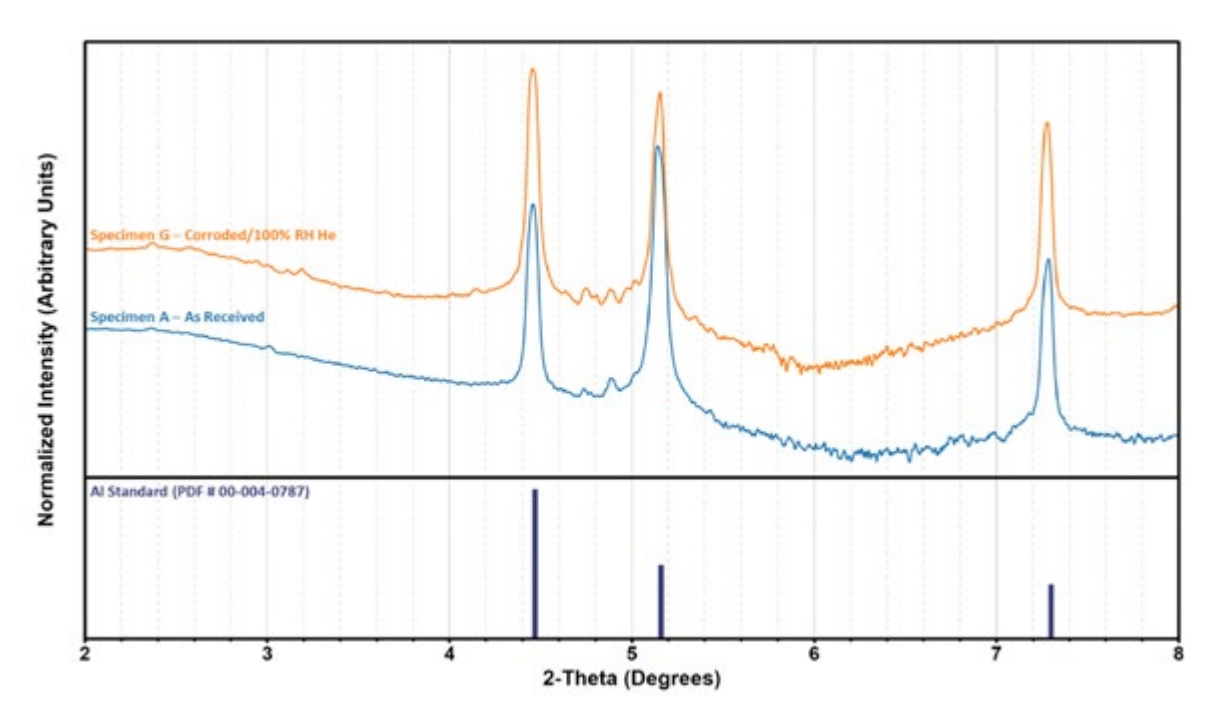


Figure 4. XRD patterns acquired from in situ analysis of AA 1100 wires, specimen condition given in Table 1.

RTE 4406: Irradiation Behavior of Nanostructured Ferritic/Martensitic Grade 91 Steel at High Dose

PI: Haiming Wen (Missouri University of Science and Technology)

Co-PI: Joshua Rittenhouse (Missouri University of Science and Technology)

Technical Leads: Gary Was (University of Michigan) and Yaoqiao Wu (CAES)

Facility: Microscopy and Characterization Suite, Center for Advanced Energy Studies; Michigan Ion Beam Laboratory, University of Michigan

Grade 91 (G91), also referred to as T91 in the form of tubing, is classified as an F-M steel. With the positive mechanical properties and improved radiation resistance that the F-M microstructure provides relative to more-traditional alloys, G91 is a prospective candidate for use in structural components in upcoming LWRs as well as a fuel-cladding material in advanced gas-cooled reactors. G91 is being investigated as a means of further improving irradiation resistance as well as the mechanical properties and bulk grain refinement including nanostructuring. The hypothesis behind such grain refinement is that grain boundaries act as effective sinks for irradiation-induced defects, and increasing the volume fraction of such sinks will allow for more-efficient absorption of defects at such boundaries.

The focus of this study was to examine the microstructural behavior of G91 with three different grain sizes under heavy dose ion irradiation at multiple temperatures. More specifically, samples of as received, CG (grain diameters > 1 μ m), ultra-fine grained (UFG, where 1 μ m > grain diameters > 100 nm), and nanocrystalline (NC, where grain diameters < 100 nm) G91 were self-ion-irradiated at the University of Michigan lon Beam Laboratory at room temperature and 300, 400, 450, and 500°C to a target dose of 200 dpa at a depth of 600 nm below the sample surface. Equal channel angular pressing was used to achieve the UFG microstructure and high-pressure torsion was used to achieve the NC microstructure.

Following irradiation, all samples irradiated at both room temperature and 450°C were sent to CAES for PIE. Characterization of the samples irradiated at the other temperatures is left for future work. In order to provide initial insight into the mechanical properties of the room-temperature and 450°C irradiated G91 samples, nanoindentation at multiple depths was performed. Nanoindentation was also performed on unirradiated CG, UFG, and NC G91 for comparison. The compiled results from nanoindentation are shown below in Table 1. It was expected that, under irradiation, hardening of the G91 would occur, especially in the CG samples, with the UFG and NC samples experiencing less hardening. Such a trend is observed in the nanoindentation data (Table 1) taken from the unirradiated samples and those irradiated at room temperature. However, with the measurements taken from the samples irradiated at 450°C and the observations of poor surface conditions made from optical micrographs of those samples, it is believed that the measured hardness of the 450°C irradiated G91 is invalid. Nonetheless, comparisons can still be made between the unirradiated samples and those irradiated at room temperature. At an indent depth of 200 nm, a distinct increase in hardness of 1.39 GPa can be seen for the irradiated CG G91. For the UFG G91, an increase in hardness of 1.26 GPa can be seen in the irradiated condition, and for the NC G91, a decrease in hardness of 0.23 GPa after irradiation at room temperature is observed. These results indicate that the NC microstructure is effective, at least from an initial

mechanical perspective, in improving irradiation resistance as a comparatively slight change in hardness is observed after irradiation. Possible explanations for the decrease in hardness after irradiation at room temperature in the NC G91 include radiation-assisted grain growth as well as the potential for martensite to transition to ferrite. Closer examination of these phenomena will be included in a planned publication.

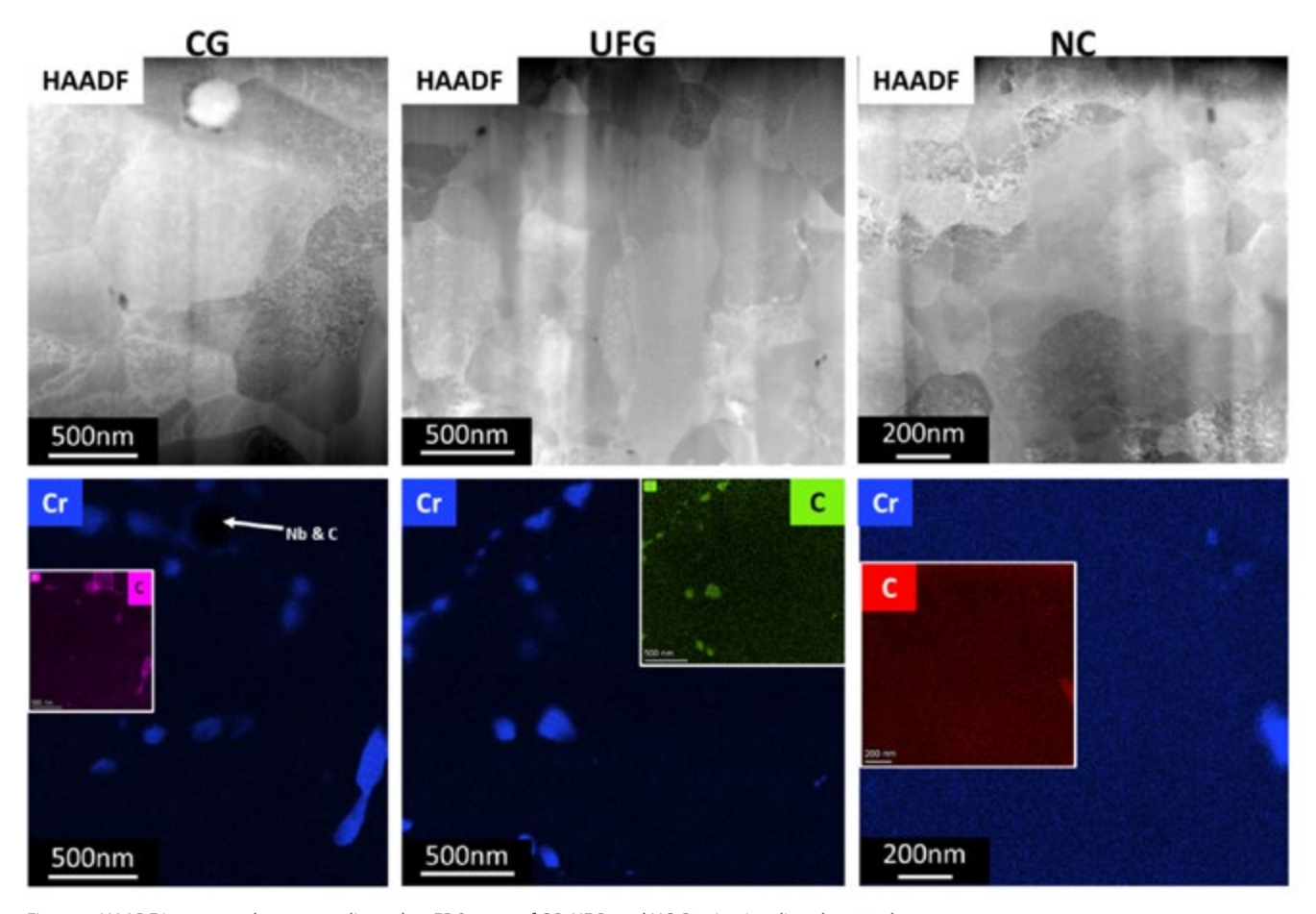
Table 1. Nanoindentation results from CG, UFG, and NC G91 ion-irradiated to 200 dpa (at a depth of 600 nm) at room temperature and 450°C as well as results from unirradiated CG, UFG, and NC G91 as a baseline

Grain Size	Depth (nm)	Average Hardness (GPa)	Condition	Grain Size	Depth (nm)	Average Hardness (GPa)	Condition	Grain Size	Depth (nm)	Average Hardness (GPa)	
CG	100	3.57		CG	100	5.23		CG	100	2.84	
	150	3.13			150	4.64			150	2.50	
	200	3.06	UFG RT 200 dpa			200	4.45			200	2.77
UFG	100	4.24		UFG	100	5.50	450°C 200 dpa	UFG	100	3.21	
	150	4.01			150	4.92			150	3.14	
	200	3.74			200	5.00			200	3.17	
NC	100	5.90		NC	100	6.89		NC	100	3.77	
	150	5.36			150	5.72			150	3.55	
	200	5.21			200	4.98			200	3.87	

After nanoindentation was performed, TEM sample preparation was performed using FIB techniques in a FEI Quanta scanning electron microscope FIB. TEM characterization of the CG, UFG, and NC G91 irradiated at room temperature and 450°C was performed in a Thermo Fisher Scientific Spectra transmission electron microscope. Characterization included TEM and HR-TEM imaging as well as SAED. BF and high-angle annular DF (HAADF) STEM images of the irradiated microstructures were also collected. Because investigation of precipitation and segregation behavior in the irradiated, grain refined G91 was a focus of this investigation, EDS scans were also performed using STEM providing high-resolution elemental maps. Examples of HAADF images and EDS elemental maps taken from the CG, UFG, and NC G91 samples irradiated at room temperature and at 450°C are shown below in Figure 1 and Figure 2, respectively. In comparing the microstructures of the samples irradiated at room temperature (Figure 1) versus those irradiated at 450°C (Figure 2), it can be seen that voids are visible in all three grain-size conditions after irradiation

at 450°C whereas no such features are visible in the room temperature irradiated conditions. Also of note, it appears that with a reduction in grain size, the reduction in density of voids indicates that grain boundaries are acting as effective sinks to vacancies stemming from irradiation damage. Large precipitates that are believed

to be chromium carbides are observed in all three grainsize conditions after irradiation at room temperature, with indication that there is a reduction in density of such precipitates in the NC condition. Quantification and more careful analysis will be included in the planned publication.



Figure~1.~HAADF~images~and~corresponding~select~EDS~maps~of~CG,~UFG,~and~NC~G91~ion~irradiated~to~200~dpa~at~room~temperature.

Along the same lines and of significant note, in the NC condition after irradiation at 450°C, formation of what are believed to be dislocation loops is prevalent. It appears that Cr precipitation and/or segregation occurs preferentially on such features. More precisely chromium carbide precipitation is not discounted as the carbon EDS map shows enrichment along these features (faintly observed in the inset shown in Figure 2), but detection of C using EDS pushes the technique's capabilities. It should also be noted that a denuded zone does appear on either side of a grain boundary where the believed dislocation loops are absent in NC G91 after irradiation

at 450°C. This would indicate that the grain boundary is acting as a sink to irradiation-induced defects. Overall, the observation that precipitation appears to be reduced in the room-temperature-irradiated NC G91 and void density also appears to decrease with decreasing grain size. This is positive evidence that grain refinement acts to improve irradiation resistance. However, the observations of such precipitation or segregation along the believed dislocation loops and the potential effects such phenomena have on material properties will require further analysis and investigation.

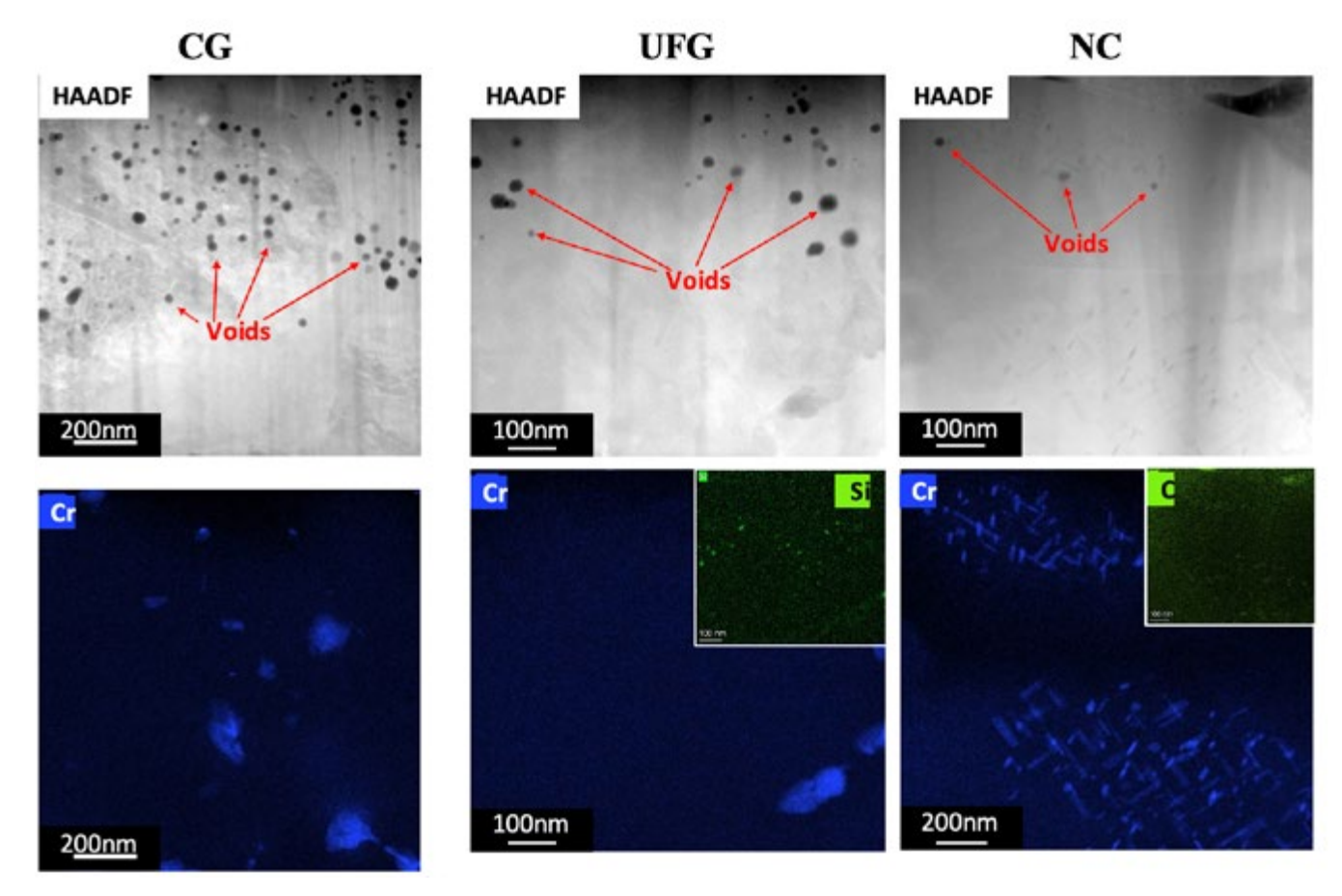


Figure 2. High-angle annular dark field images and corresponding select energy dispersive X-ray spectroscopy maps of CG, UFG, and NC G91 ion irradiated to 200 dpa at 450°C.

Another part of TEM characterization of the CG, UFG, and NC G91 irradiated at room temperature and 450°C was scanning precession electron-diffraction (ASTAR) scans were performed. ASTAR scans provide high-resolution diffraction data over the scanned area and, subsequently, provides crystallographic information. An example orientation-reliability map, as well as an inverse-pole-figure map generated using the scans from the NC G91 irradiated at room temperature is shown below as Figure 3. The data from the ASTAR scans of the

other conditions are still being processed, but the results from these scans will provide information on grain size as well as GB characteristics such as misorientation angles. Comparing grain size before and after irradiation will allow for identification and analysis of microstructural stability with regards to thermal and irradiation effects. GB characteristics are also important when considering effectiveness of sinks because of the difference in sink strength between high-angle and low-angle GBs.

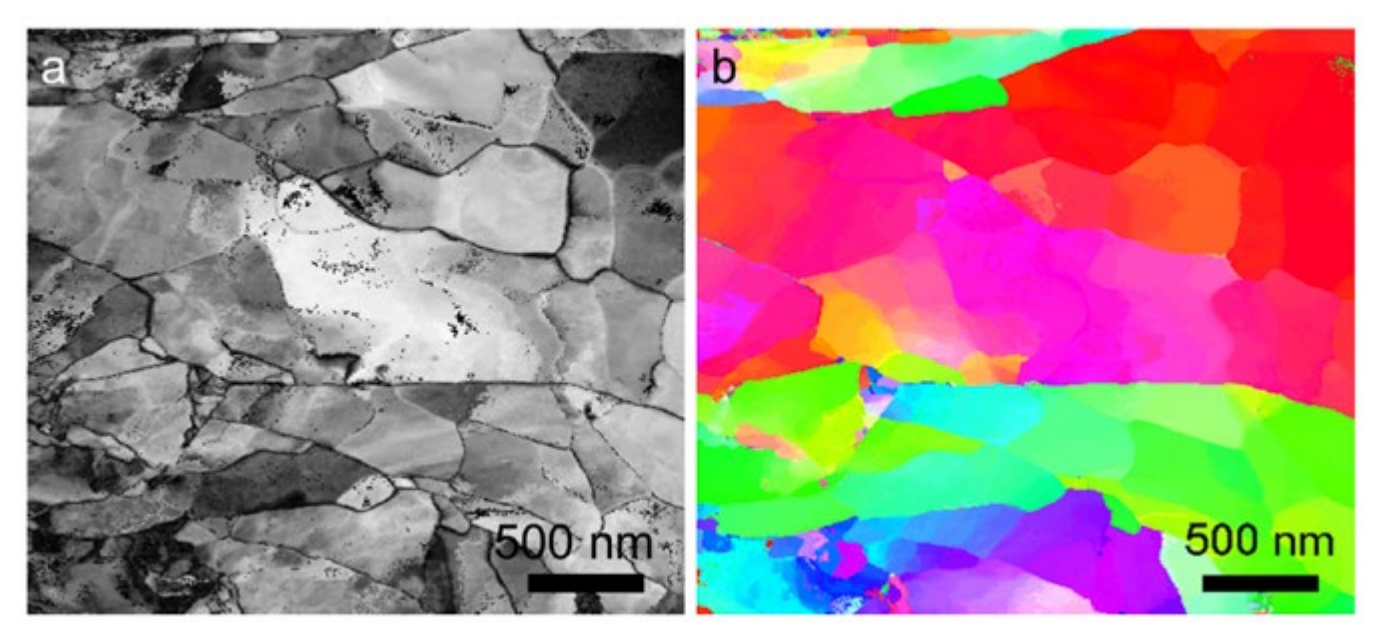


Figure 3. Orientation reliability map (a) and inverse-pole-figure map (b) as generated from an ASTAR scan of the NC G91, irradiated at room temperature.

As mentioned previously, F-M steels hold many desirable characteristics with regards to structural applications within current and advanced nuclear-reactor designs, and grain refinement within such alloys has the potential to further improve these characteristics while improving irradiation resistance. This project takes a comprehensive approach that allows comparison between grain-size, thermal, and high-irradiation-dose effects. Although irradiationinduced precipitation and segregation have been studied in traditional CG F-M alloys, comprehensive studies involving grain-size effects such as those presented here are lacking. With careful analysis of the precipitation and segregation behaviors in the grain-refined conditions using data collected, potentially positive effects on mechanical properties can be identified, and phenomena leading to negative characteristics can be discussed. This will allow further positive development of an already promising material. Identification and discussion of precipitation and/or segregation behavior, as seen along the believed dislocation loops in the NC G91 irradiated at 450°C (Figure 2), will also, for example, help direct further study into the combined effects of irradiation and corrosion on these materials.

RTE 4434: *In Situ* TEM Studies on Thermodynamic Stability and Microstructural Evolution of Zirconium Hydrides in Irradiation and Thermal Environments

C. A. Kohnert Taylor, M. A. Tunes, D. Parkison, T. S. Smith, A. P. Shivprasad, T. Saleh (LANL)

Facility: Intermediate Voltage Electron Microscopy-Tandem Facility, Argonne National Laboratory

Zirconium is the base metal of the U.S. nuclear industry, and it builds the nuclear fuel rods that are currently in operation within the technology that informed the U.S. nuclear power plant (NPP) fleet. Despite more than 70 years of NPP operations without major incidents, predicting and understanding degradation of Zr-based alloys (Zircaloy) under both in-service and severeaccident conditions remain goals of paramount importance to support the mission of two ongoing U.S. Department of Energy (DOE) research and development efforts: the Accident Tolerant Fuels (ATF) and Light Water Reactor Sustainability (LWRS) Programs. Over its lifetime, Zircaloy can be subjected to hydrogen embrittlement and reduction at high temperatures, degrading material properties. The reduction reaction of zircaloy within a hydrogen-rich environment induces the formation of ZrH within its microstructure. These hydrides are quite detrimental to the designed mechanical properties. Our understanding of the effect of irradiation on the thermal stability of these hydrides is limited and the result, at least so far, of using ex situ research methods. Therefore, this proposal sought the use of in situ transmission electron microscope ion irradiation and annealing methods available in the Intermediate Voltage Electron Microscope (IVEM) Facility at the Argonne National Laboratory (ANL) to investigate the real-time evolution of ZrH when subjected to extreme conditions.

During work at IVEM, two sets of in situ ion irradiations were conducted. One set used 10-keV helium to study bubble formation and growth over time at different temperatures. The second set of experiments used 1-MeV krypton ions to determine phase stability and radiation tolerance as a function of dose and temperature. Ten kiloelectron volt He was implanted at room temperature and 200 and 400°C in order to determine the effect of temperature on bubble formation and time. A fluence of 1×10^{17} ions/cm² was implanted into each foil over the course of approximately 4 hours. The total irradiation times were adjusted according to He-beam stability. Analysis of these data is still ongoing.

Kr ions at 1 MeV were used to irradiate the d-ZrH foils to a dose of approximately 7 dpa, as determined by SRIM. The high energy of these ions ensured that implantation of Kr into the foil was negligible. SAED was done in multigrain regions to determine the phase stability of the hydrides as a function of

temperature and dose. Tests were conducted at room temperature, 200, and 400°C. A test was attempted at 600°C, but the sample underwent a phase change caused by thermal desorption of hydrogen. This experiment was then used to compare thermal desorption to possible irradiation-induced desorption.

The room temperature sample was found to show no phase instability under irradiation. Accumulation of black-spot damage was seen over the course of the test, but it was not quantified. The 200 and 400°C samples were found to have a phase transformation at the end of the irradiation period. However, unlike the thermal-desorption sample, which partially transformed into the hcp α zirconium phase, the irradiated samples have instead been transformed into the bcc high-temperature β phase, despite being significantly below the $\alpha \rightarrow \beta$ phase-transition temperature of approximately 550°C.

Figure 1 compares the Δ foil after irradiation at 400°C to the foil after thermal desorption using a SAED. Lower index rings are labeled in the figure, and the different phases

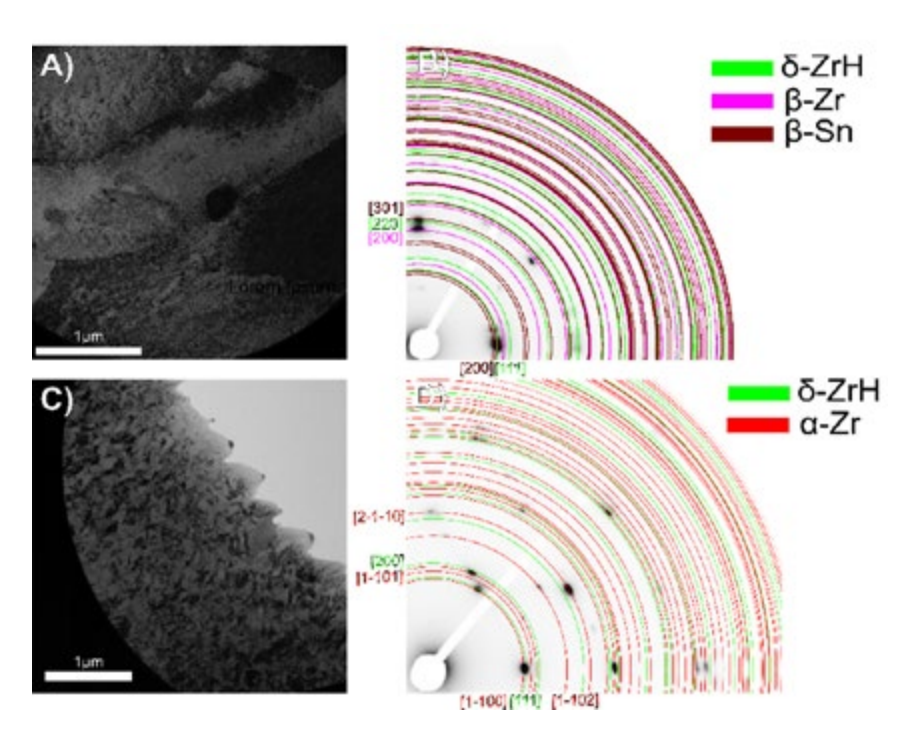


Figure 1. (A) BF image after the 400°C irradiation, showing an image of the area selected by the selected area aperture. (B) The resulting diffraction pattern with the prominent phases overlaid. (C) BF image after the attempted 600°C anneal, showing the image of the area selected by the selected area aperture. (D) The resulting diffraction pattern with the prominent phases overlaid.

are differentiated by color. β -Sn is from the precipitant. The peaks that do not fit to the listed phases are suspected to be a monoclinic ZrO_2 phase. These rings have been omitted for clarity. This result is contrasted to the micrograph and diffraction pattern shown in C and D of the hydrogen desorption caused purely by temperature.

Potential impact to the state of knowledge includes the fact that zirconium hydrides are present in reactor cladding and under consideration for use as moderating materials in both microreactors and space reactors. In each of these applications, the hydrides will undergo radiation damage. The impact of radiation damage on phase stability and hydrogen release is currently unknown. To the best of our knowledge, this is the first attempt to quantify the effect of radiation damage on phase stability and hydrogen release in bulk zirconium hydride. Ion irradiation results help provide some fundamental understanding of results from ongoing neutron-irradiation studies.

RTE 4453: Effect of Neutron Irradiation on the Microstructure of NF616 (Grade 92) as a Function of Dose and Temperature

PI: Indrajit Charit (University of Idaho)

Co-Pls: Ramprashad Prabhakaran and Dan Edwards (PNNL), Kumar Sridharan (University of Wisconsin-Madison)

Facility: Materials Science and Technology Laboratory, Pacific Northwest National Laboratory

Introduction

F-M steels are being considered as candidate in-core structural materials for fast reactors and advanced LWRs due to their excellent resistance to radiation-induced void swelling, microstructural stability, thermal conductivity, and superior irradiation-creep properties. NF616 (Grade 92) is being considered for nuclear applications due to its greater strength, which tends to provide greater safety margins and design flexibility and lower cost of reactor components. Although elevated-temperature mechanical properties favor NF616, neutron-irradiation data are limited when compared to HT-9. Hence, it is necessary to conduct systematic investigations on the mechanical behavior and microstructure of NF616 over a wide range of doses and temperatures. As a part of the UW-Madison Nuclear Science User Facilities (NSUF) Pilot Irradiation Experiment (led by Dr. Kumar Sridharan, Co-PI of this RTE project), NF616 was neutron irradiated in the Advanced Test Reactor (ATR) at various temperatures and doses.

Project Objectives

The objective of RTE Project 4454 is to understand the effect of neutron irradiation on the microstructure of NF616 as a function of irradiation temperature (388–469°C) and dose (3–8 dpa). and electron backscatter diffraction (EBSD) were used to evaluate control and irradiated samples and determine the general grain structure, prior austenite grain size, martensite packet, lath structure, primary carbide structure, and failure mode (fractography) as a function of irradiation doses and temperatures because these parameters can significantly affect the mechanical behavior and radiation resistance of NF616.

Tables 1 and 2 show the chemical composition and heat treatment performed on NF616. Table 3 shows the summary of ATR neutron-irradiated NF616 samples that were studied at Pacific Northwest National Laboratory (PNNL) under this RTE award.

Table 1. Chemical composition of NF616 heats (weight %).

Alloy/heat	Cr	C	Si	Mn	W	V	Мо	Ni	Others; Fe: balance
NF616 Jaea	8.82	0.11	0.10	0.45	1.87	0.19	0.47	0.17	N 0.047; AI 0.005; P 0.012; S 0.003 O 0.004; Nb 0.064; B 0.0017

Table 2. Heat treatment performed on NF616.

Alloy (heat/supplier)	Heat Treatment (Normalizing and Tempering); AC: air cooling
NF616 (JAEA)	1070°C/120 minutes/AC; 770°C/120 minutes/AC

NOTE: AC: Air cooling

Table 3. Summary of ATR neutron-irradiated samples studied under this RTE award.

Alloy/ heat	ID	Irradiation Temp. (°C)	Dose (dpa)	Tensile Test [†] Temp. (°C)	VickersMicro- hardness Tested [†]	Fractography	SEM	EBSD
	NF-SP1	_	_	RT	RT	✓	✓	✓
	NF-SP2	_	_	292	_	✓	_	_
	NF-SP3	_	_	388	_	✓	_	_
	NF-SP4	_	_	452	_	✓	_	_
	KGT 407	388	4.1	RT	RT	✓	_	✓
NF616	KGT 1588	388	4.1	388	RT	✓	_	_
JAEA	KGT 3507	452	3.9	RT	RT	✓	_	✓
	KGT 3508	452	3.9	452	RT	✓	_	_
	KGT 3509*	448	4.8	N/A	RT	N/A	✓	_
	KGT 3510*	430	7.7	N/A	RT	N/A	✓	✓
	KGT 3511*	450	3.0	N/A	RT	N/A	✓	✓
	KGT 867*	469	4.3	N/A	RT	N/A	✓	✓

NOTES:

^{*} TEM disc

[†] Tensile and microhardness testing was performed under a different RTE award (#2879; PI: Ramprashad Prabhakaran)

Research Work

Materials

NF616 tensile and TEM samples (see Table 3) that were neutron irradiated in the ATR were used for this study. The control samples were available at PNNL. The actual irradiation temperatures and doses are listed in Table 3. PNNL received these irradiated samples earlier and obtained mechanical properties (tensile and microhardness testing) of NF616 as a function of irradiation temperature and dose under funded RTE Project 2879 (PI: Ramprashad Prabhakaran, PNNL). Failed/tested (control and irradiated) tensile specimen shoulders and TEM discs were available at PNNL for this study.

PIE

Under this RTE (Project 4453), microstructural (SEM, fractography, and EBSD) characterization of control and neutron irradiated NF616 samples were performed at PNNL, a partner NSUF facility with well-established capabilities for performing microstructural studies.

Task 1: SEM fractography on tensile-tested NF616 samples: efforts were made to identify tested tensile specimens in the PNNL Radiochemical Processing Laboratory modular hot cell. Dose rates and smear information were obtained, and these were moved out to the Radiochemical Processing Laboratory microscopy suite. SEM fractography was performed on tensile-tested samples to determine the mode of

failure, as shown in Table 3. A few representative images obtained from neutron-irradiated NF616 sample are shown in Figure 1.

Task 2: Preparation of SEM/EBSD specimens from tested NF616 tensile samples and TEM discs: a low-speed saw was earlier employed to section small samples from the shoulders of previously tensile-tested specimens (where there is no deformation). These sections along with TEM discs, were polished to a 1-µm finish, and microhardness testing was performed at PNNL earlier, under a RTE Project 2879 (PI: Ramprashad Prabhakaran). As a part of RTE Project 4453, vibratory polishing (colloidal silica) was performed on the samples for SEM and EBSD studies, as shown in Table 3.

Task 3: SEM/EBSD studies on (control and neutron irradiated) NF616 samples: SEM/EBSD was used to evaluate control and irradiated NF616 to determine the general grain structure, prior austenite grain size, martensite packet, lath structure and primary carbide structure (inter- and intra-lath precipitation of carbides). EDS was used to map the carbide distributions and observe local microchemical variations. SEM-EBSD images were obtained to provide a quantitative measurement of the prior austenite grain size, high-angle GBs and martensitic laths. A few representative SEM and EBSD images obtained from neutron-irradiated NF616 samples are shown in Figures 2 and 3.

Ongoing Work After the Completion of the RTE Project

Image-analysis techniques are employed to evaluate the prior austenite grain size, and sizes and fraction of the carbides. EBSD data-analysis software is also used to determine the prior austenite grain size and martensitic-lath width and to obtain information related to the texture.

Currently, efforts to comprehensively understand the effects of radiation damage on NF616 at LWR and fast-reactor relevant temperatures and to develop appropriate structure-properties-temperaturedose correlations are ongoing. The microstructural information obtained from RTE 4453, along with mechanical characterization performed under RTE Project 2879 (PI: Ramprashad Prabhakaran) will aid an understanding the effect of neutron irradiation as a function of irradiation temperature and dose. The information obtained from these RTE studies could be extended beyond NF616, and it would be relevant to many F-M steels.

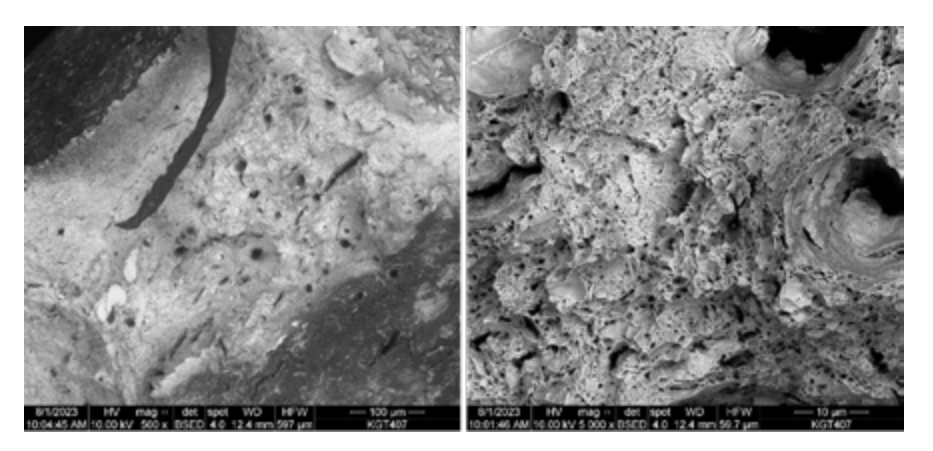


Figure 1. SEM fractography: fracture face of the tensile-tested (room-temperature) neutron-irradiated NF616 Specimen KGT 407 (388°C; 4.1 dpa).

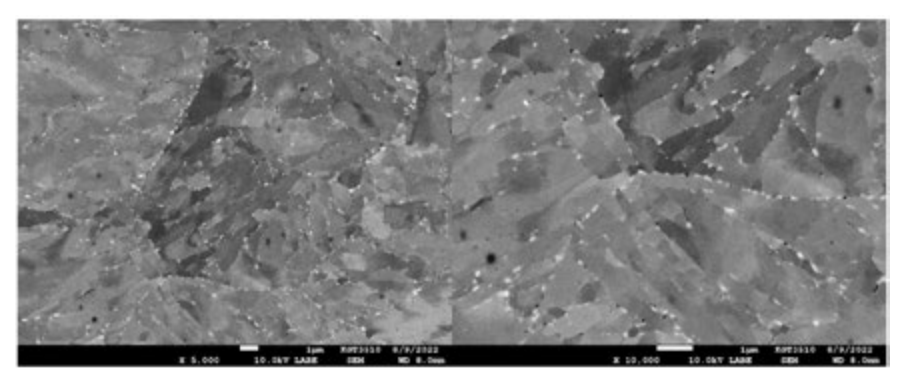


Figure 2. SEM fractography: neutron irradiated NF616; KGT 3510 (430°C; 7.7 dpa).

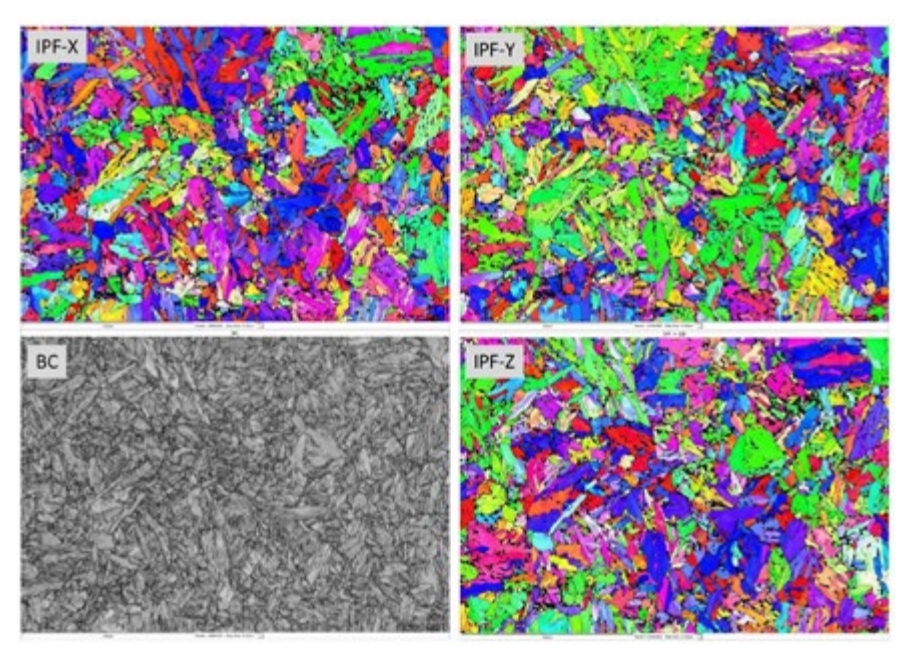


Figure 3. EBSD data obtained from NF616.

RTE 4476: Probing the Effect of Specific Chemical Elements on the Irradiation-Induced Defects Formation and Evolution in High-Entropy Alloys

PI: Djamel Kaoumi, North Carolina State University (NCSU)

Collaborator: Lucia Rebeca Gomez Hurtado (NCSU)

Facility: Intermediate Voltage Electron Microscopy-Tandem Facility, Argonne

National Laboratory

Materials and Methods

Alloy Synthesis

Tables 1 and 2 list the elemental compositions of the two different classes of HEAs that were analyzed in this work (with compositions given in wt%). To process the material, high-purity powders were milled together cryogenically. The bulk specimens were prepared via spark-plasma sintering (SPS). The SPS process was performed under vacuum after first purging in an inert atmosphere (He) and used up to 10000-A current and 1000-kN force. Each composition was added to a graphite die under a dry environment for which the moisture content was controlled to less than 20% relative humidity. The die and sintering set were then ambiently cooled to room temperature naturally with no quenching or control of cooling rate. The 40-MPa load was held for the entire sintering run until the die temperature dropped to under 100°C (~50 min in total).

Table 1. Composition of Mo-Nb-Ti series of alloys (wt%).

Alloy	Мо	Nb	Ti	Zr	V	Cr
MoNbTi	40.53	39.25	20.22	_	_	
MoNbTiZr	29.26	28.33	14.6	27.82	_	_
MoNbTiZrV	25.32	12.63	12.63	24.08	13.44	_
MoNbTiCrV	28.25	27.35	14.09	_	15.00	15.31

Table 2. Composition of Fe-Cr-Ni series of alloys (wt%).

Alloy	Fe	Cr	Ni	Mn	Cu	Al
FeCrNiMn	25.22	23.48	26.50	24.81	_	_
Al _{0.3} FeCrNiMn	24.33	22.65	25.57	23.93	_	3.53
Al _{0.8} FeCrNiMn	22.48	20.93	23.62	22.11	_	10.86
Al _{0.3} FeCrNiCu	23.45	21.83	24.83	_	26.68	3.4
Al _{0.8} FeCrNiCu	21.72	20.23	22.83	_	24.72	10.5

Sample Preparation and Transmission Electron Microscopy

The fabricated specimens were mechanically polished and lift-out samples were prepared using a FIB with an FEI Quanta 3-D FEG dual-beam scanning electron microscope. TEM characterization was done with an FEI Talos 200X transmission electron microscope to obtain HAADF images, SAED patterns, and chemical analysis through STEM and EDS.

In situ Irradiation

The samples were irradiated at the IVEM Tandem Facility at ANL. The micrographs obtained during the irradiation experiments were tilted 15 degrees with respect to the ion beam to ensure the samples were exposed to both the ion and electron beams while the pre- and post-characterization was performed at 0-degree tilt. The samples were irradiated with 1-MeV Kr⁺ ions at room temperature and at 300°C for FeCrNi based alloys and at 500°C for MoNbTi-based alloys.

The counts to reach 1 dpa were calculated using SRIM simulations assuming 40 eV as the displacement threshold energy for all elements of the alloy. The maximum dose reached was 10 dpa for all samples. Table 3 lists the details of the irradiation experiments carried out on the HEA samples.

Table 3. Details of the irradiation experiments carried out on the HEA samples.

Irradiation Temperature	Maximum Dose
Room Temperature	10 dpa
	Room Temperature

Results

RT Irradiation of FeCrNi HEA Series

RT irradiation of FeCrNiMn alloy

TEM-BF images captured during in situ irradiation of the matrix region of CrFeMnNi alloy up to 10 dpa are given in Figure 1. No significant microstructural changes happened throughout the irradiation process. This observation shows the resistance of this alloy to irradiation, even up to a high dose of 10 dpa. Respective pre- and post-irradiation microstructural and microchemical analyses of this region, as shown in Figure 2 (a and b) reveals that no elemental segregation took place due to irradiation. This shows this alloy's resistance to RIP or RIS. Additionally, no void or cavity formed, proving this alloy's irradiation stability. Comparison of pre- and post-irradiation selective area diffraction (SAD) analysis (Figures 2 [a and b], respectively) confirms fcc structure of the matrix without the existence of any secondary reflection spots or streaks, proving the alloy's stability against irradiation-induced ordering or precipitation.

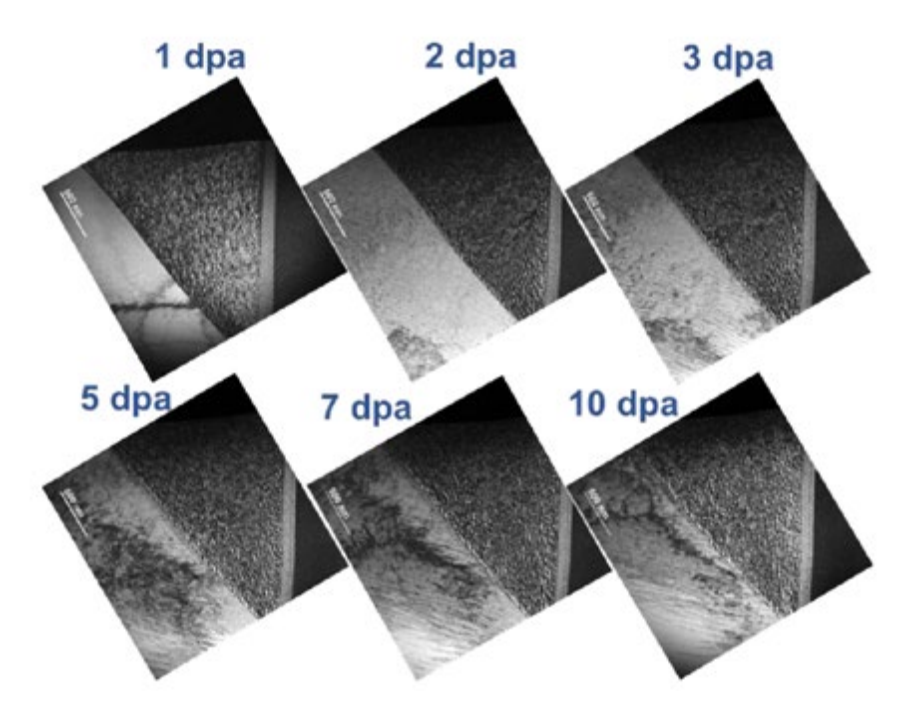


Figure 1. Irradiation at room temperature of matrix region of CrFeMnNi showing microstructural stability during irradiation up to 10 dpa.

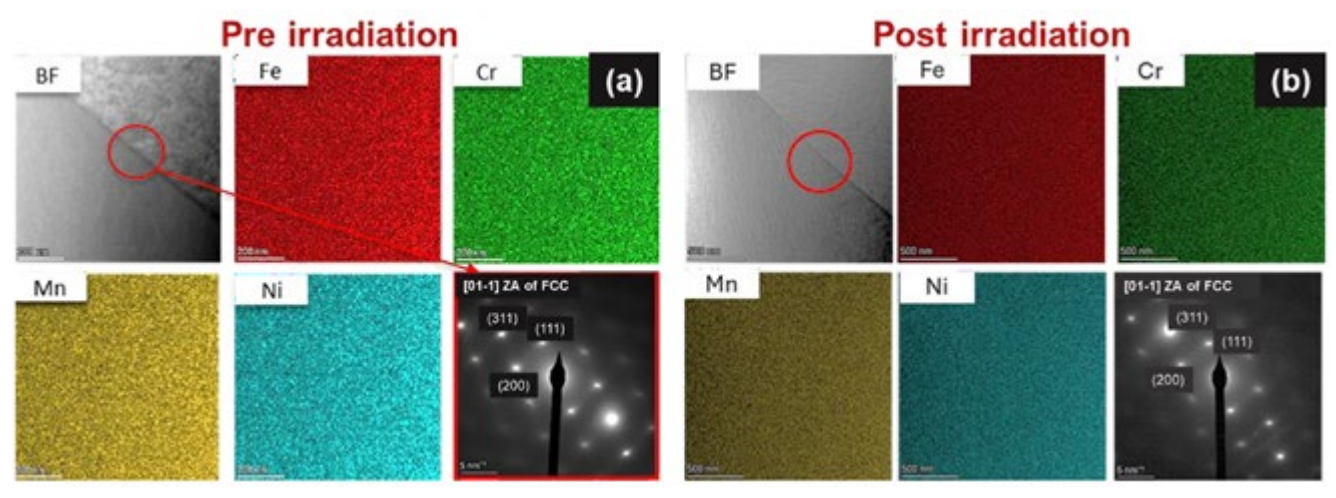
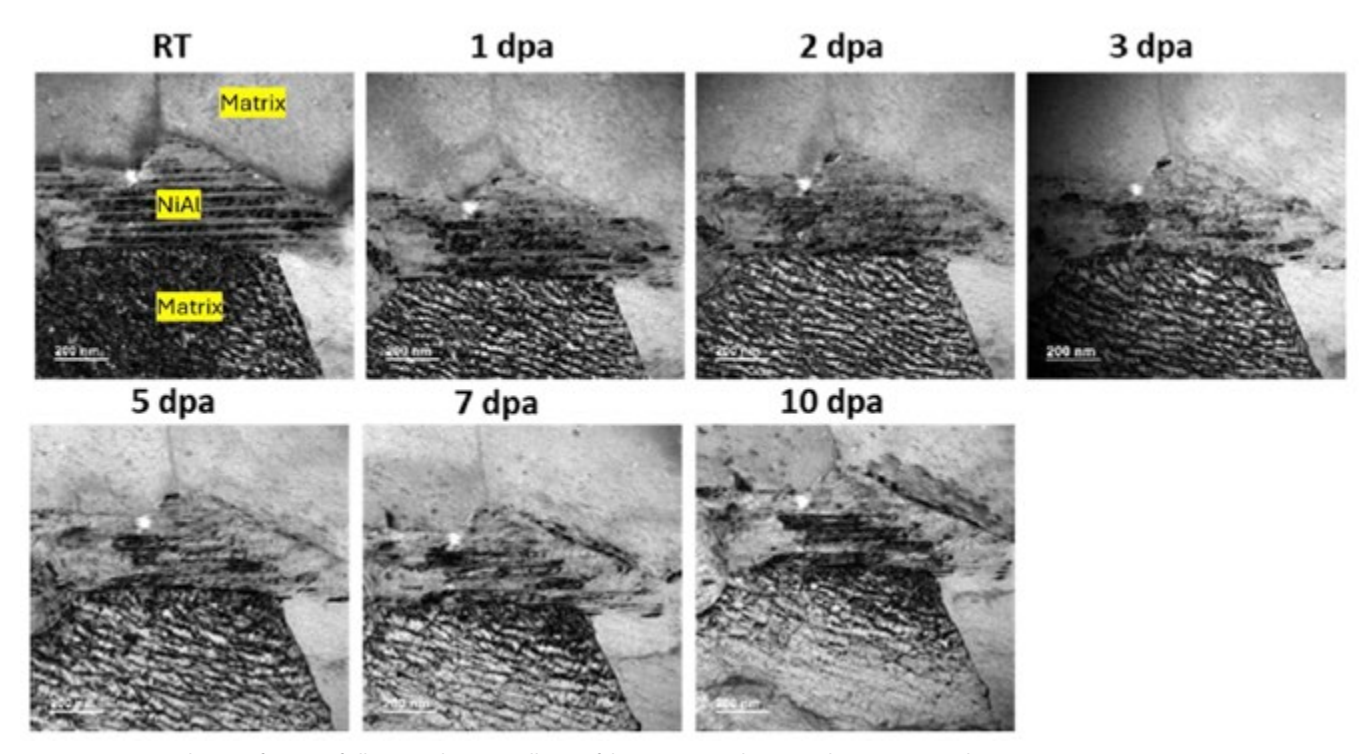


Figure 2. (a) Pre- and (b) post-irradiation characterization of CrFeMnNi alloy (region in Figure 8. showing no change in the distribution of elements and crystal structure post irradiation.

RT Irradiation of Al_{0.3}FeCrNiMn Alloy

Figure 3 shows the microstructural changes during irradiation of a region containing both a matrix and a Ni-rich phase with lot of twins in the Al_{0.3}CrFeMnNi alloy. It is interesting to note that the matrix shows no difference in microstructural features although it is irradiated to higher doses, which shows this phase's stability against irradiation-induced defects, voids, or precipitation. On the other hand, it can be clearly seen that as the irradiation dose increases, the twins in the NiMnAl phase start collapsing and become completely distorted at 10 dpa. Before irradiation, the edges defining the twins are sharp; however, as the sample is irradiated to higher doses, defects appear to diffuse into the twinning geometries, which ultimately collapse within the grain. This results in the gradual disappearance of the linear edges at the twin boundaries and the formation of defect clusters within the grain. Post-irradiation characterization of this area is shown in Figure 4, along with the chemical maps. The structure hosting the distorted twin boundaries was confirmed to be rich in NiMnAl. One explanation for this phenomenon is that the ion bombardment that the alloy was exposed to provided sufficient energy to displace the atoms, resulting in the lattice strain required for the mobilization of dislocations that annihilated the ordered twin boundaries in the Ni-rich grain.



Figure~3.~In~situ~irradiation~of~Area~5~of~alloy~B18, showing~collapse~of~the~microtwins~due~to~irradiation~up~to~10~dpa.

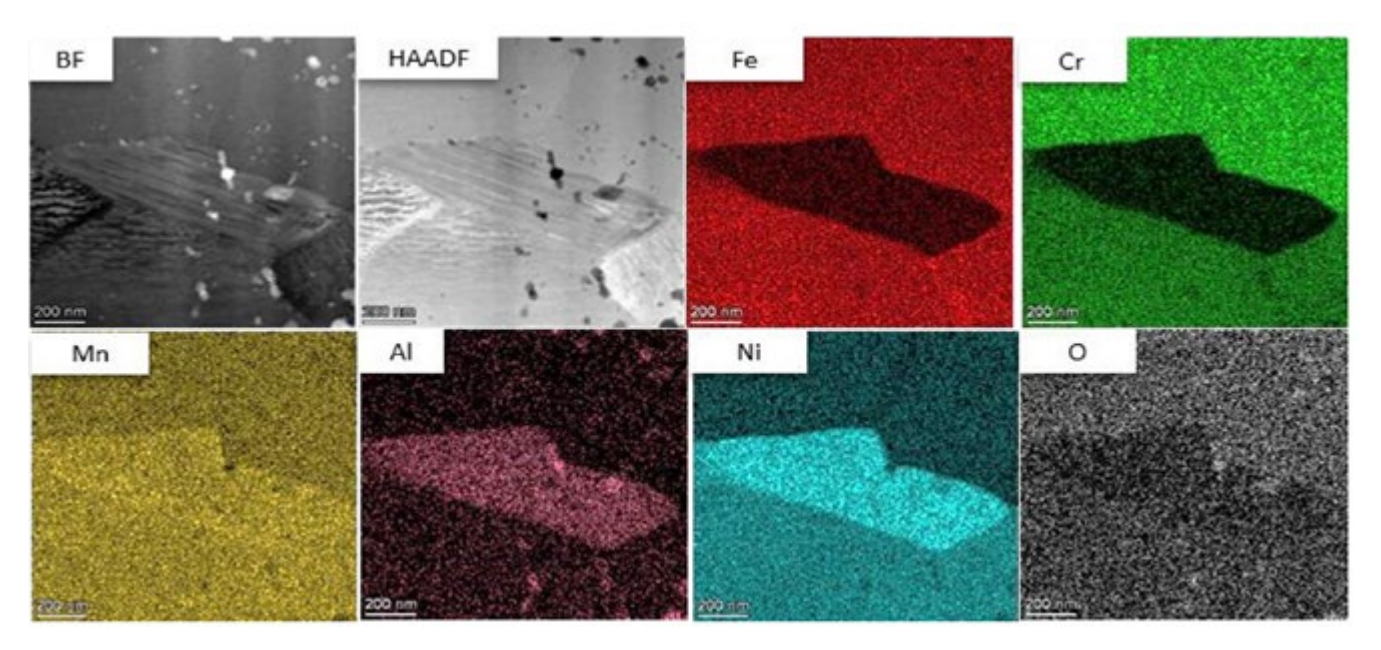
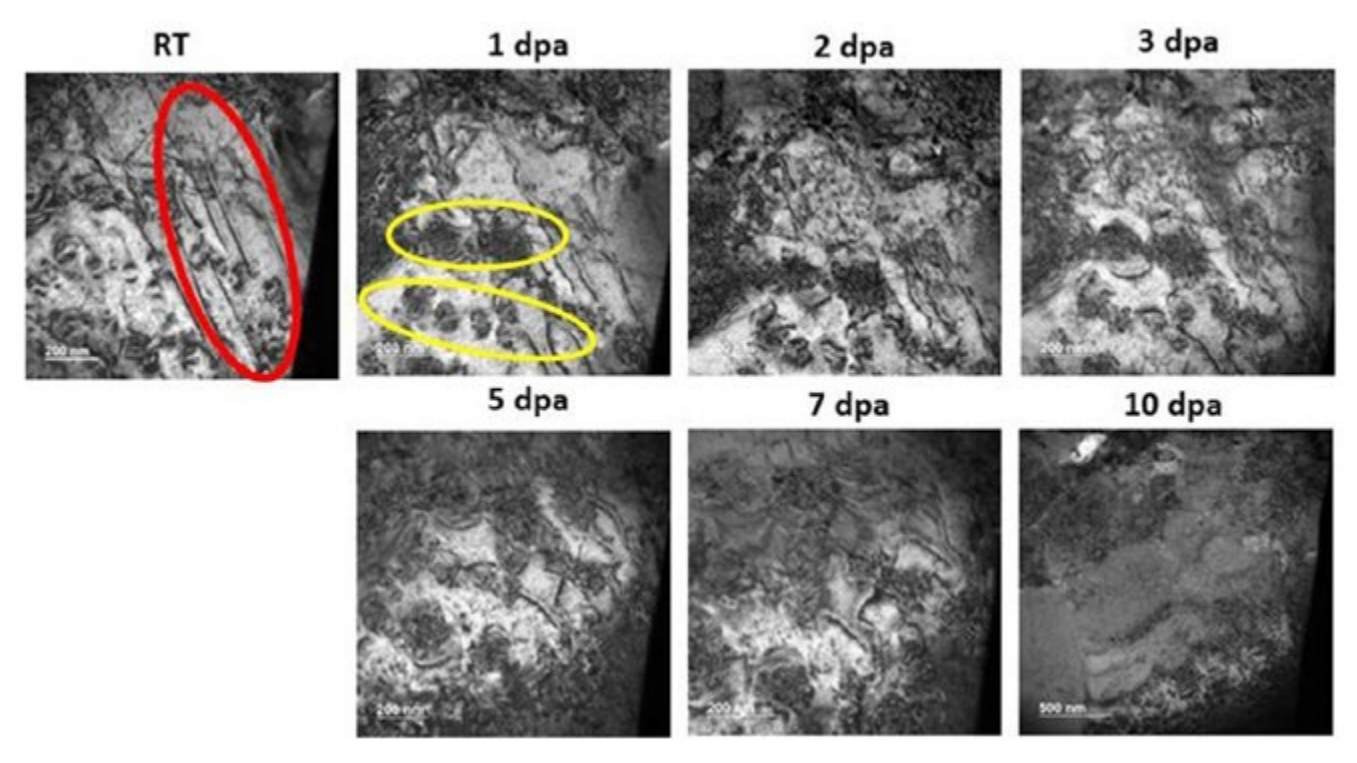


Figure 4. Post-irradiation characterization of Alloy B18, showing no change in microchemistry of phases before and after irradiation.

RT Irradiation of Al_{0.8}CrFeMnNi

In situ irradiation observations of matrix of Al_{0.8}CrFeMnNi alloy are shown in Figure 5 from 0 to 10 dpa. This region contains some line dislocations (marked in red) prior to irradiation. With increased irradiation dose, these dislocations seems to gradually disappear at 10 dpa, at which point the BF image shows a clear grain microstructure, devoid of defects. In this case, dislocation climb happens even at room temperature due to irradiation, which provides sufficient energy for the dislocation motion and ultimate annihilation at the surface. Figure 6 presents the post-irradiation characterization of this region along with the chemical maps of the alloy's constituent elements. The region shows the presence of a FeCrMn-rich matrix along with a phase rich in Ni and Al and precipitates rich in Ni and Al as well. In addition, the dislocations that were present prior to irradiation and the RIDs were not observed during post-irradiation characterization, indicating their annihilation at higher doses. However, the chemistry of the phases remains the same before and after irradiation, as is consistent with the previous two alloys.



 $Figure \ 5. \ In \ situ\ irradiation\ of\ matrix\ of\ Al0.8 Cr FeMnNi\ alloy, showing\ annihilation\ of\ the\ dislocations\ at\ 10\ dpa.$

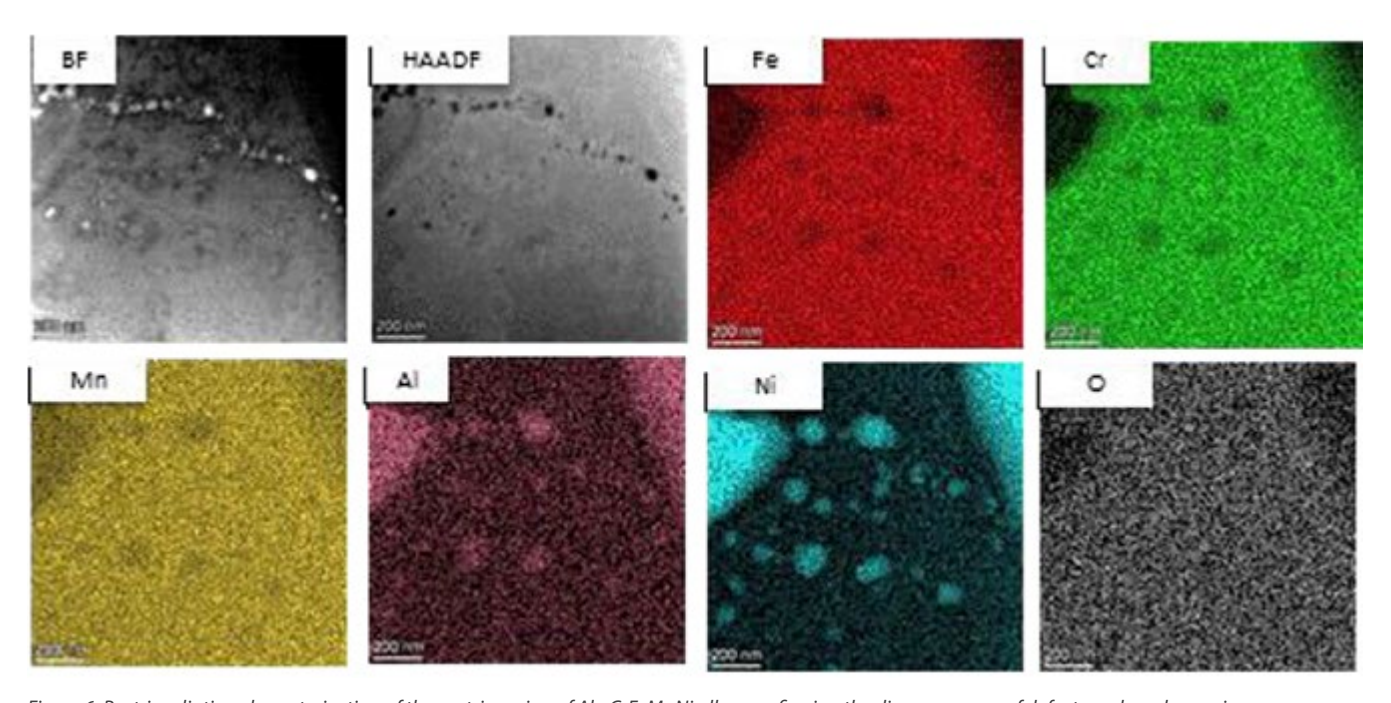


Figure 6. Post-irradiation characterization of the matrix region of $Al_{0.8}$ CrFeMnNi alloy, confirming the disappearance of defects and no change in microchemistry before and after irradiation.

RT Irradiation of Alo,3 FeCrNiCu Alloy

The in situ irradiation micrographs from 0 to 10 dpa of the matrix region given as Figure 7 show almost no change in the microstructural features during irradiation. Figure 8 (a and d) depicts the respective pre- and post-irradiation characterization of Al_{0.3}CrFeNiCu alloy, with elemental distribution maps that show uniform distribution of elements throughout the matrix. No difference in chemical behavior of elements was observed after irradiation. Figure 8 (b and c) shows the pre-irradiation BF image and the corresponding SAD pattern, respectively, which confirms fcc structure of the matrix. However, the post-irradiation SAD analysis given in Figure 8 (f) shows some evidence for ordering in the matrix due to irradiation. This can be seen as minor spots decorating the major diffraction points with hexagonal symmetry. The matrix structure, however, is still fcc with similar lattice parameter along [3-2-3] zone axis.

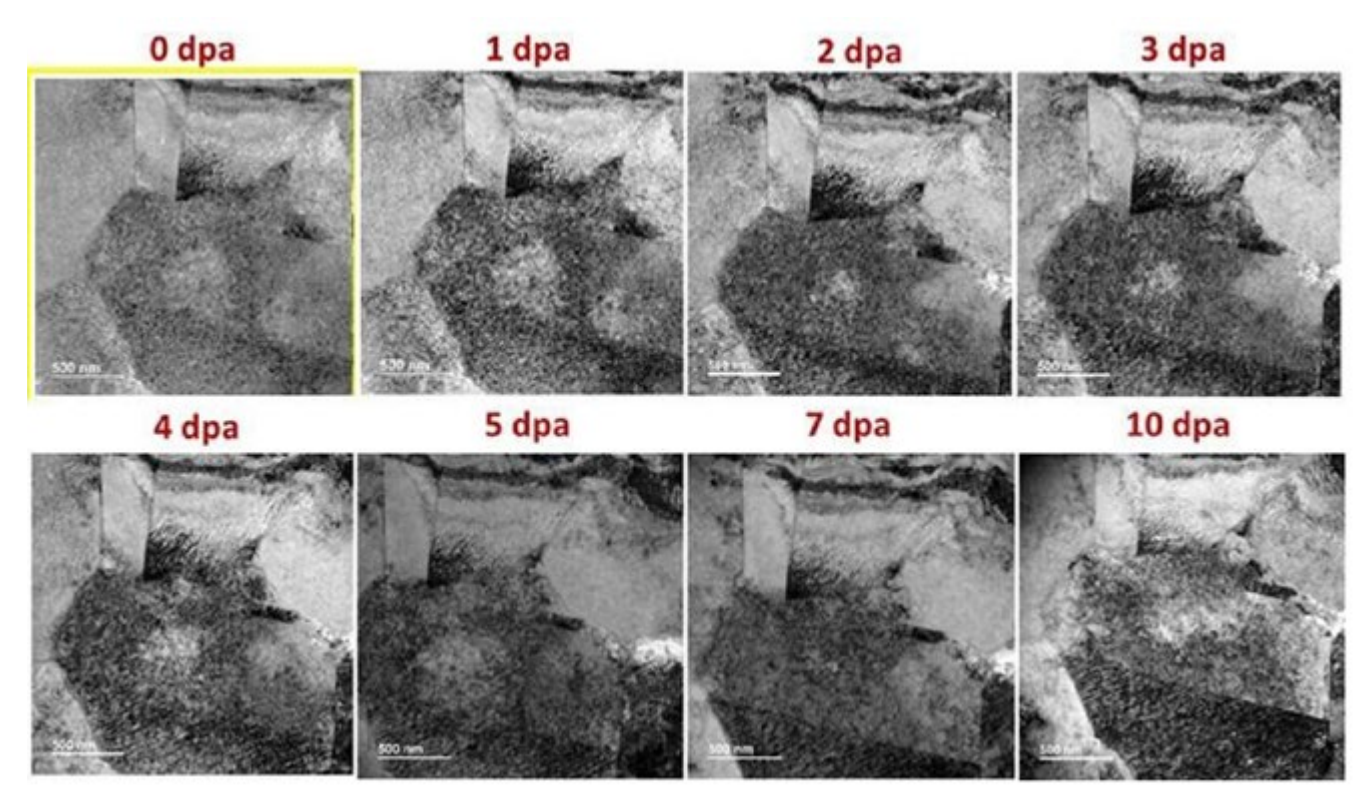


Figure 7. The in situ irradiation micrographs from 0 to 10 dpa of the matrix region of $Al_{0.3}$ CrFeCuNi alloy.

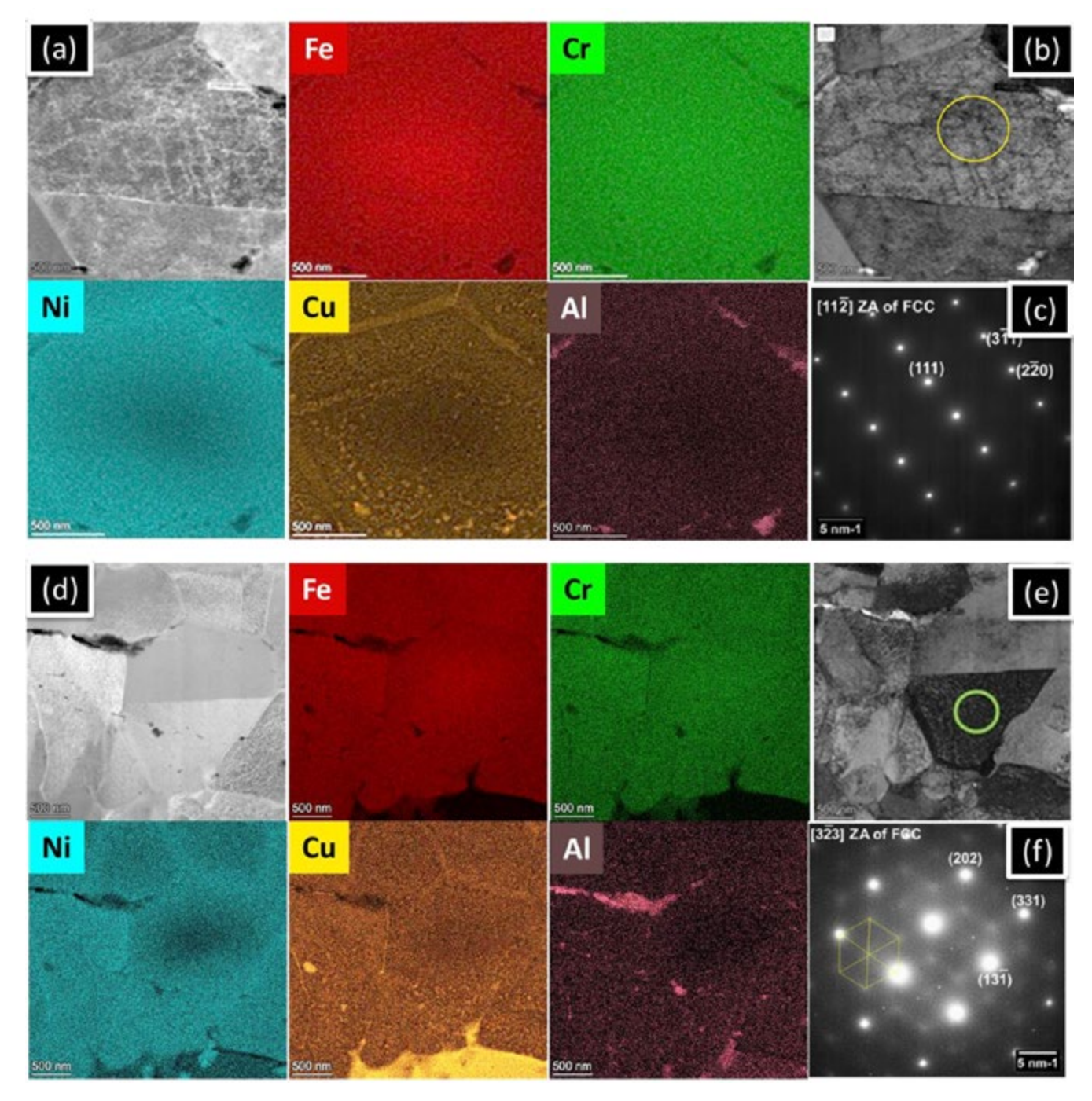


Figure 8. Post-irradiation elemental maps of $Al_{0.3}$ CrFeCuNi alloy, showing uniform distribution of elements throughout the matrix (similar to that seen in pre-irradiation); (b) pre-irradiation SAD analysis of the matrix showing fcc structure without any evidence of short-range order (SRO); (c) post-irradiation SAD analysis of the matrix showing fcc structure and evidence of SRO as minor spots decorating the major diffraction spots with hexagonal symmetry.

The in situ irradiation micrographs of the Cu-rich phase of $Al_{0.3}$ CrFeCuNi alloy, from 0 to 10 dpa, is given in Figure 9. The figure shows no change with increasing dose except for some contrast change from 5 dpa, which may be due to bending of the foil during irradiation. Figure 10 (a) shows the post-irradiation STEM-EDS characterization that reveals Cu enrichment in the grain along with the surrounding matrix. The post-irradiation SAD analysis of the Cu-rich phase in Figure 10 (b) shows that structure of this phase is still ordered fcc ($Cu_{2.9}Ni_{0.1}$)Al similar to that of pre-irradiation.

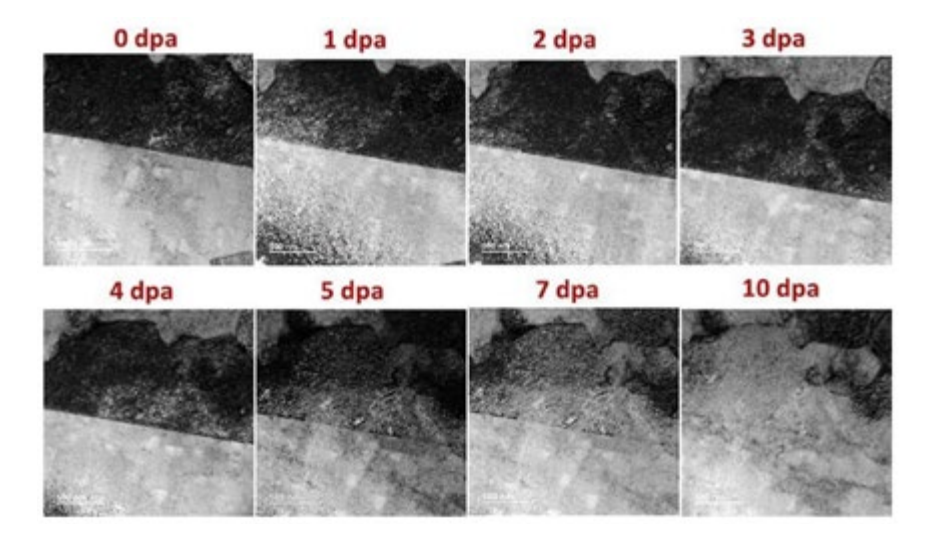


Figure 9. BF micrographs of the Cu-rich phase of $Al_{0.3}$ CrFeCuNi alloy during in situ irradiation from 0 to 10 dpa, showing no change in the microstructural features.

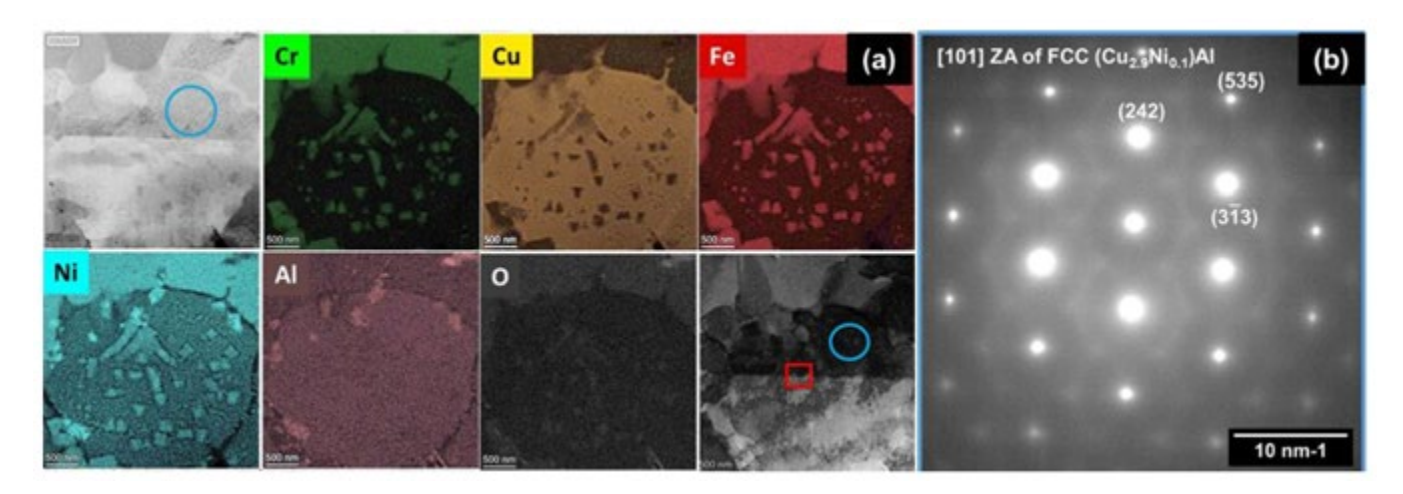


Figure 10. (a) Post-irradiation STEM-EDS characterization of Cu-rich phase of $Al_{0.3}$ CrFeCuNi alloy showing Cu enrichment in the grain along with equidistribution of elements in the surrounding matrix; (b) post-irradiation SAD analysis of the Cu-rich phase confirming (Cu_{2.9}Ni_{0.1})Al phase with ordered fcc structure; room-temperature irradiation behavior of $Al_{0.9}$ CrFeNiCu alloy.

Figure 11 shows the room-temperature in situ irradiation micrographs from 0 to 10 dpa of matrix phase of Al0.8CrCuFeNi alloy. As can be seen from the figure, absolutely no change in contrast of the images is seen from 0 to 10 dpa. This shows the stability of the matrix towards irradiation-induced loop formation and RIP. The pre- and post-irradiation characterization of the matrix of Al_{0.8}CrFeNiCu alloy is given in Figure 12. The pre-irradiation characterization shows uniform distribution of elements with fcc structure, as can be seen in Figure 12 (a–c). The post-irradiation STEM-EDS characterization of this region is shown in Figure 12 (d), which shows uniform distribution of elements throughout the matrix, similar to that of pre-irradiation, This shows its resistance towards RIS. The post-irradiation BF micrograph (Figure 12 [e]) shows no formation of voids. The corresponding SAD pattern in Figure 14 (b) shows only the major spots of bcc phase along [3-3-1] ZA, with no evidence of SRO after irradiation with the absence of minor spots or streaks.

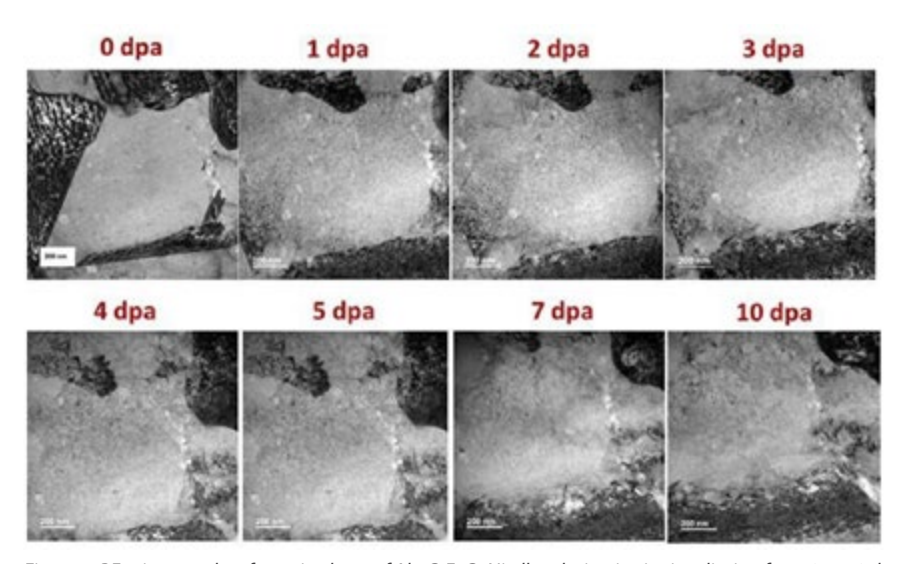


Figure 1. BF micrographs of matrix phase of Alos CrFeCuNi alloy during in situ irradiation from 0 to 10 dpa showing no change in the microstructural features.

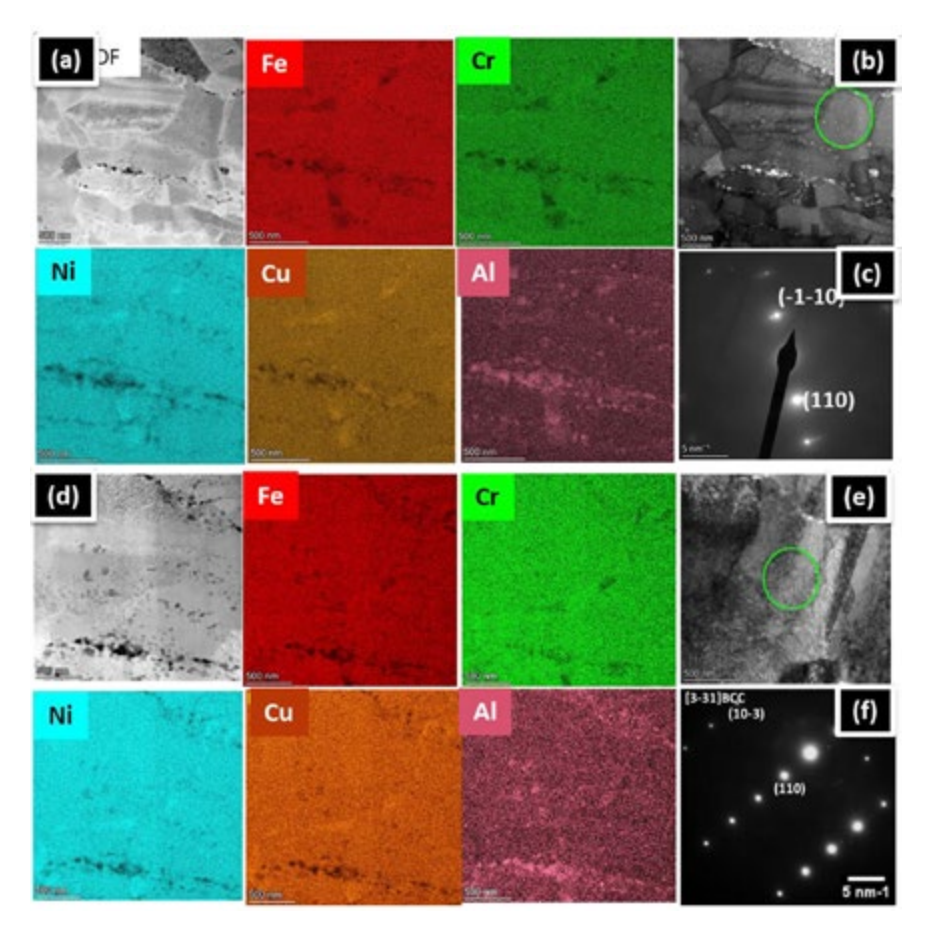


Figure 13 shows the roomtemperature in situ irradiation BF micrographs from 0 to 10 dpa of Ni₃Al phase of Al_{0.8}CrCuFeNi alloy. As can be seen from the figure, absolutely no change in contrast of the images is seen from 0 to 10 dpa. This shows the stability of this phase towards irradiationinduced loop formation and RIP. The respective pre- and post-irradiation characterization of this region is given in Figure 14 (a and b), which shows Ni and Al enrichment in this phase similar to pre-irradiation. The post irradiation SAD pattern shows only the major spots of Ni₃Al phase.

Figure 1. (a-c) Pre- and (d-f) post-irradiation STEM-EDS characterization of matrix phase of $Al_{0.8}$ CrFeCuNi alloy, showing uniform distribution of elements in the matrix; (b) post irradiation SAD analysis of the matrix of $Al_{0.8}$ CrFeCuNi alloy, showing bcc structure with absence of SRO spots.

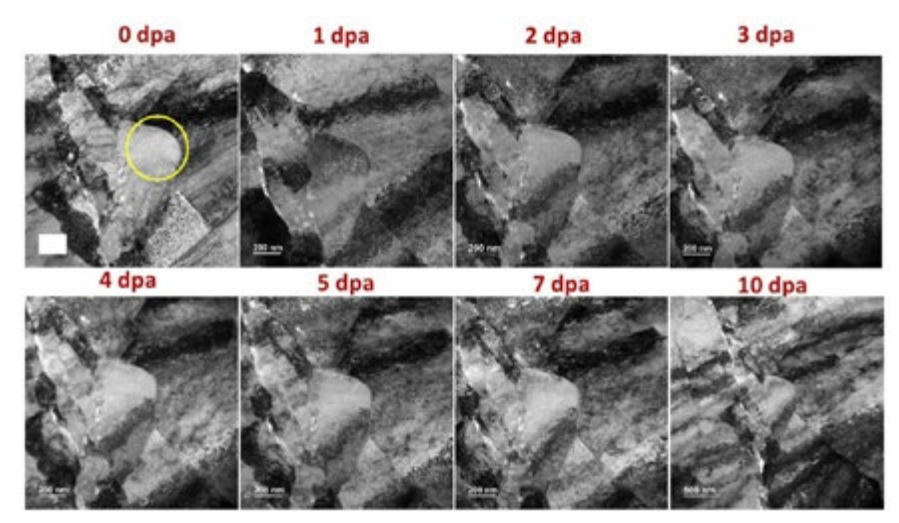


Figure 1. In situ irradiation BF micrographs from 0 to 10 dpa of Ni₃Al phase Al_{0.8}CrCuFeNi alloy.

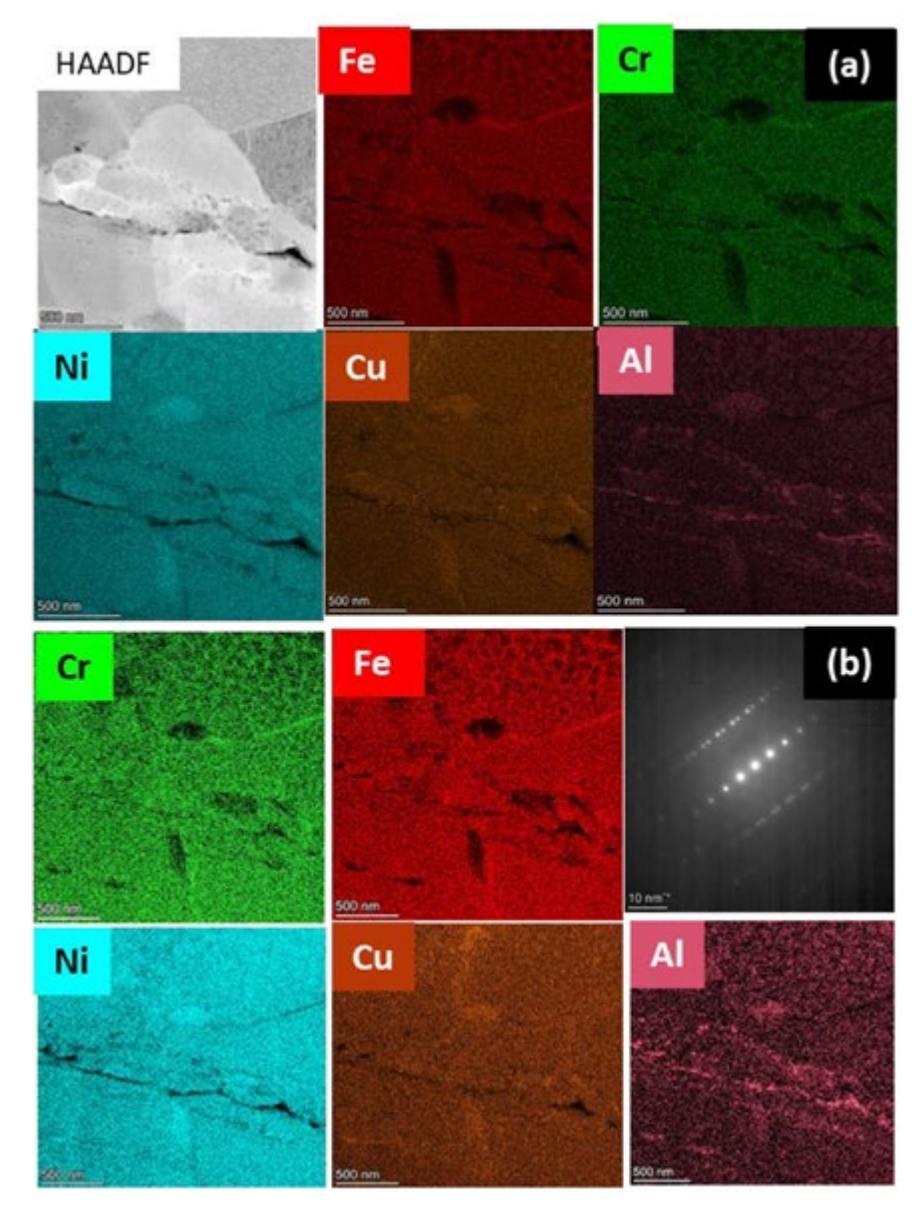


Figure 1. (a) Pre-irradiation STEM-EDS characterization of Ni-rich phase of Al $_{0.8}$ CrFeCuNi alloy; (b) post-irradiation STEM-EDS along with SAD analysis of the Ni-rich phase of showing Ni $_{3}$ Al structure.

RT Irradiation of MoNbTi HEA Series

RT Irradiation of MoNbTi Alloy

Figure 15 (a) represents the microstructure of alloy MoNbTi under TEM-BF condition from 1 to 10 dpa. The peak disorder in the matrix occurred at around 3 dpa, when the most defects agglomerated in the grain, as marked in Figure 4, followed by diffusion and annihilation of defects towards the grain boundary up to 10 dpa. It can be observed that, even at room temperature, the diffusion of defects leads to defect annihilation before they develop into such larger stable defects as voids or loops.

Figure 15 (b) depicts the post-irradiation microstructure and chemistry of MoNbTi alloy of the region in Figure 15 (a). The matrix continued to show a mostly homogenous distribution with some Ti enrichment scattered across the sample, as shown by the EDS maps. Thus, it can be observed that the MoNbTi alloy did not show much change in microstructure and phases, even after irradiation up to 10 dpa. This shows its excellent ability to withstand irradiation up to very high doses.

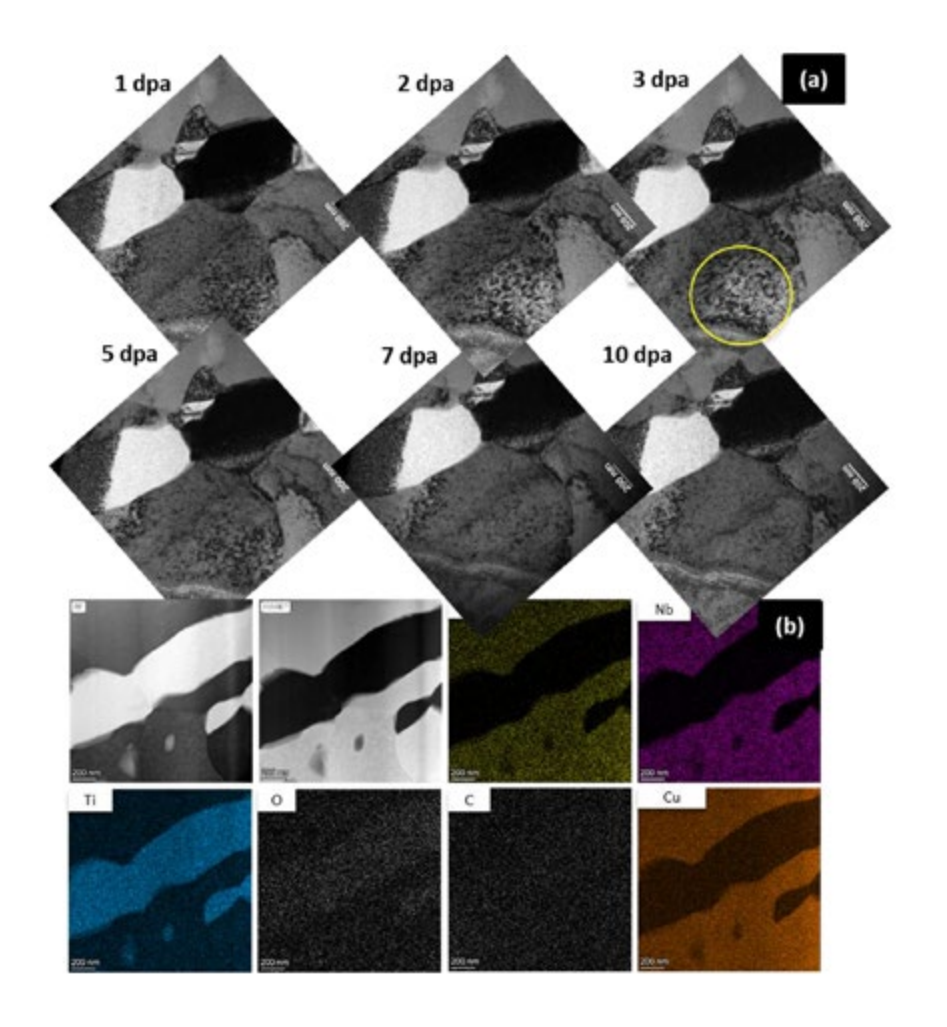


Figure 1. (a) In situ irradiation micrographs showing defect evolution in the matrix of MoNbTi alloy during irradiation; (b) post irradiation STEM-EDS maps of the region in (a).

Figure 16 depicts a matrix grain of MoNbTi alloy, which proved to be the most-stable region during irradiation. This showcases the stability of the alloy against RIS, RIP, loop formation, and void or bubble formation. This stability may be attributed to the severe site-to-site lattice distortion due to compositional complexity in these equiatomic alloys. Post-irradiation characterization of this region given in Figure 16 (b) shows usual segregation behavior of elements relative to MoNbTi distributed matrix plus Ti-rich phase.

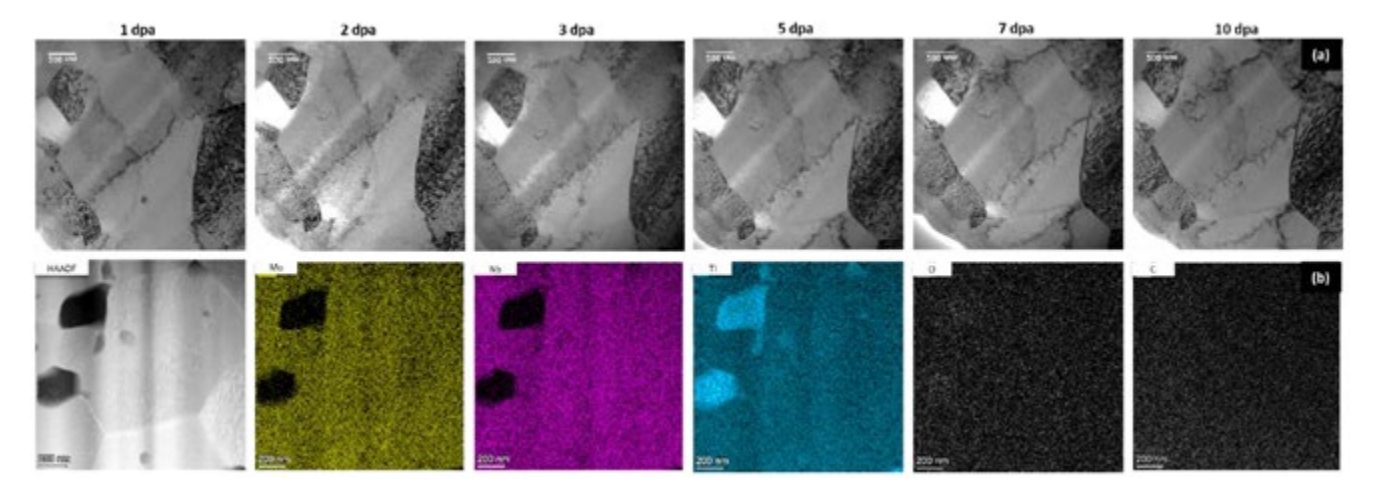
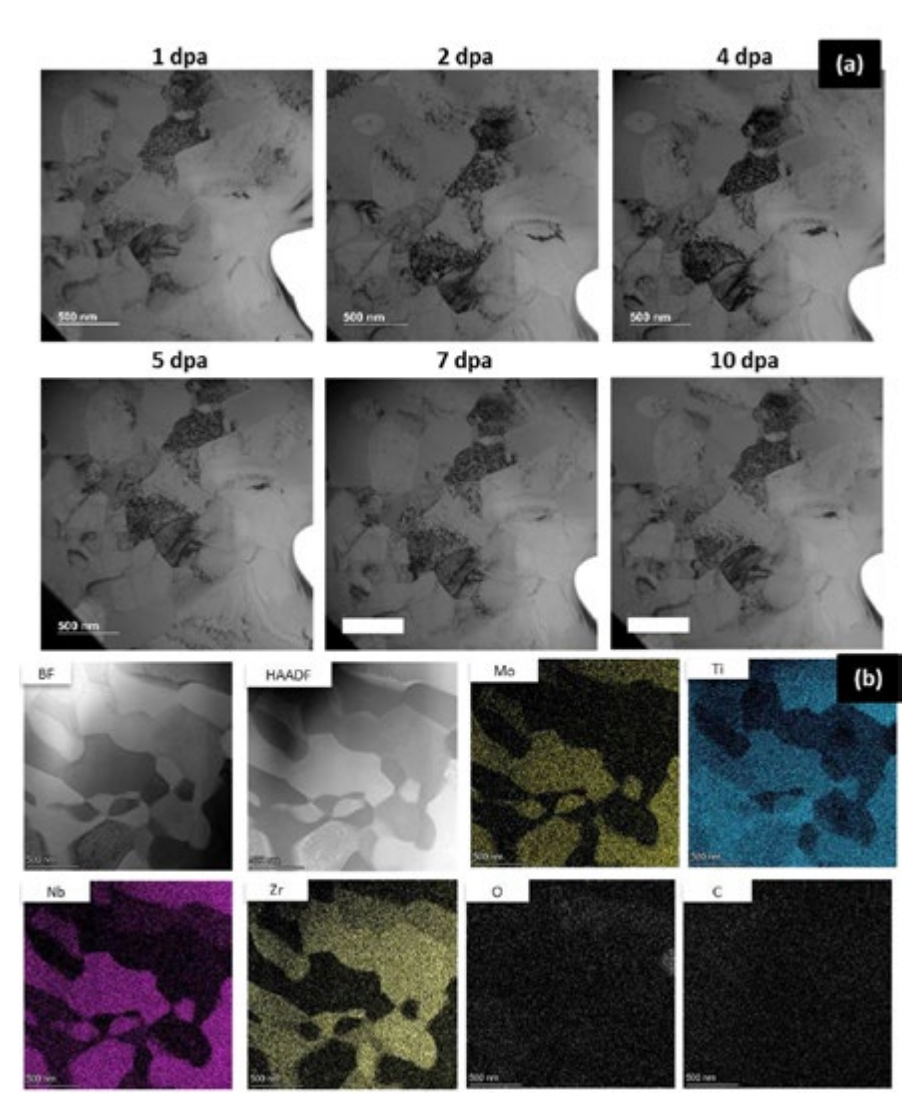


Figure 1. (a) In situ irradiation micrographs of matrix in the MoNbTi alloy irradiated up to 10 dpa showing stability against RIS, voids, or RIP; (b) post-irradiation characterization of region in (a), showing no difference in segregation behavior of elements after irradiation.

RT Irradiation of MoNbTiZr Alloy

Figure 17 (a) represents the in situ irradiation BF micrographs of a region in MoNbTiZr alloy that happens to be the most-stable region under irradiation. It did not show any microstructural changes with regards to loops or voids during irradiation. This proves the alloy's ability to withstand irradiation, which may be due to its high lattice distortion that is the characteristic feature of HEAs. Post-irradiation characterization of this region, given in Figure 17 (b), shows the existence of matrix and Zr-rich phases similar to the prior irradiation. This demonstrates the alloy's resistance to RIS or RIP.



 $\label{thm:prop:continuous} \emph{Figure 1. (a) In situ} \ \emph{irradiation micrographs of MoNbTiZr alloy, (b) which shows structural stability under irradiation.}$

RT Irradiation of MoNbTiZrV Alloy

Unlike the previous alloys, after V addition, alloy MoNbTiZrV shows different kinds of irradiation behavior, including twin-boundary distortion, amorphization, and cavity formation. These are discussed in this section.

Twin boundary distortion:

The evolution of twin boundaries can be observed starting at 1 dpa, as represented in Figure 18 (a). Before irradiation, the edges defining the twins are sharp; however, as the sample gets irradiated to higher doses, defects seem to diffuse into the twinning geometries, which ultimately collapse within the grain. This results in the gradual disappearance of the linear edges at the twin boundaries and the formation of defect clusters within the grain. Post-irradiation characterization of this region, given in Figure 18 (b), shows that the grain that showed the twin-boundary distortion is Zr rich.

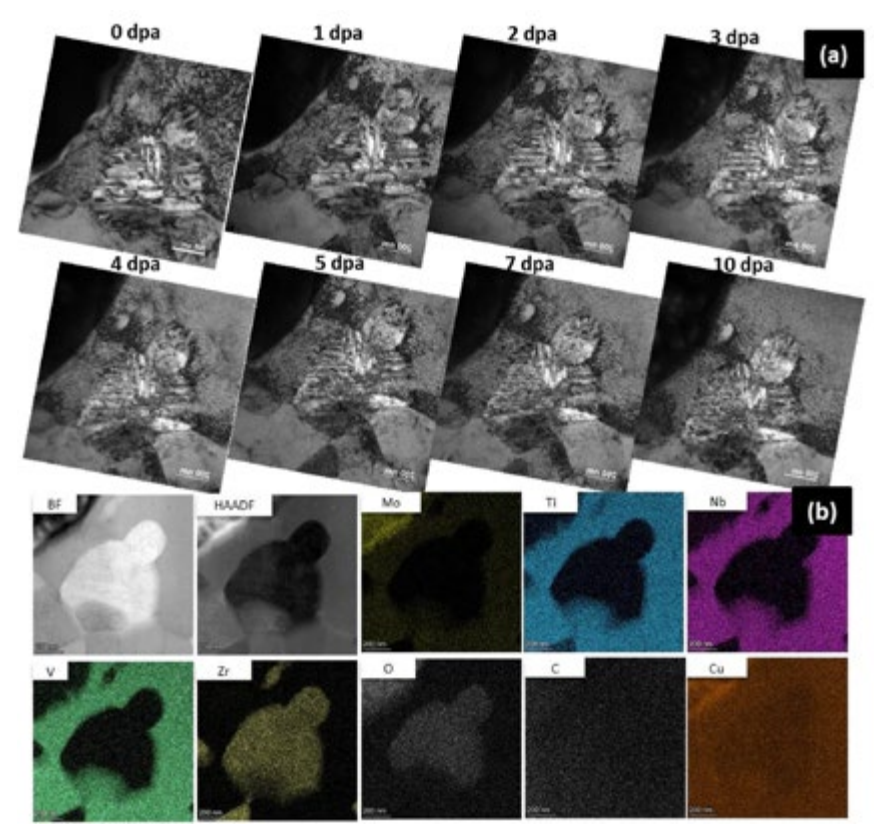


Figure 1. (a) Microstructure of MoNbTiZrV alloy during irradiation, showing the collapse of twin boundaries with increased dose; (b) post-irradiation characterization of the region in (a), showing Zr enrichment in the phase.

Radiation-induced amorphization:

Figure 19 represents the region during in situ irradiation of MoNbTiVZr alloy, It shows radiation-induced amorphization. Amorphization can be seen as a kind of milky appearance in the BF micrographs in Figure 19 (a). The SAED patterns recorded during in situ irradiation clearly show the formation of amorphous rings which proves radiation-induced amorphization in this alloy. The phase tended toward amorphization as the sample reached 1 dpa and included the same area until the end of the experiment. Figure 19 (b) depicts post-irradiation characterization of this region, through which it can be understood that the phase which was amorphized due to irradiation is rich in V-Zr.

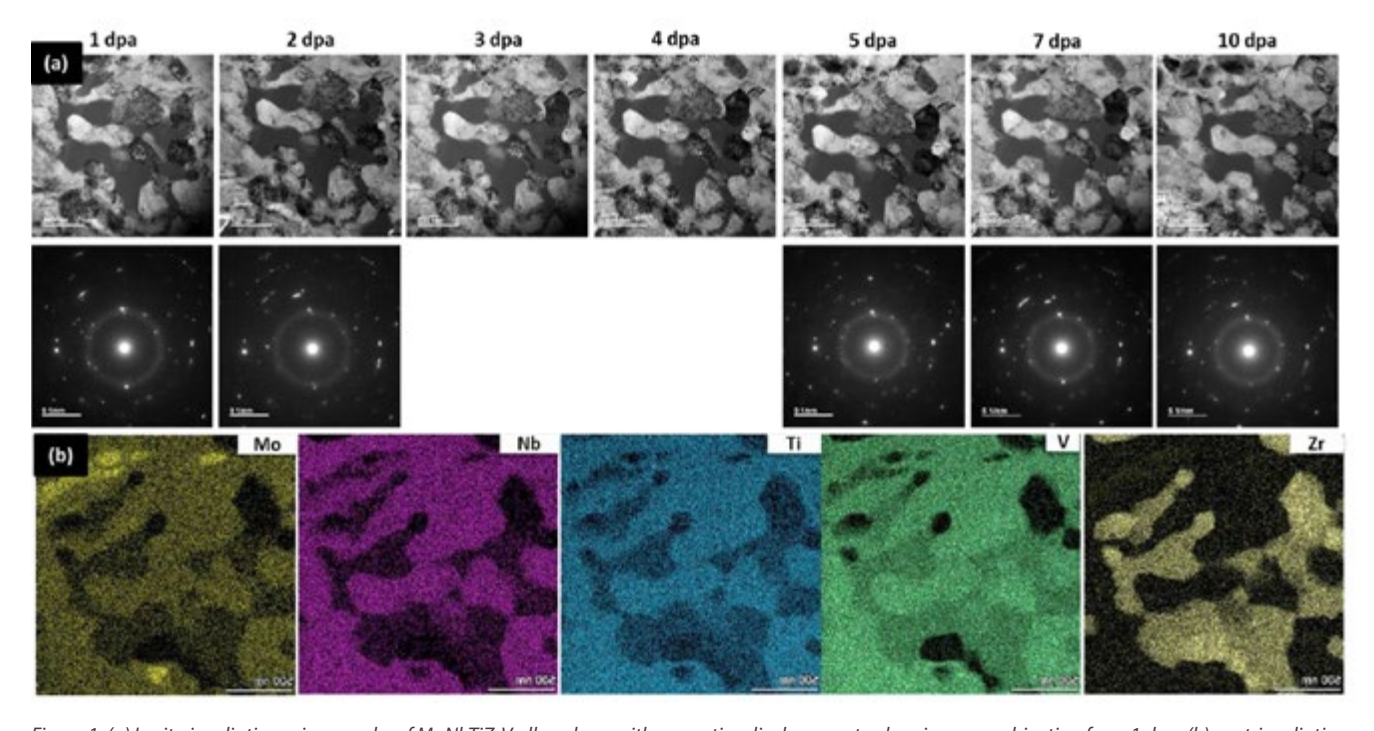
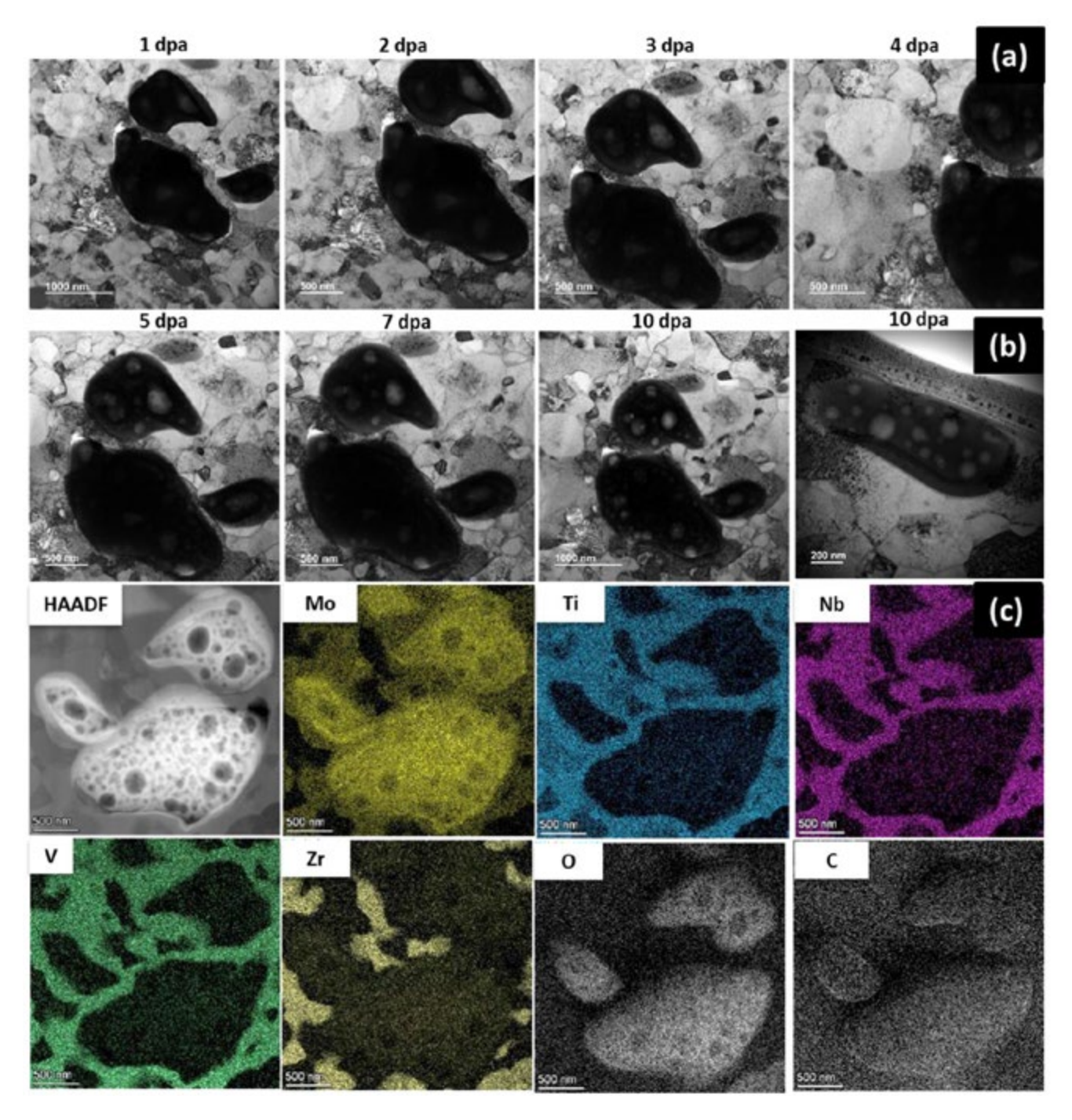


Figure 1. (a) In situ irradiation micrographs of MoNbTiZrV alloy along with respective displacements, showing amorphization from 1 dpa; (b) post-irradiation characterization of the region in (a), showing that the amorphized phase is rich in V and Zr.

Cavity formation and radiation-induced precipitation:

Figure 20 (a and b) reveals that the large Mo-rich phase of MoNbTiZrV alloy is prone to formation of cavities that appear inside the irregular-shaped black grains as white circular cavities with pores on them throughout the experiment. The cavities start forming at 1 dpa and grow in size and number as the sample is irradiated to higher doses. They seem to form in random locations within the grain. The post-irradiation characterization of the region (Figure 20 [b]) confirms that the grains are rich in Mo. Thus, the Mo-rich segregation in this alloy is shown to have the deleterious effect of RIP of molybdenum carbide.



 $Figure\ 2.\ (a)\ In\ situ\ BF\ micrograph\ of\ MoNbTiZrV\ alloy\ showing\ formation\ of\ cavities; (b)\ post-irradiation\ characterization\ of\ the\ region\ in\ (a),\ showing\ RIP\ inside\ the\ Mo-rich\ phase\ of\ alloy\ MoNbTiZrV.$

Irradiation phase stability in alloy MoNbTiZrV:

The region shown in Figure 21 (a) of MoNbTiZrV alloy did not show any significant change throughout the experiment. This demonstrates that the material can be irradiation-resistant to doses as high as 10 dpa. The post-irradiation characterization of this area in Figure 21 (b) shows that this region consists of both matrix and Zr-Ti-rich phases. Thus, it can be understood that the alloy also shows good stability with regards to irradiation-induced voids or loops in areas where the matrix is equiatomic (i.e., bcc matrix) although it is prone to deleterious irradiation effects, as discussed above. These effects may only be caused by the existence of multiple complex phases, such as Zr and Mo segregations.

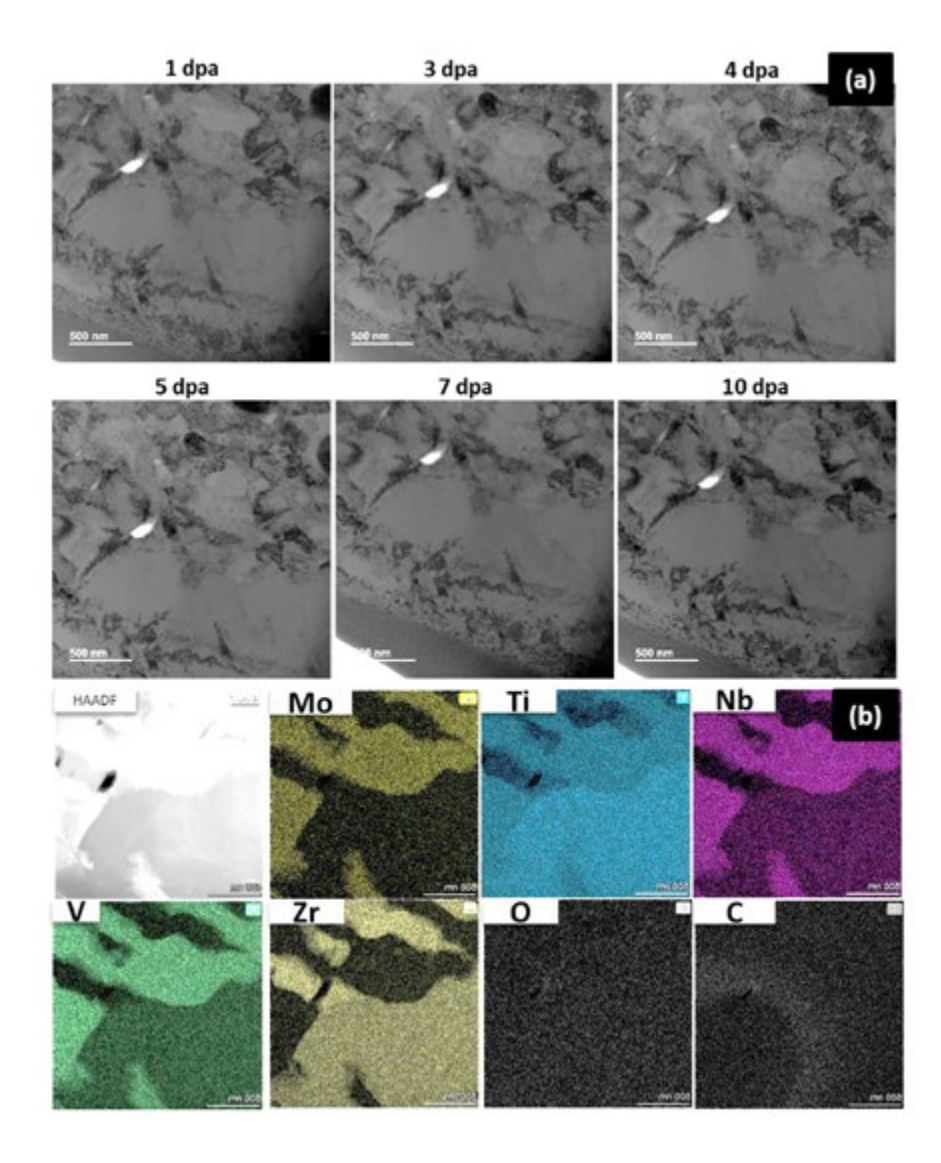


Figure 2. (a) BF micrographs of a region in alloy MoNbTiZrV alloy during in situ irradiation, showing its irradiation phase stability; (b) post-irradiation characterization of this area showing the presence of matrix and Zr-Ti-rich phases in this region.

List of Conference Presentations from this Work

[1] Kara Krogh, Saikumaran Ayyappan, Geoffrey Beausoleil, Matt DeJong. "Effects of Varying Al Content on the Microstructure of the Fe-Cr-Ni-Mn-Al Multi-Component Alloy System." TMS-2024.

- [2] Saikumaran Ayyappan, Matthew deJong, Kara Krogh, Geoffrey Beausoleil, Djamel Kaoumi. "Effect of Al addition to the Multi-Principal Element CrFeCuNi system in terms of resulting microstructure and radiation resistance." TMS-2024.
- [3] Saikumaran Ayyappan, Matthew deJong, Kara Krogh, Geoffrey Beausoleil, Djamel Kaoumi. "Effect of Al addition to the Multi-Principal Element CrFeMnNi system in terms of resulting microstructure and radiation resistance." MRS-2024.
- [4] Saikumaran Ayyappan, Matthew deJong, Kara Krogh, Geoffrey Beausoleil, Djamel Kaoumi. "Effect of Al addition on the microstructure and radiation response of equiatomic AlxCrFeNi (Mn/Cu) alloys." ANS-2024.

List of Manuscripts Under Preparation

- [1] Saikumaran Ayyappan and Djamel Kaoumi. "Irradiation induced ordering/martensitic transformation in AlxFeCrNiMn Multi-principal elemental alloys."
- [2] Saikumaran Ayyappan and Djamel Kaoumi. "Effect of Zr and V additions to the Refractory Multi-Principal Element MoNbTi system in terms of resulting microstructure and radiation resistance."
- [3] Saikumaran Ayyappan, Kara Krogh, Geoffrey Beausoleil, and Djamel Kaoumi. "Effect of Al addition to the Multi-Principal Elemental Al-xCrFeCuNi alloy system in terms of the resulting microstructure and radiation resistance."
- [4] Saikumaran Ayyappan, Kara Krogh, Geoffrey Beausoleil, and Djamel Kaoumi. "Effect of Al and Cu addition to the Multi-Principal Elemental CrFeMnNi alloy system in terms of the resulting microstructure and radiation resistance."

RTE 4513: Measurement of 254-eV Nuclear Recoils in Germanium

Igor Jovanovic, Alexander Kavner (University of Michigan)

Facility: OSU Research Reactor, The Ohio State University

Introduction

Nuclear recoils are one of the primary signals employed for the measurement of neutral particles, notably the detection of fast neutrons. While the scintillation and ionization produced by high-energy nuclear recoils, $\gtrsim 100$ keV, is well studied and understood, at lower energies, $\lesssim 10$ keV, tensions exist among various measurements for a variety of detector media [1, 2, 3].

A better understanding of low-energy nuclear recoils is of particular importance when considering reactor monitoring via coherent elastic neutrino nucleus scattering (CEvNS), first detected in 2017 using an accelerator source [4]. Many groups are investigating this process for reactor monitoring, particularly thanks to CEvNS's three orders-of-magnitude-higher cross-section than the standard mode, inverse beta decay [4, 5, 6, 7]. Notably, several groups are investigating the use of high-purity germanium (HPGe) detectors for CEvNS, both due to their commercial viability as well as the need for only a ~5–10 kg detector or small array for practical monitoring [8, 9].

In pursuit of a better understanding of germanium's response to low-energy nuclear recoils, we have deployed and executed our experiment at the Ohio State University (OSU) Nuclear Reactor Laboratory. A small (2 cm³) Ortec Model GLP HPGe detector was irradiated via thermal neutrons. Monoenergetic 0.254-keV nuclear recoils were produced via emission of 5.8-MeV gamma rays of ^{73m}Ge following neutron capture on naturally abundant ⁷²Ge.

This RTE study aimed to measure the ionization produced by the nuclear recoil summed with a 68.752-keV gamma ray associated with the same gamma cascade. The relevant energy levels of ⁷³Ge and our experimental setup are shown in Figure 1.

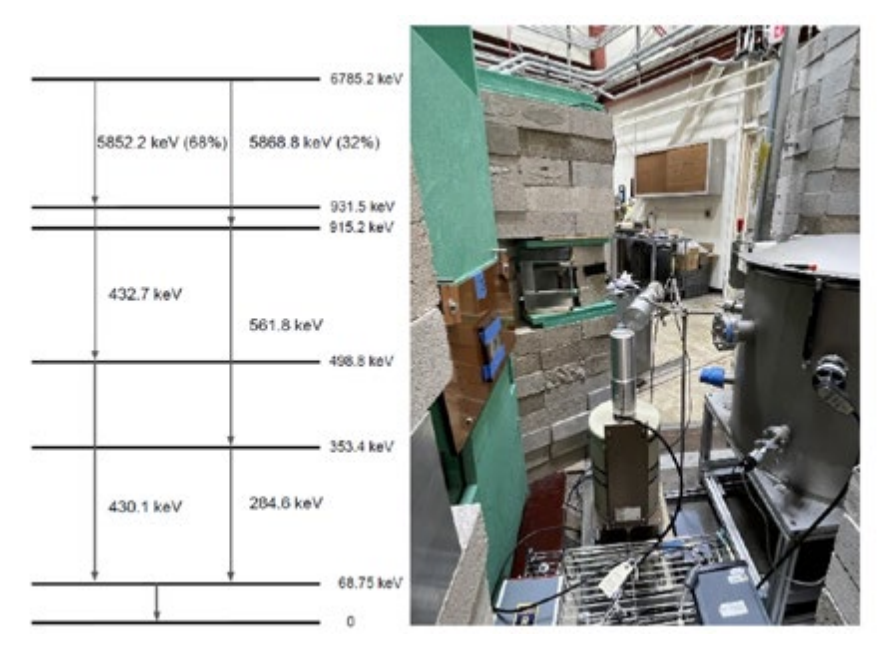


Figure 1. (Left) Relevant energy levels of 73 Ge with the γ cascade of interest. (Right) Experimental configuration with Ortec GLP detector in the OSU thermal-neutron beamline, with NaI γ -tagging detector in the background.

Preliminary Results

To ensure minimal bias, two data subsets, composed of approximately 10% of the total data, were selected for a preliminary analysis. Once this initial analysis is complete, the same signal processing and algorithms will be applied to the entirety of the data set.

The energy spectrum from one of these data subsets is depicted in Figure 2. With minimal cuts to the data to eliminate pileup, the peak of interest becomes readily evident—i.e., the middle peak in Figure 2. The ^{241}Am and Pb X-ray peaks, along with other peaks outside the shown energy range, allow for precise calibration of the energy scale. Fit to the peak of interest yielded an energy of 68.818 ± 0.008 keV for the summed γ -ray and nuclear-recoil ionization. Subtracting the γ -ray energy of 68.752 ± 0.007 keV yields an ionization of 0.066 ± 0.011 keV from the 0.254-keV nuclear recoil or $26 \pm 4\%$. We expect the uncertainty to improve with increased statistics as, again, these values are derived from only a small fraction of the total data.

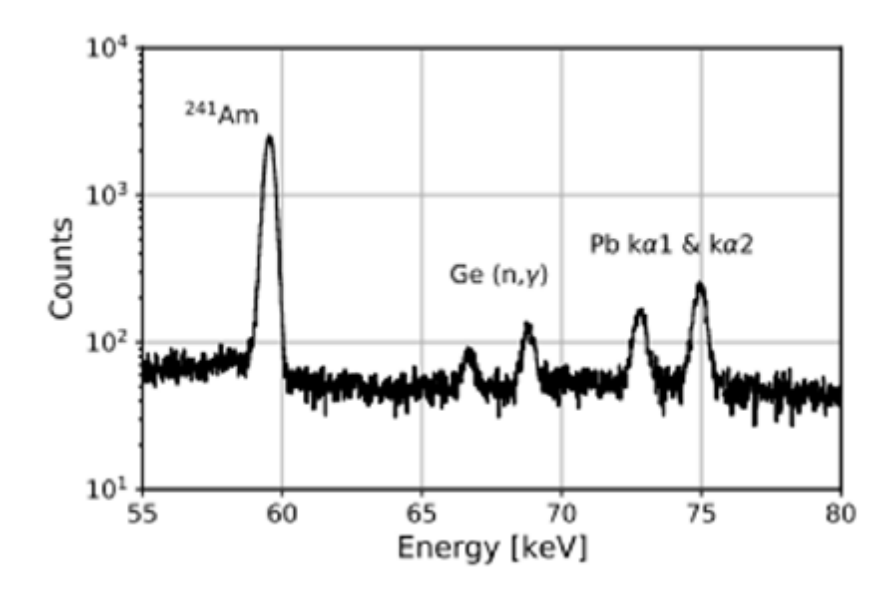
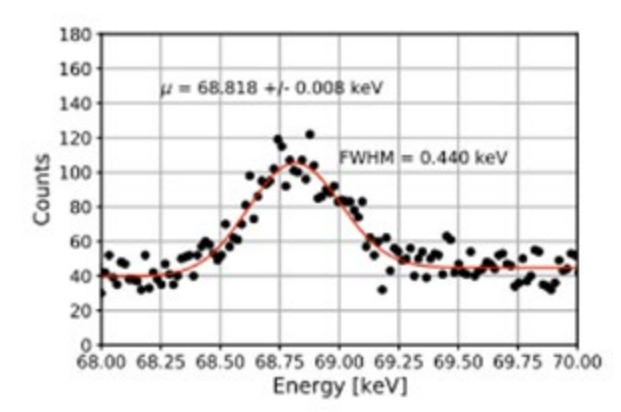


Figure 2. Experimentally measured energy spectrum in the energy range of interest around the 68.725- $keV\gamma + nuclear$ recoil.

Program Relevance

The results of the initial blinded analysis indicate confirmation of the earlier result [2] and are in agreement with the sum of γ and recoil energy of 68.815 keV (Figure 3). This indicates an enhanced ionization produced by the 0.254-keV recoiling ^{73}Ge ion inconsistent with the Lindhard region of the Bethe-Bloch stopping-power model. Such a result could enable large multikg HPGe detectors to conveniently monitor advanced reactors for nuclear-material accountancy, thereby supporting nuclear safeguards. A detailed analysis is required to confirm this preliminary analysis result. The resultant publication is expected to be submitted by mid-2024.



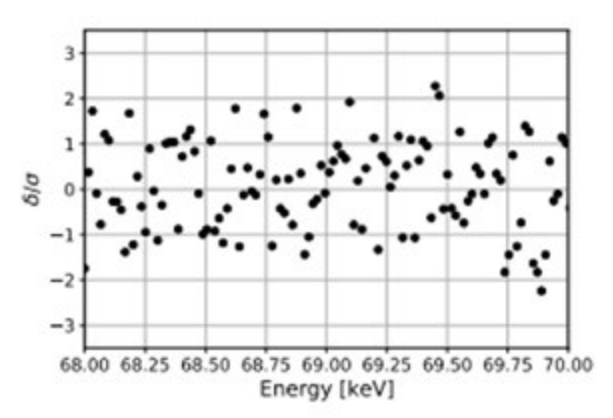


Figure 3. (Left): Fit to the 68.725-keV γ + nuclear recoil peak. (Right) Residual expressed in terms of the difference between data and fit, divided by the statistical uncertainty.

References

[1] J. I. Collar, A. R. L. Kavner, and C. M. Lewis. "Response of CsI[Na] to nuclear recoils: Impact on coherent elastic neutrino-nucleus scattering," *Phys. Rev. D* 100 (2019) 033003. doi:10.1103/PhysRevD.100.033003. URL https://link.aps.org/doi/10.1103/PhysRevD.100.033003

- [2] J. I. Collar, A. R. L. Kavner, and C. M. Lewis. "Germanium response to sub-kev nuclear recoils: A multipronged experimental characterization," *Phys. Rev. D* 103 (2021) 122003. doi:10.1103/PhysRevD.103.122003. URL https://link.aps.org/doi/10.1103/PhysRevD.103.122003
- [3] A. E. Chavarria, J. I. Collar, J. R. Pen˜a, P. Privitera, A. E. Robinson, B.Scholz, C. Sengul, J. Zhou, J. Estrada, F. Izraelevitch, J. Tiffenberg, J. R. T. de Mello Neto, and D. Torres Machado. "Measurement of the ionization produced by sub-kev silicon nu- clear recoils in a ccd dark matter detector," *Phys. Rev. D* 94 (2016) 082007. doi: 10.1103/PhysRevD.94.082007. URL https://link.aps.org/doi/10.1103/PhysRevD.94.082007
- [4] D. Akimov, et. al., Science 357 (2017) 1123–1126. doi:10.1126/science.aao0990.
- [5] A. Bernstein, N. Bowden, B. L. Goldblum, P. Huber, I. Jovanovic, and J. Mattingly. "Col- loquium: Neutrino detectors as tools for nuclear security," *Rev. Mod. Phys.* 92 (2020) 011003. doi:10.1103/RevModPhys.92.011003. URL https://link.aps.org/doi/10.1103/RevModPhys.92.011003
- [6] N. S. Bowden. "Reactor monitoring and safeguards using antineutrino detectors," Journal of Physics: Conference Series 136 (2) (2008) 022008. doi:10.1088/1742-6596/136/2/022008. URL https://dx.doi.org/10.1088/1742-6596/136/2/022008
- [7] L. Wen, J. Cao, and Y. Wang. "Reactor neutrino experiments: Present and future," *Annual Review of Nuclear and Particle Science* 67 (1) (2017) 183–211. doi:10.1146/annurev-nucl-101916-123318.
- [8] C. Buck, K. Fu'lber, J. Hakenmu'ller, G. Heusser, M. Lindner, W. Maneschg, T. Rink, H. Strecker, T. Schierhuber, V. Wagner, and R. Wink. "A novel experiment for coherent elastic neutrino nucleus scattering: Conus," *Journal of Physics*: Conference Series 1342 (1) (2020) 012094. doi:10.1088/1742-6596/1342/1/012094. URL https://dx.doi.org/10.1088/1742-6596/1342/1/012094
- [9] J. Colaresi, J. I. Collar, T. W. Hossbach, A. R. L. Kavner, C. M. Lewis, A. E. Robinson, and K. M. Yocum. "First results from a search for coherent elastic neutrino-nucleus scattering at a reactor site," *Phys. Rev. D* 104 (2021) 072003. doi:10.1103/PhysRevD.104.072003. URL https://link.aps.org/doi/10.1103/PhysRevD.104.072003

RTE 4530: Irradiation of Radiation-Hard GaN Transistors for Mixed Gamma and Neutron Field Under High Temperature

PI: Jack Lanza, The Ohio State University (OSU)

Collaborators: N. Dianne Bull Ezell, F. Kyle Reed (ORNL), Lei "Raymond" Cao, Siddharth Rajan (OSU)

Facility: OSU Research Reactor, The Ohio State University

Monitoring of nuclear reactor conditions is critical to ensuring the safe and efficient operation of reactors while sensors and instrumentation are crucial to providing the real-time data to do so. Presently, sensors such as thermocouples require lengthy cabling, which can reduce signal integrity through electromagnetic noise and interference. Furthermore, these sensors require penetrations in reactor-containment structures for cabling. Alternatively, electronics capable of withstanding the elevated temperature and radiation environments associated with nuclear reactors could improve sensor-signal integrity through amplification or digitization, reduce cabling and penetrations through multiplexing or wireless communications and provide multimodal sensors with adaptive calibration. Currently, the state-ofthe-art Si-based transistors and electronics do not withstand radiation and temperature adequate to these environments. However, GaN-based highelectron-mobility transistors (HEMTs) have shown high tolerance to ionizing radiation [1], though the neutronic performance of these devices remains untested. In this RTE, we sought to investigate the neutron limitations of GaN semiconductors.

The GaN HEMTs for this irradiation were fabricated by OSU. During the unheated portion of the experiment, nine D-mode transistors and seven E-mode transistors across three dies were measured during irradiation. An example die can be seen below on the left of Figure 1. The second portion consisted of two dies with eight E-mode and eight D-mode semiconductors monitored in an elevated-temperature environment in the range of 80–120°C. We tested various sizes of semiconductors to test the effect of transistor dimensions on the radiation tolerance. We opted to irradiate at the Ohio State University Nuclear Reactor Laboratory (OSUNRL) to enable in situ measurement of the effects of the irradiation on device characteristics, as opposed to performing a purely post hoc analysis, as is traditionally done. This approach also allowed us to more precisely study the radiation effects on the devices' modes and points of failure. The final irradiation assembly can be seen below on the right of Figure 1.

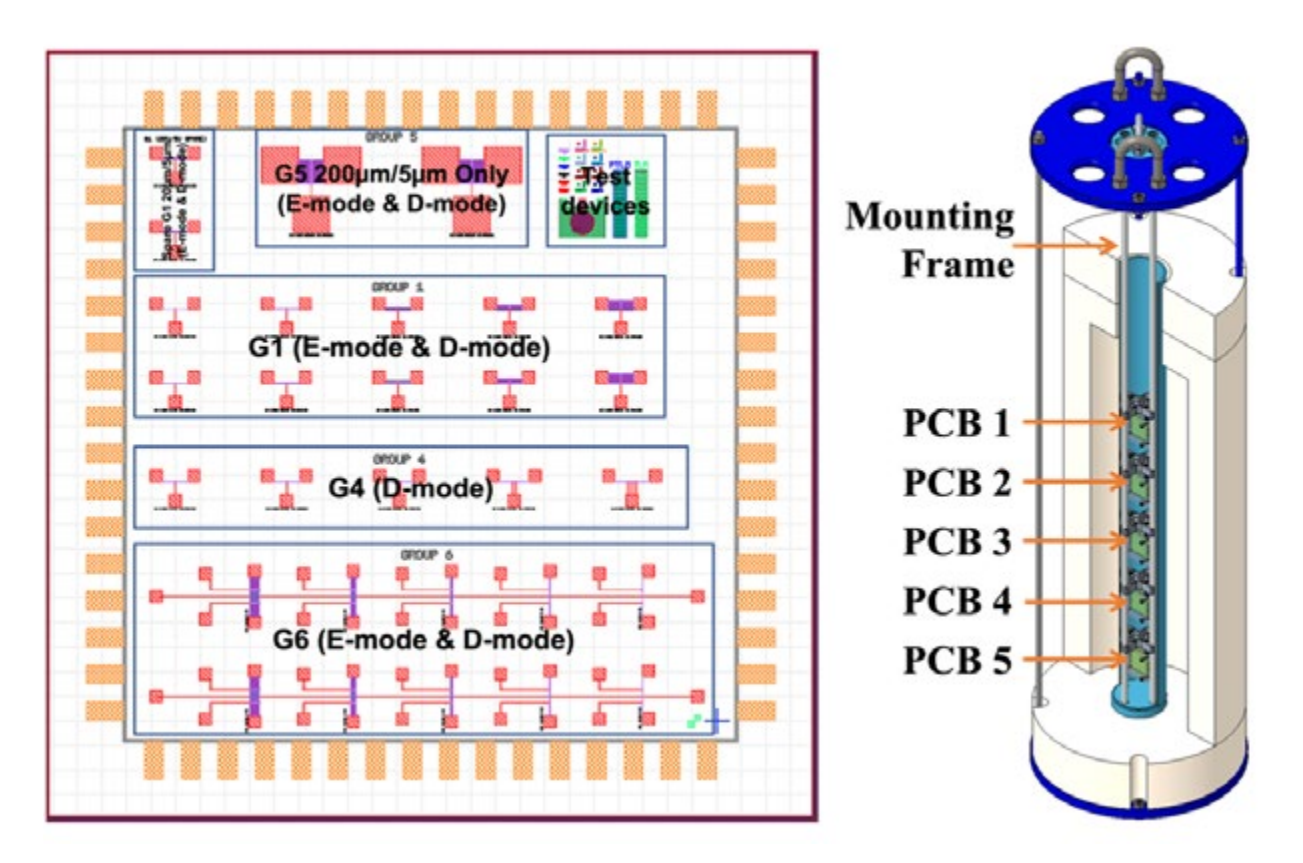


Figure 1. Experimental setup: (left), example die (right) furnace, basket, and printed circuit boards (PCBs) assembled.

A Monte Carlo N-Particle (MCNP) model, provided by OSUNRL, was used to generate the neutron- and gamma-flux profiles of the irradiation experiment in the 9.5-in. dry-well facility at the OSUNRL. This MCNP model included a custom furnace that was used to heat samples in the second experiment as well as a basket designed by ORNL to mount the samples inside the furnace. With this model, we characterized the neutron-flux profile along the central axis to determine the optimal height at which to place the devices to achieve the desired fluences 10¹⁵ n/cm² after Day 1, and a cumulative fluence of 10¹⁶ n/cm² after Day 2. The neutron-flux profile at 450 kW can be seen below in Figure 2.

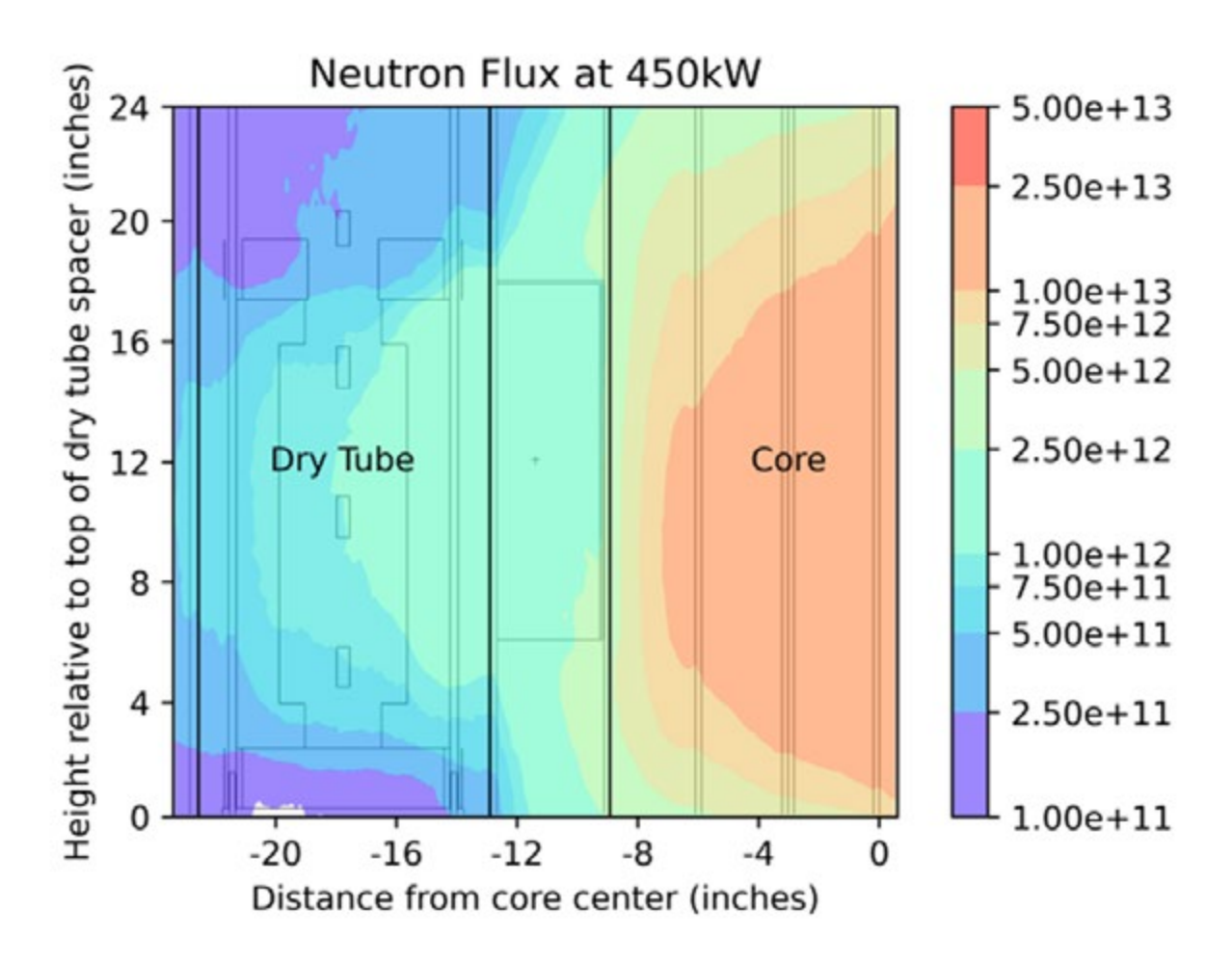


Figure 2. Neutron-flux mapping of OSUNRL at 450 kW.

After determining device placement and reactor power, we constructed the test fixture at the reactor prior to irradiation, setting up the data acquisition (DAQ) system with connections to all 16 transistors to continuously cycle through measuring characterization curves of each transistor in situ. The DAQ system continued monitoring overnight after reactor shutdown to observe the self-healing that occurs overnight. The heated portion ran at 4% of max power (20 kW) on the first day and 34% of max power (170 kW) on the second day, with no furnace heating. For the heated portion, the reactor ran at 6% of max power (30 kW) on the first day of radiation and 40% of max power (200 kW) on the second day. On both days of the heated portion, the temperature was held in the range of 80–120°C to explore the temperature effects when compared to the first experiment.

By the end of the experiment, all transistors from the heated and unheated portion of the irradiation experiment remained operational beyond 10¹⁶ n/cm². Preliminary findings suggest that devices show increased radiation tolerance when irradiated and heated simultaneously. This work provides novel insight into the capabilities of GaN HEMTs in harsh environments. GaN HEMTs are a promising technology that may have the potential to survive the high-temperature and radiation environments associated with nuclear reactors. The radiation tolerance results found in this RTE are encouraging for the successful development of radiation-hardened electronics to support sensors and instrumentation for nuclear reactors.

The full results and data will be published soon in a nuclear engineering or radiation-hardened electronics journal.

References

[1] M. Rahman, et al. "Super-Radiation Hard Detector Technologies: 3-D and Widegap Detectors," *IEEE Transactions on Nuclear Science* 51 (5) (2004), 2256–2261.

RTE 4537: Compositional and Defect Analysis of the FCCI in High-Burnup UO₂

A. Probert (University of Florida), C. McKinney, T. Lach, J. Harp (ORNL), A. Aitkaliyeva (University of Florida)

Facility: Irradiated Fuels Examination Laboratory / Low Activation Materials Development and Analysis Laboratory, Oak Ridge National Laboratory

Current efforts to improve the nuclear-fuel economy and minimize spent-fuel waste involve extending the discharge burnup limit for commercial light water reactors (LWRs) in the U.S. beyond 68 MWd/kgU. During operation, fuel undergoes drastic microstructural changes, including fission-product accumulation, swelling, and formation of a high-burnup structure (HBS) along the periphery of the fuel. The latter is associated with grain subdivision, a high density of large bubbles, the relocation of fission gas in the matrix (dissolved or as nanometer-size bubbles) into these large bubbles, and elimination of defects in the rim region where higher local burnups are present under lower temperatures. As a result, HBS microstructure has unique thermomechanical and fission-gas retention properties that are significantly different from the rest of the fuel. Beyond these microstructural changes, fuels can react with the cladding, thus providing reaction pathways between the mobile fission products and the cladding, which can weaken the integrity of the cladding. fuelcladding chemical interaction (FCCI) is complex and can be further exacerbated by HBS formation.

Therefore, understanding of the FCCI in HBS regions in high-burnup fuels is needed to accurately predict fuel performance and extend the lifetime of commercial nuclear fuel.

In this RTE study, an examination of FCCI in the HBS region was conducted on a block (with approximate dimensions of 30 μ m imes 30 μ m imes30 µm) lifted out from the interface of the HBS and FCCI region of a LWR UO₂ fuel pin irradiated to ~73 MWd/kgU in the North Anna PWR, Figure 1). The microstructural evolution and chemical composition of the fuel, pore structures, and precipitates at the pellet-clad interface was observed using a combination of FIB and EDS. The block was milled with a slice thickness of 50 nm, and an EDS acquisition was taken between each mill, with a total depth set to the length of the block. Currently, SEM micrographs are undergoing manual segmentation due to issues with thresholding when they were segmenting using Avizo software. Once the images are segmented, a reconstruction will be generated and included for publication. Also, individual element maps from the EDS are being analyzed for reconstruction

to provide a visualization of the chemical composition and 3-D structure of the FCCI region.

Additionally, two lift-outs were prepared from the FCCI region to study grain-size distribution, defect structures, and precipitates using transmission Kikuchi diffraction (t-KD), TEM, and STEM with EDS. Low-length analysis revealed penetration of noble-metal fission products and Nb up to approximately 8 mm into the cladding oxide, which is consistent with the previous study conducted on Quad Cities I BWR fuel. The analysis of grain size and orientation distribution as a function of radial position is ongoing, leveraging TEM and whole-block EBSD data. Generally, a gradient of grain sizes is observed, beginning with the larger, tetraclinic phase at the oxide and moving to much smaller, monoclinic phases beyond the interaction layer. Size and density of fission products decrease as the monoclinic phases are approached. Finally, precipitation at gas bubbles within the fuel matrix is being analyzed from the STEM-EDS results. Particles analyzed contained the fission metal products, Ag, Te, Cs, and remnants of Xe (Figure 2).

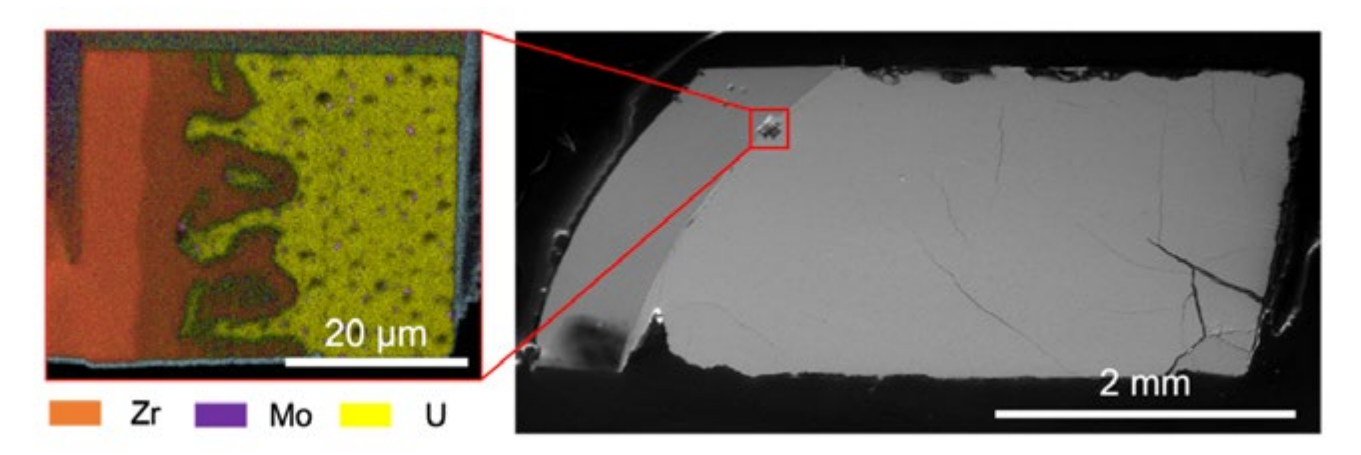


Figure 1. Micrograph of the PWR fuel, depicting location of the block of interest.

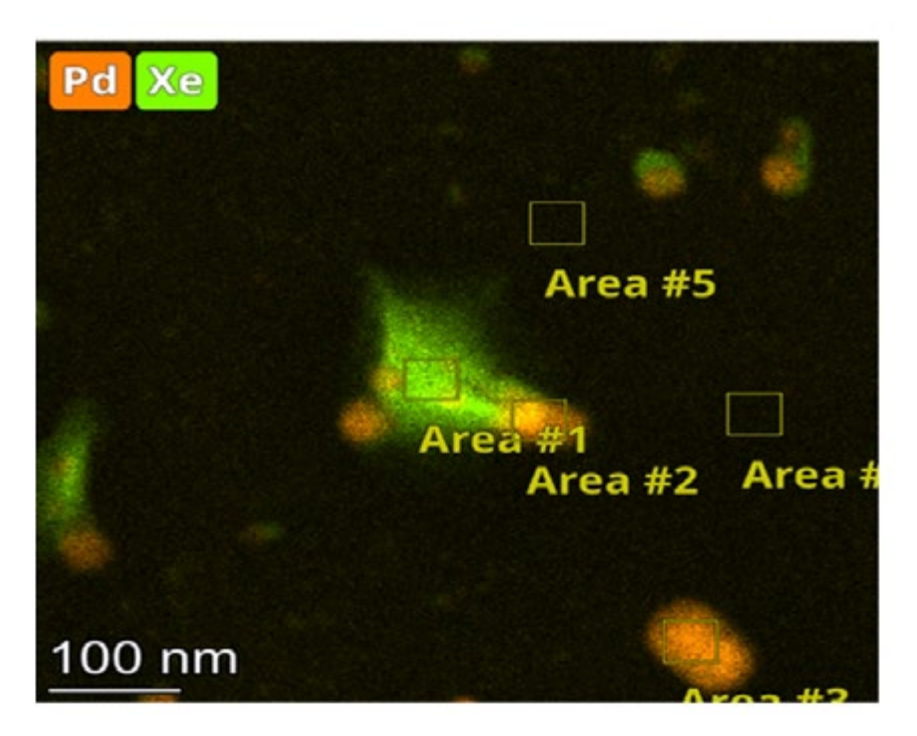


Figure 2. STEM-EDS map showing gas bubbles and particle precipitates.

The data collected are undergoing further analysis, but they will provide key structural and chemical information that will be used to understand high-burnup UO₂ irradiation behavior and in modeling to extract key thermomechanical properties.

RTE 4546: Deconvoluting Void and Bubble Effects on Deformation-Induced Martensitic Transformations in Austenitic Stainless Steel Using 4-D STEM Strain Mapping

PI: Keyou S. Mao (Florida State University)

Team Member: Janelle P. Wharry (Purdue University)

Technical Leads: Yaqiao Wu (CAES), Lin Shao (TAMU)

Facility: Microscopy and Characterization Suite, Center for Advanced Energy Studies; Accelerator Laboratory,

Texas A&M University

This RTE project investigates the effects of voids from bubbles, on deformation-induced martensitic transformations in irradiated austenitic stainless steels. Deformation-induced martensitic transformations are diffusionless. solid-state transformations from fcc γ-austenite to hcp ε-martensite and/or bcc α'-martensite in stainless steels. These martensites can compromise the structural integrity of nuclear components because they lead to irradiation embrittlement and greater corrosion susceptibility. NSUF project DE-NE0008525 found that cavities—a general term to describe voids and/or bubbles promote martensitic transformations in irradiated stainless steel [1-4] because their internal surface energy reduces the externally applied strain energy required to exceed the critical transformation energy and trigger the transformation [5], The surface energy of voids and bubbles significantly influences martensitic transformations in irradiated austenitic stainless steels. Voids, with their lower surface energy and faceted shapes, promote martensitic transformation through

localized shear-strain accumulation. Bubbles, with higher surface energy and internal gas pressure, create uniform stress fields that also drive phase transformations. Understanding these effects is crucial to predict and mitigate irradiation-induced embrittlement and corrosion in nuclear materials. Voids and bubbles could have markedly different effects on the transformation due to differences in surface energy, which are sensitive to cavity shape, void facets, and bubble-gas pressure [6–9].

Because the relative void and bubble populations are highly dependent on irradiation flux and temperature, we set up this experiment to discern individual void and bubble effects on deformationinduced transformations to improve prediction of mechanical heterogeneities arising in nuclear components subject to in-reactor flux and thermal gradients. Our test matrix determines strain distributions around voids and bubbles with varying surface energies (i.e., shapes and sizes) and link these strains to phase transformability with ion

irradiation and post-irradiation TEM characterization. Ion irradiations will create void- or bubble-dominated microstructures in 304L stainless steel to emulate void/bubble distributions in the well-studied neutron irradiated 304L hex blocks [10-12]. Finally, we conducted 4-dimensional (4-D) scanning TEM (STEM) strain mapping (Figure 1c) around voids that have varying surface energies. Spectra 300 STEM with electron-microscope pixel-array detector (EMPAD) at CAES. EMPAD enables rapid collection of 4-D data (i.e., 2-D convergent-beam electron diffraction + 2-D position) over large areas, relative to previous precession electron diffraction (PED) technique (Figure 2) that collected 2-D data from limited orientations and area. A Thermo Scientific QUANTA 3-D FEG with EDS and equipped with an EBSD detector, was used to characterize the microstructure morphology and phase components. Strain mapping and phase mapping of pore structures were performed using PED in an FEI Tecnai TF30 transmission electron microscope with Topspin software from NanoMEGAS. A precession angle of 0.6 degrees was

used for strain mapping of pore structures in the as-printed specimens and 0.48° for phase mapping of the tensile-tested specimens. The strain and orientation mappings were performed by collecting a series of PED patterns under a scanning condition. Topspin strain analysis uses cross-correlation to estimate the diffraction-spot position with sub-pixel accuracy, and the strain was calculated from the lattice distortion extracted from the PED patterns (Figure 2). A reference PED pattern away from the pore structures and grain boundaries was designated as the strain baseline.

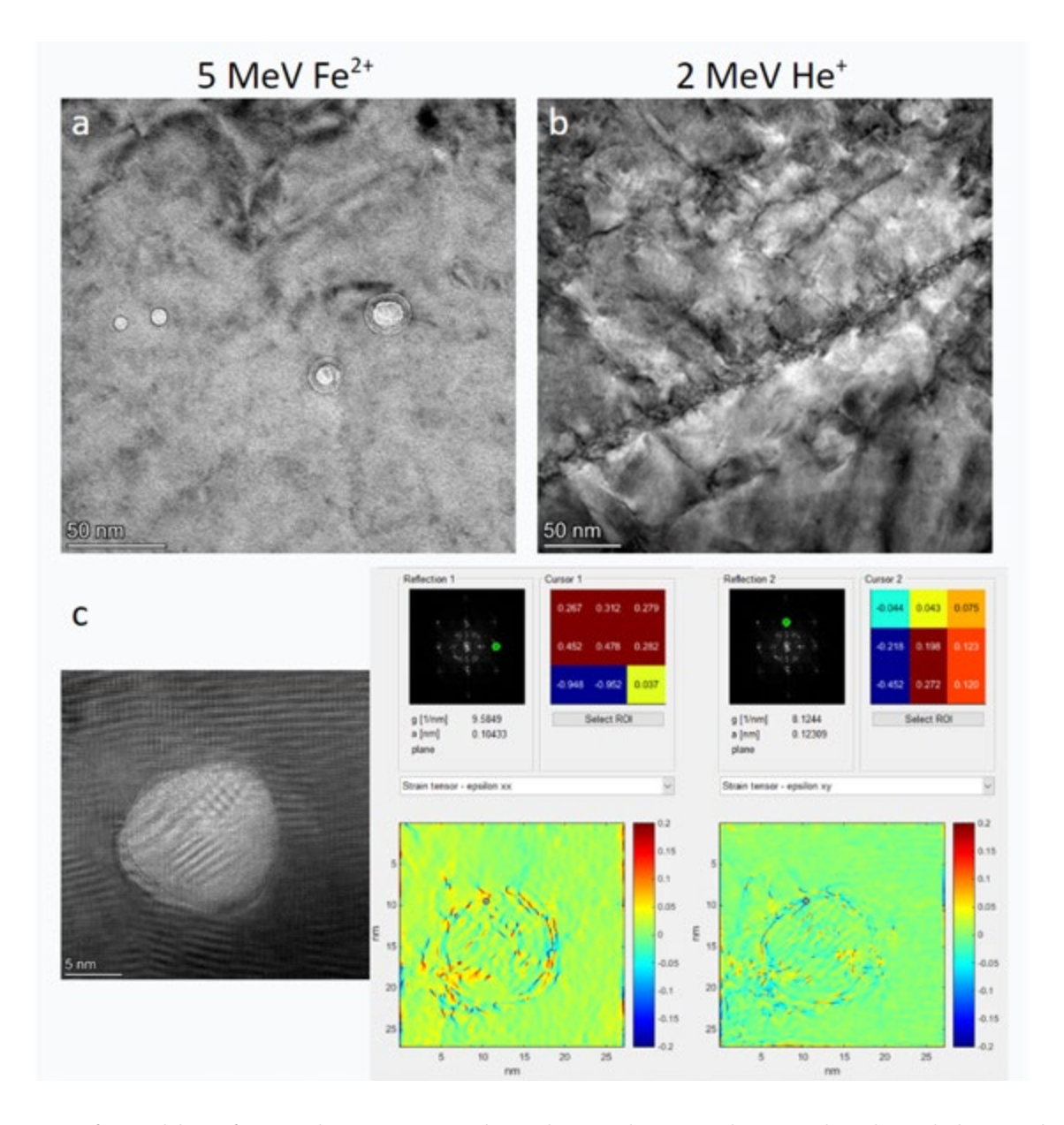


Figure 1. Summary of accomplishment for Proposal 23-1862: (a) 5 MeV Fe^{2+} to 28 dpa (at implantation peak) at 550° C; (b) 68-degree tilted 2-MeV He beam to create a depth equal to the 600-keV He beam suggested in the proposal. The dose was 2.48×10^{15} ions/cm², corresponding to a 550 appm peak-He implantation level. (c) geometric phase analysis (GPA) generates fully quantitative deformation and two-dimensional strain maps from standard high-resolution STEM images. GPA was originally developed by Martin Hytch and is a complementary plug-in to peak-pairs analysis (plug-in), another strain-measurement plug-in based on the atomic-column positions in HR-STEM images. Using the GPA technique, we demonstrated the multi-layered strain fields consisting of both compressive and tensile fields around one individual void in the Fe^{2+} irradiated specimen as the He irradiated specimen has no voids.

TEM data were collected to study effect of void formation and the corresponding strain field near the vicinity of the voids shown in Figure 1 to highlight the type of information obtained and the data analysis carried out to elevate understanding of microstructural changes. A 304L stainless steel specimen from the EBR-II hex block 3A2, irradiated to 23 dpa,

3 appm He at 415°C (EBR-II-HEX-008), serves as the reference material. This specimen has already exhibited deformation-induced γ→ά martensitic transformation. To isolate the effects of voids and bubbles, two ion irradiations (Figure 1a-b) will be performed on virgin 304L stainless steel to create either void-dominated or bubble-dominated microstructures.

The irradiation temperature of 550°C is expected to produce a relatively consistent void nucleation rate over the ~1300 nm damage profile, accounting for the injected interstitial effect. This temperature also fulfills the temperature shift relative to the reference specimen. HR-TEM imaging identifies cavities of varying surface energies (size and faceting in Figure 1c).

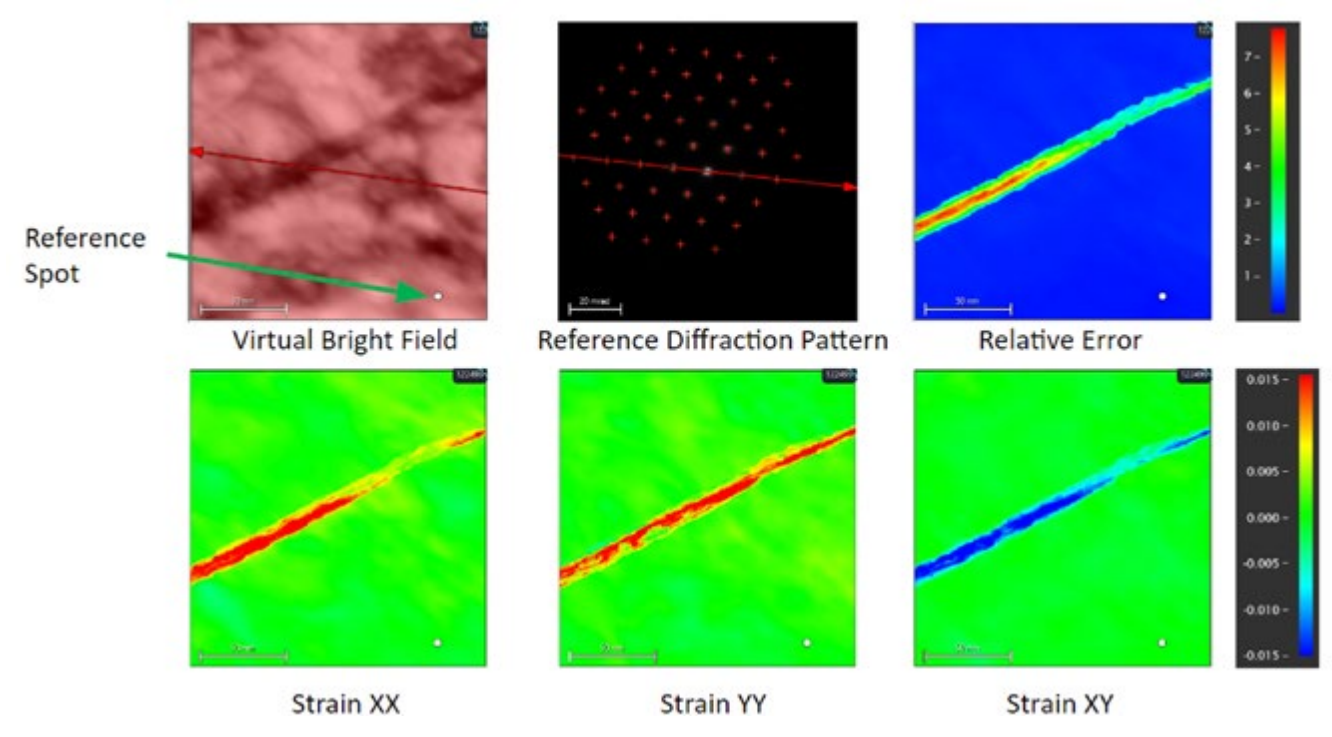


Figure 2. Strain mapping of a twin structure in He-ion irradiated microstructure. For ε_{xx} , ε_{yy} , and ε_{xy} strain distribution.

References

[1] K. Mao, et al. 2018. "Microstructure-property relationship for AISI 304/308L stainless steel laser weldment." Materials Science and Engineering: A 721: 234–243. https://doi.org/10.1016/j.msea.2018.02.092.

- [2] K. Mao, et al. 2019. "Grain orientation dependence of nanoindentation and deformation-induced martensitic phase transformation in neutron irradiated AISI 304L stainless steel." Materialia 5: 100208. https://doi.org/10.1016/j. mtla.2019.100208.
- [3] K. Mao, et al. 2020. "Role of cavities on deformation-induced martensitic transformation pathways in a laser-welded, neutron irradiated austenitic stainless steel." Scripta Materialia 178: 1–6. https://doi.org/10.1016/j.scriptamat.2019.10.037.
- [4] K. Mao, et al. 2020. "Effect of laser welding on deformation mechanisms in irradiated austenitic stainless steel." Journal of Nuclear Materials 528: 151878. https://doi.org/10.1016/j.jnucmat.2019.151878.
- [5] H. Han, et al. 2004. "A model for deformation behavior and mechanically induced martensitic transformation of metastable austenitic steel." Acta Materialia 52(17): 5203–5214. https://doi.org/10.1016/j.actamat.2004.07.031
- [6] U. Kaiser and W. Richter. 2001. Jap Soc Elec Microsc 50 (2001) 3.
- [7] M. Castell. 2003. "Wulff shape of microscopic voids in UO2 crystals." Physical Review B 68: 235411. https://doi.org/10.1103/PhysRevB.68.235411.
- [8] R. Chatzimichail, S. Bebelis, and P. Nikolopoulos. 2016. "Temperature Dependence of the Surface Energy of the Low Index Planes of UO2 and ThO2." Journal of Materials Engineering and Performance 25: 1691–1696. https://doi.org/10.1007/s11665-016-2030-7.
- [9] W. Xu, et al. 2013. "In-situ atomic-scale observation of irradiation-induced void formation." Nature Communications 4: 2288. https://doi.org/10.1038/ncomms3288.
- [10] Y. Huang, et al. 2015. "Microstructural characterization and density change of 304 stainless steel reflector blocks after long-term irradiation in EBR-II." Journal of Nuclear Materials 465: 516–530. https://doi.org/10.1016/j.jnucmat.2015.06.031.
- [11] Y. Dong, et al. 2015. "Microchemical and microstructural evolution of AISI 304 stainless steel irradiated in EBR-II at PWR-relevant dpa rates." Journal of Nuclear Materials 467(Part 2): 692–702. https://doi.org/10.1016/j.jnucmat.2015.10.041.
- [12] F. A. Garner, et al. 2007. "Measurement of Helium Generation in AISI 304 Reflector and Blanket Assemblies after Long-term Irradiation in EBR-II." Journal of ASTM International 4(1): 1–8. https://doi.org/10.1520/JAI100342.
- [13] M. P. Short, et al. 2016. "Modeling injected interstitial effects on void swelling in self-ion irradiation experiments." Journal of Nuclear Materials 471: 200–207. https://doi.org/10.1016/j.jnucmat.2015.10.002.
- [14] L. Mansur.1978. "Correlation of neutron and heavy-ion damage: II. The predicted temperature shift if swelling with changes in radiation dose rate." Journal of Nuclear Materials 78(1): 156–160. https://doi.org/10.1016/0022-3115(78)90514-7.
- [15] M. Saleh, et al., 2019. "Oblique cross-section nanoindentation for determining the hardness change in ion-irradiated steel." International Journal of Plasticity 112: 242–256. https://doi.org/10.1016/j.ijplas.2018.08.015.
- [16] K. Mao, et al. 2018. "Laser weld-induced formation of amorphous Mn–Si precipitate in 304 stainless steel." Materialia 3: 174–177.

RTE 4603: Neutron Irradiation of Updated In-Pile Steady-State, Extreme Temperature Experiment (INSET)

PI: Emily Hutchins, University of Tennessee, Knoxville (UTK)

Collaborators: N. Dianne Bull Ezell, Brandon Wilson, Richard Howard (ORNL), Lawrence Heilbronn (UTK)

Facility: OSU Research Reactor, The Ohio State University

The characterization of materials and instrumentation at temperatures up to and exceeding 2000°C under neutron irradiation is limited. The survivability of the materials and instrumentation in extreme environments limits the nextgeneration nuclear-reactor technologies that will operate in these conditions. Full-scale testing of each advanced-reactor design is costly and unrealistic for the selection of candidate materials, fuels, and sensors. The need is for an experiment vehicle capable of producing the prototypic radiation, thermal, and atmospheric environments expected for each advanced technology. Oak Ridge National Laboratory (ORNL) and University of Tennessee, Knoxville (UTK) designed the In-Pile Steady State Extreme Temperature (INSET) experiment to address this gap in adaptable experiment capabilities. INSET is a hightemperature experiment vehicle compatible with research reactors across the U.S. to achieve the prototypic fluence and temperatures anticipated by such advanced nuclear-reactor designs as nuclear thermal rockets, microreactors, and high-temperature gas-cooled reactors. INSET has been used as a guick and inexpensive option for scalable candidate material and sensor testing at high temperatures under neutron irradiation. The INSET design was updated with a new graphite heating element and insulation structure, allowing for higher temperatures and larger samples than the previous iteration. This study demonstrates the upgraded design of INSET under neutron irradiation to characterize its steady-state operation at temperatures above 2000°C.

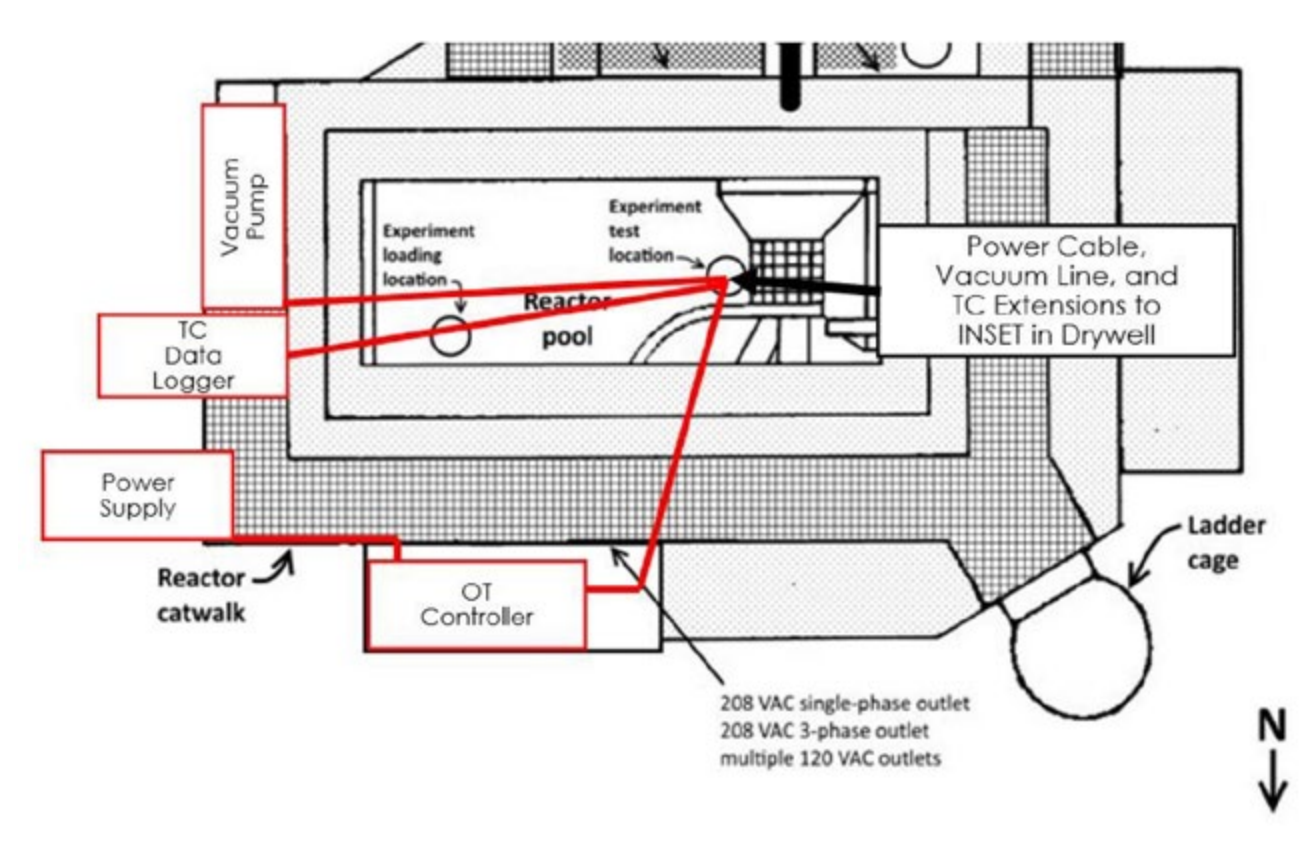


Figure 1. Configuration of equipment connected to INSET at the OSUNRL.

INSET was assembled at ORNL and irradiated in the at the Ohio State Research Reactor (OSURR) 10-in. dry-tube facility. A power supply, vacuum pump, thermocouple data logger, and over-temperature (OT) controller were set up and connected to INSET at the OSUNRL the day prior to irradiation, as illustrated in Figure 1. The direct current power was supplied to INSET using a 3-kw Elektro-Automatik power supply, and the experiment maintained an internal vacuum using an Edwards dry-scroll pump. The internal and external temperature of INSET was monitored in situ with two K-type and two C-type thermocouples, shown in Figure 2. The temperature at each thermocouple was collected throughout the entire irradiation using a Grant Squirrel SQ2020 data logger. OSU provided an OT controller, which was configured at ORNL to shut off the direct-current power supply if the external surface temperature of INSET exceeded 300°C.

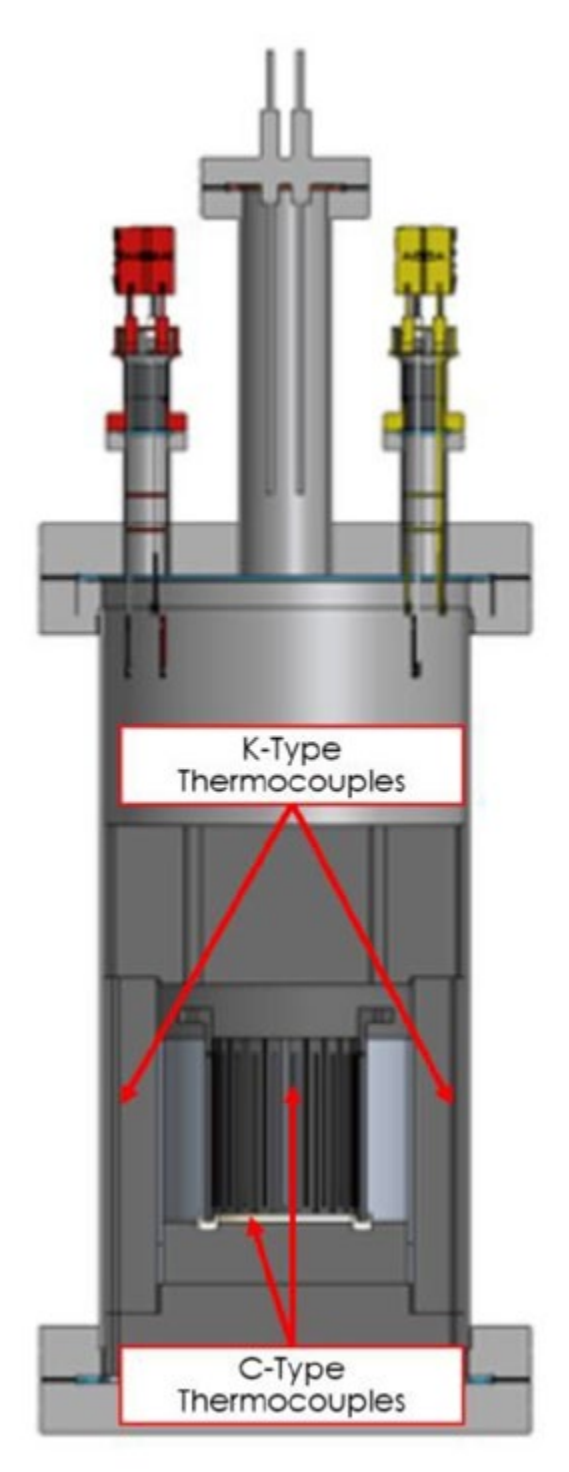


Figure 2. Thermocouple placement within INSET.

The approved reactor power levels and anticipated INSET operation temperatures for the 2-day irradiation are shown in Figure 3, and the resulting neutron fluence, calculated from the power profiles, is shown in Table 1. Figure 4 illustrates the placement of INSET in the dry well, overlaid with the neutron-flux map of the OSURR at 450 kW.

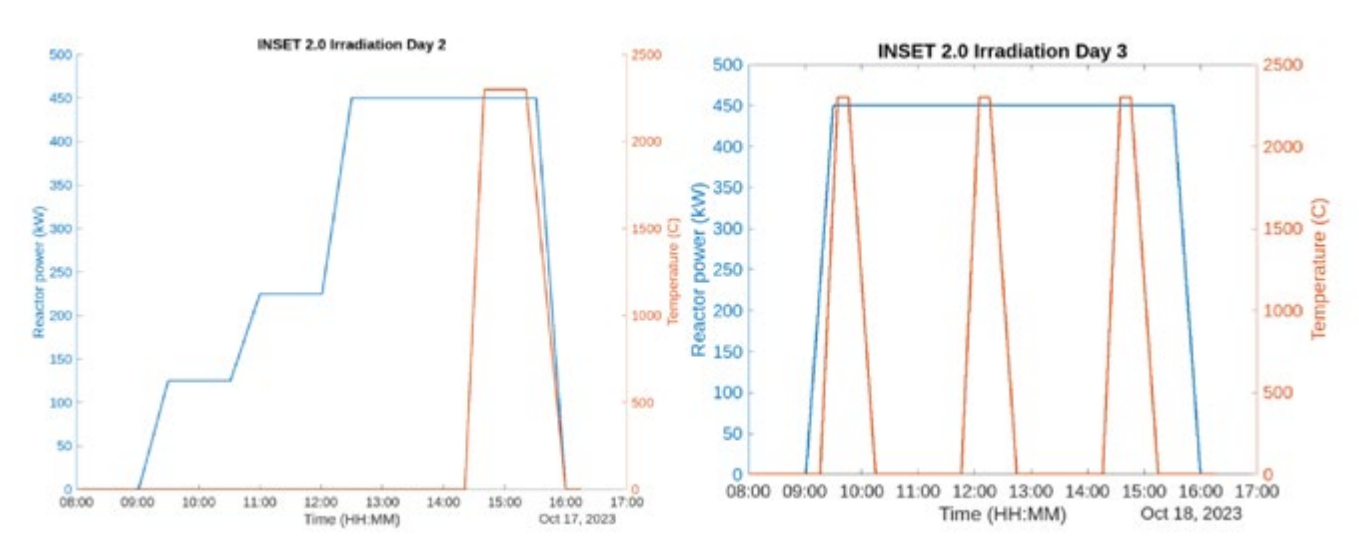


Figure 3. Anticipated reactor power levels and experiment temperatures.

Table 1. Accumulated neutron fluence for INSET irradiation.

Date Neutron	Fluence (n/cm²)
10/17/2023	2.40×10^{16}
10/18/2023	3.28×10^{16}
Total	5.68×10^{16}

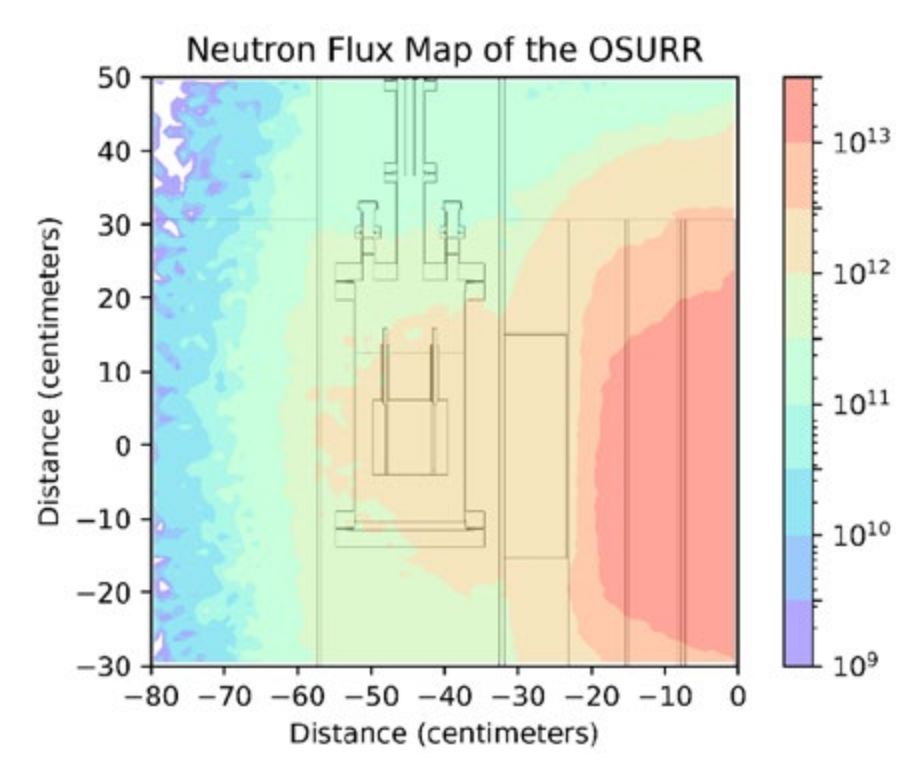


Figure 4. Neutron-flux map and INSET placement in dry tube.

This RTE was designed to demonstrate the upgraded INSET experiment vehicle under neutron irradiation to characterize its performance at temperatures above 2000°C. The temperature data recorded by the thermocouples confirm the successful demonstration of the INSET furnace. The experiment operated for a total of four thermal cycles throughout the 14-hour neutron irradiation, accumulating roughly 30 minutes of steady-state operation at the target temperature. These cycles are shown with the reactor power in Figure 5. Though the length of steady-state operation diminished with each successive cycle, these results establish INSET as the only high-temperature furnace capable of testing candidate materials, fuels, and instrumentation for advanced-reactor technologies under neutron irradiation.

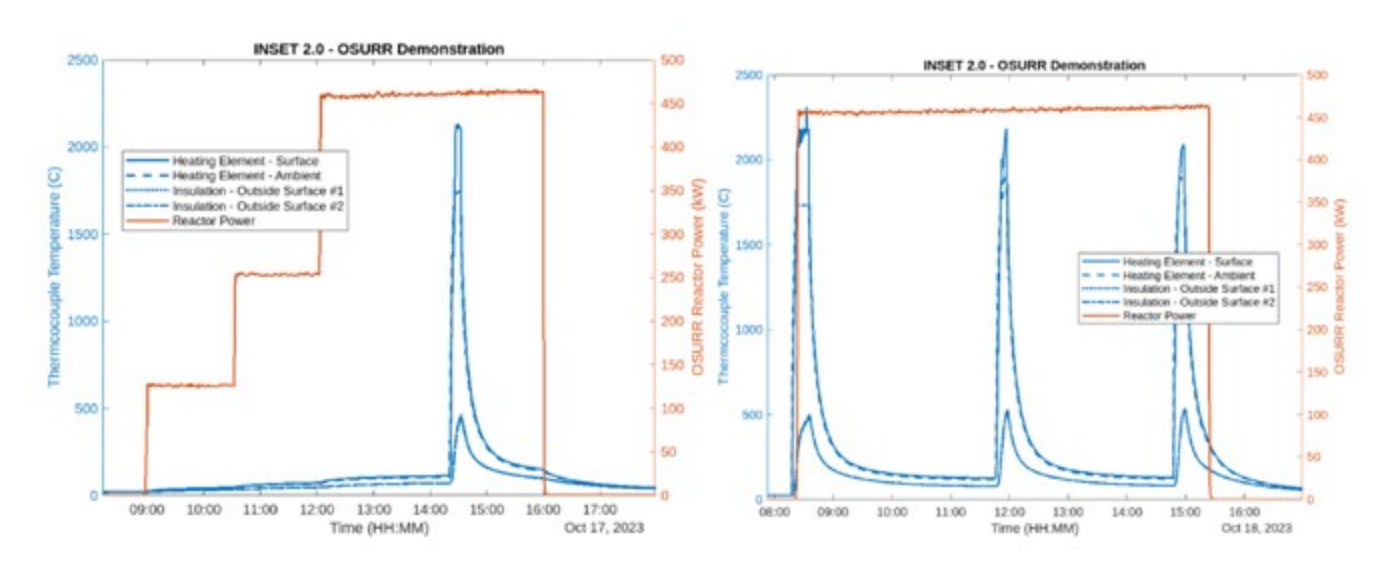


Figure 5. Power and temperature profiles of completed INSET irradiation demonstration.

The full results will be published in a nuclear engineering or nuclear technologies journal.

RTE 4629: Atom Probe Characterization of HT-9 as a Function of Neutron-Irradiation Temperature

Ramprashad Prabhakaran (PNNL)

Facility: Microscopy and Characterization Suite, Center for Advanced Energy Studies; Materials Science and Technology Laboratory, Pacific Northwest National Laboratory

Introduction

F-M steels such as HT-9 are being considered as candidate in-core structural materials for fast reactors and advanced light water reactors (LWRs) due to their excellent resistance to radiation-induced void swelling, microstructural stability, thermal conductivity, and superior irradiation-creep properties [1–5]. The progressive change in microstructure with irradiation dose and temperature includes void formation, changes in dislocation density, second-phase formation, and other changes that can lead to swelling, hardening, and embrittlement. Notable hardening and embrittlement occurs at temperatures of ~425°C and below in F-M steels due to significant increases in dislocation density and the formation of various compositions and number densities of second-phase particles that act to reduce dislocation mobility [2]. Previous studies have shown that the formation of second-phase precipitates along with pointdefect clusters can increase the ductile-to-brittle transformation temperature and yield strength that is accompanied with a decrease in ductility [6]. The mechanical properties of HT-9 after neutron

irradiation varies based on the manufacturing process, chemical composition, initial microstructure, second-phase particles— α' , G-phase, Chi, M₂₃C₆, M₆C and Laves—irradiation dose, and temperature [2].

To address the issue of lowtemperature (<425°C) neutronirradiation hardening and embrittlement, it is necessary to conduct systematic investigations on the mechanical behavior and microstructure of HT-9 with slight variations in chemical composition and heat treatment over a range of doses and temperatures. Three HT-9 heats (ORNL, LANL and Experimental Breeder Reactor II [EBR-II]: see Tables 1 and 2) with variations in manufacturing process, chemical composition, and heat treatment were neutron irradiated (~4 dpa) in the ATR at different temperatures (241–469°C), as a part of the UW-M **NSUF** Pilot irradiation experiment (led by Dr. Kumar Sridharan, a collaborator in this RTE project). PNNL recently won an NSUF RTE Award (1687, PI: Ramprashad Prabhakaran) and completed microhardness and tensile testing of HT-9 variants (~4 dpa) as a function of irradiation temperature. Tensile

testing at irradiation temperatures showed the highest increase in yield strength at 241°C, followed by 388 and 469°C. Maximum impact of this work will be obtained by performing TEM and APT characterization of these neutron-irradiated samples present at PNNL to correlate the measured hardening with microstructural features.

Objectives

The objective of RTE Project 4629 is to evaluate the formation of α' and Ni/Mn/Si precipitation in neutron irradiated (~4 dpa) HT-9 as a function of irradiation temperature (~241, ~388, and ~469°C). Considering the RTE funding availability, we limited the number to four irradiated samples (as shown in Table 3) to study a range of temperatures that is relevant for α' precipitation studies and LWR and advanced-reactor applications.

Research Work

No irradiation task was included in the scope of RTE Project 4629 because the neutron irradiation on HT-9 tensile specimens was already performed at the ATR through a UW-M NSUF irradiation experiment led by Dr. Kumar Sridharan.

HT-9 samples (ORNL and EBR-II heats) were neutron irradiated (~4 dpa) at LWR- and fast-reactorrelevant temperatures (i.e., 241-469°C) in ATR. Tables 1 and 2 show the chemical composition and heat treatment of three HT-9 heats. These samples were shipped to PNNL from the NSUF library earlier, and PNNL recently completed tensile and microhardness testing using polished sections from shoulders of tested tensile specimens (i.e., from undeformed regions, as shown in Table 3) under a RTE Project 1687. Four mounted and polished irradiated HT-9 samples were available for RTE Project 4629, as shown in Table 3.

PIE work on RTE Project 4629 involved preparing four neutron-irradiated HT-9 liftouts (i.e., 5–6 unsharpened tips from each sample), using FIB at PNNL, and then shipping unsharpened tips to CAES. Researchers at CAES prepared APT needles and then conducted APT characterization of neutron irradiated HT-9 samples, as shown in Table 3.

Task 1: Prepare APT liftouts from neutron-irradiated HT-9 samples and shipped from PNNL to CAES

The FIB at PNNL was employed to prepare APT liftouts of unsharpened tips from four polished HT-9 samples (KGT 3466, 1622, 265, and 287). Figure 1 shows the layout of APT liftouts obtained from neutron irradiated HT-9 samples. These APT liftout unsharpened tips (at very low activity levels due to the smaller volume) were shipped from PNNL to CAES.

Task 2: Prepare APT needles from neutron-irradiated HT-9 liftouts at CAES

CAES received APT liftout unsharpened tips from PNNL and then prepared APT tips from neutron irradiated HT-9 samples.

Task 3: Perform APT studies on neutron irradiated HT-9 samples at CAES

APT evaluations were performed on neutron irradiated HT-9 samples (as shown in Table 3) using a LEAP 4000X HR) at CAES to study the atomic-level details (elemental segregation, precipitation, and second phases) and determine the size, number density, and chemical composition of the α' and G-phase precipitates. The resulting data were reconstructed (as seen in Figures 2 and 3) using IVAS data visualization and analysis software at CAES and INI.

The APT data were successfully obtained from two irradiated HT-9 samples (KGT 265 and 287; 5-6 tips per sample) placed on one side the array (in a sample holder). However, the APT data could not be obtained from other two samples (KGT 3466) and 1622; 5-6 tips from each sample) placed on the other side of the array. CAES and INL researchers employed both voltage and laser modes to obtain APT data, but they were not successful. It appears that all the tips (5–6 tips from each sample) from two samples (KGT 3466 and 1622) may have been destroyed while obtaining data from the first two samples. They mentioned that this type of issue (all tips getting destroyed on one side while getting data from the other side) is very rare, but it did happen at times over the past 10 years. The reason is unknown. CAES researchers mentioned that they had a discussion with other researchers in the field, but they could not find a satisfactory root cause.

The PI contacted NSUF staff and obtained permission to add these two irradiated HT-9 samples (KGT 3466 and 1622) that did not give APT results to another recently funded RTE project (4900, PI: Ramprashad Prabhakaran) that also deals with neutron-irradiated HT-9 samples with different irradiation conditions, as shown in Table 3.

Table 1. Chemical composition of three neutron-irradiated HT-9 heats (ORNL, LANL and EBR-II).

Alloy/Heat	Cr	C	Si	Mn	W	V	Мо	Ni	Others, Fe: balance
HT-9/ORNL	11.63	0.20	0.22	0.52	0.52	0.30	1.00	0.50	N 0.047; Al <0.01; P 0.02; S 0.006; Ti <0.01; Cu 0.04; Co 0.08
HT-9/LANL	12.10	0.17	0.41	0.61	0.58	0.34	0.97	0.59	N 0.031; Al 0.007; P 0.007; S 0.004; Ti 0.002; Cu 0.03; Co 0.009; O 0.013
HT-9/EBR-II	11.92	0.22	0.39	0.76	1.04	0.22	1.01	0.92	_

Table 2. Heat-treatment information of three neutron-irradiated HT-9 heats (ORNL, LANL and EBR-II).

Material	Heat Treatment
HT-9/ORNL	1040°C for 60 min, air cooled; 740°C for 45 min, air cooled
HT-9/LANL	1040°C for 30 min, air cooled; 760°C for 60 min, air cooled
HT-9/EBR-II	1060°C for 60 min, air cooled; 730°C for 120 min, air cooled

Table 3. Summary of ATR neutron-irradiated samples studied under RTE 4629.

Alloy/ heat	ID	Irradiation Temp. (°C)	Dose (dpa)	Tensile Tested [†]	Hardness Tested [†]	APT liftouts (PNNL)	APT tips and data (CAES)
HT-9 (ORNL)	KGT 3466	241	3.37	Irr T	RT	✓ (RTE 4629) will be repeated under RTE 4900	✓ x (RTE 4629) will be repeated under RTE 4900
	KGT 1622	388	4.08	Irr T	RT	✓ (RTE 4629) will be repeated under RTE 4900	✓ x (RTE 4629) will be repeated under RTE 4900
	KGT 265	469	4.28	Irr T	RT	✓ (RTE 4629)	✓ ✓ (RTE 4629)
	Unirradiated	_	_	RT & Irr T	RT	Ongoing RTE 4900	Ongoing RTE 4900
HT-9		Irr T	RT	Ongoing RTE 4900	Ongoing RTE 4900		
(EBR-II)	KGT 287	388	4.10	Irr T	RT	✓ (RTE 4629)	✓ ✓ (RTE 4629)
	KGT 1759	452	3.88	Irr T	RT	Ongoing RTE 4900	Ongoing RTE 4900
	Unirradiated		_	RT & Irr T	RT	Ongoing RTE 4900	Ongoing RTE 4900

[†] Tensile and microhardness testing at PNNL was performed earlier under a different RTE award (1687, PI Ramprashad Prabhakaran).

The PI obtained permission from the NSUF staff to prepare APT liftouts at PNNL from KGT 3466 and 1622 and to repeat APT data collection at CAES to obtain data along with RTE 4900 project samples.

[✓] APT liftouts were fabricated using FIB at PNNL and shipped to CAES (under RTE Project 4629, PI: Ramprashad Prabhakaran).

 $[\]checkmark$ APT needles were fabricated, and APT data were obtained successfully at CAES (under RTE Project 4629).

 $[\]checkmark$ X APT needles were fabricated, but did not obtain APT data successfully at CAES (under RTE Project 4629). NSUF RTE 4900 is currently ongoing at PNNL and CAES.

RT: Room temperature

Irr T: Irradiation temperature.

Ongoing work—Develop Appropriate Structure-Property Temperature Correlations

Microhardness and tensile testing of control and irradiated HT-9 samples were recently completed under a funded RTE project (1687). The mechanical test and APT data (as a function of irradiation temperature at ~4 dpa for RTE Project 4629) would be analyzed (using advanced-cladding development R&D funds at PNNL) to understand the effects of radiation damage on HT-9 at LWR- and fast-reactor-relevant temperatures, and to develop appropriate structure-property temperature correlations.

Potential Impact to the State of Knowledge

The phase instability under neutron irradiation is known to strongly impact the mechanical properties of structural materials and is one of the lifetime-limiting factors for high-Cr steel for nuclear applications. Alloy HT-9 can form detrimental Cr-rich α' precipitates and Ni/Si clusters under radiation, like most high-Cr ferritic alloys. The formation of these two types of precipitates will result in radiation hardening and embrittlement. Hence, it is essential to identify the thermal- and irradiation-induced second-phase precipitates and understand their influence on mechanical behavior.

We employed APT to enhance understanding of the underlying mechanisms for α' and Ni/Mn/Si-precipitate evolution in HT-9 upon neutron irradiation. Currently, comprehensive data analysis is ongoing to determine the size, number density, and chemical composition of α' and Ni/Mn/Si precipitates. To understand the contributions to irradiation hardening, the dispersed barrier-hardening model will be employed to determine the changes in yield strength induced by each type of obstacles, and then compare the measured hardening (tensile and microhardness data from previously funded RTE 1687; $\Delta\sigma_y \sim 28\%$ at 241°C; 11% at 291°C; 8% at 388°C) with microstructure-deduced hardening contributions obtained from APT (this RTE project; α' and G phases) and TEM.

This RTE project—for which data collection is complete and data analysis, ongoing—enabled our team to contribute to fill the gap in the literature on understanding the irradiation effects on HT-9 and F-M steels in general. The RTE project test results and comprehensive data analysis will benefit the Office of Nuclear Energy R&D programs involved in developing advanced structural materials with greater radiation resistance. Thus, this work is well-aligned with the office's missions and vision for the deployment of next-generation advanced reactors.

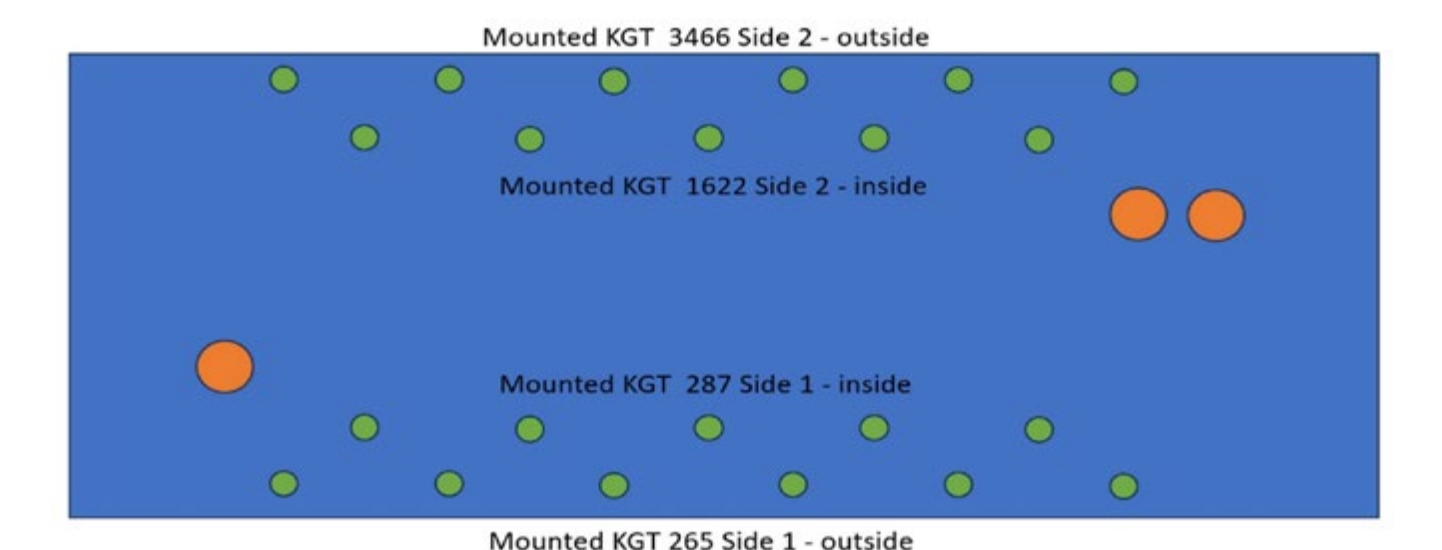


Figure 1. Layout of neutron-irradiated HT-9 APT liftouts (shown by green circles) prepared at PNNL and shipped to CAES.



lon Type	Concentration (at. %)	Error (%)
Fe	86.81	0.01
Cr	10.48	0.02
Mn	0.59	0.02
С	0.41	0.00
Ni	0.50	0.00
Мо	0.48	0.00
Si	0.26	0.00
W	0.10	0.00
Со	0.07	0.00
Cu	0.04	0.00
Р	0.02	0.00
Al	0.01	0.00

Figure 2. APT reconstruction data from neutron-irradiated HT-9 ORNL heat (KGT 265, 469°C, ~4 dpa).



lon Concentration **Error** (at. %) Type (%) Fe 86.45 0.01 Cr 10.55 0.02 Mn 0.70 0.02 Si 0.65 0.00 Ni 0.59 0.00 Мо 0.49 0.00 (0.14 0.00 W 0.11 0.00 Co 0.04 0.00 Cu 0.02 0.00 Р 0.01 0.00 Αl 0.00 0.00

Figure 3. APT reconstruction data from neutron-irradiated HT-9 EBR-II heat (KGT 287, 388 °C, \sim 4 dpa).

Acknowledgements

The neutron irradiation at ATR, sample preparation at PNNL, and PIE at CAES were supported primarily by the U.S. DOE, Office of Nuclear Energy under DOE Idaho Operations Office Contract DE-AC07-051D14517 as part of NSUF experiments under the UW-M Pilot Irradiation Experiment and PNNL RTE Project 4629, respectively.

The PI would like to acknowledge the assistance of Collin Knight and other NSUF staff at INL for their help earlier in identifying neutron-irradiated HT-9 samples and shipping them to PNNL for RTE Project 1687. The PI would like to thank Kumar Sridharan of UW-M for providing information about the chemical composition and heat treatment of neutron-irradiated HT-9 samples.

The PI would like to recognize the technical support of Kayla Yano for preparing APT liftouts at PNNL, and Yu Lu and Yaqiao Wu at CAES for preparing APT needles and performing APT data collection. The PI appreciates the support of Mukesh Bachhav and Sohail Shah at INL for APT data reconstruction and analysis. The PI would also like to acknowledge Stuart Maloy of PNNL, the NSUF technical lead, for NSUF RTE project coordination.

References

- [1] S. A. Maloy, et al. 2011. "Core materials development for the fuel cycle R&D program." *Journal of Nuclear Materials* 415: 302–305. https://doi.org/10.1016/j.jnucmat.2011.04.027.
- [2] R. L. Klueh and A. T. Nelson. 2007. "Ferritic/martensitic steels for next-generation reactors." *Journal of Nuclear Materials* 371: 37–52. https://doi.org/10.1016/j.jnucmat.2007.05.005.
- [3] T. S. Byun et al. 2012. "Impact properties of irradiated HT9 from the fuel duct of FFTF." *Journal of Nuclear Materials* 421: 104–111. https://doi.org/10.1016/j.jnucmat.2011.11.059.
- [4] M. B. Toloczko and F. A. Garner. 1996. "Irradiation creep and void swelling of two LMR heats of HT9 at \sim 400°C and 165 dpa." *Journal of Nuclear Materials* 233–237: 289–292. https://doi.org/10.1016/S0022-3115(96)00413-8.
- [5] O. Anderoglu et al. 2013. "Mechanical Performance of Ferritic Martensitic Steels for High Dose Applications in Advanced Nuclear Reactors." *Metallurgical and Materials Transactions* A 44A: 70–83. https://doi.org/10.1007/s11661-012-1565-y.
- [6] M. Bachhav et al. 2014. "α' precipitation in neutron-irradiated Fe–Cr alloys." *Scripta Materialia* 74: 48–51. https://doi. org/10.1016/j.scriptamat.2013.10.001.

Conference Presentations

- [1] Ramprashad Prabhakaran, Indrajit Charit, Dan Edwards, Mychailo Toloczko, Stuart Maloy, Kumar Sridharan, "Mechanical and microstructural characterization of neutron irradiated HT-9 and NF616 (Grade 92) at LWR and fast reactor relevant temperatures," 2023 TMS Annual Meeting & Exhibition, Mar 19–23, 2023, oral presentation (RTE 1687).
- [2] Ramprashad Prabhakaran, Indrajit Charit, Dan Edwards, Mychailo Toloczko, Stuart Maloy, Kumar Sridharan, "Mechanical and microstructural characterization of neutron irradiated HT-9 and NF616 (Grade 92) at LWR and fast reactor relevant temperatures," Materials in Nuclear Energy Systems (MiNES) 2023, New Orleans, LA, Dec 10–14, 2023, oral presentation (RTE 1687).

RTE 4636: Stability of VN, TaN, and TaC MX-Type Precipitates in Ferritic Steels Under Neutron Radiation

PI: Emily Proehl (UTK)

Collaborators: Weicheng Zhong (ORNL), Steve Zinkle (UTK)

Facility: Low Activation Materials Development and Analysis Laboratory, Oak Ridge National Laboratory

One prominent strategy for designing mechanically robust and radiationresistant nuclear-reactor structural materials is engineering a high density of nanoscale precipitates to act as barriers to dislocation motion and point defect sinks for RIDs. The stability of these nanoscale precipitates is crucial to maintaining favorable mechanical properties in a radiation environment. F-M steels are a leading structural-material candidate for such advanced-reactor concepts as cladding in sodium-cooled fast reactors, the Traveling Wave Reactor, and various other small-modular-reactor designs. F-M steels have several precipitate phases, but the introduction of minor alloying elements to form relatively stable, nanosized MX-type (M=metal, X=C, N) precipitates in F-M steels from the 1970s through the 2000s has, in part, enabled an increase in operating temperature of fossil plants of ~100°C, leading to major increases in thermal efficiency and significant cost savings. Similarly, stable MX-type precipitates could appreciably enhance the radiation tolerance of FM steels for advanced-reactor concepts. However, the relative stability of specific MX-precipitate compositions in a nuclear-reactor environment is not well understood.

The objective of the proposed work was to investigate the stability of various MX-type precipitate compositions in a ferritic matrix under neutron irradiation. Three model ferritic alloys containing different MX-type precipitate compositions, TaC, TaN, and VN, were designed, fabricated, and irradiated in the High Flux Isotope Reactor (HFIR) at 490°C to 7.4 dpa. FIB was used to prepare samples of the as-received and irradiated materials. STEM imaging and EDS were used to study the relative stability of the three MX-type precipitate compositions in a ferrite matrix after irradiation. The samples included and work accomplished in this study are enumerated in Table 1. Representative images from the STEM work are displayed in Figure 1.

Table 1. Summary of work accomplished in part with NSUF proposal #23-4636.

MX precipitate composition in model ferritic alloy	Irradiation conditions in HFIR	TEM sample preparation with FIB	Acquisition of S/TEM data
TaC	As received	Χ	Χ
TaC	490°C, 7.4 dpa	Χ	Χ
TaN	As received	Χ	Χ
TaN	490°C, 7.4 dpa	Χ	Χ
VN	As received	Χ	Χ
VN	490°C, 7.4 dpa	Χ	Χ

The size, shape, and number density of the MX-type precipitates were quantified and shown quantitatively and schematically in Figure 2. The hypothesis of the proposed research stated that TaC was anticipated to have the greatest stability under neutron irradiation, based on previous thermalaging and ion-irradiation results. The hypothesis was confirmed that TaC has superior stability to TaN and VN after neutron irradiation, using size, morphology, and number density as the relevant stability metrics. Up to 7.4 dpa, transmutation of Ta to W did not seem to significantly impact the TaC-precipitate stability. TaN precipitates elongated into thin platelets after irradiation, and VN precipitates exhibited some size instability after irradiation.

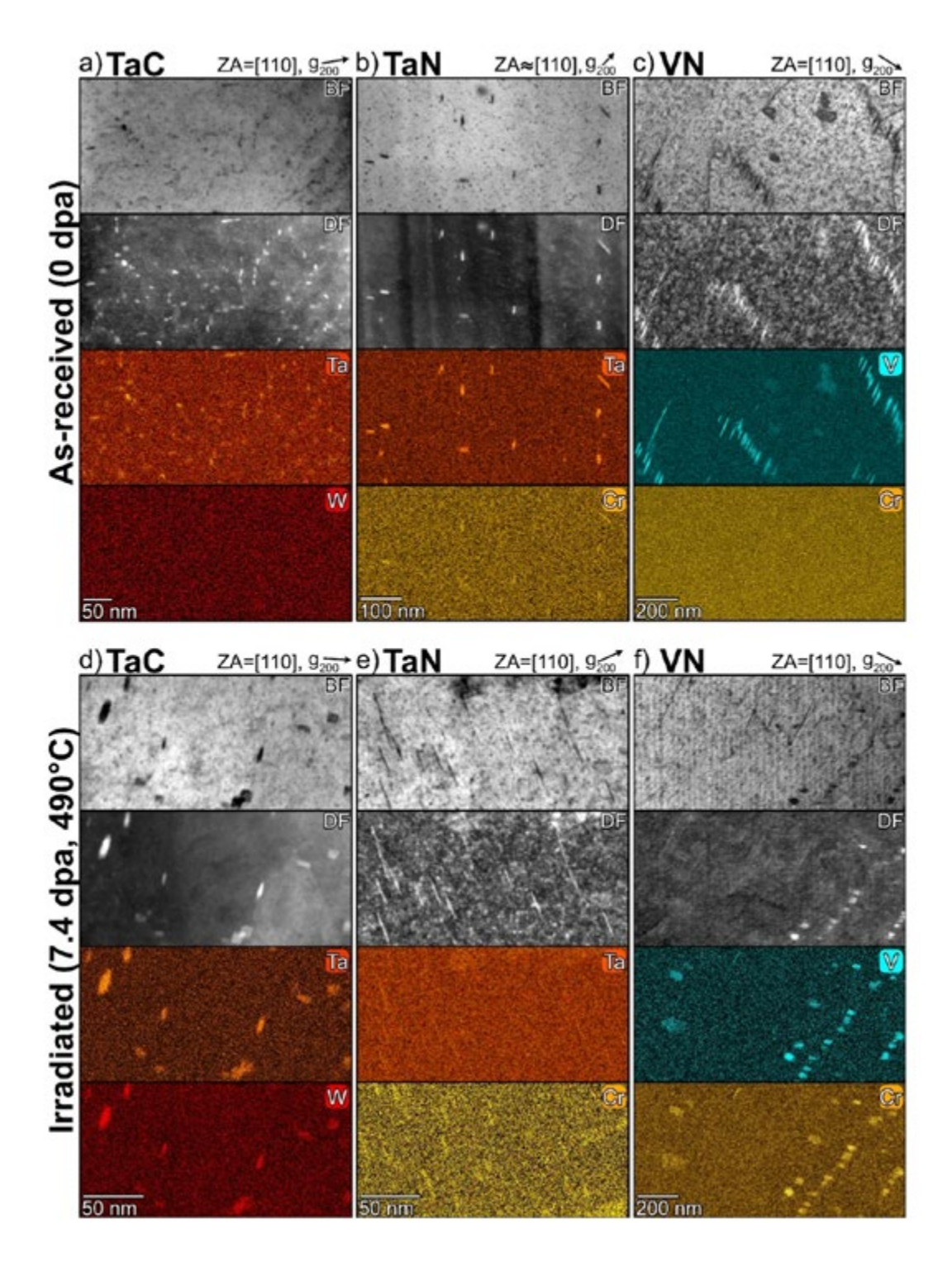


Figure 1. STEM images and EXS maps of the as-received model ferritic alloys with (a) TaC, (b) TaN, and (c) VN MX-type precipitates and irradiated model ferritic alloys (7.4 dpa at $490^{\circ}C$ in HFIR) containing (d) TaC, (e) TaN, and (f) VN MX-type precipitates. The columns of images in (a-f) consist of a STEM- BF image (top), STEM-DF image (second from top), STEM-EDS map of the main cation-site element in the MX-type precipitates (second from bottom), and most-likely element enriched in the MX-type precipitate (bottom).

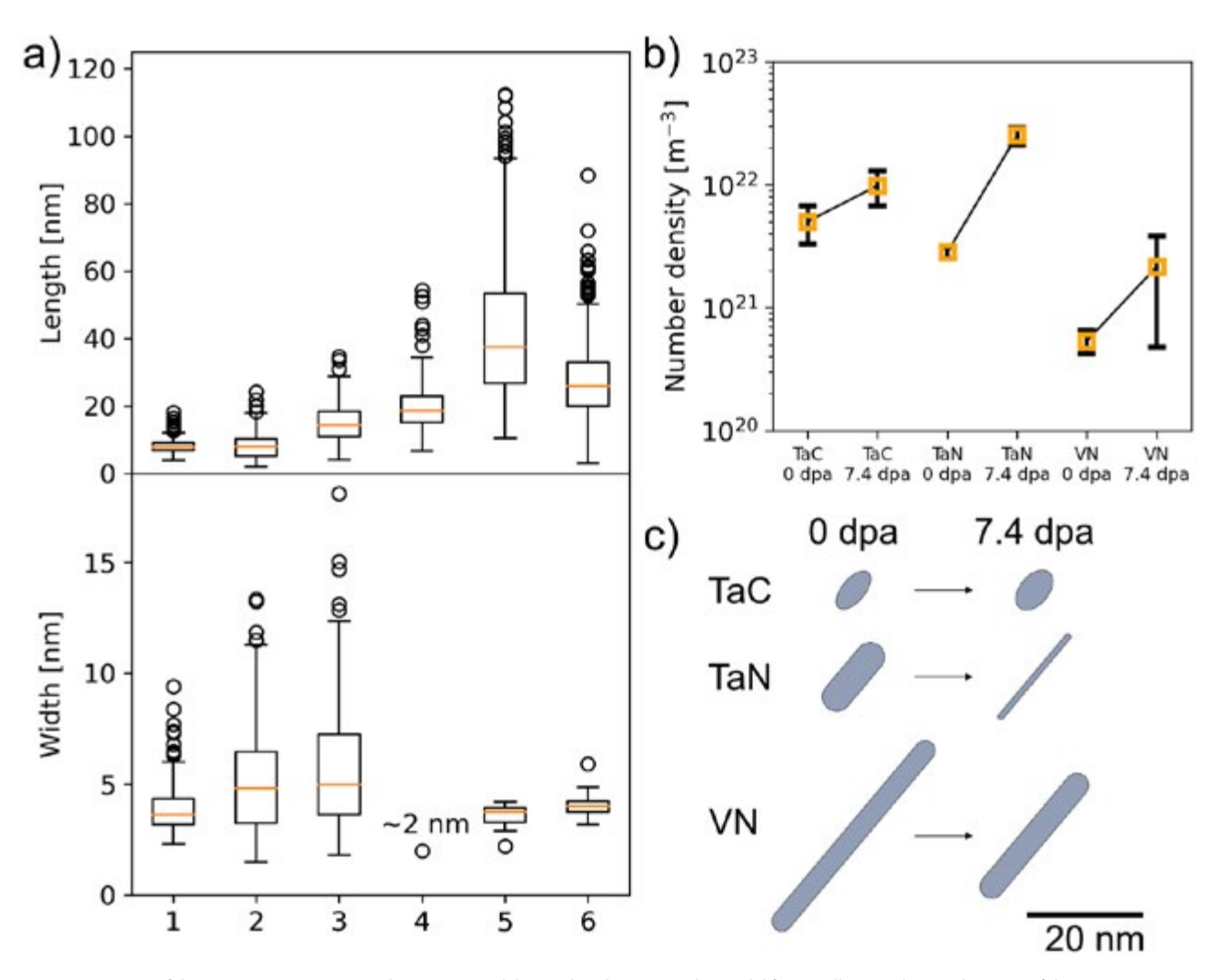


Figure 2. Summary of the MX-type precipitate (a) dimensions and (b) number densities in the model ferritic alloys, and (c) a schematic of the MX-type precipitates depicting the average precipitate morphology before and after irradiation.

RTE 4652: Irradiating a Novel Thin-film Scintillator for Neutron Radiography

PI: Zhibin Yu (Florida State University)

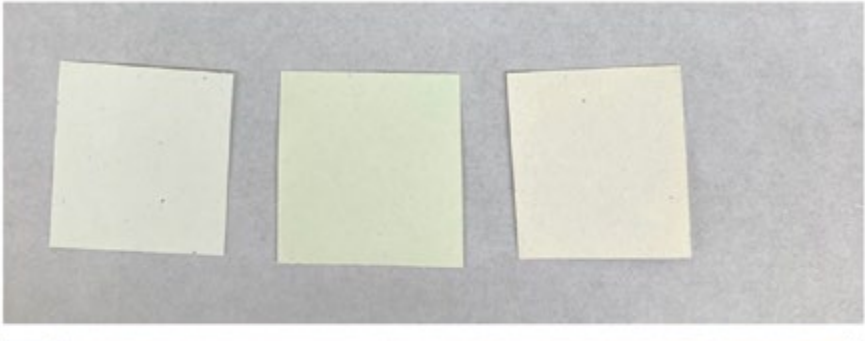
Collaborators: Raymond Cao, Ibrahim Oksuz (OSU)

Facility: OSU Research Reactor, The Ohio State University

Neutron radiography of spent nuclear fuel and other critical components provides comprehensive diagnosis about the internal conditions of a fuel pin for swelling, cracking, and void formation during its normal operation or accident-tolerant testing. Neutron radiography has also shown an increasing importance to examine additively manufactured parts for nuclear applications and structural integrity of dry-cast storage canisters for nuclear waste storage. Gadolinium films, combining X-ray imaging plates, have frequently been used for

neutron radiography. However, the information must be read offline. In contrast, digital neutron radiography delivers simultaneous results for examined objects. State-of-the-art commercial neutron scintillators for digital neutron radiography are based on ⁶LiF/ZnS and ⁶LiF/ gadolinium oxysulfide scintillators, which suffer from a relatively low efficiency of thermal-neutron absorption and a high sensitivity to background X-ray and gamma-ray photons. Dr. Zhibin Yu of Florida State University has developed a novel thin-film scintillator using nanomaterials of a transparent

boron compound (10B enriched) embedded in an organic, inorganic, or hybrid phosphor matrix. During this RTE project period, we tested samples with different ¹⁰B:phosphor ratios and different ¹⁰B areal densities. To summarize, we obtained comparable light output as the commercial gold standard (LiF:ZnS) scintillation screen. Moreover, we achieved even better spatial resolution. The new scintillation screens are also more flexible than the commercial ones. Detailed results are presented in Figures 1 and 2 and Table 1.



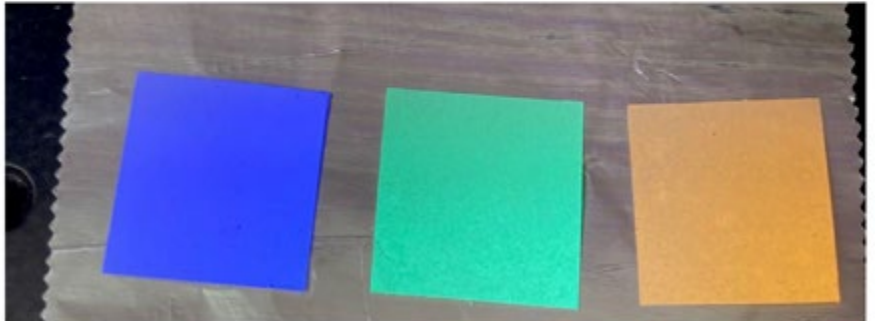


Figure 1. Scintillation screens prepared at Florida State with different phosphors.

Table 1. Summary of light output and spatial resolution of tested samples and comparing with commercial gold standard of LiF:ZnS scintillation screens.

Sample	Light Output, normalized to LiF-ZnS light output (%)	Spation Resolution (μm @ 10% MTF)
S1	33.40	173
S2	39.70	242
S3	45.49	242
S4	49.00	215
S5	32.80	217
S6	45.29	221
S7	52.69	226
S8	49.75	228
S9	45.85	237
S10	54.28	243
S11	56.01	243
S12	52.72	237
S13	44.21	227
S14	44.30	175
200 μm LiF:ZnS	38.77	175
450 μm LiF:ZnS	100.00	259

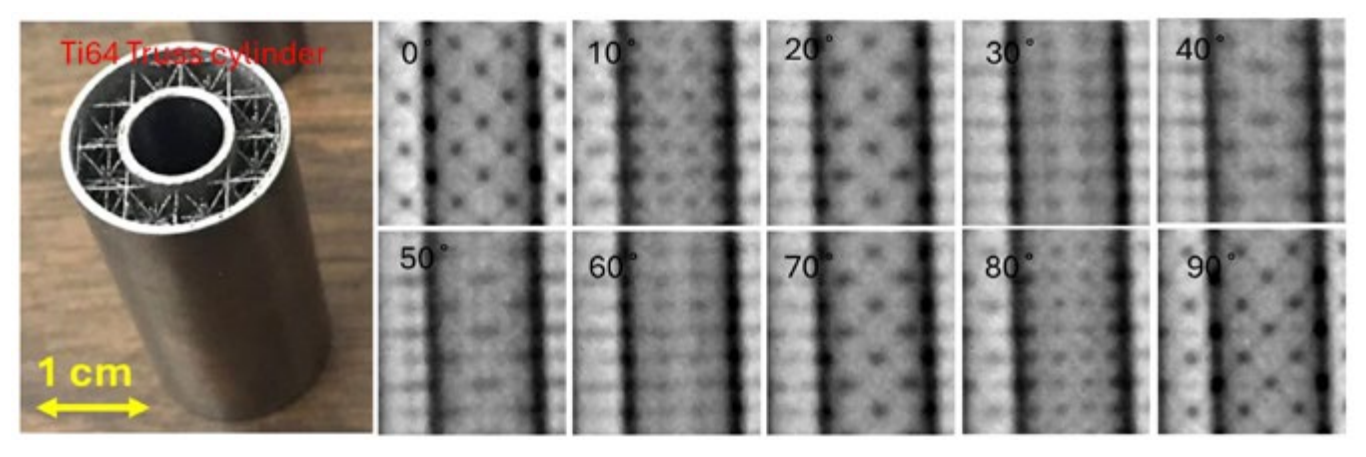


Figure 3. Radiographic images using the new scintillation screen.

RTE 4680: Investigation of Void Swelling and Chemical Segregation in Heavy-Ion Irradiated Compositionally Complex Alloys

PI: Calvin Parkin (UW-M, Sandia National Laboratories)

Collaborators: Adrien Couet, Nathan Curtis (UW-M), Khalid Hattar (UTK), Yaqiao Wu (Boise State University)

Facility: Microscopy and Characterization Suite, Center for Advanced Energy Studies

RTE 4680 has been completed as of August 2024. Ag-coated compositionally complex alloy (CCA) samples, irradiated to 150 dpa at various high temperatures using heavy ions, were successfully characterized using the Super-X EDS and DuelEELS Electron Energy Loss Spectroscopy (EELS) capabilities of the Spectra300 transmission electron microscope at Center for Advanced Energy Studies (CAES).

Ni⁺⁺ ion irradiations at 4.0 MeV were performed to 150-plateau dpa at UW-M Ion Beam Laboratory on Ag-coated fcc CCAs: Cr₁₈Fe₂₇Mn₂₇Ni₂₈ and Cr₁₅Fe₃₅Mn₁₅Ni₃₅, as well as stainless steel 316H at 600 and 650°C. Previously, due to the high vapor pressure and mobility of Mn, significant loss of Mn was observed along the irradiation depth at 600°C in Cr₁₈Fe₂₇Mn₂₇Ni₂₈, which suppressed all void nucleation. It was suspected that this also resulted in partially suppressed swelling in Cr₁₅Fe₃₅Mn₁₅Ni₃₅. Irradiations were reperformed with a 100-nm coating of sputtered Ag to help retain the Mn during irradiation at 600 and 650°C. Stainless steel

reference samples were also coated and irradiated in this way to better understand the holistic effects of the Ag coating on irradiation effects. Lamellae were created using FIB at UW-M and the Center for Integrated Nanotechnologies at Sandia National Laboratories and were characterized by TEM prior to chemical analysis at CAES.

Voids were observed in all materials at both temperatures, with higher levels of void swelling than previously observed at 600°C without the Ag coating (Figure 1), confirming that the coating prevented the egress of Mn, allowing the natural void-swelling behavior of the alloys to occur. A slight depletion of Mn was observed at the surface relative to bulk, but it was significantly less severe than the uncoated Cr₁₈Fe₂₇Mn₂₇Ni₂₈ sample irradiated at 600°C. Both CCAs swelled significantly less than SS316H at 600°C, with comparable swelling at 500 and 650°C. While the swelling decreased in Cr₁₈Fe₂₇Mn₂₇Ni₂₈ and SS316H from 600 to 650°C, the much-lower swelling in Cr₁₅Fe₃₅Mn₁₅Ni₃₅ did not

change significantly, indicating that the swelling peak is likely in between the two temperatures. Although the average void size did increase with temperature in all samples, the reduction in void number density resulted in the reduced swelling that was observed overall (see Table 1). The sample thickness for swelling calculations was performed using the DualEELS capability of the Spectra300, also shown in Figure 1. All samples were characterized for chemical redistribution using Super-X EDS at CAES, both near voids and along the depth profile. Clear Ni enrichment near the surface of voids was observed in all cases. while Fe and Cr are left depleted due to enriched Ni, shown in Figure 2. Away from voids, Mn and Ni show depth-dependent enrichment and depletion, which will provide info about vacancy diffusion (see Figure 3). Mn tends to be enriched near the displacement-damage peak and depleted beyond, with the peak shifting ~400-500 nm deeper in Cr₁₈Fe₂₇Mn₂₇Ni₂₈ due to the slightly increased mobility of the higher Mncontent alloy.

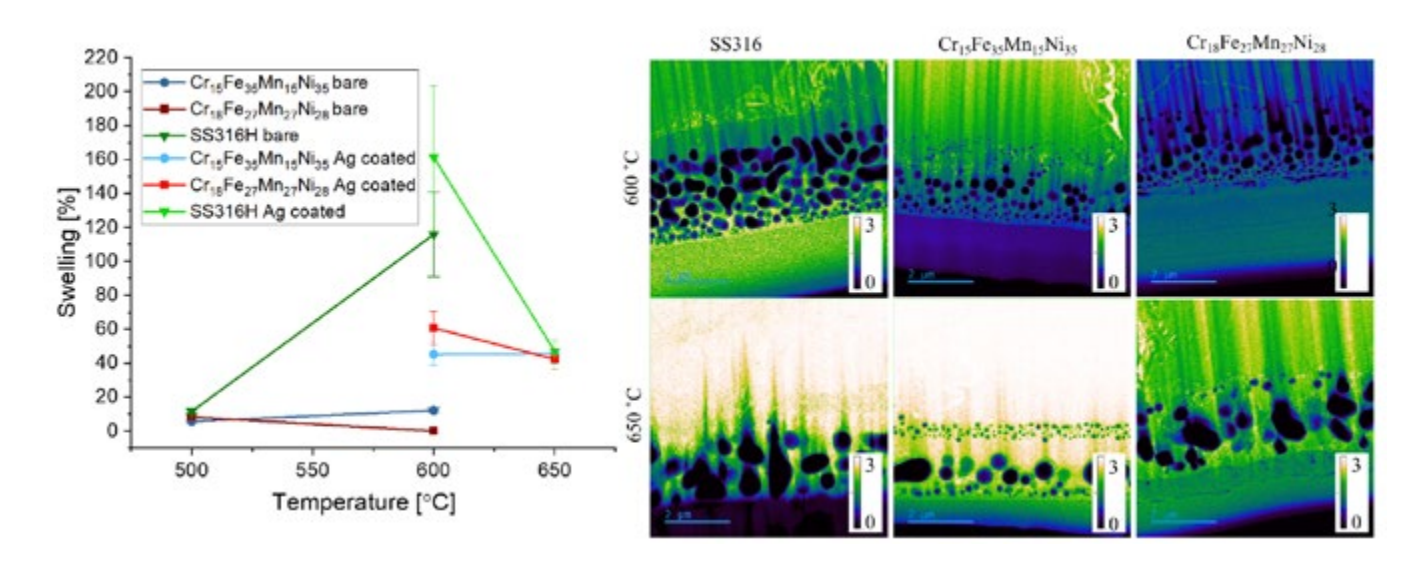


Figure 1. Calculated void swelling compared to uncoated samples irradiated at 500 and 600° C (left) and EELS mean-free path maps of all lamellae, used to calculate sample thickness and swelling (right). Note: only plateau voids were used to calculate swelling (see population of deep small voids in $Cr_{15}Fe_{35}Mn_{15}Ni_{35}$).

Table 1. Average void size and void number density for all irradiated samples.

	SS316H	Cr ₁₅ Fe ₃₅ Mn ₁₅ Ni ₃₅	Cr ₁₈ Fe ₂₇ Mn ₂₇ Ni ₂₈
600°C	$263 \pm 202 \\ 3.64 \times 10^{19}$	$148 \pm 89 \\ 1.20 \times 10^{20}$	152 ± 78 1.50×10^{20}
650°C	404 ± 258 8.51×10^{18}	248 ± 175 1.93×10^{19}	319 ± 243 1.23×10^{19}

Average void size shown as % Void number density within m⁻³

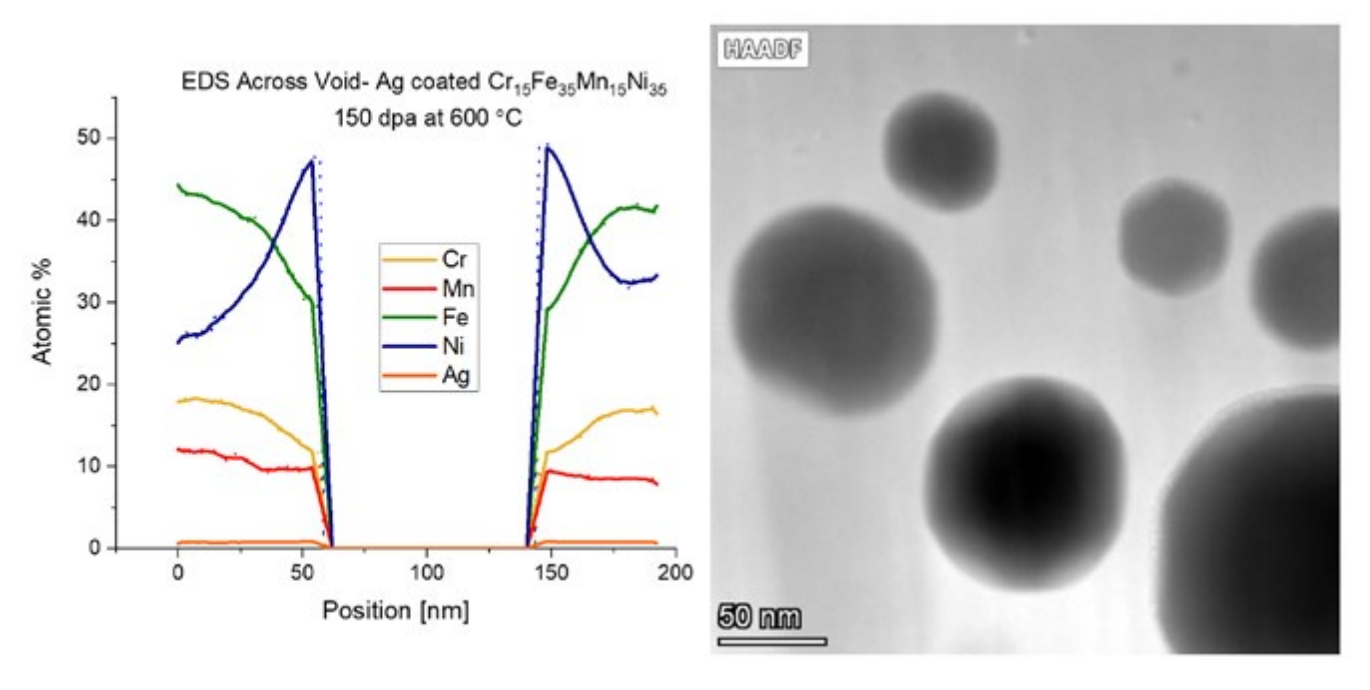


Figure 2. Example chemical redistribution linescan across a void (left) and HAADF image of void (right) in $Cr_{15}Fe_{35}Mn_{15}Ni_{35}$. Linescan value at each position is a result of averaging over 50–60% of the void width.

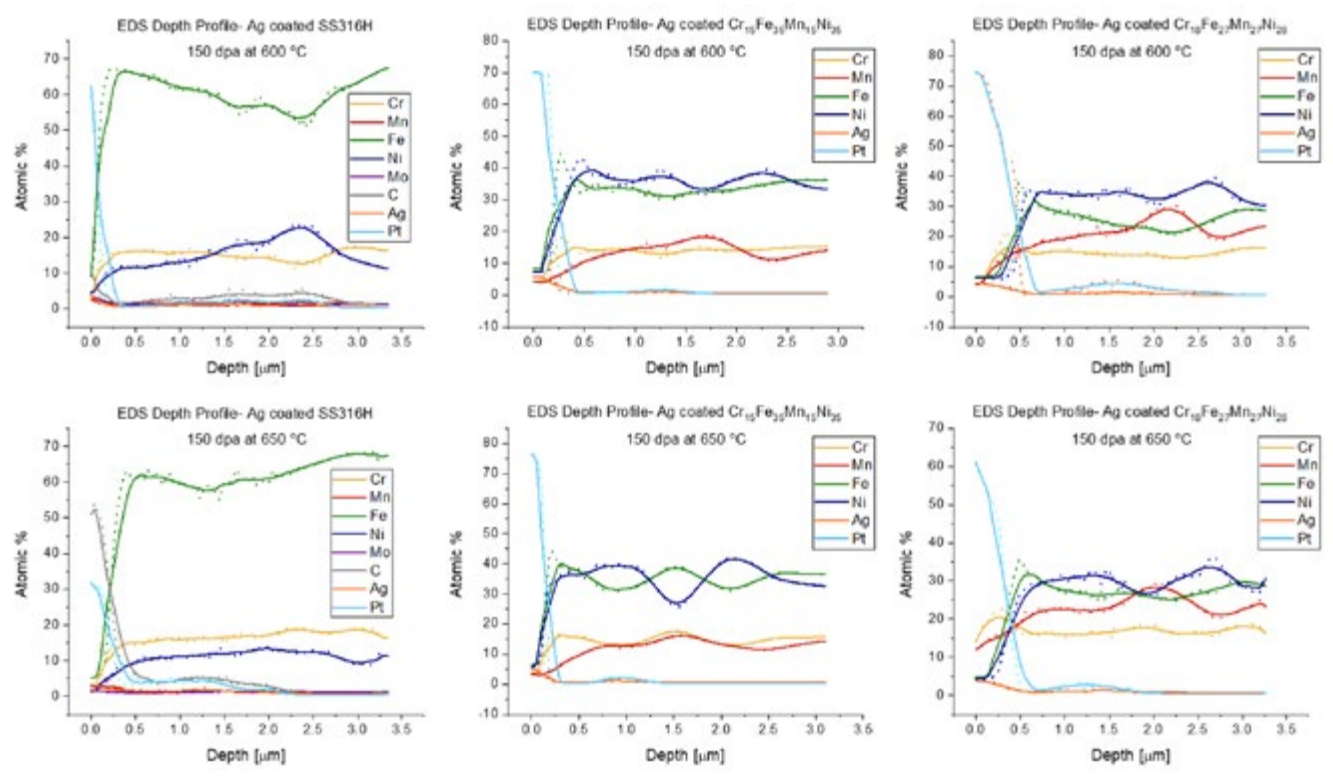


Figure 3. Super-X EDS chemical maps and depth profile line scan of Ag-coated SS316H, $Cr_{18}Fe_{27}Mn_{27}Ni_{28}$, $Cr_{15}Fe_{35}Mn_{15}Ni_{35}$ irradiated to 150 dpa at 600 and 650°C using 4.0-MeV Ni heavy ions. Linescan value at each position is a result of averaging over the width of the lamella, typically 12–15- μ m width.

This work contributes to the fundamental understanding of compositional complexity as it affects microstructural and microchemical evolution under irradiation by helping to pinpoint the majorly diffusing species. The work completes a comprehensive study comparing the temperature and dose dependence of irradiationinduced swelling and chemical redistribution in these alloys to SS316H, a conventional structural material, and will be published alongside previous results. Whereas, previously, the egress of Mn at temperatures above 600°C rendered characterization of swelling in Cr₁₈Fe₂₇Mn₂₇Ni₂₈ useless and swelling in Cr₁₅Fe₃₅Mn₁₅Ni₃₅ suspect, the Ag coating provides a novel solution for retaining high-vapor-pressure constituent elements under high-temperature,

high-vacuum-level conditions over the long times required for high-dpa irradiation experiments. An opportunity remains for future optimization of the Ag layer to strike a balance between the favorable diffusion-barrier effects and any unforeseen phenomena that may arise from alteration of the local chemical landscape at the polished sample surface. The study also underscores the importance of high-throughput studies in CCA swelling because, while a reduction in swelling is evident compared to conventional structural materials, significant variation in the temperature dependence of irradiation effects is observed within the same CCA family.

RTE 4681: Completion Report: The Role of Nb and Impurities on Nano-Oxide Retention Under Neutron Irradiation

PI: Elizabeth Getto (United States Naval Academy)

Collaborator: Stephen Taller (ORNL)

Facility: Low Activation Materials Development and Analysis Laboratory, Oak Ridge National Laboratory

Several Fe-based alloys using various compositions and processing techniques are currently being considered for ATF applications in currently operating commercial LWRs, advanced reactors, and small modular reactors. These reactor environments require materials that can perform under extreme conditions including elevated temperatures, high displacement damage, and corrosive conditions. Unique metallurgical methods, such as powder metallurgy processing techniques, can produce oxide dispersion strengthened (ODS) alloys to form nanoclusters and nanooxides within the microstructure for elevated creep strength and radiation resistance. These alloys, namely OFRAC [1] and 14YWT [2, 3], also use compositional control to tailor the nanofeatures present in the as-processed condition as well as promote elevated-temperature corrosion and oxidation resistance. Interstitial impurity elements such as C and N in 14YWT, as well as alloying-element impurities, lead to significant variations in mechanical properties [2]. For example, the SM11 heat of 14YWT had significantly higher impurity

content (wt% of 0.034 C, 0.390 N and 0.247 O) relative to other 14YWT heats and exhibited a tensile strength exceeding 2 GPa at room temperature. Cleaner heats, such as SM12, (wt% of 0.036 C, 0.011 N and 0.094 O), only measured 1.2 GPa in ultimate tensile strength at room temperature, but had higher fracture toughness. OFRAC was designed to reduce the elemental impurities through the deliberate addition of Nb for its strong affinity to form Nb-carbonitrides. However, there is a significant gap in the material-performance database for these alloys within an elevated temperature (>275°C) neutron-radiation environment. The objective of this work was to evaluate the effectiveness of impurity sequestration under irradiation conditions relevant to current and advanced reactors using detailed PIE. We hypothesized that the addition of a more-stable carbonitride former, such as Nb. would reduce the amount of Ti loss from (Y,Ti,O) nano-oxides through the reduction of Ti capture in the lattice by impurities following ballistic dissolution, thereby retaining nano-oxide density and

size and enhancing nano-oxide effectiveness as a defect sink across all temperatures. The outcome of this work provided quantitative analysis of the irradiated microstructure, including dislocation loops, nano-oxides, and any secondary precipitate phases as a function of temperature to compare with the as-fabricated alloys. The availability of this dataset will support ongoing development activities in determining composition windows for ODS steels that will provide both acceptable creep resistance and irradiation resistance both for current reactors and for advancedreactor applications.

The alloys in this work were irradiated in the HFIR for four cycles (~8 dpa) at nominal temperatures of 300, 385, and 525°C to represent conditions for LWR and advanced-reactor designs. While five ODS variants were included in the irradiation campaign, the primary focus of this RTE will be a comparison of "legacy" ODS steel (i.e., 14YWT) with an ODS steel designed for impurity sequestration (OFRAC) through the addition of Mo, Ti, and Nb to form (Nb,Ti) rich carbonitrides.

In this work we used the NSUF capabilities at the LAMDA laboratory at ORNL for lamella preparation using FIB methods and STEM on the FEI Talos G200X S/TEM instrument. Multiple lamella were produced for each specimen and progressively thinned using lower-energy ions until a final polishing step of 2 kV Ga

ions. General images for comparison were obtained using multiple imaging modes of STEM-BF, two low-angle DF detectors (STEM-DF1 and STEM-DF2), and a HAADF detector. To separate out oxides, precipitates, and cavities, all of which can appear as dark circular figures in STEM-HAADF, EDS mapping was performed over several areas of each lamella. The dislocation microstructure was imaged using STEM-BF with the lamella tilted to a low-order zone axis.

Preliminary results from this NSUF RTE study are given in Figures 1 and 2. Preliminary work demonstrated the resilience of the nano-oxides from these heats to common manufacturing processes required for claddingtube production through detailed microstructural characterization of the fabricated components [1, 4]. In Figure 1, Nb stabilized Y/Ti-rich dispersed phases. Dispersoid diameter was shown in Figure 2. Diameter decreased with temperature for both alloys. Number density of dispersed phases was retained in OFRAC, but increased with temperature in 14YWT. As hypothesized, the general population of dispersoids did not change significantly in OFRAC under these irradiation conditions, especially compared to 14YWT. Additional work will be needed to confirm or refute the loss of Ti as a mechanism, but this NSUF RTE study provided the data to continue the analysis.

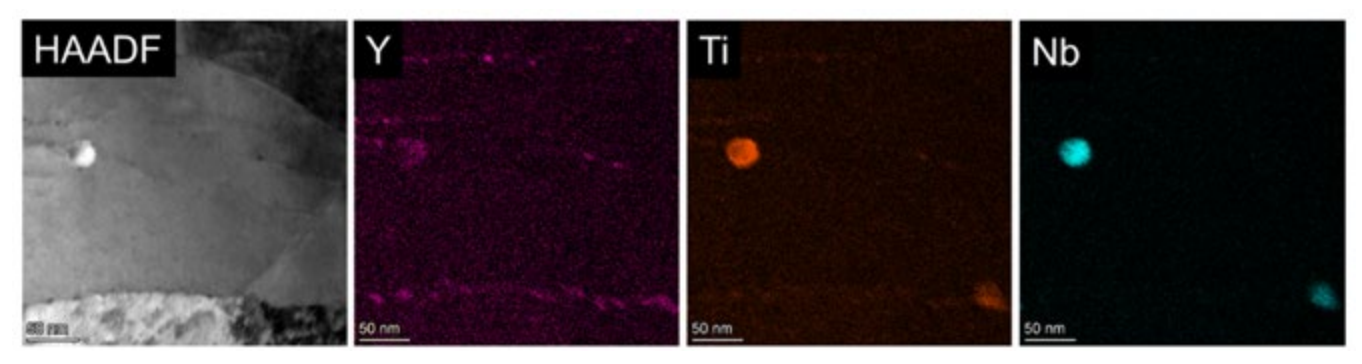


Figure 1. STEM-HAADF and corresponding EDS maps for Y, Ti, and Nb, showing the retention of precipitates after \sim 8 dpa irradiation in HFIR at a target temperature of 525°C.

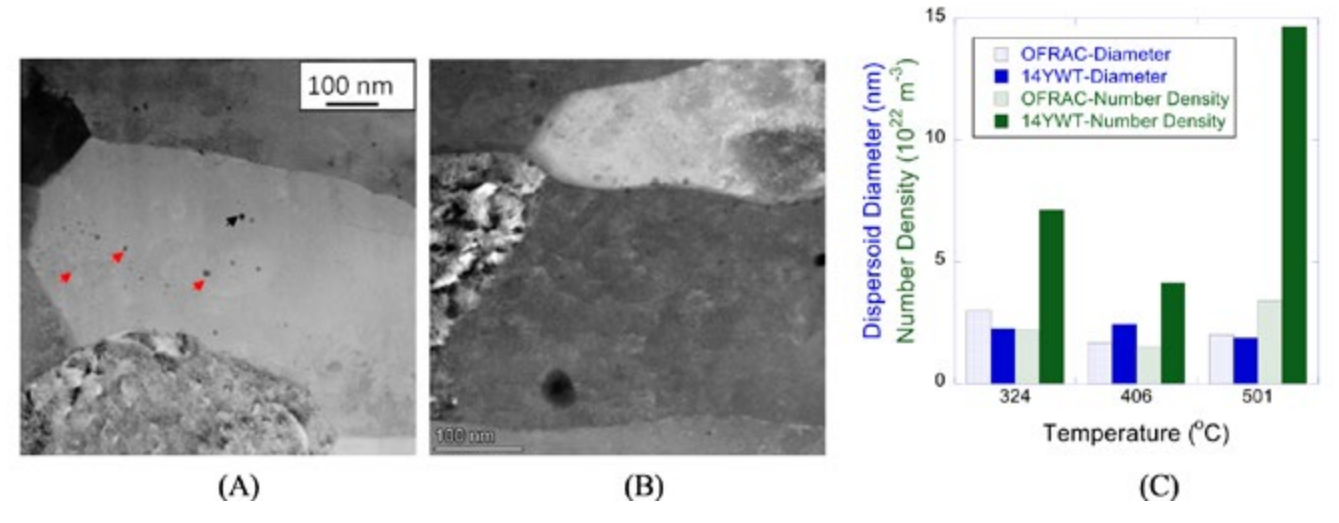


Figure 2. (A) 324° C, 8 dpa, OFRAC HAADF STEM (B) 324° C, 8 dpa, 14YWT HAADF STEM (C) Quantification of dispersoid diameter and number density. The black arrow points out a cavity observed while the red arrows highlight dispersoids.

Acknowledgements

The team acknowledges Jesse Werden, Caleb Massey, David Hoezler and the technical staff at the LAMDA laboratory for sample preparation, HFIR-irradiation parameters, and detailed discussions of the alloy fabrication routes.

Anticipated Publications and Presentations

- [1] E. Getto, S. Taller, C. Massey, D. Hoelzer. "Microstructure and mechanical properties of ODS steels irradiated in HFIR to 8 dpa." Manuscript in preparation.
- [2] E. Getto, S. Taller, C. Massey, D. Hoelzer. "The Role of Nb and Impurities on Nano-oxide Retention under Neutron Irradiation" *NuMat*, 2024.

Lessons Learned

Samples were available, and we encountered no problems at LAMDA. The final time for sample preparation was not given to the PI, so it was a little unclear how many hours were left for the actual imaging. As far as RTEs go, the whole process was extremely efficient and easy.

RTE 4743: Swelling Resistance of Additively Manufactured Grade 91 Steel Produced with Integrated Thermal Processing

PI: Daniel Codd (KVA Stainless)

Collaborators: Stephen Taller (ORNL), Valentin Pauly, Kai Sun (University of Michigan)

Facility: Michigan Ion Beam Laboratory, University of Michigan

The uniquely hostile environment within a nuclear reactor poses extreme challenges for materials because of high thermal flux, intense irradiation fields, high stresses, and reactive fluids and gases. Operational conditions of Generation IV nuclear reactor concepts will place significant demands on their structural materials, and irradiation-induced swelling is a concern for several proposed reactor types. Thus, any material solutions must be scalable, sustainable, and low cost; nuclear-materials development can be accelerated by innovative materials processing such as additive manufacturing [1]. Variable solidification parameters and temperature gradients inherent to AM as layers progressively build can change microstructures and impart significant residual stresses, distortion, weakening, or cracking [2]. These variations are compounded in hightemperature nuclear materials; specific microstructural features (precipitates, phases) which impart swelling resistance [3, 4] can degrade across an AM-print volume. This is apparent in F-M materials such as Grade 91 (Gr.91) modified 9Cr-1Mo steel, which possess sufficient Cr and C content that they respond to heat

treatments—rapid cooling from the austenitization temperature results in a martensitic microstructure. These are nominally processed for high strength and toughness through subsequent treatments to obtain tempered martensite along with MX and M2X carbonitrides, and M₂₃C₆ carbide precipitates. AM deposition without additional heat treatments creates brittle untempered martensite, which severely reduces ductility. In contrast, controlling the AMbuild thermal profile with integrated thermal processing offers the possibility to produce desired, tempered martensitic microstructures without offline heat treatments.

In this work, we used the NSUF capabilities at the MIBL for dualion irradiation of three variants of wire-arc additively manufactured (WAAM) Gr.91 steel with and without integrated thermal processing and one traditional wrought Gr.91 sample. We also used the Michigan Center for Materials Characterization for TEM lamella preparation and characterization of dislocation loops, nano-oxides, precipitates, and cavities. WAAM narrow walls (120 mm long × 22

mm high) were produced with samples extracted in the X-Z plane parallel to the transverse (X) and build (Z) directions. Specimens were irradiated in late January 2024 at MIBL with co-injected Fe and He ions to produce displacement damage and transmutant He for simulating the neutron-irradiation environment using the dual-ion configuration at MIBL [5] and following ASTM procedures as close as possible [6]. Fe³⁺ ions at 9 MeV, with a midrange dose rate of $\sim 7.5 \times 10^{-4}$ dpa/s and energy-degraded 3.42 MeV He²⁺ ions were used to produce a target dose of 184 dpa at midrange depth of ~1200 nm with the irradiation conducted at 475°C (Table 1). The energy-degraded He beam was created through an aluminum foil 6.2 µm thick, mounted in a rotating motorized foil degrader and implanted in the sample from normal to an angle of 60 degrees from normal. The He-beam energy was reduced through the foil to deliver a consistent injection profile of 0.8 appm He/dpa between 600 and 1500 nm from the surface using the methodology described in Ref. [7]. The temperature for dualion irradiation was monitored by both a thermocouple attached to one specimen and a 2-D thermal

imager, resulting in a measured temperature of $474.9 \pm 3.5^{\circ}$ C ($T_{avg}\pm 2\sigma$). The possibility of carbon contamination was reduced using the combination of a plasma cleaner prior to irradiation and the continuous use of a liquid-nitrogencooled anti-contamination device during the ion bombardment, as described in Ref. [8]. The pressure in the target chamber remained before 10^{-7} torr for the approximately 68-hour experiment.

After ion irradiation, samples were transferred to the Michigan Center for Materials Characterization for TEM lamella production using the FIB liftout method. Multiple

lamella were produced for each specimen and progressively thinned using lower-energy ions until a final polishing step of 2-kV ions. Generalized images for comparison were obtained using multiple imaging modes of STEM-BF, two low-angle dark-field detectors (STEM-DF1 and STEM-DF2), and a STEM-HAADF detector. In the current study, the TEM specimens were tilted to either [100] or [110] zone axis and imaged at STEM-BF conditions to identify the type of dislocation loops based the methodologies presented in Refs. [9, 10]. The precipitates were characterized by EDS mapping on a FEI Talos S/TEM. Lamella thickness was estimated using EELS.

Table 1. Alloy and experimental conditions with associated PIE time.

Material, processing	Ion Irradiation Conditions	Target dpa / Fe³+ Fluence	Irradiation Temperature (°C)
Traditional Gr.91, heat 30176	9 MeV Fe ³⁺ with He co-injection,	184 at 1200 nm	475 ± 3.5
WAAM DED Gr.91, as-fabricated	7.5×10^{-4} dpa/s, 0.8 appm He/dpa depth		
WAAM DED Gr.91 post-build heat treatment			
WAAM DED Gr.91 KVA integrated thermal processing			

An overview of the irradiated microstructure can be found in Figure 1, presented with both STEM-BF and STEM-HAADF. As expected for Gr.91, the lath microstructure is clearly visible at the TEM length scale. Higher-magnification images demonstrate the complexity of the irradiated microstructure as a mixture of dislocation loops, dislocation lines, carbides precipitates, a silicon oxide inclusion, and radiation-induced cavities. The wrought Gr.91/T91 heat 30176 contains a small density of larger

dislocations while the conventional as-fabricated and offline 730°C, 30 min post-build heat treatment resulted in larger dislocation-loop densities. Qualitatively, the dislocation microstructure in the integrated-processing condition is more similar to T91 compared to either the as-fabricated or post-build heat treatment. The traditional T91 heat had a large distribution of cavities, with diameters ranging from several nanometers to greater than 50 nm, likely showing the largest amount of swelling of the

four conditions. In all three WAAM variants, the maximum cavity size is reduced and appears to be the lowest in the integrated-processing specimen. The Gr.91 WAAM variants did not result in more swelling than a traditional Gr.91 steel, indicating their potential for nuclear applications where swelling is a concern. The impact of these results is that WAAM may be a viable manufacturing method for Grade 91 structural components and repairs, and further evaluation of its performance is needed.

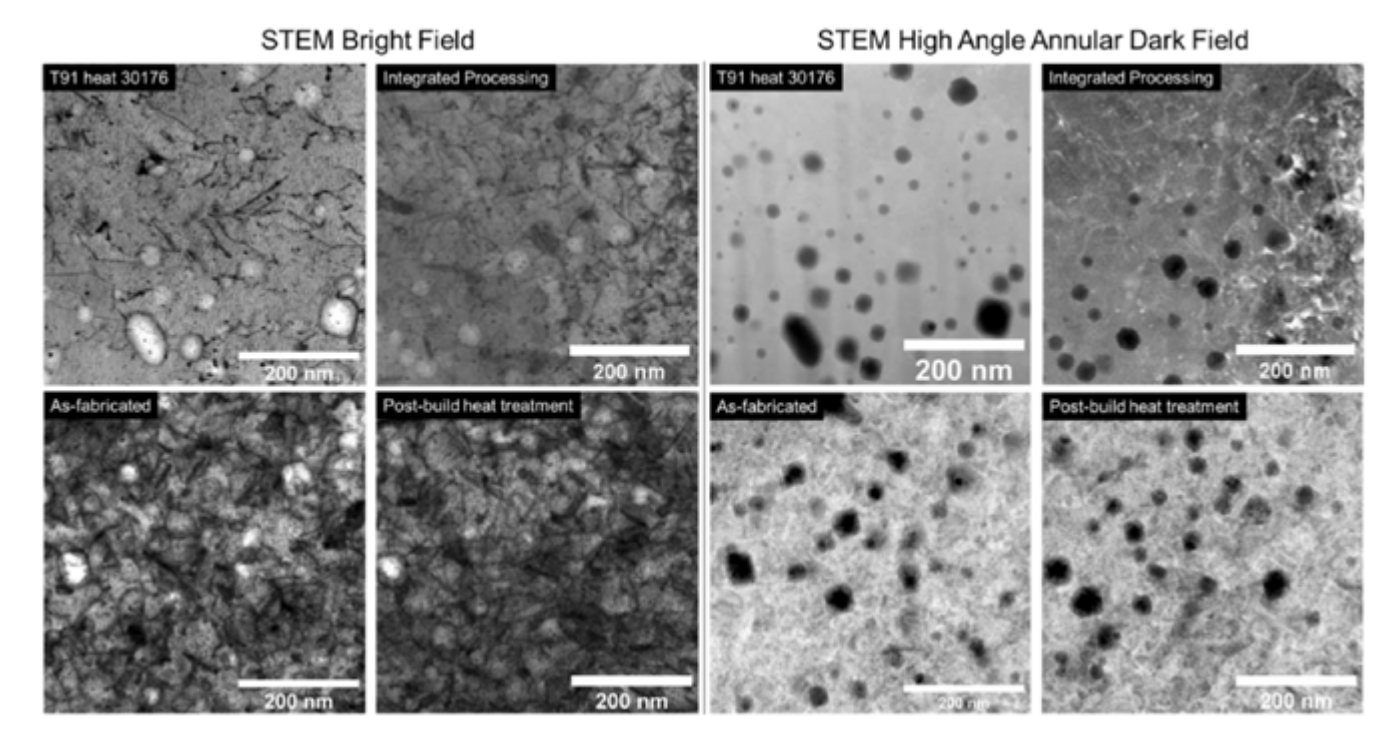


Figure 1. (Left) STEM-BF images taken on either the [001] or [011] zone axes to show the dislocation loop and dislocation line microstructure in the regions of interest, (right) with STEM-HAADF images taken to show the cavity microstructure in the regions of interest across the four examined variants of Grade 91.

Acknowledgement

Integrated thermal processing and conventional WAAM specimen generation supported by the U.S. Department of Energy, Office of Science, Office of Nuclear Energy, under Award Number DE-SC0023735.

Disclaimer

This report may contain research results which are experimental in nature. Neither the United States Government, nor any agency thereof, nor UT-Battelle, LLC, nor any of their employees, makes any warranty, express or implied, or assumes any legal responsibility for the accuracy, completeness, or usefulness of any information, apparatus, product, or process disclosed, or represents that its use would not infringe privately owned rights. Reference to any specific commercial product, process, or service by its trade name, trademark, manufacturer, or otherwise, does not constitute or imply an endorsement or recommendation by the United States Government or any agency thereof, or by UT-Battelle, LLC. The United States Government reserves for itself a royalty -free, worldwide, irrevocable, non-exclusive license for Governmental purposes to publish, disclose, distribute, translate, duplicate, exhibit, prepare derivative works, and perform any such data included herein. The views and opinions of authors expressed herein do not necessarily state or reflect those of the United States Government or any agency thereof, or by UT-Battelle, LLC and shall not be used for advertising or product endorsement purposes.

References

- [1] F. Balbaud et al. "A NEA review on innovative structural materials solutions, including advanced manufacturing processes for nuclear applications based on technology readiness assessment," *Nuclear Materials and Energy*, 2021, pp. 101006–101006, doi: 10.1016/j.nme.2021.101006.
- [2] T. DebRoy et al. "Scientific, technological and economic issues in metal printing and their solutions," *Nat Mater* 18, (10), Oct 2019, pp. 1026–1032, doi: 10.1038/s41563-019-0408-2.
- [3] F. A. Garner, M. B. Toloczko, and B. H. Sencer. "Comparison of swelling and irradiation creep behavior of fcc-austenitic and bcc-ferritic/martensitic alloys at high neutron exposure," *Journal of Nuclear Materials* 276, (1), 2000, pp. 123–142, doi: 10.1016/S0022-3115(99)00225-1.
- [4] A. Bhattacharya and S. J. Zinkle. "Cavity Swelling in Irradiated Materials," in *Comprehensive Nuclear Materials* 1, 2020, Elsevier, pp. 406–455.
- [5] S. Taller et al. "Multiple ion beam irradiation for the study of radiation damage in materials," *Nuclear Instruments and Methods in Physics Research, Section B: Beam Interactions with Materials and Atoms* 412, 2017, pp. 1–10, doi: 10.1016/j. nimb.2017.08.035.
- [6] A. International. "Standard Practice for Investigating the Effects of Neutron Radiation Damage Using Charged-Particle Irradiation," 2023, doi: 10.1520/e0521-23.
- [7] S. Taller, F. Naab, and G. S. Was. "A methodology for customizing implantation profiles of light ions using a single thin foil energy degrader, *Nuclear Instruments and Methods in Physics Research*," Section B: Beam Interactions with Materials and Atoms 478, June 2020, pp. 274–283, doi: 10.1016/j.nimb.2020.07.017.
- [8] G. S. Was et al. "Resolution of the carbon contamination problem in ion irradiation experiments," *Nuclear Instruments and Methods in Physics Research*, Section B: Beam Interactions with Materials and Atoms 412, 2017, pp. 58–65, doi: 10.1016/j.nimb.2017.08.039.
- [9] B. Yao, D. J. Edwards, and R. J. Kurtz, "TEM characterization of dislocation loops in irradiated bcc Fe-based steels," *Journal of Nuclear Materials* 434, (1-3), 2013, pp. 402–410, doi: 10.1016/j.jnucmat.2012.12.002.
- [10] C. M. Parish, K. G. Field, A. G. Certain, and J. P. Wharry, "Application of STEM characterization for investigating radiation effects in BCC Fe-based alloys," *Journal of Materials Research* 30, (9), 2015, pp. 1275–1289, doi: 10.1557/jmr.2015.32.

RTE 4797: An Evaluation of Effects of Ion Irradiation on Crystal, Microstructural, and Mechanical Properties of Alloy 709

Chinthaka M. Silva, Shalini Tripathi, Isabella J. van Rooyen (PNNL)

Collaborators: Lin Shao, Zhihan Hu (TAMU)

Facility: Ion Beam Laboratory, Texas A&M University

Among the austenitic steels of interests for next-generation nuclear reactors, Alloy 709 has shown good creep strength and ion-irradiation behavior up to 400 dpa [1]. However, reported studies of irradiation behavior of Alloy 709 fabricated using unconventional methods are rare in the literature. In this NSUF-RTE, ion irradiation behavior of Alloy 709 samples fabricated using friction-consolidation was investigated.

Irradiation of as-received material, which was used as a reference

material, fabricated using conventional casting was also performed. Out of the eight samples irradiated at 100, 200, 300, and 400 dpa (four friction consolidated and four as-received), preliminary statistics on radiation-induced voids of five samples are given in this report. These five samples consist of four friction-consolidated and one as-received irradiated samples. Irradiation of an area of 5 mm \times 5.5 mm of each sample using 3.5 MeV double charged Fe²⁺ with a beam current of 140 nA and a dpa rate of 1.7×10^{-3} dpa/s at $575 \pm 3^{\circ}$ C

was performed at TAMU Ion Beam Laboratory. A chamber vacuum of 8×10^{-8} torr was maintained using a liquid-nitrogen cold trap. Figure 1a shows the SRIM calculated displacements per atom and injected interstitials profiles as a function of depth of the sample. The maximum energy deposition and, therefore, the maximum void swelling is expected at a depth of ~1 μ m from the sample surface. This observation was confirmed by STEM-HAADF image given in a typical irradiated sample in Figure 1b.

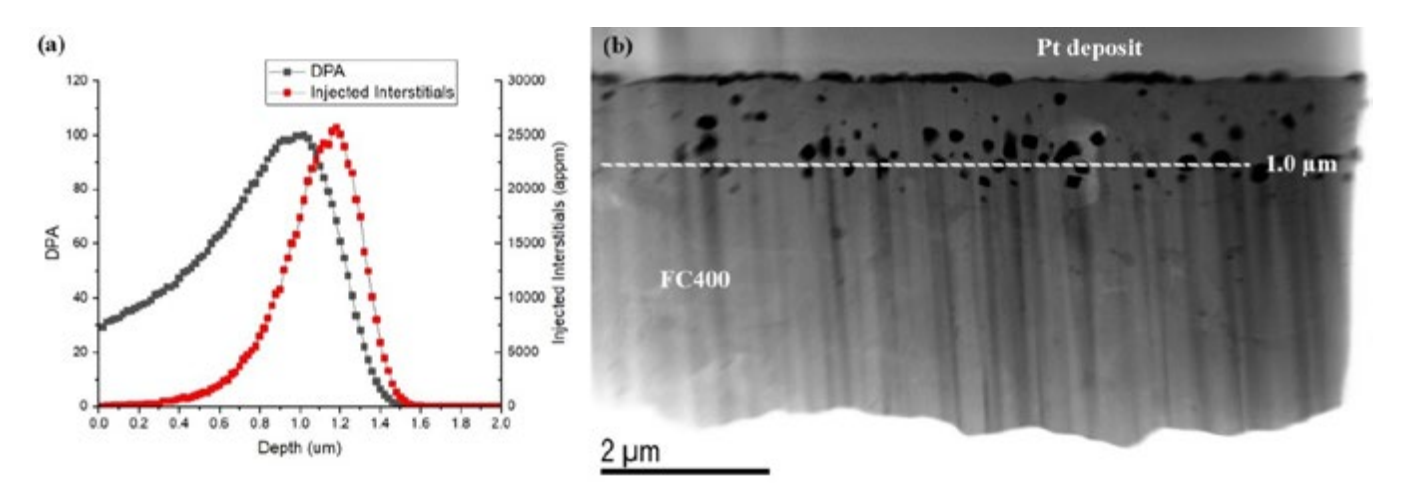


Figure 1. (a) Displacements per atom and injected-interstitials profiles as a function of depth and (b) a typical STEM-HAADF micrograph of ion-irradiated friction-consolidated sample (FC400).

The dotted line in (b) indicates maximum void swelling region at ~1 µm deep from the sample surface. Table 1 depicts size, density, and swelling of radiation-induced voids in the samples. Void swelling was calculated using the method (or equation) reported elsewhere. [2] An approximate specimen thickness of 100 nm, which is typical for FIB lamella, and an assumption of spherical shape for the voids were used in the calculations. As expected, overall size of the voids of friction-consolidated Alloy 709 increased with the increase in dpa values of the ion irradiation. The change in void size is insignificant from 100 to 200 dpa, compared to the change from 200 to between 300 and 400 dpa irradiations.

At 300 and 400 dpa, size of voids remains similar, considering the standard deviations of the size distributions. Void density, on the other hand, showed a significant increase from 100 to 200 dpa irradiation. At 300 and 400 dpa, void density decreased back to a value that is slightly larger than that of the 100 dpa. This observation reflects the void-size variation of the samples—that is, lower void density for 300 and 400 dpa samples with larger voids. While a slight increase in void swelling was obtained when irradiation increased from 100 to 200 dpa, ~5 times larger void swelling was observed for the 300 dpa irradiation. A slight voidswelling increase was also observed when the irradiation increased

from 300 to 400 dpa. Relative to the friction-consolidated sample, the as-received sample showed similar void size, smaller void density, and smaller void swelling at 200 dpa irradiation. These preliminary results suggest that the irradiation behavior of the friction-consolidated Allloy 709 sample is poorer than that of the cast sample at 200 dpa. However, more data are needed for the as-received samples irradiated at other dpa values (i.e., 100, 300, and 400 dpa) for further comparison of the two fabrication techniques. Future investigation will include characterization of as-received samples irradiated to other dpa values, and this effort may have to include new irradiation as well.

Table 1. Void statistics acquired form the ion-irradiated friction-consolidated and as-received Alloy 709.

Sample	dpa avg.	Void radius (nm)	Void density (×10 ¹⁹ m ⁻³)	Void swelling (%)
FC100	100	60 ± 19	9.5 ± 0.8	0.40 ± 0.01
FC200	200	64 ± 17	26.2 ± 1.4	0.89 ± 0.02
FC300	300	125 ± 52	11.9 ± 1.4	4.42 ± 0.30
FC400	400	140 ± 55	11.3 ± 0.5	5.95 ± 0.35
AR200	200	50 ± 20	12.8 ± 7.3	0.41 ± 0.02

References

[1] H. Kim, J. G. Gigax, J. Fan, F. A. Garner, T.-L. Sham, and L. Shao. "Swelling resistance of advanced austenitic alloy 709 and its comparison with 316 stainless steel at high damage levels." *J. Nucl. Mater.* 527, 2019. 151818.

[2] J. G. Gigax, T. Chen, H. Kim, J. Wang, L. M. Price, E. Aydogan, S. A. Maloy, D. K. Schreiber, M. B. Toloczko, F. A. Garner, L. Shao. "Radiation response of alloy T91 at damage levels up to 1000 peak dpa." *J. Nucl. Mater.* 482 2016, 257–265.

ACRONYMS

AFM	Atomic force microscopy
AFSD	Additive friction stir deposition
AM	Additive manufactured
AML	Activated Materials Laboratory
AMTS	Automated Mechanical Testing System
ANL	Argonne National Laboratory
ANSTO	Australian Nuclear Science and Technology Organization
APS	Advanced Photon Source
APT	Atom-probe tomography
ASNF	Aluminum-clad spent nuclear fuel
ATF	Accident-tolerant fuel
ATR	Advanced Test Reactor
bcc	body-centered cubic
BF	Bright-field
BWR	Boiling-water reactor
G	Collaborative Computing Center
CAES	Center for Advanced Energy Studies
CCA	
CEvNS	Coherent elastic neutrino nucleus scattering
CG	
CINR	Consolidated Innovative Nuclear Research
CRC	Center for Radiation Chemistry
CTB	Coherent twin boundaries
CVD	Chemical vapor Deposition
CW	Cold-worked
DAQ	Data acquisition
DED	Direct energy deposition
DF	Dark-field
D0E	Department of Energy

DOE-NE Department of Energy Office of Nuclear Energy
EBR Experimental Breeder Reactor
EBSDElectron backscattered diffraction
EDS Energy dispersive X-ray spectrometry
EELS Electron energy loss spectroscopy
EMPAD Electron-microscope pixel-array detector
EPMA Electron probe microanalysis
EPRI Electric Power Research Institute
EXS Energy-dispersive X-ray spectroscopy
FASBFuels and Applied Science Building
FAST Fission Accelerated Steady-state Test
FCCIFuel/cladding chemical interaction
FIBFocus ion beam
GAGeneral Atomics
GBS
GIFGamma Irradiation Facility
GPAGeometric phase analysis
HAADFHigh-angle annular dark field
HBSHigh-burnup structure
HEA High-entropy alloys
HEMT High-electron-mobility transistors
HEX-MHigh-Energy X-ray Microscope
HFEFHot Fuel Examination Facility
HFIR High Flux Isotope Reactor
IACIrradiation-accelerated corrosion
IASCCIrradiation-assisted stress corrosion cracking
IMCLIrradiated Materials Characterization Laboratory
INL
INSETIn-Pile Steady State Extreme Temperature

IVEM	Intermediate Voltage Electron Microscope	PNNLPacific Northwest National Laboratory
LAMDA	Low Activation Materials Development and Analysis	PWRPressurized water reactor
LANL	Los Alamos National Laboratory	RIDRadiation-induced defects
LEAP	Local-electrode atom-probe	RIP
LPBF	Laser powder-bed fusion	RISRadiation-induced segregation
LWR	Light-water reactors	RTERapid Turnaround Experiment
LWRS	Light Water Reactor Sustainability	SAEDSelective-area electron diffraction
MaCS	Microscopy and Characterization Suite	SEMScanning electron microscopy
MCNP	Monte Carlo N-Particle	SFSlip faults
MIBL	Michigan Ion Beam Laboratory	SFEStacking-fault energy
MIT	Massachusetts Institute of Technology	SPSSpark-plasma sintering
M00SE	Multiphysics Object Oriented Simulation Environment	SRIMStopping and Range of lons in Matter
MPEA	Multi-principal element alloy	SROShort-range order
NE	Nuclear Energy	STEMScanning transmission electron microscopy
NEUP	Nuclear Energy University Program	STTRSmall Business Technology Transfer
NFML	Nuclear Fuels and Materials Library	SuperRTESuper Rapid Turnaround Experiment
NPP	Nuclear power plants	TAMUTexas A&M University
NRDS	Nuclear Research Data System	TCM Thermal conductivity microscope
NSLS	National Synchrotron Light Source	TEMTransmission electron microscopy
NSUF	Nuclear Science User Facilities	TJ Triple junctions
ODS	Oxide dispersion-strengthened	TRIPTransformation-induced plasticity
ORNL	Oak Ridge National Laboratory	TRISOTri-structural isotropic
0SU	The Ohio State University	UCSBUniversity of California at Santa Barbara
OSU-NRL	The Ohio State University Nuclear Reactor Laboratory	UFGUltra-fine grained
OSURR	The Ohio State University Research Reactor	UIUCUniversity of Illinois at Urbana-Champaign
OT	Over-temperature	UNTUniversity of North Texas
PALM	Power Axial Locator Mechanism	U.S
PANDA	Predictive Automation of Novel Defect Anomalies	UTKUniversity of Tennessee, Knoxville
PCB	Printed circuit boards	WAAM Wire-arc additively manufactured
PED	Precession electron diffraction	WAXSWide-Angle X-ray Scattering
PFM	Piezoresponse force microscopy	XCTX-ray computed tomography
PI	Principal investigator	XPDX-ray powder diffraction
PIE	Post-irradiation examination	XRDX-ray diffraction
PM-HIP	Powder metallurgy-hot isostatic pressing	

INDEX

Partner Institutions

Argonne National Laboratory	11, 12, 42, 56, 58, 64, 74, 96, 134, 140, 141, 210, 214
Advanced Photon Source	12, 74, 210, 212, 214
Intermediate Voltage Electron Microscopy-Tandem Facility	
Brookhaven National Laboratory	
National Synchrotron Light Source-II	124
Center for Advanced Energy Studies12, 20, 32, 33, 34, 35,	48, 51, 49, 52, 70, 84, 94, 114, 120, 128, 172, 178, 182, 183, 185, 186, 189, 196, 210
Microscopy and Characterization Suite	
Idaho National Laboratory	40-43, 45, 46, 52, 53, 56, 70, 72, 74, 78, 90, 108, 111, 112, 124, 183, 189, 210
Advanced Test Reactor	36, 37, 39, 42, 45, 48, 72, 75, 106, 107, 108, 136, 137, 138, 182, 183, 185, 189, 210
Electron Microscopy Laboratory	
High Performance Computing	
Materials and Fuels Complex	
Irradiated Materials Characterization Laboratory	12, 27, 28, 29, 32, 33, 35, 52, 53, 72, 78, 210
Hot Fuel Examination Facility	12, 18, 22, 26, 35, 72, 210
Lawrence Livermore National Laboratory	12
Los Alamos National Laboratory	11, 12, 38, 40, 41, 43, 134, 182, 184, 211
Massachusetts Institute of Technology	
Nuclear Reactor Laboratory	
North Carolina State University	
Oak Ridge National Laboratory	43, 46, 76, 80, 112, 166, 167, 170, 176, 177, 182-185, 190, 200, 201, 204, 211
Low Activation Materials Development and Analysis Facility	
Irradiated Fuels Examination Laboratory	
Gamma Irradiation Facility	210
Pacific Northwest National Laboratory	4, 90, 94, 106, 107, 108, 111, 114, 136, 138, 182, 183, 185, 186, 189, 208, 211
Material Science and Characterization Laboratory	213

Pennsylvania State University	213
Purdue University	
Ion Beam Laboratory	70, 90, 128, 196, 204, 208, 211, 213
Accelerator Laboratory	
The Ohio State University	162, 163, 166, 176, 177, 194, 211, 213
University of California, Berkeley	213
University of Florida	70, 78, 94, 170, 213
University of Michigan	90, 112, 128, 162, 204, 213
Michigan Ion Beam Laboratory	90, 128, 204, 211, 213
University of Texas at Austin	213
University of Wisconsin	106, 136, 213
Westinghouse	90, 213



(Top left) University of Michigan doctoral student Alexander Kavner calibrates the germanium detector placed in the thermal neutron beam and the tagging sodium iodide detector. (Bottom left) PI Igor Jovanovic reviews the in-situ data from testing. Irradiations for Jovanovic's RTE, "Measurement of 254-eV Nuclear Recoils in Germanium" were performed at The Ohio State University Research Reactor using the Thermal Neutron Beam Facility.

